

https://dspace.org/

Thermodynamics of metal-insulator systems

Kasl, Charles.

1996
https://hdl.handle.net/10539/26123

Downloaded from a DSpace repository. https://dspace.org/

THERMODYNAMICS OF METAL-INSULATOR SYSTEMS

by

Charles Kasl

A dissertation submitted to the Faculty of Science, University of the Witwatersrand, Johannesburg, in fulfilment of the requirements for the degree of Master of Science.

Johannesburg, 1996

DECLARATION

I declare that this dissertation is my own, unaided work. It is being submitted for the Degree of Master of Science in the University of the Witwatersrand, Johannesburg. It has not been submitted before for any degree or examination in any other University

29 day of JULY 1996

ABSTRACT

The properties of systems which undergo a metal-insulator (MI) transition are currently being extensively studied. Both the transport and thermodynamic properties of these MI systems show interesting behaviour, particularly near the MI transition. A complete theory to describe MI systems does not yet exist.

In the present work the focus is on the thermodynamic properties of MI systems, in particular on the specific heat and susceptibility. The thermodynamic properties in the absence of a magnetic field are now well understood, with models such as the two-fluid model giving a good account of the behaviour.

In finite magnetic fields the thermodynamic properties are even more interesting and varied. It is the aim of the present work to develop and test models to explain the effects of applying magnetic fields to MI systems. The focus is mainly on phosphorous doped silicon, and the results are gratifying. The theory should, however, also apply to other similar MI systems.

ACKNOWLEDGEMENTS

I wish to thank my supervisor, Prof. M.J.R. Hoch, for his advice and support. I also wish to thank him for his patience, and for giving me the opportunity to continue my studies in physics. My gratitude also extends to his wife, Mrs. R.J. Hoch, for her time and advice on the contents of th dissertation.

I am grateful to the Foundation for Research Development for their financial assistance.

Lastly, I wish to express my gratitude to H. von Löhneysen and S. Wagner from the University of Karlsruhe, Germany. They supplied some original specific heat data without which the results obtained in this dissertation would have been much less complete.

Contents

List of Figures 4

1 Introduction 8
1.1 Preview . . . 13
1.2 A Brief History of MI Transition Models and their Application to MI Systems 15
1.2.1 The Mott Transition . . . 15
1.2.2 The Anderson Transition . . . 17
1.2.3 The Lifshitz Model . . . 19
1.2.4 Scaling Theories . . . 20
1.3 Recent Studies of Si:P near the MI Transition . . . 22
1.3.1 The Insulating Phase . . . 23
1.3.2 The Metallic Phase . . . 29
1.3.3 The Metal-Insulator Transition . . . 32

2 Model 1: The Poisson Distributed Spin-Pair System 38
2.1 Introduction . . . 38
2.2 The Distribution and Exchange Couplings of the Disordered Spin System . 39
2.3 The Spin-Pair Model . . . 41
2.3.1 The J-Coupled Spin-Pair . . . 42
2.3.2 The Distribution of Exchange Couplings J . . . 45
2.3.3 The Specific Heat . . . 49
2.3.4 The Susceptibility . . . 52
2.3.5 Conclusions . . . 55
2.4 The Spin-Triad Model . . . 55
2.4.1 The Specific Heat . . . 58
2.4.2 The Suceptibility . . . 60
2.4.3 The Validity of this Spin-Triad Model . . . 64
2.5 Comparisons of the Singlet, Pair, and Triad Models . . . 66
2.5.1 Specific Heat Analysis . . . 66
2.5.2 Susceptibility Analysis . . . 68
2.6 Discussion . . . 70
2.7 Publication . . . 71

3 The Extended Two-Fluid Model 72
3.1 Introduction . . . 72
3.2 The Extended Two-Fluid Model Equations . . . 75
3.3 The Specific Heat . . . 78
3.4 The Susceptibility . . . 80
3.5 The Entropy . . . 83
3.6 The Wilson Ratio . . . 84
3.7 Corrections to the Extended Two-Fluid Model Equations . . . 88

4 Testing the Extended Two-Fluid Model 91
4.1 Introduction . . . 91
4.1.1 The Specific Heat . . . 93
4.1.2 The Susceptibility . . . 94
4.2 Determination of the Excess Specific Heat . . . 95
4.2.1 Standard Method . . . 95
4.2.2 Alternative Method . . . 96
4.3 A Note on the Experimental Data Analysis . . . 98
4.4 Analysis on the Experimental Specific Heat Data . . . 100
4.4.1 Zero-Field Analysis on "Standard" Excess Specific Heat . . . 100
4.4.2 Analysis on "Standard" Excess Specific Heat in a Magnetic Field . 104
4.4.3 Review of the Results . . . 107
4.4.4 Alternative Analysis on Zero-Field Specific Heat . . . 109
4.4.5 Alternative Analysis on Specific Heat in a Magnetic Field . . . 116
4.4.6 Low Temperature Behaviour and the Nuclear Contribution . . . 124
4.5 Analysis on the Experimental Susceptibility Data . . . 129
4.5.1 Low B-Field Susceptibility . . . 129
4.5.2 High B-Field Susceptibility . . . 132
4.6 Discussion . . . 133
4.7 Publication . . . 136

5 Conclusion 137
5.1 The Spin-Pair Model Revisited . . . 137
5.2 Conclusion . . . 138

A Some Basic Theoretical and Experimental Results 140
A.1 The Partition Function Z and Thermodynamic Quantities . . . 140
A.2 The Isolated Spin System and Free Electron Model . . . 141
A.3 The Silicon Lattice Specific Heat and Diamagnetic Susceptibility . . . 145

B Mathematical Details for the Poisson Distributed Spin-Pair System 147
B.1 The Poisson Distribution . . . 147
B.2 The Distribution $P(J)dJ$ of Exchange Couplings J . . . 149
B.3 Numerical Procedures . . . 153

C Mathematical Details for the Extended Two-Fluid Model 154
C.1 Evaluation of the Integrals $I_\delta(y)$ and $I_\varepsilon(y)$ 154
C.2 Extending Integrals to Infinity 158
C.3 Numerical Integration 159
C.4 Improper to Proper Integral Conversion 159
C.5 Upper Limit Analysis 160
C.6 Details of the Corrections to the Extended Two-Fluid Equations 165
C.7 Limits on α in the Extended Two-Fluid Model Formalism 170
C.8 The Extended Two-Fluid Model in the Limit $\alpha \to 1_-$ 172
C.9 The Specific Heat Peak: Some Details 173

D Evaluation of the Asymptotic Forms of $\delta(y)$ and $\varepsilon(y)$ 176
D.1 Introduction 176
D.2 The Asymptotic Form of $I_\delta(y)$ 177
D.3 The Asymptotic Form of $I_\varepsilon(y)$ 182
D.4 Conclusion 184

E Digitising Data 185

Bibliography 187

List of Figures

1.1 Plot of the absolute zero conductivity showing the MI transition for Si:P. Reproduced from [1]. For Si:P, $n_c \simeq 3.5 \times 10^{18} cm^{-3}$ [2]. 9
1.2 Plot of (a) Specific heat of 'insulating' Si:P for various magnetic fields, and (b) normalized susceptibility of Si:P on both sides of the MI transition (χ_0 is the Pauli value). Reproduced from [5] and [6] respectively. 11
1.3 Energy level diagram showing the Mott transition. Reproduced from [3]. . . 17
1.4 Density of states $n(E)$ in the Anderson model. 18
1.5 The scaling parameter $\beta(g)$. Reproduced from [4]. 21
1.6 Plots of (a) C/T versus T^2 for $B = 0$, (b) γ versus n obtained from the analysis of (a), and (c) the corresponding excess specific heat ΔC obtained from (a). The effective concentration of localized moments obtained from the $B \neq 0$ specific heat analysis is shown in (d). Reproduced from [5]. . . . 34
1.7 The (a) Wilson ratio and (b) χ/χ_0 versus γ/γ_0 plots, reproduced from [11]. 36

2.1 Plot of (a) the Poisson distribution function $P(R)$, using the Si:P values for a_B^* and $n = n_c$, and (b) the Herring-Flicker expression for the exchange coupling. The point (R_{max}, J_{max}) denotes the maximum in this function. . . 40
2.2 A spin-pair, with exchange coupling J, and corresponding energy levels. . . 41
2.3 The (a) specific heat C_0 and (b) susceptibility χ_0 of a single J-coupled spin-pair. The peak positions and asymptotic forms are also included. 43
2.4 Plot of (a) the function $p(J) = \int_0^J P(J)dJ$, and (b) the distribution function $P(J) = p'(J)$. 46
2.5 The distribution $P(\log J)$ of $\log J$ values. 47
2.6 The magnetic field dependence of the absolute zero susceptibility $\chi_{T=0K}$. . 48
2.7 The dependence of the spin-pair system specific heat C on (a) the magnetic field B, (b) the Bohr radius a_B^*, and (c) the concentration n. Fig. (d) is shown to explain a feature of fig. (c). 50
2.8 The dependence of the spin-pair system susceptibility χ on (a) the magnetic field B, (b) the Bohr radius a_B^*, and (c) the concentration n. 53
2.9 A spin-triad, where R_{ij} is the separation and J_{ij} the exchange coupling between spins i and j. 56
2.10 The energy level diagram for the spin-triad shown. 57

2.11 Dependence of the spin-triad specific heat C on (a) the parameter α, (c) the magnetic field B, and (d) the concentration n. Figure (b) plots J^*/J versus α as an aid to fig. (a). 59
2.12 Dependence of the spin-triad susceptibility χ on (a) the parameter α, (b) the magnetic field B, and (c) the concentration n. 62
2.13 Comparisons with the specific heat data in the insulating phase. Reproduced from the publication in §2.7. 67
2.14 Comparisons with the specific heat data in the metallic phase. Reproduced from the publication in §2.7. 68
2.15 Comparisons with the susceptibility data. Reproduced from the publication in §2.7. 69

3.1 A plot of (a) the function $\delta(y)$ versus $1/y$, for $\alpha = 0.63$, with (b) showing its dependence on the parameter α. 79
3.2 A plot of (a) the function $\varepsilon(y)$ versus $1/y$, for $\alpha = 0.63$, with (b) showing its dependence on the parameter α. 81
3.3 The entropy S, in arbitrary units, for various magnetic fields. 85
3.4 The magnetic field dependence of the Wilson Ratio. 86
3.5 The (a) surface of allowed $(\gamma/\gamma_0, \chi/\chi_0)$ values predicted by the extended two fluid model, and (b) a plot of $\varepsilon(y)/\delta(y)$, which determines this surface. . . . 87
3.6 Plots of the specific heat C for a (a) zero, and (b) non-zero magnetic field, showing the effects of introducing the corrections to the extended two-fluid model. 89

4.1 Plots showing (a) the field-dependence of the effective localized moment concentration N_{Sch} and itinerant contribution $\gamma(B)$, and (b) the excess specific heat ΔC in non-zero fields for a metallic sample. Reproduced from (a) [20] and (b) [5]. 97
4.2 Values obtained for α and σ from fitting the zero-field data of various donor concentrations n. 101
4.3 The excess specific heat ΔC for $B = 0$, with (a) a plot of $\Delta C/\sigma T^{1-\alpha}$ versus T, together with fits of eqn. (4.19), while (b) shows a plot of ΔC for $n = 1.6 \times 10^{18} cm^{-3}$, indicating the power law form as well as the corrected fit given by eqn. (4.18). 103
4.4 Plots of (a) the total specific heat C of an insulating sample in various magnetic fields, with (b) showing the corresponding excess specific heat ΔC obtained with the use of eqn. (4.11). Reproduced from [5]. 105
4.5 The specific heat data for $n = 0.79 \times 10^{18} cm^{-3}$ from fig. 4.4b, together with the predictions of the extended two-fluid model. 106
4.6 Predictions of the extended two-fluid model to the $n = 4.5 \times 10^{18} cm^{-3}$ specific heat data in fig. 4.1b. 107
4.7 Plots of the values obtained for β, α, σ, and γ from the fitting of eqn. (4.20) to the zero-field specific heat data. 111

4.8 The average values of σ and γ, from figs. 4.7, in a single plot to compare the relative behaviour. The insert shows γ in the metallic phase, together with predictions of the free-electron model with two different effective masses. . . 113
4.9 The excess specific heat ΔC obtained using (a) procedure 1, and (b) procedure (2). The power law form predicted by the model is shown by the straight lines. 114
4.10 The zero-field specific heat, with the phonon contribution subtracted from the data, for an (a) insulating, and (b) metallic sample. The straight lines indicate the form of the data. 115
4.11 The zero-field specific heat data for $n = 1.6 \times 10^{18} cm^{-3}$, as shown in fig. 4.10a, plotted as C/T versus T^2. This plot shows the apparent constant contribution at high T attributed to the itinerant component in the "standard" method (§4.2.1). 116
4.12 The excess specific heat ΔC for a just-insulating sample. The curves are fits of $\sigma\delta(y)T^{1-\alpha}$, with the parameters used shown in the figure. 118
4.13 The excess specific heat ΔC for a just-metallic sample. The curves are fits of $\sigma\delta(y)T^{1-\alpha}$, with the parameters used shown in the figure. 118
4.14 The electronic specific heat for $n = 3.3 \times 10^{18} cm^{-3}$ (refer to fig. 4.12). The curves are fits of eqn. (4.22) with $\gamma = 0$. The value of $\alpha = 0.4$ is much lower than expected. 120
4.15 The electronic specific heat for $n = 0.79 \times 10^{18} cm^{-3}$. The curves are fits of (4.22), with no itinerant contribution ($\gamma = 0$), and $\alpha = 0.85$. The value of $\sigma = 0.225$ was used for all fields. 120
4.16 The electronic specific heat for $n = 0.89 \times 10^{18} cm^{-3}$. The curves are fits of (4.22), with no itinerant contribution ($\gamma = 0$), and $\alpha = 0.83$. The value of $\sigma = 0.275$ was used for all fields. The $B = 1.5T$ deviation for $T \gtrsim 2K$ could be attributed to the larger uncertainties in the data occurring at these temperatures [5]. 121
4.17 The electronic specific heat for $n = 1.6 \times 10^{18} cm^{-3}$. The curves are fits of (4.22), with no itinerant contribution ($\gamma = 0$), and $\alpha = 0.7$. The values of $\sigma = 0.64$ and 0.71 were used for $B = 1.5T$ and $5.7T$. The low temperature behaviour, predicted by (4.2), is also shown. 122
4.18 The electronic specific heat for $n = 7.3 \times 10^{18} cm^{-3}$ in various magnetic fields. The curves are linear fits to the data. 123
4.19 Plots of C and C/T versus T for $n = 7.3 \times 10^{18} cm^{-3}$, in two magnetic fields. The curves are fits of (4.26) and (4.27). The low T anomaly is clearly visible as the upturn in the data. 126
4.20 Plots of C/T versus T for various concentrations, with the curves being fits of eqn. (4.27). The arrows indicate the predicted temperature up to which this expression should describe the data. 127
4.21 Plot of the nuclear contribution η versus the donor concentration n. The curve gives the expected value (eqn. (4.25)) for a non-interacting ^{31}P nuclear system. 128

4.22 Fits of the prediction in eqn. (4.30) to the low magnetic field susceptibility χ, for various concentrations in the insulating phase. The arrows indicate the temperature above which we predict the $T^{-\alpha}$ power law form. The magnetic fields used for each curve are shown. For the data we use "■" and "▲" for $B = 10G$ and $50G$ respectively. 130
4.23 Plot of the values of α and ρ obtained from the fittings in figs. 4.22. 131
4.24 Comparisons to the susceptibility data in higher fields for a just-metallic sample. Reproduced from the publication in §4.7. 132

5.1 The $B = 1.5T$ specific heat data for the concentrations (a) $n = 0.79 \times 10^{18} cm^{-3}$ and (b) $n = 1.6 \times 10^{18} cm^{-3}$. The upper curves are the predictions of the spin-pair model, while the lower curves show these results when the concentrations are scaled down 138

B.1 A random spatial distribution of spins. 148
B.2 Graphical aid to the determination of $P(J)$, showing a plot of the Herring-Flicker exchange coupling $J_{HF}(R)$. 149
B.3 A plot of the factor $I(n/n_c)$ appearing in expression (B.18), which was evaluated numerically. 152

C.1 A plot of the terms I_1 and I_2. 156
C.2 Plots of the integrands $F_C(x,y)$, $F_\chi(x,y)$, and $F_S(x,y)$ to show the exponentially decaying tails. 158
C.3 Plots of the integrands $F_C(x,y)$, $F_\chi(x,y)$, and $F_S(x,y)$, for various values of y, to determine a suitable upper cutoff for the integration. 161
C.4 Spin-pair energy levels. 162
C.5 A plot of $1/Z$ versus x, giving the probability of the singlet state of the spin-pair being occupied. 163
C.6 Plots of the correction function Δ_δ. 167
C.7 Plots of the correction function Δ_ε. 169
C.8 The dependence of the zero-field correction Δ_δ on the parameter α. 170
C.9 The normalized specific heat for various α values, together with the Scottky specific heat, for comparison. 172
C.10 A plot of $\ln(\delta)$ versus $\ln(y)$, for $\alpha = 0.63$. Indicated is the position y_0 of the maximum. 174

D.1 Plots of the functions (a) $\delta(y)$, and (b) $\varepsilon(y)$, versus y. Also shown are the determined asymptotic forms. 176

Chapter 1

Introduction

Our studies focus mainly on the Si:P system (crystalline silicon which has been doped with phosphorous donor impurities), but the models developed here are equally valid for similar systems. We are primarily concerned with explaining the thermodynamic properties, such as the specific heat and susceptibility, of heavily doped Si:P. The study of disordered Si:P has in recent years received a lot of attention. There is continuing interest in the transport and thermodynamic properties of this disordered system, particularly in relation to varying the impurity concentration. These studies, both experimental and theoretical, mainly focus on the impurity concentrations where Si:P undergoes a metal-insulator transition.

A metal-insulator (MI) system is any system that undergoes a MI transition as one of its physical parameters is varied. This transition is not necessarily one from a normal metal to an insulator, but instead describes a change in the absolute zero ($T = 0K$) conductivity $\sigma(0)$. The "metal" phase corresponds to a state in which $\sigma(0)$ is non-zero, whereas the "insulator" phase is distinguished by a vanishing $\sigma(0)$. Fig. 1.1 shows the extrapolated absolute zero conductivity $\sigma(0)$ versus the donor concentration n for Si:P. The MI transition is clearly visible in this plot.

Depending on the system, the MI transition can be brought about in several ways. For Si:P, and other similar systems[3], the MI transition occurs as the donor concentration is changed through the critical concentration n_c. (This critical concentration can be noted in fig. 1.1.) Other physical factors, such as an applied magnetic field, an applied stress, and impurity compensation, can drive the systems through the MI transition.

In Si:P, the MI transition can also be stress tuned, with an insulating sample driven

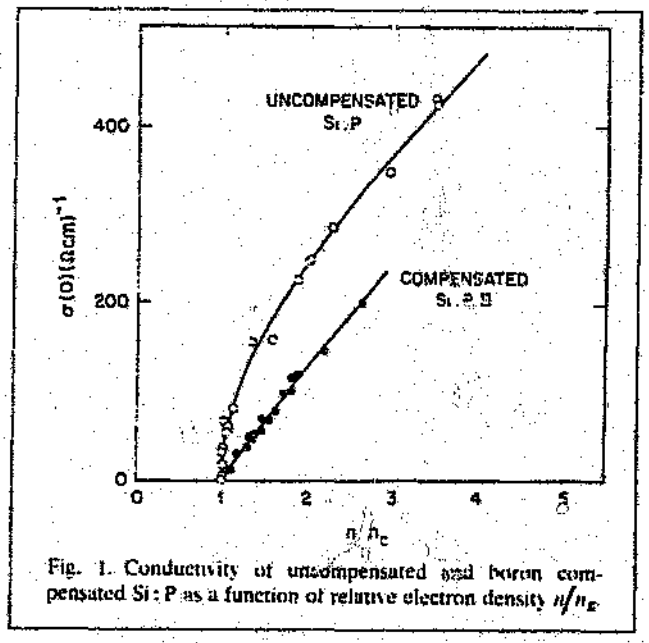


Fig. 1. Conductivity of uncompensated and boron compensated Si : P as a function of relative electron density n/n_c

Figure 1.1: Plot of the absolute zero conductivity showing the MI transition for Si:P. Reproduced from [1]. For Si:P, $n_c \simeq 3.5 \times 10^{18} cm^{-3}$ [2].

metallic by the application of uniaxial stress[3], while it has also been observed that a just-metallic sample can be driven into the insulating phase by the application of a sufficiently large magnetic field[3]. As observed in fig. 1.1, the properties of boron compensated Si:P (Si:P,B) are different from those of uncompensated Si:P. The degree of compensation K ($= N_D/N_A$, where N_D and N_A are the donor and acceptor concentrations respectively) can also determine the MI transition properties.

The reasons for favouring Si:P in MI studies are numerous. The large scale use of this material in technology and the relative ease of producing and classifying good samples make Si:P a useful system to study. The properties of Si:P have been extensively studied and are well documented. Due to the shallow nature of the donor states, the isolated donor properties can be described theoretically with good precision, such as with the use of the effective mass approximation. (Shklovskii and Efros[4] give a good account of the properties of these isolated donors.)

In Si:P, this metal-insulator transition is attributed to the donor electrons derived

from impurity phosphor atoms. The Si lattice provides a host for the random positioning of the P impurities, and does affect the properties of Si:P. The lattice affects the attributes of the donor electrons such as the effective mass and effective Bohr radius (which are determined by properties such as the Si conduction band structure and dielectric constant). For our analysis, the Si lattice also introduces additional unwanted contributions to the thermodynamic properties, which have to be removed. The diamagnetic contribution to the susceptibility and the lattice contribution to the specific heat have to be considered before the donor electron properties can be extracted.

Well below the critical concentration ($n \ll n_c$) the system is properly modelled by considering the donor electrons as isolated localized moments in hydrogenic $1s$ states, well described by theories such as the effective mass approximation. Here the classic Schottky specific heat and Curie susceptibility describe the donor subsystem. Well into the metallic phase, when $n \gtrsim 2n_c$, the impurity electrons are believed to be well described by the nearly-free-electron model (although factors such as the effective mass anisotropy and the multi-valley nature of Si also have to be taken into account). The interesting properties, however, which have as yet not been fully explained, occur in the vicinity of the transition ($n \approx n_c$), both in the insulating and metallic phases. Although the conductivity shows a critical behaviour at n_c, as indicated in fig. 1.1, the thermodynamic properties such as the specific heat and susceptibility appear to change smoothly through the transition.

Figures 1.2a and 1.2b show examples of the specific heat and susceptibility of Si:P near the MI transition. Fig. 1.2a shows the specific heat C in various magnetic fields for $n/n_c \simeq 0.5$. Note the development of the Schottky-type peaks in the non-zero fields. At these concentrations it is already evident that a breakdown in the isolated spin-model, which predicts a Schottky specific heat, is present. Note the significant zero-field contribution to C, which should vanish (point 6 of App. A.2) in the free spin system. Here we already see the need to include electron-electron (e-e) interactions to explain observed data. Fig. 1.2b shows the normalized electron spin susceptibility χ/χ_0 (where χ_0 is the metallic Pauli value) both below and above the MI transition. The free electron model would predict $\chi/\chi_0 \equiv 1$ (expected well into the metallic phase) while the free spin-1/2 model would predict the Curie susceptibility (expected well into the insulating phase) indicated in the figure. The data near the MI transition lie in between these two predictions. For the insulating sample $n/n_c = 0.78$ we see a reduction in χ over the Curie susceptibility, which indicates an antiferromagnetic coupling between electrons. Notice also that the susceptibility for the

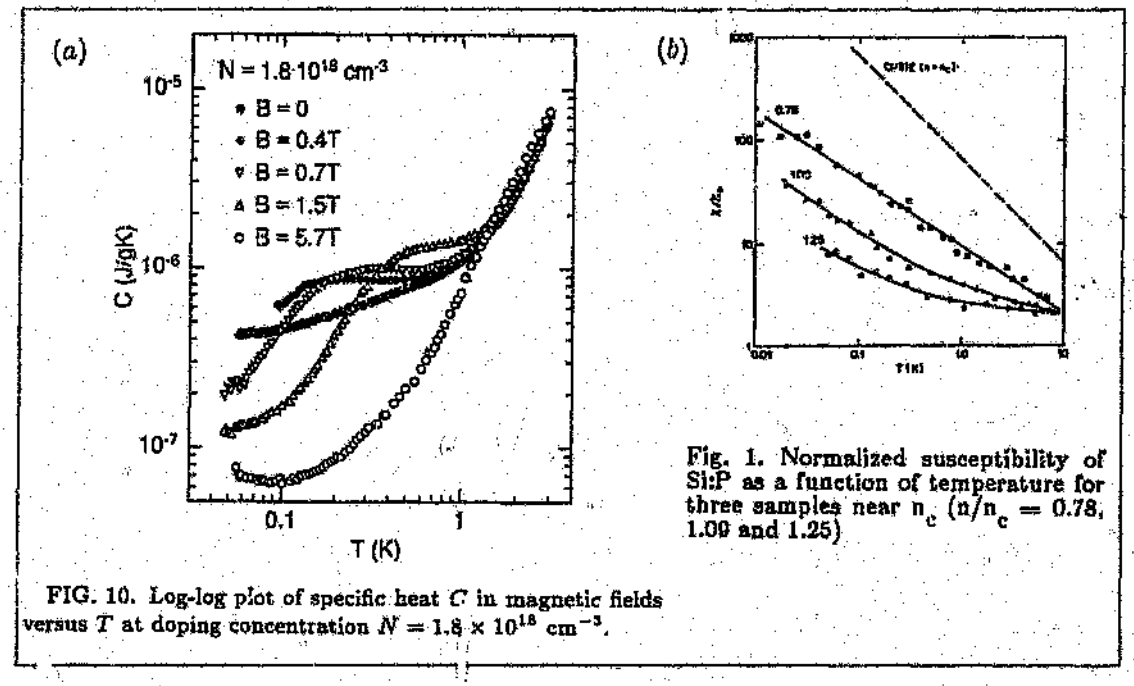


FIG. 10. Log-log plot of specific heat C in magnetic fields versus T at doping concentration $N = 1.8 \times 10^{18}$ cm^{-3}.

Fig. 1. Normalized susceptibility of Si:P as a function of temperature for three samples near n_c (n/n_c = 0.78, 1.09 and 1.25)

Figure 1.2: Plot of (a) Specific heat of 'insulating' Si:P for various magnetic fields, and (b) normalized susceptibility of Si:P on both sides of the MI transition (χ_0 is the Pauli value). Reproduced from [5] and [6] respectively.

two metallic samples ($n/n_c = 1.09$ and $n/n_c = 1.25$) is greatly enhanced over the expected Pauli susceptibility χ_0 at the lower temperature. This indicates the possible presence of localized spins, even in the metallic phase.

Several experimental measurements (specific heat, susceptibility, NMR Knight shifts, etc.) have shown that in the metallic phase there are localized moments present, while in the just-insulating phase the presence of itinerant electrons is also detected. Experimental results therefore suggest that the impurity electrons have both a localized and itinerant nature in the vicinity of the MI transition. This led to the development of the phenomenological two-fluid model[7] where the system is considered as consisting of two distinct subsystems: the itinerant electron and localized electron subsystems. This model and the experimental evidence are discussed further in §1.3.

The main focus is on the localized component of the donor electron system, and properly describing the existence and properties of these localized states. It is of interest

to extend the studies and to allow for the presence of an arbitrary magnetic field. This is what we have done in our analysis, and we have developed and tested two related models to extend zero-field models to include the effects of finite magnetic fields.

The most dramatic effect of a magnetic field is believed to be on the localized moments, where, for example, the specific heat develops Schottky-type peaks (fig. 1.2a). The susceptibility can also be greatly affected. The effect on the itinerant component is believed to induce localization effects. Our purpose was therefore primarily concerned with the effects a magnetic field would have on the localized moments, and to derive models to predict the experimental results.

We developed two separate models, mainly distinguishable by the modelling of the e–e interactions which have to be taken into account in a successful description. In the first model we used the Poisson distribution to describe the spatial distribution of donor states, while using the Herring-Flicker[8] expression to approximate the exchange couplings between electrons. In the second model we used the Bhatt-Lee[6] exchange coupling distribution to describe the e-e interactions. The second model leads to a more flexible analysis of results, and also describes the data at larger concentrations.

It should be noted that for both models we used the spin-pair approximation, where we partition the donor electrons into interacting pairs, and then model the distribution and couplings of these spin-pairs. For a random system such as Si:P, the spin-pair approximation should be a logical extension to the isolated spin model, where the e-e interactions start to appear and deviations from the free spin predictions occur.

For higher donor concentrations, close to and above the MI transition, we do not, however, use an *ab initio* approach to describe the spin-pairs. Instead, we have to use special techniques describing the exchange couplings to maintain the spin-pair approximation approach. One such technique is to use instead a renormalized exchange coupling, which can be used to describe larger clusters of spins in terms of effective spin-pairs[1]. In this case the effective concentration of spin-pairs in the system will be less than the actual donor concentration, due to this scaling procedure. This renormalized or effective exchange coupling in spin-pairs can also contain additional effects due to the interactions of the spin-pairs with the surroundings. So the spin-pair approximation can be used near the MI transition, provided we consider effective spin-pairs with effective exchange couplings.

[1]The scaling procedure of Bhatt-Lee is introduced in §1.3.1.

Although there was a lack of sufficient data to fully test the predictions of the models, the analysis done was gratifying, and showed that our models could be useful in explaining several of the phenomena in Si:P near the MI transition. They also give some indication as to possible future experiments that are required to fully confirm the predictions. It should be noted that although we focussed on Si:P in our experimental comparisons, the models are quite general and can apply to other MI systems. Similar properties have been reported in other doped semiconductors which undergo a MI transition, such as Ge:Sb[9].

1.1 Preview

Here we briefly discuss the outlay of this dissertation:

- The rest of this introductory chapter provides some historical background and recent studies that relate to the analysis we have done. The next section (§1.2) briefly reviews the concepts of the classical Mott and Anderson transitions. It also introduces the Lifshitz model, an extension of the Anderson model for disordered systems, and mentions the recent scaling theories, which have been successfully used to understand the transport properties in MI systems. The following section (§1.3) introduces recent theoretical and experimental results, and also indicates the use and success of the spin-pair approximation to describe the localized states in the disordered systems.

- In chapter 2 we describe the first model that we developed and tested. This model was developed *ab initio*, and does not consider effective spin-pairs or effective exchange couplings. The spatial random distribution of donors is partitioned into nearest neighbour pairs, and described by Poisson statistics. We then used the Herring-Flicker expression to describe the direct exchange coupling between the electrons in a spin-pair. At the end of chapter 2 we include a publication from Physical Review B which reviews the results of that chapter.

- In chapters 3 and 4 we introduce an extension to the phenomenological two-fluid model developed by Paalanen *et al.*[7]. The extension involved the inclusion into the model of finite magnetic fields. The main purpose of this model, and also that of the first model, was to predict the thermodynamic properties in the presence of

magnetic fields. The development of this model was more extensive than the first, and we have separated the results into two chapters. Chapter 3 contains the theoretical development and predictions of the extended two-fluid model, while chapter 4 contains the results of the comparisons to the experimental data. Finally, the end of chapter 4 includes a publication from Physical Review B, summarizing the extended two-fluid model and showing some of the main results obtained.

- In chapter 5 we compare the results of the two models, and discuss their validity at various ranges of donor concentrations. We also revisit the first model, in view of newer data that became available and the results of the two-fluid model, and consider the effects of scaling the concentrations in this model. We also summarize the results obtained from the complete analysis done by us, and point to some future experimental work that needs to be done for further studies.

- Appendices A to E have been included as references to the contents of the dissertation, and provide results that are not essential to the understanding of the main results.

  App. A: Here we include some of the basic theoretical and experimental results to which we refer several times in the chapters. The results of the isolated spin-1/2 system (the Schottky specific heat and Curie susceptibility) and the nearly-free-electron model (the linear specific heat and Pauli susceptibility) are included in this appendix. The experimental results for the silicon lattice specific heat and susceptibility are also included. We also include in this appendix the use of the partition function, and the determination of the required thermodynamic quantities from it.

  App. B: This appendix contains some of the mathematical details that were used in the development of the first model contained in chapter 2.

  App. C: This appendix contains some of the mathematical details for the development of the extended two-fluid model which is contained in chapters 3 and 4. We describe the procedures used for the numerical evaluations, and also indicate some additional properties of this model.

  App. D: Here we include the details of the determination of the asymptotic behaviours of the two important expressions required for the extended two-fluid model.

App. E: We briefly describe the methods used to digitize plots to obtain some experimental data, and also mention the problems that arose from these digitizing procedures.

1.2 A Brief History of MI Transition Models and their Application to MI Systems

In this section we review some of the early models devised to explain a MI transition in real systems. The Mott and Anderson models are some of the earliest and well known, and lead to what is now known as the Mott and Anderson transitions, and are used to explain the MI transition in a variety of systems. Although individually they cannot fully explain the MI transition in real systems, combined they do provide a useful insight into this process.

We will briefly review these two models, the Mott and Anderson models, and consider in particular their relevance to MI systems such as Si:P. Both these models consider an ordered (periodic) system, and so we also mention the Lifshitz model, which relies on the Anderson transition concepts, and specifically takes into account the possibility of having spatial randomness in the system. It is therefore particularly suited for the disordered systems such as Si:P, where we have a random distribution of donor impurities. All three models, however, play important roles in doped semiconductors.

Finally, we shall introduce some newer concepts, such as the scaling theories developed to describe disordered systems, but which are not directly applicable to our studies, since they mainly focus on the transport properties.

The reader is referred to books such as "Electronic Properties of Doped Semiconductors" by Shklovskii and Efros[4], which contains the points mentioned in this section, and also contains references to the papers that have been published on these topics.

1.2.1 The Mott Transition

Mott considered an array of hydrogen atoms, or any mono-valent atoms, arranged on a lattice, whose lattice parameter can be varied through any range. The periodicity of the lattice allows us to classify the electronic states in terms of Bloch waves, and the theory of band structures can be applied to the system. The atomic level in hydrogen splits into a

band of energies, which, for monovalent atoms such as hydrogen, is half filled. From band theory, it is therefore expected that the system is metallic for all inter-atomic separations.

However, as the lattice parameter is increased indefinitely, we would expect the system to be an insulator as the electrons become localized on each atom. The problem here is due to the independent-electron approximation used. This approximation, which works well for metals due to their wide bands, breaks down here because we are dealing with narrow bands. As the lattice parameter increases, so the width of the band decreases (exponentially), and the standard band theory approach breaks down.

It is essential therefore to consider the electron interactions, and the Hubbard potential is used to explain the metal-insulator transition in this hydrogen system. We take into account the interactions between electrons on the same site, and ignore interactions between electrons on different sites. Therefore, in the isolated neutral atom, an additional electron would occupy a state of higher energy due to this repulsive potential. We therefore lift the spin-degeneracy of the original level and obtain two non-degenerate levels separated by the interaction energy. As the lattice parameter is reduced, these two levels spread into bands (fig. 1.3), with the lower band (called the lower Hubbard band) completely filled, and the upper band (upper Hubbard band) empty. The system is hence an insulator at sufficiently low temperatures. As the lattice parameter is further decreased, the bands widen further, and the gap between the lower and upper Hubbard band decreases, until at some critical concentration, the gap vanishes. At this stage the system becomes metallic. This is the Mott-Hubbard transition.

The Mott transition is usually studied quantitatively by using Hubbard's model, which is a simplified model that assumes electrons only repel each other when they are on the same site. From the Mott model we see the importance of electron-electron interactions in describing MI transitions. Although this simplified model cannot be directly applied to most real systems, it does give us a feeling for the effects of electron interactions. Also, a simple formula, known as the Mott criterion, relates the effective Bohr radius a_B^* to the critical concentration n_c for a MI transition, and shows the universality of the phenomenon. The Mott criterion, given by

$$n_c^{1/3} a_B^* \simeq 0.25 \quad , \tag{1.1}$$

is satisfied by a variety of systems[3] which undergo a MI transition, including doped semiconductors such as Si:P.

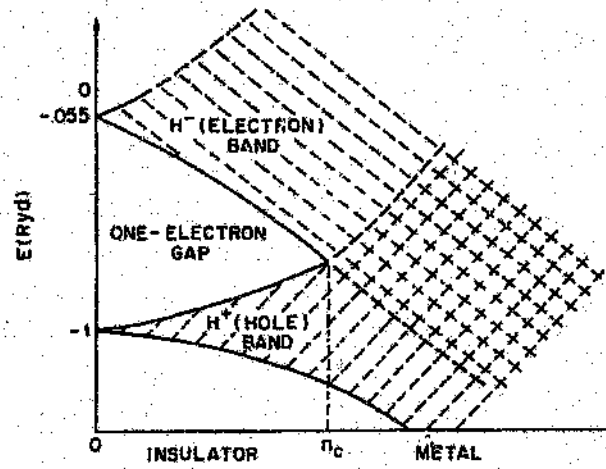


Fig. 1. Schematic diagram of the electron (H^-) and hole (H^+) bands (also referred to as the upper and lower Hubbard bands) for a lattice of hydrogen atoms, as a function of density: a useful diagram for locating n_c though incomplete in its description of random systems such as doped semiconductors.

Figure 1.3: Energy level diagram showing the Mott transition. Reproduced from [3].

1.2.2 The Anderson Transition

Anderson also considered a regular array of potential wells, but instead focused on the effects of having some disorder in the system. This disorder was brought about by assigning a random energy to each state in each well, thereby creating a band (of width W say) of allowed energies for the site states. The model considers a single-electron approach, and the question is whether the electronic states are localized, or delocalized. A proper mathematical description of the properties of the electronic states does not as yet exist, but a qualitative approach based on sound physical ideas was used to describe the system.

Another parameter used in this model, apart from the band width W, is the overlap integral I. For large lattice parameters, when the inter-well separation becomes large, and $I \rightarrow 0$, we can expect the states to be localized on the sites. When the overlap becomes significant, the admixture of localized states could produce delocalized states, extending over the system. Anderson used the following criterion to determine whether states were localized or not:

An electron is placed in a state with its wave function coinciding with the site

wave function. Since this wave function is not an eigenstate of the Hamiltonian, the wave function will change in time, and develop admixtures of the other site wave functions. By determining the absolute value squared $|\Psi|^2$ of the wave function for large times, we can specify whether states are localized or not. If the states are not localized, then the wave function spreads over the whole system, and we then have that $|\Psi|^2 \to 0$, while for localized states $|\Psi|^2$ will remain finite, with the initial wave function only developing exponentially small contributions from the neighbouring states.

The Anderson model contains the dimensionless parameter W/I which determines properties of the band. For sufficiently large values of W/I (large disorder) all the states are localized, with the system insulating at $T = 0K$. As the disorder is reduced (with W reduced), a critical value $(W/I)_c$ is reached where delocalized states begin to appear in the middle of the band. This is the MI transition known as the Anderson transition. As W/I is reduced even further, these delocalized states grow in number until the whole band consists of delocalized states.

So we see in the Anderson transition, that it is not electron-electron interactions, but disorder which can bring about a MI transition.

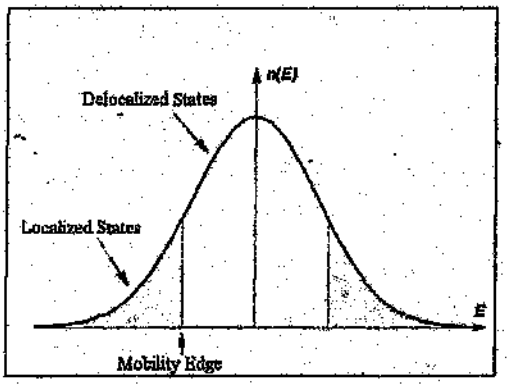


Figure 1.4: Density of states $n(E)$ in the Anderson model.

The Anderson transition discussed above considers a single-particle approach, and looks at the properties of the energy band created by the periodic array of random wells. The Anderson transition can also refer to a MI transition which is brought about by closing what is known as the mobility gap.

Suppose the disorder is such that the impurity band already consists of localized

and delocalized states, as shown in fig. 1.4. The mobility edge is shown in this figure, and separates the localized states from the delocalized ones. If we now consider the many-electron system, the Fermi level will increase from the bottom of the band as the number of electrons is increased. The system is therefore insulating at $T = 0K$ at low concentrations. The separation between the mobility edge and the Fermi level is the mobility gap. With an increasing electron concentration, the Fermi level increases, and the mobility gap closes. We then have the appearance of delocalized states and the system becomes metallic at $T = 0K$. This type of MI transition where a mobility gap is closed is often also referred to as an Anderson transition.

1.2.3 The Lifshitz Model

Both the Mott and Anderson transition refer to ordered periodic systems, and cannot fully describe disordered systems such as doped semiconductors. If the donor impurities in systems such as Si:P were arranged on a lattice, then the Mott model could be applied to this MI transition. Although the above two models do not have any direct connection to disordered systems such as Si:P, the concepts developed do influence the behaviour of the system. The electron-electron interactions and the disorder do play a crucial role in Si:P, and the Mott and Anderson models do at least provide some guide as to their effects.

Lifshitz considered instead the opposite to the Anderson model. Instead of an ordered array of random wells, Lifshitz considered the case where identical wells are randomly positioned in space. (This would be the case for doped semiconductors such as Si:P.) The question is again whether states are localized or spread out over the entire system. In as much as the wells are identical, we might be led to believe that the electron states would be extended throughout the system. In view of the Anderson model this would be true (the energy width W is zero, and all states would be delocalized). However, due to the random position of wells, this need not be the case. If we consider two nearest neighbour wells, then due to the overlap of the site wave functions, the resultant electronic state will have an energy shift, and this energy shift, which depends on the overlap integral, is random due to the random distribution of wells. The parameter (W/I) used to classify the Anderson transition cannot be used here. In the Anderson model the dispersion of energies W and the overlap I are considered as two separately controlled parameters. In the Lifshitz model the dispersion W will depend on the overlap I, and be of similar order of magnitude. The

parameter that is of interest here is instead the ratio of the Bohr radius of the site wave function over the inter-well separation. Due to this dispersion of two-well state energies, admixtures of several wells to form delocalized states need not occur, and we may then have localization of states in the system. To quote (p. 47 of [4]) "states in which wave functions of three or more wells enter on equal footing are not realized unless the wells are positioned in a strictly symmetric configuration".

At low concentrations, we have that the electrons are either localized around a single well, or are shared by a pair of neighbouring wells, and hence the system is insulating. Referring to Si:P, we therefore see that at these concentrations, the important states are spin-singlet states and spin-pair states. In view of the Lifshitz model, we therefore also see the importance of the spin-pair approximation to describe the properties of doped semiconductors such as Si:P.

1.2.4 Scaling Theories

Scaling theories were developed to understand the localization phenomenon by considering the dependence of the conductance on the system size. Although several workers introduced the concepts of the scaling theories, it was Thouless (1977) and Abrahams *et al.* (1979) who gave the first clear formulation. Scaling theory considers non-interacting electrons in disordered systems and studies the localization properties, with the assumption that the only relevant parameter needed to describe the properties is the conductance.

Mott's calculations predict that the conductivity should attain a minimum value as the MI transition is approached from the metallic side (fig. 1.1), and that the conductivity should therefore be discontinuous at the transition. The new theory asserts that it should be the conductance which should possess a critical value, and not the conductivity.

The scaling theory does use the ideas from the Anderson transition. In the Anderson model the dimensionless quantity W/I, which classifies the system, is determined by the conductance of that system, and the idea of the mobility edge is also used to explain the ideas in scaling theory. The conductance plays the same role in scaling theory as the parameter W/I plays in the Anderson model.

The main assumption in this theory is as follows. If, from a system whose dimensions have a size L and a conductance $g(L)$, we construct a new system of dimension $2L$, then the conductance $g(2L)$ of the composite system is entirely determined by the initial

conductance $g(L)$. Therefore, the conductance after an arbitrary number of edge-doubling processes depends only on the initial conductance of the system and not on the actual initial dimensions. This assumption can be expressed in mathematical form as

$$\frac{\partial lng}{\partial lnL} = \beta(g) \tag{1.2}$$

which states that the logarithmic derivative of g with respect to L is a function $\beta(g)$ of g, and not a function of the size L. Some of the properties on the function $\beta(g)$ can be obtained by considering the limit as $L \to \infty$, i.e. by considering the macroscopic conductance of the system, since the function $\beta(g)$ does not depend on the size L of the system. Fig. 1.5 shows a plot of $\beta(g)$ as inferred from this analysis, and from the form of $\beta(g)$ several predictions of one, two, and three dimensional systems can be made.

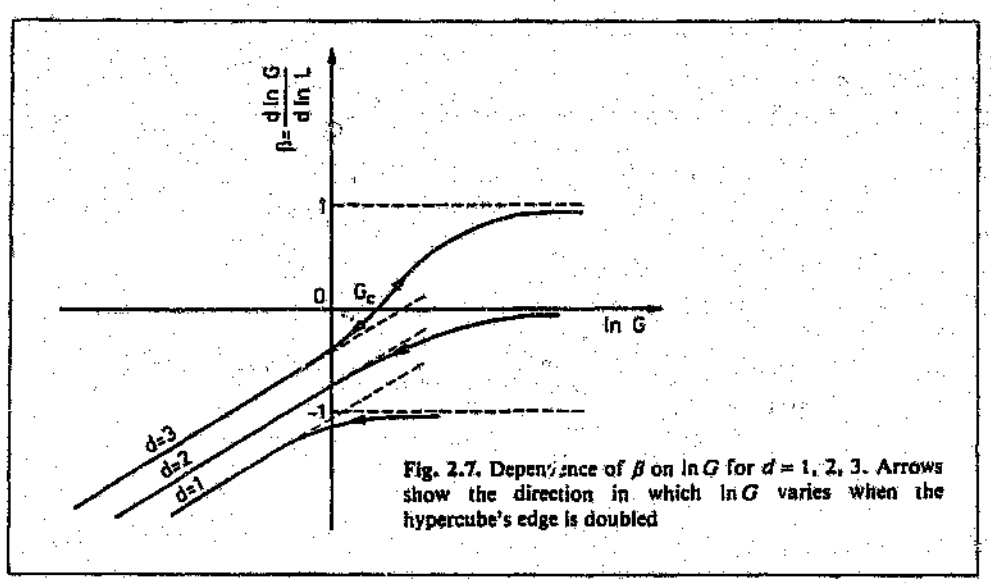


Fig. 2.7. Dependence of β on $\ln G$ for $d = 1, 2, 3$. Arrows show the direction in which $\ln G$ varies when the hypercube's edge is doubled

Figure 1.5: The scaling parameter $\beta(g)$. Reproduced from [4].

One of the important results suggested by scaling theories is that the zero-temperature conductivity $\sigma(0)$ behaves as

$$\sigma(0) = \sigma_0 \left(\frac{n}{n_c} - 1\right)^{\nu} \tag{1.3}$$

near the transition in the metallic phase, where σ_0 and ν are constants. This expression is obtained from the correlation length, $\xi = \xi_0 (n - n_c)^{\epsilon}$, which diverges as $n \to n_c$. This diverging correlation length ξ also suggests that the dielectric constant should have the

form $4\pi\chi = \chi_0 (n_c/n - 1)^{-\zeta}$ in the insulating phase. This form is indeed observed in experimental data[3]. The fits in fig. 1.1 use this form with the exponent $\nu = 0.55$ for the uncompensated and $\nu = 1$ for the compensated samples. This form for the conductivity is obeyed by several systems, although some of the critical exponents (such as $\nu = 0.55$ for Si:P) are not in agreement with those predicted by the scaling theories. Comparisons of scaling theory with experimental results are made difficult since this theory does not consider electron-electron interactions, which surely play an important role near the transition.

1.3 Recent Studies of Si:P near the MI Transition

In this section we review some of the recent studies that have been made on disordered systems such as Si:P. Some of these results to be discussed here have initiated the studies we have done.

First to be discussed is the insulating phase. The spin-pair approximation, cluster calculations, the Bhatt-Lee scaling procedure, and the Bhatt-Lee (Rice) local moment model, have all contributed to a deeper understanding of the insulating side of the transition. Today the insulating phase is well understood and the physical properties can be predicted with good accuracy in quantitative ways.

The metallic phase, which is discussed next, is less understood and as yet no complete theory exists to fully explain the properties on the just-metallic side. Explanations describing certain properties do exist, such as the phenomenological two-fluid model, which considers the donor electron system as consisting of two independent parts: the localized and itinerant electrons. The itinerant electrons determine properties such as the transport properties and the NMR Knight shifts, while the localized electrons strongly affect properties such as the specific heat and susceptibility. The results justifying the existence of localized moments in the metallic phase will be reviewed.

Finally, we consider some of the results pertaining to the actual metal-insulator transition, and consider the properties as the MI transition is crossed from the insulating to metallic side. Except for the conductivity at sufficiently low temperatures, which exhibits a critical behaviour at the MI transition (fig. 1.1), other physical quantities such as the specific heat and susceptibility do not indicate this critical behaviour and instead show a smooth variation across the MI transition[10, 1].

The MI transition can be probed by several means. Physical properties such

as the optical (IR and Raman spectroscopy), transport (conductivity and thermoelectric power), magnetic (ESR, NMR, and susceptibility), and thermodynamic (specific heat and susceptibility) properties all contribute to understanding this phenomenon. The results and interpretation of these measurements will be discussed as we describe the insulating and metallic phases.

"Tuning" of the MI transition has also been achieved to improve the precision and accuracy of studies close to the transition. The standard way was to prepare samples of various dopant concentrations n, above and below the critical concentration n_c, and then probe each sample to obtain the properties near n_c. Instead of this method of using several samples to vary n through the MI transition, it is possible to use a single sample with n close to n_c, and instead vary n_c. This "tuning" of the critical concentration can be achieved by either applying stresses or magnetic fields[3]. The donor wave functions are strongly dependent on the characteristics of the conduction band. The application of stresses can destroy the symmetries of the conduction band, with a corresponding change occurring in the donor wave functions, leading to a change in the critical concentration of the sample. The application of a sufficiently large magnetic field can drive a barely metallic sample into the insulating phase. An explanation is that the field causes a shrinkage of the donor electron orbit, and this shrinkage may be sufficient to reduce the wave function overlaps and induce localization.

1.3.1 The Insulating Phase

The insulating phase today is regarded as being well understood and good quantitative analysis can be achieved up to the MI transition. The generally accepted model for the insulating phase is that of randomly distributed donor electrons with antiferromagnetic exchange couplings between them[11, 6, 1]. Due to the random spatial distribution and the exponential dependence of the exchange coupling on the electron separations, the range of exchange coupling magnitudes spans several orders of magnitude. This allows the system to be well described[12] in terms of a system of random finite clusters of donor electrons. The cluster calculations of disordered systems such as Si:P do have their uses and can be used to explain the physical properties, but they do have limitations. As mentioned by Bhatt and Lee[12], the limitations of the use of finite sized clusters prevent a description of the apparent lack of magnetic ordering at low temperatures.

At very low donor concentrations, deep into the insulating phase ($n \ll n_c$), the donor electrons can be considered as being isolated and localized around P^+ ions in hydrogenic type states. These isolated donor states[2] are then well described by techniques such as the effective mass approximation, using modifications such as the 'central cell correction', and taking into account the multi-valley characteristics of the Si conduction band. The physical properties at low temperatures[3] of this isolated spin-1/2 system are well known, with the Curie law describing the susceptibility and the Schottky expression describing the specific heat in a magnetic field. However, as the donor concentration is increased towards n_c and significant wave function overlap starts to occur, the isolated donor picture fails, and it becomes necessary to include electron-electron (e-e) interactions to maintain feasibility with experimental studies. We now briefly review several of these results which clearly indicate the need to include e-e interactions and consider clusters of donor electrons in calculations.

Infrared (IR) studies[3] on Si:P for low concentrations ($n \sim 10^{15} cm^{-3}$) show an absorption spectrum consisting of sharp absorption lines at lower photon energies followed at higher energies by a broad continuum. These sharp absorption lines are characteristic of isolated donors and the broad absorption band at higher energies corresponds to the transitions into the conduction band. As the donor concentration is increased, so these narrow lines broaden and eventually vanish (at $n \sim 10^{18} cm^{-3}$) to form a continuum. The initial broadening of the peaks in Si:P has been attributed to donor pairs. The overlap of nearby electrons creates energy bands and as the concentration increases, so the overlap and spreading of energy levels increases, eventually wiping out the presence of the narrow absorption lines to form a continuum of absorption energies. An interpretation of this broadening of the sharp absorption lines was done in terms of absorption from random donor clusters[3]. At lower concentrations, considering spin-pairs is sufficient, but larger clusters have to be included as the concentration is increased and n approaches n_c.

Electron spin resonance (ESR) measurements[3, 13] indicate a similar picture to that of the IR studies for the insulating phase. At very low concentrations ($n < 10^{16} cm^{-3}$) the ESR spectrum contains the hyperfine doublet, characteristic of isolated donors. As the concentration is increased, signals from donor-pairs and donor triads appear ($n \sim 10^{17} cm^{-3}$). At even higher concentrations ($> 10^{17} cm^{-3}$) signals from larger clusters ap-

[2]Reference [4] gives a good description of the isolated donor states.
[3]At low temperatures the only relevent transitions are spin-excitations.

pear. The overlap of signals from various clusters causes a broad central peak in the ESR spectrum. It has also been claimed[13] that cluster-cluster interactions smear out this central resonance, and remove traces of the signals from the different-sized clusters. The appearance of this central resonance, attributed to the formation of clusters of electrons, is evidence of e-e interactions in the system on the insulating side. As the concentration is increased through the MI transition, the central resonance grows and becomes narrow rapidly, characteristic of delocalized electrons. Thus ESR measurements also indicate the need for e-e interactions to be included in calculations, and the need for random donor clusters in obtaining an understanding of the insulating phase.

The IR and ESR studies do not indicate the presence of isolated donors close to the MI transition in the insulating phase. However, the existence of isolated donors at low concentrations is also inferred from Raman spectroscopy[3], and the signal is still visible just below the critical concentration.

The susceptibility χ of Si:P has been extensively studied in the insulating phase, and has been fundamental in understanding this part of the MI transition. Andres *et al.*[14] measured χ at low temperatures ($30mK \rightarrow 4K$) in low magnetic fields ($10G < B < 300G$). Even at concentrations of $n = 1.1 \times 10^{17} cm^{-3}$, there is a deviation from the Curie law ($\chi \sim 1/T$) for isolated donors. Cluster calculations were required to describe these susceptibility data. The simplest case is the spin-pair approximation, where pairs of donor electrons are coupled antiferromagnetically. Also, the attraction of the spin-pair approximation is that the physical properties of the system can be explicitly expressed in terms of only a distribution of spin-pair exchange couplings.

To develop the spin-pair approximation, the exchange coupling between two donor states is required. Since silicon is a multi-valley semiconductor and the effective mass is anisotropic[4], the donor states are not spherically symmetric hydrogenic states (although cubic symmetry is retained[4, 14]). Andres *et al.* determined the distribution of exchange couplings for this anisotropic case, and also the isotropic (spherical) case, and found them to be sufficiently close to be able to approximate this distribution with the isotropic model. Here the donor states are considered to be spherical hydrogenic states (with an effective Bohr radius of $a_B^* \sim 15\mathring{A}$ for Si:P chosen to fit the data) with the exchange coupling depending only on the separation of the donors. The random spatial distribution can be described by Poisson statistics, while the exchange coupling can be approximated using the Herring-Flicker[8] expression. Herring and Flicker calculated the exchange coupling $J(R)$ between

two spatially separated hydrogen wave functions as a function of the separation R (R is in effective Bohr radius units). Their calculations, valid for large separations $R = r/a_B^* \gg 1$, produced

$$J(R) \sim R^{5/2} e^{-2R} \quad . \tag{1.4}$$

This spin-pair approximation does describe the susceptibility quite well for concentrations up to about $n \sim 10^{17} cm^{-3}$, over almost three orders of magnitude in temperature. It did, however, break down for higher concentrations ($4.3 \times 10^{17} cm^{-3} < n < 7.2 \times 10^{17} cm^{-3}$) and the data had to be described by incorporating larger clusters in the calculations. A modified pair approximation which took into account the existence of larger clusters, and a computer simulation of larger clusters (324 spins), were also produced by Andres *et al.* and improved the predictions over the bare spin-pair approximation. This again showed that to explain the physical properties in the insulating phase close to the MI transition, it was essential to consider larger clusters of spins.

An important observation by Andres *et al.* was that χ varied as $T^{-\alpha}$ for $T > 30mK$, for nearly three decades in temperature. The exponent α varied from 0.9 for the lowest to 0.64 for the highest concentration. Noting that $\alpha = 1$ describes the Curie law for isolated spins, the reduction in α shows the deviation from the Curie law as n increases, and shows the increased antiferromagnetic couplings present in the system. This power law form $T^{-\alpha}$ has been observed by other researchers[15, 11, 16], and is evident up to the MI transition. (Fig. 1.2b shows this power law form in χ for $n/n_c = 0.78$, and also shows the magnitude relative to the Curie and Pauli values). Experimental and theoretical studies suggest that the susceptibility behaves approximately as $\chi(T) \sim T^{-\alpha}$ (with $\alpha \sim 0.6$) for $T < 10K$ and concentrations $0.2n_c < n < n_c$. For smaller concentrations α increases rapidly to values as high as $\alpha = 0.90$ (for $n/n_c \sim 0.03$)[15]. An explanation for this behaviour of the susceptibility was introduced by Bhatt and Lee using their scaling procedure for highly disordered spin-1/2 antiferromagnetic systems.

The results of Andres *et al.* showed that the simple spin-pair approximation failed well into the insulating phase, and could not explain the properties near the MI transition, which is the region of interest. For this purpose numerical calculations involving larger clusters had to be employed. However, Bhatt and Lee showed, with their scaling procedure, that the simplicity of the spin-pair approximation could be maintained and at the same time explain the properties on the insulating side up to the MI transition.

The scaling procedures developed by Bhatt and Lee[12] take advantage of the large range of exchange couplings present in these disordered systems. At the low temperatures of interest, the high-lying excitation levels of the system do not influence the properties of the system. These levels are then iteratively discarded by scaling down the system of interacting spins to produce a system with the same low lying energy levels. The low temperature thermodynamics of the original and scaled system should then be similar. This scaling procedure involved the iterative removal of the strongest coupled spin pair, with a corresponding renormalization of the exchange couplings between the rest of the spins. So it is possible, in principle, to reduce a large cluster to a smaller cluster by introducing effective exchange couplings within the scaled system.

These scaling ideas by Bhatt and Lee were applied to Si:P. The spin-pair system was again used, but instead of using the direct exchange coupling, an effective exchange coupling was introduced to take into account the possible presence of larger clusters (i.e. all the larger clusters in the system are assumed to scale down to spin pairs with an effective exchange interaction). This spin-pair system was then described in terms of a renormalized distribution of antiferromagnetic exchange couplings, $P(J)$, and all relevant quantities can then be explicitly obtained from a knowledge of $P(J)$. For example, the susceptibility for this system is then[15]

$$\chi(T) = \frac{4C}{T}\int_0^{J_c} \frac{P(J)dJ}{3+e^{J/k_BT}} \quad , \tag{1.5}$$

where C is the Curie constant and J_c is an upper cutoff for the exchange coupling distribution (estimated at $\sim 500K$ by Sarachik *et al.*[15]). The power law form $\chi \sim T^{-\alpha}$ observed in the susceptibility follows[15] from a renormalized distribution $P(J) \sim J^{-\alpha}$, with $\alpha < 1$ parameterizing the system. This renormalized distribution was also applied to calculate the magnetization of Si:P in magnetic fields[15, 17] and successfully described the experimental data. This Bhatt-Lee (BL) model could therefore describe the magnetic properties of Si:P on the insulating side in terms of a hierarchical exchange coupled spin-pair system.

The BL model with its renormalized $J^{-\alpha}$ distribution was also used to calculate the specific heat C in a zero magnetic field, and predicts[7] that a power law form also holds for C, with $C \sim T^{1-\alpha}$. This power law form for the zero-field specific heat has also been observed by other researchers[18, 5], and is present up to the MI transition. (Fig. 1.2a gives a hint of this power law form $C \equiv T^{1-\alpha}$ on the interval $(100mK, 1K)$ for $n/n_c \simeq 0.5$.) The values for the parameter α obtained from the susceptibility and specific heat analysis are

very close ($\alpha = 0.60 \pm 0.10$ for C and $\alpha = 0.63 \pm 0.03$ for χ)[7] and provide justification for the BL model. The parameter α is found to vary with concentration[15], with α decreasing with an increase in n, and close to the MI transition α levels off and appears to be constant ($\alpha \sim 0.6$). The existence of a zero-field electronic specific heat also indicates the need to consider e-e interactions. For a non-interacting spin-system, no specific heat contribution is present for $B = 0$ (App. A.2).

The specific heat in the presence of a magnetic field has even more interesting details (as an example, refer to fig. 1.2a). The specific heat developes Schottky-type anomalies in large ($\sim 1T$) magnetic fields[19, 5]. At very low concentrations ($\sim 10^{17} cm^{-3}$) these peaks are close to the Schottky specific heat[19]. However, as the concentration is increased towards the MI transition, deviations occur. At these higher concentrations the data are then expressed in terms of a Schottky expression, using an effective field and effective concentration (App. A.2), and a term linear in temperature (γT). This linear contribution hinted at an itinerant component, even in the insulating phase. Therefore, the specific heat was expressed as

$$C(B,T) = C_{Schottky}(B,T) + \gamma(B)T + \beta T^3 \quad , \tag{1.6}$$

where βT^3 is the phonon contribution at low temperatures (App. A.3). Several studies[19, 18, 20, 5] fitting the above expression to experimental data obtain similar results. The "itinerant" contribution $\gamma(B)$ increases from zero as $n \rightarrow n_c$. The effective magnetic field B_{eff} is smaller than the applied field B, suggesting an antiferromagnetic coupling; and B_{eff}/B systematically decreases as the MI transition is approached, showing the increased antiferromagnetic couplings in the system (which is supported by the susceptibility data). It is also suggested[20, 5] that the magnetic fields induce localization, as inferred from the decrease in $\gamma(B)$ as B is increased, and also from the increases in height of the Schottky-type peak. We will return to the application of eqn. (1.6) and these points in §1.3.3 when we discuss the actual MI transition.

The Bhatt-Lee model of renormalized spin-pairs with a hierarchical exchange coupling distribution has therefore been found to successfully describe the thermodynamic properties of Si:P in the insulating phase, particularly for zero magnetic fields. One of our aims was to extend the BL model to generalize it to include the effects of a magnetic field, in particular to explain the specific heat in finite fields.

1.3.2 The Metallic Phase

The metallic phase of Si:P is as yet not fully understood. Although we have a qualitative understanding of this side of the MI transition, more experimental and theoretical studies are required. The traditional view of these disordered systems in the metallic phase is in terms of Fermi liquid ideas. For large concentrations ($n \gg n_c$) the physical properties are sufficiently described using disordered Fermi liquid theories. However, for the concentrations $n_c < n \lesssim 2n_c$ these predictions for the metallic phase break down, and all evidence suggests that in this concentration range (the just-metallic phase) there exist localized moments which can dramatically alter the observed properties.

The scaling theories give a good account of the absolute zero conductivity $\sigma(0)$ in the metallic phase (eqn. (1.3)), although for Si:P there is a discrepancy in the experimentally determined[3] critical exponent $\nu \simeq 0.5$, while for other MI systems, including Si:(P,B), we have $\nu \simeq 1$, which is the value predicted by non-interacting scaling theories. Scaling theories which include e-e interactions do predict[3] a lower value for ν, indicating that it is essential to consider e-e interactions for Si:P.

This is also shown by the temperature dependence of the conductivity σ for Si:P, which gives us an indication of the relative strengths of interaction and localization effects. For Si:P[3], up to about $5K$, σ is well described by

$$\sigma(T) = \sigma(0) + mT^{1/2} \quad , \tag{1.7}$$

where the $mT^{1/2}$ term arises from Coulomb interaction effects. The coefficient m changes sign from a negative to positive value as $n \rightarrow n_c$, due to a breakdown in screening effects. For Ge:Sb[3], the above expression fits the data only up to about $100mK$. By including a localization term, $\sigma \equiv BT$, in eqn. (1.7) above, the data can be matched up to about $500mK$.

Thomas *et al.*[21] tested the conductivity predictions of Mott, which were based on the Kubo-Greenwood formulation of the conductivity. They found that Mott's analysis, which used Anderson model ideas, describes the data for $n \gtrsim 2n_c$, but with a departure for lower concentrations in the metallic phase. Their analysis involved comparing the absolute zero conductivity $\sigma(0)$ and the specific heat coefficient $\gamma = C/T$, which, according to Mott's predictions, should scale ($\sigma(0) \propto \gamma^2$). The specific heat coefficient γ was determined from the intercept of the C/T versus T^2 plots. (The specific heat is taken as $C = \gamma T + \beta T^3$,

which appears to be obeyed for temperatures larger than $\sim 1K$. The γT term arises from the itinerant electrons, while βT^3 represents the phonon contribution). $\sigma(0)$ and γ^2 were compared, and near the MI transition the data do not match, with convergence only occurring when n is increased above $2n_c$.

So the conductivity studies indicate the necessity of including Coulomb interactions, and even localization effects, to describe the properties in the insulating phase. Measurements on the magnetoresistance in barely metallic samples have been interpreted in terms of donor spins, localization, Coulomb interactions, or a combination of localization and interaction[3]. We now review studies on some other physical quantities which collaborate the disordered Fermi liquid view deep into the metallic phase ($n \gg n_c$), and indicate the anomalies that occur in just-metallic samples ($n_c < n \lesssim 2n_c$). These anomalies are attributed to the appearance of localized moments even in the metallic phase. The existence of these local moments was predicted as far back as 1979 by Kobayashi *et al.*[19] with specific heat studies, and also from susceptibility studies in 1981 by Ikehata *et al.*[10].

The thermoelectric power is a sensitive transport property. Lakner and Löhneysen[2] have measured the thermoelectric power S of Si:P, and found that for $n \gg n_c$, S has a linear temperature dependence characteristic of metals. However, S showed anomalous behaviour close to n_c, and the strong magnetic field dependence related this anomaly to magnetic scattering. This was the first experimental evidence from a transport property that localized moments exist in the metallic phase.

The susceptibility of a metal is described by the T-independent Pauli susceptibility. The susceptibility χ of Si:P on the just-metallic side was found[10, 16, 17, 11] to be strongly T-dependent at low temperatures, hinting at the existence of localized spins. Ootuka and Matsunaga[16] also found that even in their just-metallic samples, the temperature dependence of χ can be described by the power law form $T^{-\alpha}$, with $\alpha \simeq 0.45$, which is the predicted form for the insulating side by the BL model. An example of the susceptibility in just-metallic samples is shown in fig. 1.2b, for $n/n_c = 1.09$ and 1.25. Notice that χ is temperature dependent, and strongly enhanced over the Pauli susceptibility χ_0 expected for metallic samples. From this figure we see that χ decreases gradually as the MI transition is crossed. It is only for concentrations $n > 2n_c$ that a temperature independent Pauli-like susceptibility starts to appear[10, 6].

The specific heat measurements have also indicated the possibility of localized moments in the metallic phase. For a degenerate electron gas the specific heat is predicted

to be linear in T, with $C = \gamma T$, and γ depending on the density of states at the Fermi level (App. A.2). This linear component is observed in the data, but at lower temperatures ($T \lesssim 1K$) in just-metallic samples ($n_c < n \lesssim 2n_c$) there is an anomaly attributed to localized spins[21, 7, 18, 5]. (This is also observed in Ge:Sb[9].) Just as for the insulating phase, the excess specific heat in zero magnetic fields has a power law form[7, 18, 5] $C \sim T^{1-\alpha}$ below $1K$, as predicted by the BL model for the insulating side.

The specific heat in a magnetic field provides even stronger evidence for localized moments. The Schottky-type specific heat peak is still present in the just-metallic phase[19, 18, 5], and persists up to about $n \sim 2n_c$.

Spin localization in just-metallic Si:P was also established by Alloul and Dellouve[22] by means of NMR measurements. Their ^{31}P NMR signals had Knight shifts and relaxations times characteristic of a Pauli electron gas, but the signal was only associated with a fraction of the ^{31}P nuclei, the fraction decreasing as the MI transition is approached. The nuclei wiped out of the NMR spectrum, due to large hyperfine fields, were surrounded by localized donor electron states which produced the T-dependent enhanced susceptibility observed for these just-metallic samples. The susceptibility of the detected nuclei was T-independent, as expected for a degenerate electron gas (the Pauli susceptibility). The electronic susceptibility converges with the Pauli susceptibility only when $n \gg n_c$.

Other NMR measurements also support this localization idea. Paalanen *et al.*[23] observed ^{29}Si relaxation rates 1000 times larger than that expected for nuclei interacting with free electrons. Their data could be interpreted as arising from localized spins. Hoch and Holcomb[24] show that this ^{29}Si relaxation rate is strongly field dependent, and even for just-metallic samples favours a local moment model rather than a Fermi liquid model. ^{29}Si Knight shift measurements by Stoddart *et al.*[25] on just-metallic Si:P and Si:(P,B) indicate that the observed nuclei interact only with itinerant electrons, supporting Alloul and Dellouve's results. They also claim that the interactions between the localized and itinerant electrons are weak, and that their measurements are consistent with the phenomenological two-fluid model.

The two-fluid model was introduced to at least qualitatively describe the just-metallic phase of these disordered systems. Here the donor electron system is assumed to consist of the itinerant and localized components, interacting only weakly with each other. Bhatt *et al.*[11] claim that a two-fluid description of the thermodynamics is appropriate since the coupling between localized moments is much more efficient than that between the

localized and itinerant electrons, as also suggested by Stoddart *et al.*[25]. As is evident, the existence of localized moments in the just-metallic phase, coexisting with an itinerant electron system, has a lot of experimental support. However, theoretical calculations have also been applied to explain this localization phenomenon.

The general starting point for theoretical calculations on disordered systems such as Si:P is the Anderson-Hubbard Hamiltonian in the site representation:

$$H = -\sum_{i \neq j,\sigma} t_{ij} c^{\dagger}_{i\sigma} c_{j\sigma} + U \sum_{i} n_{i\uparrow} n_{i\downarrow} + \sum_{i,\sigma} (\epsilon_i - \mu) n_{i\sigma} \quad , \tag{1.8}$$

where i and j represent system sites and σ is the spin component. t_{ij} is the hopping matrix element, while e-e interactions are introduced using the Hubbard potential U (§1.2.1).

Milovanivić and Sachdev[26] claim that "off-diagonal disorder in the hopping matrix elements t_{ij} will produce local environments favouring the formation of local moments" in the metallic state. Their estimates of the number of local moments in the metallic phase are in good agreement with estimates from NMR and thermodynamic measurements (next section). They conclude that a disordered system of interacting electrons can display an instability towards the formation of localized moments. Bhatt and Fisher[27] showed that in a positionally disordered Anderson-Hubbard model, the low temperature thermodynamics is dominated by spin excitations in rare regions, even deep into the metallic phase, and is not that of a Fermi liquid. Lakner and Löhneysen[5] provided a quantitative description to estimate the density of local moments in the metallic phase. They also show that the power law form for the zero magnetic field specific heat could also be explained by the Kondo effect.

1.3.3. The Metal-Insulator Transition

The existence of localized moments in the metallic phase appears to be well supported by both theoretical and experimental studies. This justifies the view of the just-metallic phase in terms of the phenomenological two-fluid model, where the donor electron system consists of the itinerant and localized components, with only weak interactions between them.

Specific heat studies[19, 21, 18, 5] also indicate that there is an itinerant contribution ($C \equiv \gamma T$) even in the insulating phase, indicating a possible two-fluid picture on this side of the transition too. A possible explanation[5] is that due to the random donor

distribution there exist metallic "islands" in the insulating phase which gradually disappear as the concentration is reduced, but which still exhibit a finite γ. Similarly, in the metallic phase, we could have rare regions behaving as insulating "islands" to explain the localization phenomenon[1].

The specific heat data have been analyzed according to this two-fluid picture. The data for the zero-field specific heat appear to follow the form $\gamma T + \beta T^3$, for temperatures above $T = 1K$ [21, 5]. This is evident from fig. 1.6a. The anomaly ΔC appearing at lower temperatures is attributed to localized moments. The zero-field specific heat is therefore modelled as

$$C = \Delta C + \gamma T + \beta T^3 \quad . \tag{1.9}$$

The itinerant contribution γ is obtained from the intercept of the C/T versus T^2 plot[21, 5], while the phonon contribution β is determined from the slope. Results are shown in fig. 1.6b where the determined γ is plotted as a function of the donor concentration n. Note the gradual change in γ as the MI transition is crossed, and the non-zero magnitudes deep into the insulating phase. The excess specific heat ΔC (obtained by subtracting the determined γT and βT^3 terms), shown in fig. 1.6c, is found to vary, even in the metallic phase, as $\Delta C \sim T^a$, for temperatures $T < 1K$, consistent with the power law behaviour predicted by the BL model for the localized electrons.

The specific heat in a magnetic field is described in terms of eqn. (1.6), where the excess specific heat ΔC is now described using the Schottky specific heat, with the use of an effective field B_{eff} and an effective concentration of spins N_{Sch}. Fig. 1.6d shows estimates[18, 5] of N_{Sch} obtained from fittings of eqn. (1.6) to experimental data. Note again the gradual change across the MI transition, and the existence of a localized contribution even in the metallic phase. Kobayashi *et al.*[19] did a similar analysis and also found that N_{Sch} only vanishes when $n > 2n_c$.

The results of Löhneysen and Lakner[20] also indicate that $\gamma(B)$ decreases with an increasing B-field, with a corresponding increase in $N_{Sch}(B)$, both on the insulating and metallic side. This is a consequence of the increase in height of the Schottky-type excess specific heat with an increasing magnetic field, and is attributed to field-induced localization.

Our own analysis on the specific heat shows results that are very different from the

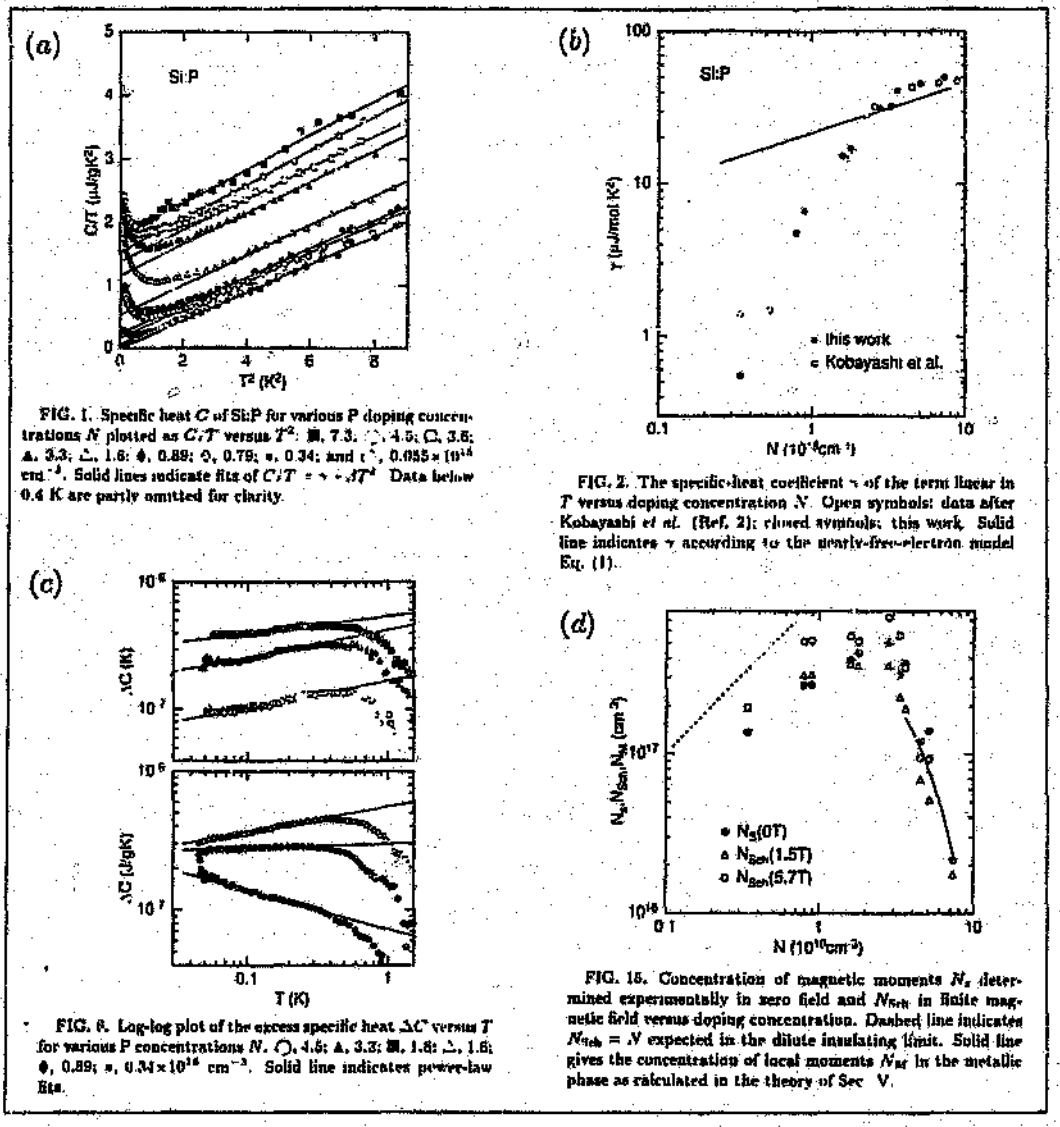


FIG. 1. Specific heat C of Si:P for various P doping concentrations N plotted as C/T versus T^2: ■, 7.3; ○, 4.5; □, 3.6; ▲, 3.3; △, 1.6; ◆, 0.89; ◇, 0.79; ●, 0.34; and ▽, 0.055×10^{18} cm^{-3}. Solid lines indicate fits of $C/T = \gamma + \beta T^2$. Data below 0.4 K are partly omitted for clarity.

FIG. 2. The specific-heat coefficient γ of the term linear in T versus doping concentration N. Open symbols: data after Kobayashi *et al.* (Ref. 2); closed symbols: this work. Solid line indicates γ according to the nearly-free-electron model Eq. (1).

FIG. 6. Log-log plot of the excess specific heat ΔC versus T for various P concentrations N. ○, 4.5; ▲, 3.3; ■, 1.6; △, 1.6; ◆, 0.89; ●, 0.34×10^{18} cm^{-3}. Solid line indicates power-law fits.

FIG. 15. Concentration of magnetic moments N_s determined experimentally in zero field and N_{Sch} in finite magnetic field versus doping concentration. Dashed line indicates $N_{Sch} = N$ expected in the dilute insulating limit. Solid line gives the concentration of local moments N_M in the metallic phase as calculated in the theory of Sec. V.

Figure 1.6: Plots of (a) C/T versus T^2 for $B = 0$, (b) γ versus n obtained from the analysis of (a), and (c) the corresponding excess specific heat ΔC obtained from (a). The effective concentration of localized moments obtained from the $B \neq 0$ specific heat analysis is shown in (d). Reproduced from [5].

results described. In particular, the use of the C/T versus T^2 plots to extract the itinerant contribution γ do come into question.

The excess specific heat ΔC obtained in the metallic phase shows very similar features to that of the insulating phase. This is also the case with the temperature dependence of the susceptibility χ. Even in the just-metallic samples, these two quantities ΔC and χ have a behaviour[18, 16] $\Delta C \sim T^{1-\alpha}$ and $\chi \sim T^{-\alpha}$ predicted by the BL model for the insulating p se. Alloul and Dellouve[22] also suggested that the BL model could be applied to describe the localized component in the metallic phase.

It was Paalanen *et al.*[7] who incorporated the BL model into the phenomenological two-fluid model. The localized spins are described by the BL model (with $C \sim T^{1-\alpha}$ and $\chi \sim T^{-\alpha}$), while the itinerant fluid is described as a Fermi liquid with an effective mass m^*. The electronic specific heat coefficient γ and the susceptibility χ in the Paalanen two-fluid model (hereafter referred to only as the two-fluid model) are then given in compact form as the sum of the itinerant and localized contributions:

$$\begin{aligned} \frac{\gamma}{\gamma_0} &= \frac{m^*}{m_0^*} + \left(\frac{T}{T_0}\right)^{-\alpha} \\ \frac{\chi}{\chi_0} &= \frac{m^*}{m_0^*} + \beta_0 \left(\frac{T}{T_0}\right)^{-\alpha} \end{aligned} \quad . \tag{1.10}$$

Here γ_0 and χ_0 are respectively the specific heat coefficient and susceptibility of the Si conduction band (App. A.2); $m_0^* \simeq 0.34 m_0$ is the silicon conduction band mass, and the itinerant electron effective mass m^* was determined as $m^*/m_0^* \simeq 1.3$. β_0 is a function of α, and close to the MI transition, where $\alpha \simeq 0.6$ is roughly constant, $\beta_0 \simeq 10.5$. The parameter T_0 measures the fraction of localized momcnts in the system.

The strength of the two-fluid model is evident from the fittings to experimental data. A useful quantity with which to compare theoretical predictions is the Wilson ratio $(\chi/\chi_0)\,/\,(\gamma/\gamma_0)$, which eliminates the need for some unknown quantities such as the Fermi level, and has therefore fewer fitting parameters. Fig. 1.7a shows the Wilson ratio for zero magnetic field data on the insulating ($n/n_c = 0.78$) and metallic ($n/n_c = 1.09$ and 1.25) side. The fits to the data are excellent, with the only parameter being T_0. The values of T_0 for these fittings indicate a ratio 20 : 5 : 2 of localized spins. Assuming 100% localization for the insulating sample, we have 25% and 10% of the electrons localized for the samples $n/n_c = 1.09$ and 1.25 respectively. These large fractions of localized moments are also supported by the NMR studies of Alloul and Dellouve[22] and the specific heat studies of

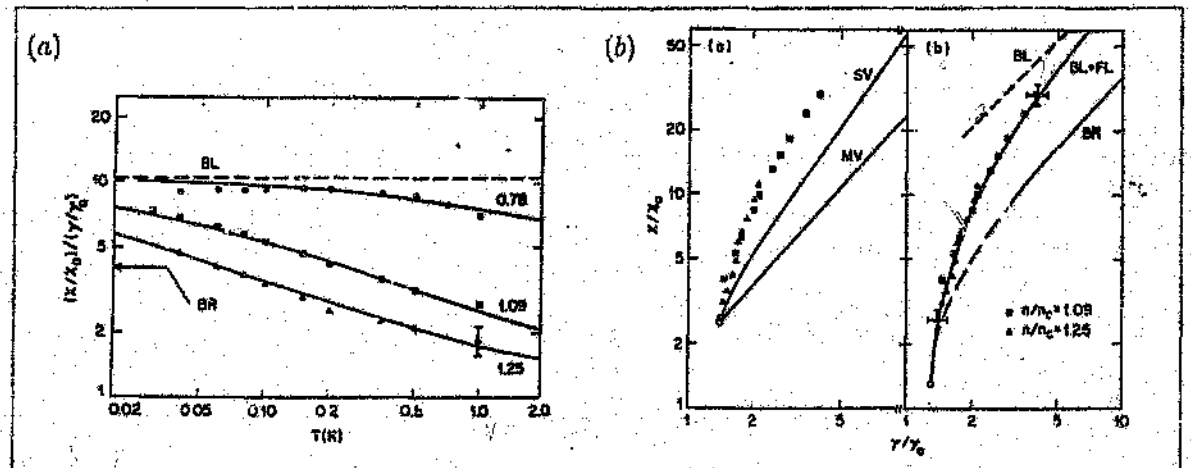


Fig. 3. – Wilson ratio as a function of temperature for the thin film samples and fits using the two-fluid model. Note the constant value for the insulating sample below $T \sim 0.2$ K, close to the Bhatt-Lee model value (dashed line).

Fig. 4. – Plot of the susceptibility versus specific heat γ for metallic samples. In (a) the experimental data are compared with the single and multi valley scaling theory, while (b) compares it with the Brinkman-Rice and the two-fluid (BL + FL) model. Dashed line is the asymptotic low temperature result where BL pairs dominate.

Figure 1.7: The (a) Wilson ratio and (b) χ/χ_0 versus γ/γ_0 plots, reproduced from [11].

Lakner *et al.*[5], and also the theoretical studies by Milovanović *et al.*[26].

Fig. 1.7b shows a plot of χ/χ_0 versus γ/γ_0, using the same data as in fig. 1.7a. The two-fluid model (indicated by BL+FL) again gives an excellent fit to the data. Also shown, for comparison, are the predictions of the single valley (SV) and multi-valley (MV) scaling theories, the Brinkman-Rice (BR) model, and the Bhatt-Lee (BL) model (which only considers the localized component). Clearly the two-fluid model is the dominant prediction here.

Reviews of the Paalanen two-fluid model can also be found in the references [7],[11],[6], and [1].

In conclusion, our aims are as follows:

- To extend the spin-pair approximation, in line with the ideas of Andres *et al.*[14], to include the effects of a magnetic field. The predictions will be compared to data, in particular to specific heat data in magnetic fields. The limitations of this model, as observed in the susceptibility by Andres *et al.*, will be determined.
- To extend the two-fluid model to include the effects of magnetic fields. The two-fluid

model has been very successful in describing the thermodynamic properties in zero-magnetic fields. Our main focus will be the magnetic field effects on the specific heat, as the BL model has already been successfully applied to describe the magnetization in large magnetic fields[15, 17].

- To develop and characterize this extended two-fluid model, and cast the predictions for the specific heat and susceptibility in the same form as the two-fluid model expressions in 1.10. This will allow us to see directly the effects a magnetic field will have on the system.

- To compare the spin-pair approximation and the BL model (an effective-spin-pair system with hierarchical $J^{-\alpha}$ distribution). As has been observed[5], the BL model predictions for the zero-field specific heat break down at low concentrations ($n \leq 0.34 \times 10^{18} cm^{-3}$, where negative values of α are obtained, which are not allowed in the BL model). These are also the concentrations below which the spin-pair approximation should have some validity.

Chapter 2

Model 1: The Poisson Distributed Spin-Pair System

2.1 Introduction

In this chapter we shall look at a particular formalism for the spin-cluster system, focusing particularly on spin-pairs (the spin-pair approximation), with an introduction to a larger cluster, the spin triad. The thermodynamic quantities for these clusters are easily obtained if the energy levels are known (App. A.1). However, for a MI system such as Si:P, where the spins are spatially distributed at random, we have a randomness to the energy levels for each cluster.

To obtain the required thermodynamic quantities we therefore need a statistical distribution function which correctly describes this random system. This choice of distribution function is in essence the key to fully describing these random spin systems, and determines the success or failure of a particular model. In this chapter we use a particular distribution and determine its validity in describing experimental data.

We will use the Poisson distribution to describe the distribution of nearest-neighbour separations in the spin-pair approximation, together with the Herring-Flicker form for the exchange coupling to describe the direct exchange interactions in spin-pairs. With this system we then determine the specific heat and susceptibility from the partition function (App. A.1), and compare to available experimental data.

We also introduce the spin triad system, where we consider a cluster of three spins,

as a natural extension of the spin-pair model. We include a coupling between a spin-pair and a nearest neighbour spin, and use a particular triad geometry to obtain results.

Included in this chapter is a paper published in Physical Review B, containing an outline of the formalism and results of this model.

2.2 The Distribution and Exchange Couplings of the Disordered Spin System

For the distribution of the separations R of nearest-neighbour spins in this disordered system, we can use the Poisson distribution, which is derived from the binomial distribution[1], and is given by

$$P(R)dR = 4\pi R^2 n e^{-\frac{4}{3}\pi R^3 n} dR \quad , \tag{2.1}$$

where $n = N/V$ is the concentration of localized spins. We are focusing on the spin-pair distribution, as spin-pairs are believed to be of dominant importance in determining the thermodynamic properties of the system: $P(R)dR$ is the probability of having a spin-pair with a separation in the interval $(R, R+dR)$. The average spin-pair separation $\bar{R}$ (together with the standard deviation Δ), using the above distribution, is then

$$\bar{R} \simeq 0.55\ n^{-\frac{1}{3}} \quad and \quad \frac{\Delta}{\bar{R}} \simeq 0.3 \tag{2.2}$$

For Si:P, with an effective Bohr radius of $a_B^* \simeq 15\mathring{A}$ [14] and a MI critical concentration $n_c \simeq 3.5 \times 10^{18} cm^{-3}$ [2], we have

$$\frac{\bar{R}}{a_B^*} \simeq 2.45 \left(\frac{n}{n_c}\right)^{-\frac{1}{3}} \quad . \tag{2.3}$$

Figure 2.1a shows a plot of the distribution function $P(R)$ in (2.1) together with an indication of the average separation of a spin-pair, which occurs close to the point $R_{\max} = 1/\sqrt[3]{2\pi n}$ at which $P(R)$ attains its maximum ($\bar{R}/R_{\max} \simeq 1.03$).

Given the separation of spin-pairs, we also require the interactions in these spin-pairs. A simple expression for the exchange coupling between two spins, originally developed

[1]The Poisson distribution is a limiting form of the binomial distribution when considering a bulk sample ($N, V \to \infty$ but $n = N/V$ remains constant). The expression used here is a direct consequence of the random distribution of donors in the sample. See App. B1 for more details on the derivation.

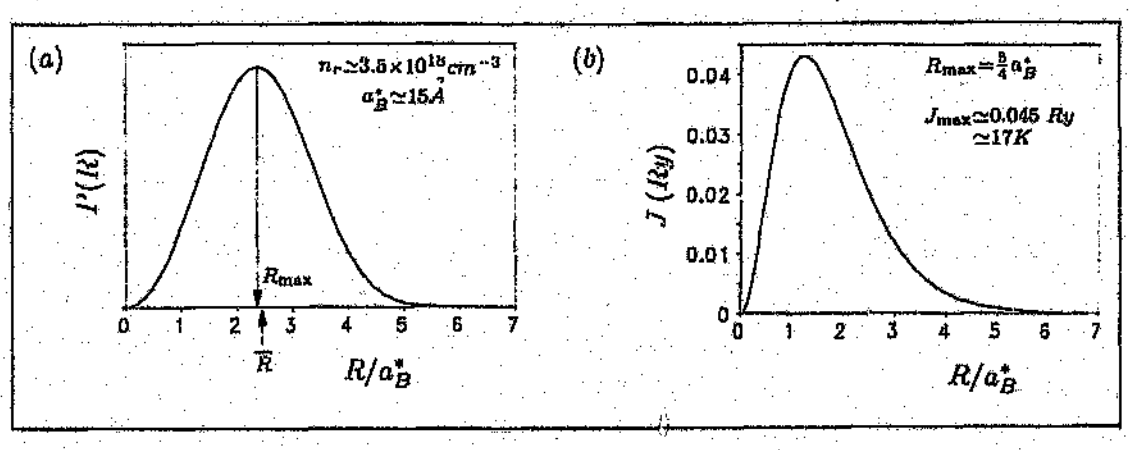


Figure 2.1: Plot of (a) the Poisson distribution function $P(R)$, using the Si:P values for a_B^* and $n = n_c$, and (b) the Herring-Flicker expression for the exchange coupling. The point (R_{max}, J_{max}) denotes the maximum in this function.

for spatially separated hydrogenic states, is given by the asymptotic Herring-Flicker[8] form

$$J(R) \simeq 0.3 \left(\frac{R}{a_B^*}\right)^{\frac{5}{2}} e^{-2\left(\frac{R}{a_B^*}\right)}, \quad \frac{R}{a_B^*} \gg 1\,, \tag{2.4}$$

where $J(R)$ is the exchange coupling (in Rydberg units: $1Ry \simeq 5.6 \times 10^{-21} J$) between the two spins separated by a distance R, while a_B^* is the effective Bohr radius of the donor state. Notice that because of the multi-valley character of Si, the Bohr radius for the donor ground state is not isotropic, and for doped Si we therefore use an average value[2] for a_B^* . Fig. 2.1b shows a plot of the Herring-Flicker expression in (2.4).

Also note that, although the above expression gives the asymptotic form for $J(R)$, being valid for $R \gg a_B^*$, we will take this expression to hold for all spin-pairs in the system. The Herring-Flicker form will be valid, using (2.3), when

$$\frac{n}{n_c} \ll 15\ . \tag{2.5}$$

So we can expect the Herring-Flicker form to be a good approximation deep in the insulating phase, with a possible breakdown around the MI transition. Note that the transformation between n and $\bar{R}$ is cubic, as seen from (2.2), so we have to be careful in

[2]Andres *et al.*[14] have shown that the anisotropic calculations are not very different, and the isotropic assumption is a good approximation.

quantitatively interpreting the relation $\ll$ in (2.5). For example, requiring $\bar{R}/a_B^* > 3$ say, would translate into $n/n_c < 0.8^3 = 0.512$.

2.3 The Spin-Pair Model

We now focus on the spin-pair model, where our system consists of isolated electron pairs, distributed randomly and described by the Poisson distribution in (2.1). The exchange coupling J between the electrons in a spin-pair is taken as the Herring-Flicker form $J(R)$, given in (2.4).

Figure 2.2 shows a spin-pair, together with an energy level diagram for this spin-pair with an exchange coupling J, in an external magnetic field B. There is one singlet $S = 0$ state, and three triplet $S = 1$ states ($S_z = -1, 0, +1$).

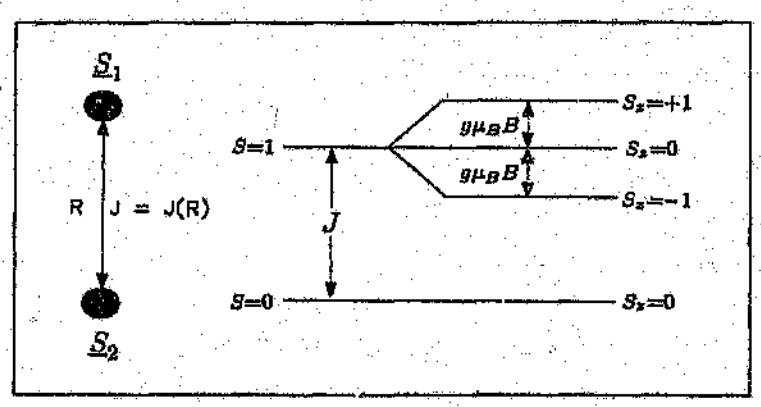


Figure 2.2: A spin-pair, with exchange coupling J, and corresponding energy levels.

The energy levels follow from the Hamiltonian H_{sp} for a spin-pair, with the dominant contributions being the exchange coupling and the Zeeman splitting:

$$H_{sp} = 2J\underline{s}_1 \cdot \underline{s}_2 + g\mu_B B S_z \quad , \tag{2.6}$$

where S_z is the z-component of the total spin $\underline{S} = \underline{s}_1 + \underline{s}_2$, $g \simeq 2$ is the electronic g-factor, and μ_B the Bohr magneton. Note that the exchange term in (2.6) is positive, indicating an antiferromagnetic coupling (leading to the singlet ground state in fig. 2.2).

The partition function Z_{sp} for a single spin-pair is then[3]

$$Z_{sp} = 1 + 2\cosh(\beta g \mu_B B) + e^{\beta J} \tag{2.7}$$

with $\beta = 1/k_B T$. (k_B is the Boltzman constant and T the temperature.) Since the spin-pairs are taken as being isolated, with no inter-cluster interactions present, the total partition function Z of the system is just the product of partition functions for each isolated spin-pair. Using the distribution of separations in (2.1), we can write for the total partition function

$$\ln Z = \left(\frac{n}{2}\right) \int_0^\infty dR\, P(R)\, \ln Z_{sp}(R) \quad . \tag{2.8}$$

We use the concentration of spin-pairs $(n/2)$ to give the partition function per unit volume. From (2.8) we obtain the specific heat C and the susceptibility χ with

$$\begin{aligned} C &= \frac{\partial E}{\partial T} = k_B \beta^2 \frac{\partial^2 \ln Z}{\partial \beta^2} \\ \chi &= \frac{\mu_0 M}{B} = \frac{\mu_0}{\beta B} \frac{\partial \ln Z}{\partial B} \end{aligned} \quad . \tag{2.9}$$

The integrals appearing in the above two expressions for C and χ have to be evaluated numerically (App. B.3). Although the factor n appears in these thermodynamic expressions, we must take care in explicitly taking these quantities as being proportional to the concentration of spin-pairs, since the concentration dependence also appears in the integral through the term $P(R)$. In the above two expressions, the specific heat and susceptibility clearly depend on T, B, n, with the only parameter being a_B^*. As mentioned, for Si:P we have $a_B^* \sim 15\text{Å}$, and so the magnitude of this parameter is limited to some extent.

2.3.1 The J-Coupled Spin-Pair

We first consider the thermodynamic properties, particularly the specific heat and susceptibility, of a single spin-pair with a fixed J. To find the total specific heat and susceptibility of the system we just sum over all spin-pairs, using the particular distribution function for the spin-pair system. Therefore, the thermodynamic properties of a single J-coupled spin-pair will be useful when looking at the properties of the whole system. We only consider the zero-field results, for simplicity, with the magnetic field behaviour of the whole system considered in the following sections.

[3]Note that we use the $|S = 1, S_z = 0\rangle$ state as the energy reference ($E = 0$) point for mathematical convenience. The physical quantities are not dependent on this reference point. See App. A1 for the use of the partition function.

Figure 2.2 shows the energy levels for the spin-pair with Z_{sp} given by (2.7). Using (2.9) we can evaluate the specific heat and susceptibility of a single J-coupled spin-pair. To find the zero-field specific heat C_0 and susceptibility χ_0, we let $B \to 0$ and, defining $x = \beta J = J/k_BT$, arrive at

$$\begin{aligned} C_0 &= 3k_B \frac{x^2 e^x}{(3+e^x)^2} \\ \chi_0 &= \frac{2\mu_0 (g\mu_B)^2}{J} \frac{x}{3+e^x} \end{aligned} \quad . \tag{2.10}$$

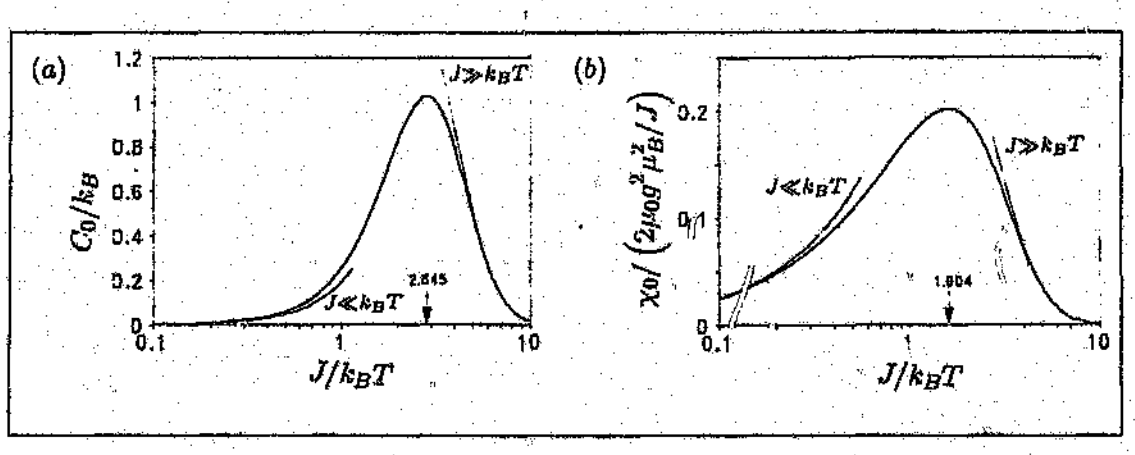


Figure 2.3: The (a) specific heat C_0 and (b) susceptibility χ_0 of a single J-coupled spin-pair. The peak positions and asymptotic forms are also included.

Figures 2.3a and 2.3b show plots of the temperature dependence (via $x = J/k_BT$) of the zero-field specific heat and susceptibility of a spin-pair as described by (2.10). We have included the positions of the maximum, as well as the asymptotic $J \ll k_BT$ and $J \gg k_BT$ behaviours of the two expressions. Notice that both the specific heat and susceptibility exhibit a peak structure, with the peak occurring at $J \sim k_BT$.

C_0 exhibits a typical Schottky-type peak structure evident from a two level system. The only difference between the Schottky expression and the expression used here is due to the three-fold degeneracy of the triplet state in the absence of a magnetic field. The asymptotic forms are

$$C_0 \equiv 3k_B \left(\frac{J}{k_BT}\right)^2 e^{-\frac{J}{k_BT}} \qquad J \gg k_BT$$

$$C_0 \equiv \frac{9}{16}k_B\left(\frac{J}{k_BT}\right)^2 \qquad J \ll k_BT \quad , \tag{2.11}$$

which are similar to the Schottky asymptotic forms (App. A.2). Note the high temperature, $J \ll k_BT$, form where $C_0 \sim 1/T^2$. If we have a maximum exchange coupling $J_{\max}$ in the distribution used, then, for temperatures such that $J_{\max} \ll k_BT$, we will have the total specific heat $C \sim 1/T^2$, independent of the actual form of the distribution.

The form of C_0 is to be expected, and no dramatic new behaviour is to be found. If we look at χ_0, however, we find a behaviour not usual for magnetic systems. χ_0 also exhibits a peak structure similar to that of C_0, with asymptotic behaviours

$$\begin{aligned} \chi_0 &\equiv \frac{2\mu_0\left(g\mu_B\right)^2}{J}\left(\frac{J}{k_BT}\right)e^{-\frac{J}{k_BT}} \qquad J \gg k_BT \\ \chi_0 &\equiv \frac{2\mu_0\left(g\mu_B\right)^2}{J}\frac{1}{4}\left(\frac{J}{k_BT}\right) \qquad J \ll k_BT \quad . \end{aligned} \tag{2.12}$$

The high temperature, $J \ll k_BT$, form is the Curie law form (App. A.2) where $\chi_0 \sim 1/T$. As in the case of the specific heat, if there is a maximum exchange coupling $J_{\max}$, then for $J_{\max} \ll k_BT$, the total susceptibility will also be of the form $\chi \sim 1/T$, independent of the distribution used. The low temperature form for the susceptibility, where χ_0 vanishes for $T \to 0$, is different from that of a "normal" magnetic system where saturation of magnetization occurs. This vanishing susceptibility is due to the antiferromagnetic nature of the interaction, which leads to the non-magnetic ground state (fig. 2.2). So, as $T \to 0K$, the magnetization vanishes as the ground state gets fully occupied (freezing out spin-pairs).

In the presence of a magnetic field the situation is different. If the magnetic field is large enough such that $g\mu_BB > J_{\max}$, from fig. 2.2 we see that the magnetic $(S = 1, S_z = -1)$ state will cross the singlet state and become the ground state. No matter what the distribution is, the ground state for each spin-pair will be the magnetic triplet state, which has a magnetic moment $\mu = g\mu_B$. So, as $T \to 0K$, we would expect the magnetization of the whole system $M \to (n/2)g\mu_B$. For smaller magnetic fields, the form of the magnetization depends on whether $g\mu_BB < J$ or $g\mu_BB > J$, which determines whether the non-magnetic singlet or magnetic triplet state is the ground state of the pair. The total magnetization will then explicitly depend on the particular J-distribution present for the system. However, from the above considerations, we know that the absolute zero magnetization $M_{T=0K}$ will increase from zero, for $B = 0$, and saturate at $M_{T=0K} = (n/2)\,g\mu_B$ for $g\mu_BB > J_{\max}$. The actual distribution will determine how $M_{T=0K}$ increases as a

function of the magnetic field, and hence determine the explicit form of the susceptibility $\chi_{T=0K} = \mu_0 M_{T=0K}/B$ at absolute zero. In the next section we look more closely at the field dependence of $M_{T=0K}$ and $\chi_{T=0K}$.

In conclusion, both the specific heat and susceptibility of a single J-coupled spin-pair have a peak structure, with dominant contributions for $J \sim k_B T$. To determine the properties of the whole system, we have to superimpose these peak structures according to the distribution used for the spin-pairs. Since the structure of the specific heat and susceptibility of a single spin-pair is primarily determined by J, a better feeling for the transition from a single spin-pair to the spin-pair system via the distribution used would be obtained if we had a sense of the actual distribution of exchange couplings J.

In this chapter we use the Poisson distribution for the spin-pair separation, and the Herring-Flicker form to describe the exchange coupling. Combining these two expressions can give us an indication as to the actual distribution of J-values.

2.3.2 The Distribution of Exchange Couplings J

Appendix B.2 contains the details for obtaining the distribution of exchange couplings $P(J)dJ$ from the Poisson distribution and the Herring-Flicker expression. The term $P(J)dJ$ gives us the probability of a spin-pair having a coupling in the interval $(J, J+dJ)$. To determine $P(J)$ we have also defined the integral $p(J) = \int_0^J P(J)dJ$, which gives us the probability of a pair coupling being in the interval $(0, J)$. So $(n/2)\,P(J)dJ$ gives us the average number of spin-pairs with couplings in $(J, J+dJ)$, while $(n/2)\,p(J)$ gives us the average number of spin-pairs with couplings less than J. Although we have used the function $p(J)$ to determine the form of $P(J)$, by differentiation, we shall see later that the function $p(J)$ is also useful, as it provides us with physical information, particularly quantities such as the absolute zero magnetization of the system.

Figures 2.4a and 2.4b show plots of $p(J)$ and $P(J)$ respectively, for various donor concentrations spanning from $n/n_c = 0.01$ to $n/n_c = 1$. We have used the expected Si:P values for a_B^* and n_c to determine these curves. Notice the logarithmic J-axis, and also note that we have converted J into thermal (Kelvin) units ($J[K] = J[Ry] * 5.6 \times 10^{-21}/k_B$). Specifying J in Kelvin (K) will give us a better connection between the distribution function and the temperature dependence of the thermodynamic quantities of the whole system.

The form of $p(J)$ in fig. 2.4a is as expected, with $p(J)$ increasing from $p(0) = 0$

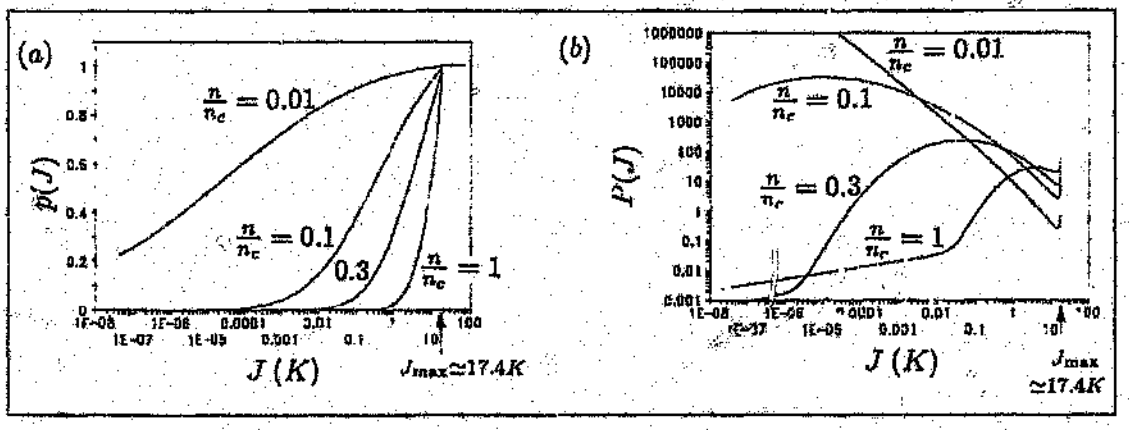


Figure 2.4: Plot of (a) the function $p(J) = \int_0^J P(J)dJ$, and (b) the distribution function $P(J) = p'(J)$.

to $p(J_{max}) = 1$, and then remaining constant at unity. Note that J spans several orders of magnitude in the region where $P(J)$ has its dominant contribution, particularly for the lower concentrations. As the concentration is increased, the exchange couplings in spin-pairs increase, and the features move to higher J values. Note $J_{max} \simeq 17.4K$, and also the appearance of the singularity (App. B.2) in $P(J)$ as $J \to J_{max}$, which is clearly seen for $n/n_c = 1$. The $J \to 0$ form of $P(J) \sim J^{1/5}$ (from eqn. (B.15) in App. B.2) is clearly visible for $n/n_c = 1$.

The Distribution $P(\log J)d\log J$

Although $P(J)$, shown in fig. 2.4b, is the function of interest when evaluating the thermodynamic properties, what is generally considered, due to the large orders of magnitudes that J takes on, is the distribution of the quantity $\log J$ ($\log \equiv \log_{10}$ and $\ln \equiv \log_e$), with $P(\log J)d\log J$ being the probability of $\log J$ being in the interval $(\log J, \log J + d\log J)$. Since $P(\log J)d\log J = P(J)dJ$, and noting that $d\log J = dJ/(J \cdot \ln 10)$, we conclude that

$$P(\log J) = (\ln 10)\, P(J)\, J \quad . \tag{2.13}$$

Figure 2.5 shows a plot of this distribution function $P(\log J)$ using the same concentrations as in fig. 2.4b for $P(J)$. Notice that we still have a peak structure with the

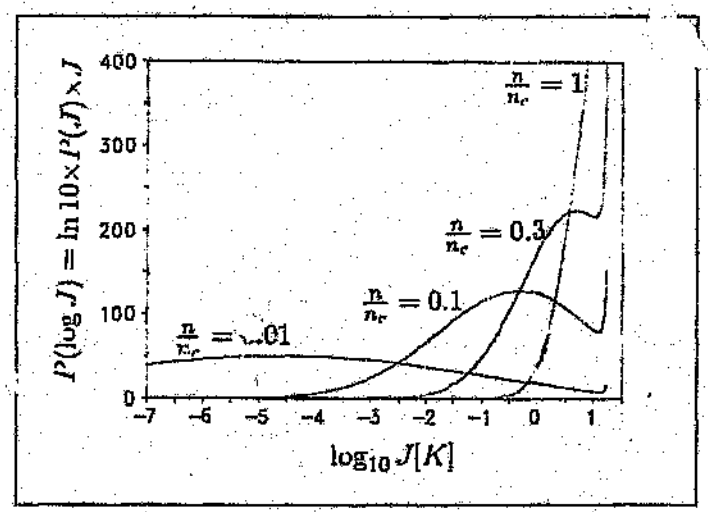


Figure 2.5: The distribution $P(\log J)$ of $\log J$ values.

peak moving to larger J values with increasing concentration. The singularity at $J_{\max}$ is still present, and, for $n/n_c = 1$, the peak is not visible due to this divergence of the curve as $J \to J_{\max}$.

The Absolute Zero Magnetization and Susceptibility

The function $p(J)$ in fig. 2.4a can provide direct physical information, such as the absolute zero magnetization $M_{T=0K}$ of the system, which is given by the simple expression

$$M_{T=0K}(B) = g\mu_B \, n(J < g\mu_B B) \quad , \tag{2.14}$$

where $g\mu_B$ is the magnetic moment of a spin-pair in the triplet state, while $n(J < g\mu_B B)$ is the concentration of spin-pairs with a coupling $J < g\mu_B B$. Referring to fig. 2.2, we can immediately see the origin of (2.14), where $n(J < g\mu_B B)$ is just the concentration of spin-pairs with a magnetic triplet ground state. The rest of the spin-pairs will have $J > g\mu_B B$, and hence be frozen in the non-magnetic singlet ground states which do not contribute to the magnetization at absolute zero. From the definition of $p(J)$, we have $n(J < g\mu_B B) = (n/2)\, p(g\mu_B B)$ and hence

$$M_{T=0K}(B) = \left(\frac{n}{2}\right) (g\mu_B) \; p(g\mu_B B) \quad . \tag{2.15}$$

So $M_{T=0K}$ is proportional to $p(g\mu_B B)$, and the plot in fig. 2.4a can therefore directly give us $M_{T=0K}$ as a function of B : we just replace the axis labels $p(J)$ and $J[K]$ respectively by $M_{T=0K}/\left(\frac{n}{2}\right)g\mu_B$ and $\frac{g\mu_B}{k_B}B \simeq 1.34\,B[T]$.

The absolute zero susceptibility

$$\chi_{T=0K}(B) = \mu_0 \frac{M_{T=0K}(B)}{B} \tag{2.16}$$

can also be determined. To find $\chi_{T=0K}(B=0)$, we let $B \to 0$, and this value will depend on how $M_{T=0K}$ converges to zero as $B \to 0$, which depends on the actual distribution used. From App. B.2 we have $p(J) \sim J^{6/5}$ for $J \to 0$, and hence $\chi_{T=0K}(B) \sim B^{1/5} \to 0$ as $B \to 0$. We therefore expect the susceptibility of the system to vanish as $B, T \to 0K$.

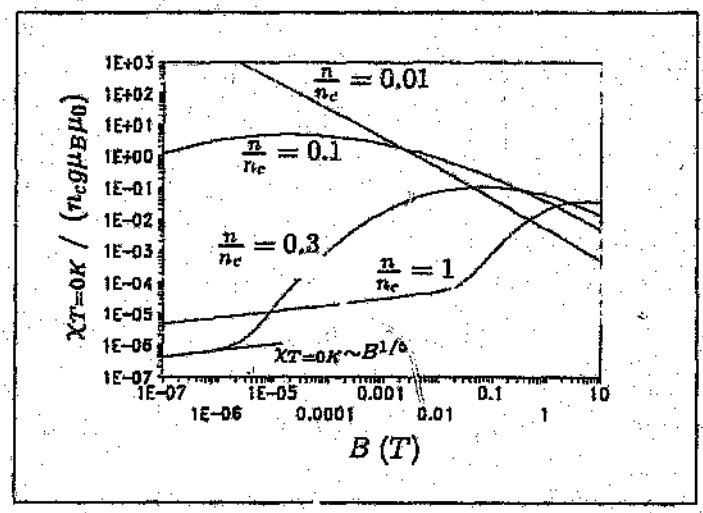


Figure 2.6: The magnetic field dependence of the absolute zero susceptibility $\chi_{T=0K}$.

A plot of $\chi_{T=0K}$ versus B is shown in fig. 2.6. Also included is the asymptotic $B \to 0$ form for the concentration $n/n_c = 0.3$, where $\chi_{T=0K} \sim B^{1/5}$. This asymptotic behaviour is also more evident for the highest concentration $n/n_c = 1$. For $B > 10T$ (when $g\mu_B B > J_{\max}$), we clearly have $\chi_{T=0K} \sim 1/B$, since this is where the magnetization has saturated to its maximum value (fig. 2.4a).

The features of the curves are similar to those of $P(J)$ in fig. 2.4b. This similarity is easily established if we explicitly express $\chi_{T=0K}$ in (2.16) in terms of $P(J)$. We then find

that $\chi_{T=0K}(B)$ is actually proportional to the average of $P(J)$ in the interval $[0, g\mu_B B]$:

$$\chi_{T=0K}(B) \propto \frac{1}{g\mu_B B} \int_0^{g\mu_B B} P(J) dJ \quad . \tag{2.17}$$

2.3.3 The Specific Heat

From (2.9), we obtain the following form for the total specific heat of the spin-pair system:

$$C = \left(\frac{n}{2}\right) k_B \beta^2 \int_0^\infty dR P(R) \left(\frac{1}{Z_{sp}} \frac{\partial^2 Z_{sp}}{\partial \beta^2} - \left(\frac{1}{Z_{sp}} \frac{\partial Z_{sp}}{\partial \beta} \right)^2 \right) \quad . \tag{2.18}$$

The integral in the above expression is evaluated numerically (App. B.3), and we now consider some of the properties of this predicted specific heat.

Figures 2.7a, 2.7b and 2.7c show plots of C, given by (2.18), versus T. In each plot we vary one of the parameters (B, a_B^*, or n) on which C depends. The actual values we have used reflect typical values found in experimental data.

Figure 2.7a shows the dependence of C on B; the logarithmic T-scale is used to resolve the peak structures for the various fields. Note the non-zero contribution for the zero-field specific heat, and the broad peak of this curve (a direct consequence of the single spin-pair specific heat shown in fig. 2.3a, and the distribution function shown in fig 2.5, both of which have a peak structure). On the other hand, the Schottky contribution describing a spin-singlet vanishes for zero magnetic field (App. A.2). For non-zero magnetic fields, we can clearly see the development of Schottky-type peaks, with the position of the peak moving to higher temperatures as the field B is increased. This behaviour is to be expected from a magnetic system. For higher temperatures the specific heat converges with the zero-field curve, and, depending on the range of magnetic fields, we can therefore use the zero-field predictions, which are simpler to use. Comparing this specific heat form with the Schottky form (App. A.2), we see several distinct differences:

1. For the Scottky specific heat, we have the condition $B/T_{\max} \approx 1.79$ for the position of the peak (point 2 of . on. A.2), while for this model this is not the case. From fig. 2.7a, we find $B/T_{\max} \sim 1.33$, 1.70, and 1.76 for $B = 100G$, $0.1T$, and $1T$ respectively, showing an increase in $B/T_{\max}$, tending to the Schottky value of 1.79, as B increases.

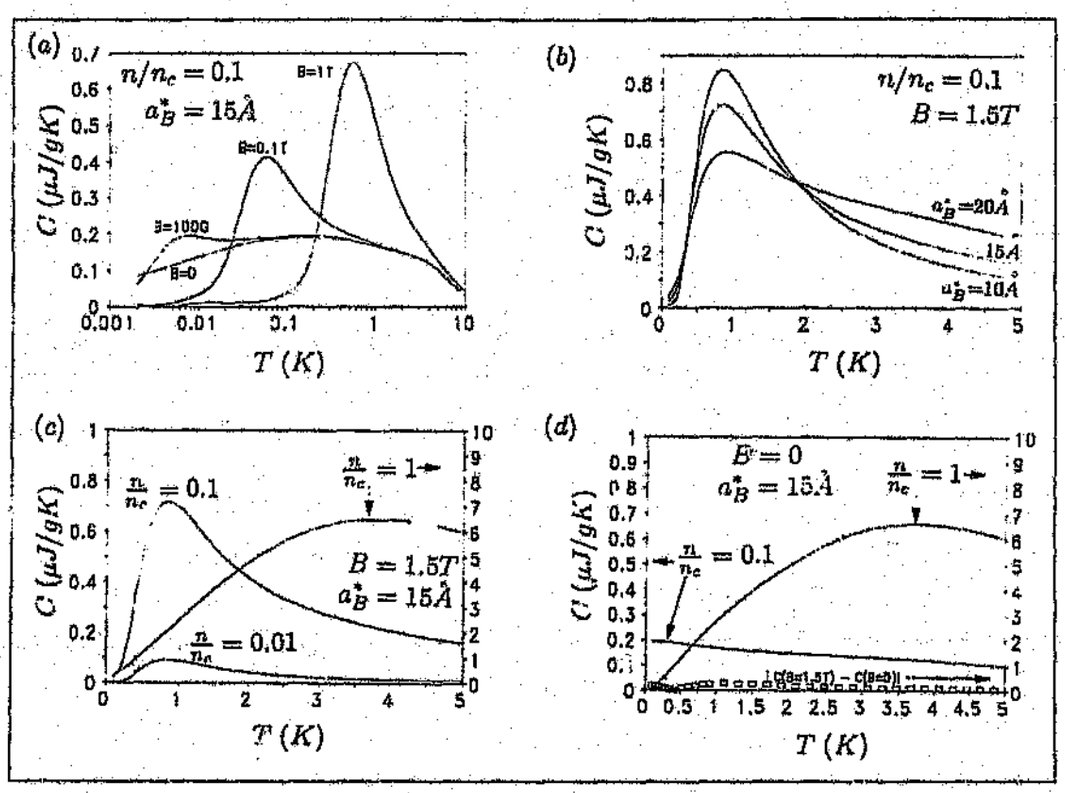


Figure 2.7: The dependence of the spin-pair system specific heat C on (a) the magnetic field B, (b) the Bohr radius a_B^*, and (c) the concentration n. Fig. (d) is shown to explain a feature of fig. (c).

2. There is an increase in the peak amplitude as the magnetic field is increased. This does not occur for the Schottky specific heat, which has a field-independent peak height for a fixed concentration (point 3 of App. A.2).

3. The peaks are broader than the Schottky peaks. This feature arises from the large range of magnitudes that J assumes in the system.

The changing peak height and shift in position with decreasing B-field, together with the higher temperature convergence with the zero-field curve, can produce the appearance of two distinct peaks in the specific heat, particularly at the lower magnetic fields. For an example of this behaviour, refer to the $B = 100G$ curve in fig. 2.7a. Here we have

a peak at about $7mK$ produced by the magnetic field, while the second peak occurs at higher temperatures (around $110mK$) and is obtained from the zero-field curve. Also note the appearance of a very small peak for the $B = 1T$ curve at around $10mK$. This peak will be difficult to confirm, since it appears at temperatures where the nuclear specific heat contribution (App. A.2) will become dominant. For larger magnetic fields ($\sim 1T$), the nuclear specific heat has a significant contribution[5] even up to about $100mK$.

For temperatures above $T = 1K$, focusing on the $B = 0$ curve, we see a change in the curvature of the curve at about $T = 4K$. This feature is due to the presence of a maximum exchange coupling $J_{max} \simeq 17K$. For temperatures $T > 17K$, we would expect $C \sim 1/T^2$, as was mentioned in §3.1.

Figure 2.7b shows the dependence of C on a_B^*. For Si:P, we have $a_B^* \simeq 15\mathring{A}$ and in this plot we include the effects of changing a_B^* above and below this value. The specific heat is clearly sensitive to changes in a_B^*, with a distinct change in the form of the curve. With an increasing a_B^*, the peak becomes broader, with the peak height decreasing. This can be understood from figs. 2.1b and 2.3a. As a_B^* is increased, we have the appearance of stronger coupled pairs, which causes the broadening of the peak. Alternatively, for a fixed concentration, eqns. 2.2 and 2.3 show that Δ, which measures the spread in R, increases with increasing a_B^*, and hence we have a larger range of J-values in the distribution.

We also note from this plot the effect of letting $a_B^* \to 0$. Since the exchange coupling depends only on the ratio R/a_B^* (eqn. (2.4)), letting the effective Bohr radius vanish essentially removes the coupling, and the system becomes an isolated spin-1/2 system. We therefore expect the specific heat to tend to the Schottky form as $a_B^* \to 0$.

Figure 2.7c shows the concentration dependence of the specific heat. We have used the concentrations $n/n_c = 0.01$, 0.1, and 1, corresponding to $\bar{R}/a_B \simeq 11.2$, 5.2, and 2.4 respectively. Note the different y-axis used for $n/n_c = 1$, which has a range ten times larger than that used for $n/n_c = 0.01$ and 0.1. For the two lowest concentrations, we have an expected behaviour, with the peak heights increasing with increasing concentration, and the peak position little affected. However, an unexpected result is the large shift in the peak position for $n/n_c = 1$.

To explain this phenomenon, we refer to fig. 2.7d, which shows the predicted zero-field specific heat for the same concentrations $n/n_c = 0.1$ and $n/n_c = 1$ as in fig. 2.7c. Notice that we have used identical scales in both these figures. For the $n/n_c = 0.1$ curves, we can clearly see the development of a peak on top of the zero-field curves for the $B = 1.5T$

specific heat. This is not the case for the $n/n_c = 1$ curves, where there is little noticeable difference between the $B = 1.5T$ and $B = 0$ curves.

In fig. 2.7d we have included the difference $|C(B = 1.5T) - C(B = 0)|$ between the two curves, to explicitly show this difference, indicated with the data label '□'. As can be seen, switching on a magnetic field to $B = 1.5T$ produces only a small perturbation to the zero-field curve, and the unusually shifted peak in fig. 2.7c is in actual fact the peak originating from the zero-field specific heat. This small perturbing effect from a magnetic field for this particular concentration arises from the large (compared to the magnetic field $B = 1.5T$) exchange couplings present in the system (fig. 2.5), with the average exchange coupling (App. B.2) for $n/n_c = 1$ being $\langle J \rangle \simeq 10K$. For $n/n_c = 0.1$. we have $\langle J \rangle \simeq 2K$, and referring to fig. 2.5, we see that we have a larger distribution of couplings less than $B = 1.5T$, giving rise to the well defined peak present in fig. 2.7c.

Notice from fig. 2.7a, for $n/n_c = 0.1$, that, even for a small field $B = 100G$, we have a well-defined peak superimposed on the zero-field curve. Going down to even lower fields will produce the same effect as for $n/n_c = 1$ in figs. 2.7c and 2.7d.

2.3.4 The Susceptibility

From (2.9) we can obtain χ of the spin-pair system:

$$\chi = \left(\frac{n}{2}\right) \frac{\mu_0}{\beta B} \int_0^\infty dR P(R) \left(\frac{1}{Z_{sp}} \frac{\partial Z_{sp}}{\partial B}\right) \tag{2.19}$$

and, using (2.7) for Z_{sp}, we obtain

$$\chi = \left(\frac{n}{2}\right) 2g\mu_B\mu_0 \left(\frac{\sinh(\beta g \mu_B B)}{B}\right) \int_0^\infty dR \frac{P(R)}{Z_{sp}} \quad . \tag{2.20}$$

Note the indeterminate form for $B = 0$ enclosed in the brackets. In order to evaluate the zero-field susceptibility, we replace this term with its limit as $B \to 0$, which is $\beta g \mu_B$. Again, the integral in the above expression has to be evaluated numerically (App. B.3). We next look at some of the properties of the susceptibility in this spin-pair model. The magnetic field dependence of $\chi_{T=0K}$ has already been discussed (fig. 2.6).

Figures 2.8a, 2.8b, and 2.8c show plots of χ, given by (2.20), versus T. In each figure we vary one of the parameters (B, a_B^*, or n) on which χ depends.

Figure 2.8a shows the dependence of the susceptibility on B. In this plot we

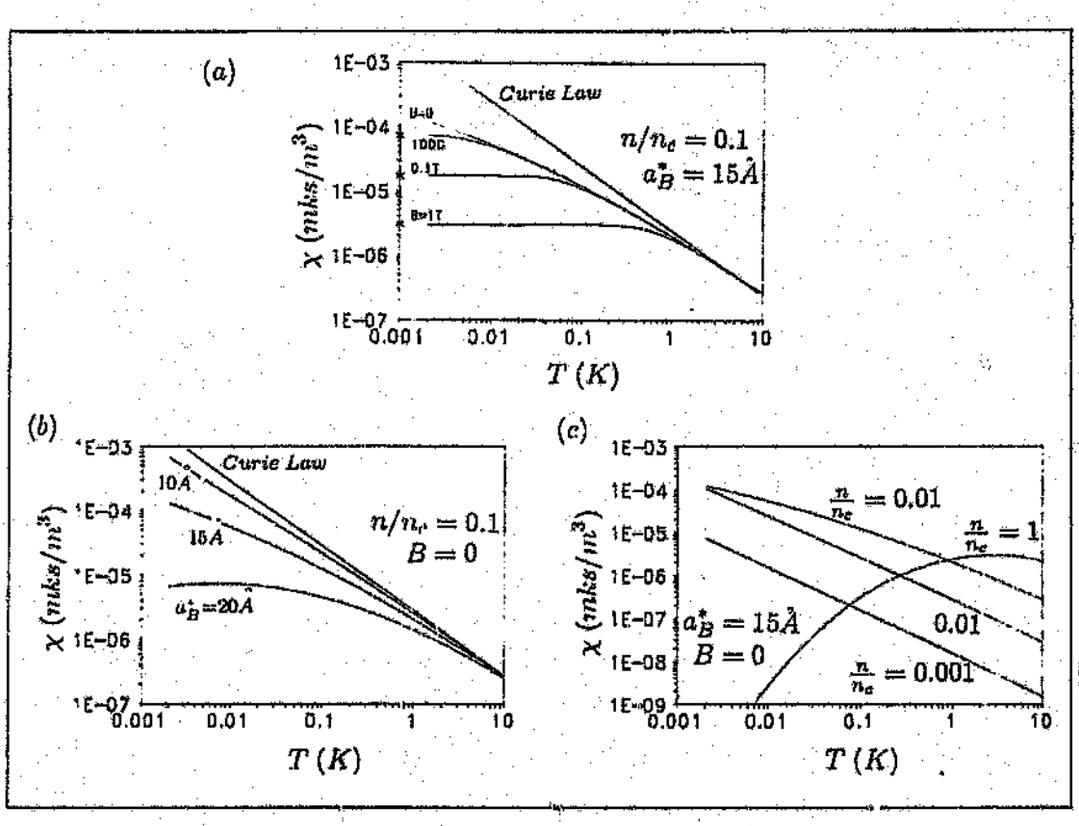


Figure 2.8: The dependence of the spin-pair system susceptibility χ on (a) the magnetic field B, (b) the Bohr radius a_B^*, and (c) the concentration n.

have included a Curie law curve[4] to show the deviation from the isolated spin system. We can clearly see a departure from this Curie law, which increases as the magnetic field is increased. This departure increases as we decrease the temperature, and for $B \equiv 0$ can be explained in terms of the freezing out of pairs (when $T \lesssim J$ for a spin-pair) into the ground state. Because of the large range of exchange couplings, this freezing out occurs gradually over a large temperature range. The Curie law increases indefinitely as $T \to 0K$, while the zero-field susceptibility for this system attains a maximum and then vanishes[5] as $T \to 0K$. For non-zero magnetic fields the situation is more complicated. Firstly, $\chi_{T=0K}$

[4] $\chi \sim 1/T$, where we have arbitratily drawn the curve to match the other curves at the highest temperatures for comparison. We do, however, expect the curves to converge with the Curie law, since, as we have mentioned in §2.3.1, for $T \gtrsim J_{\max}$ we have $\chi \sim 1/T$.

[5] $\chi_{T=0K} \to 0$ as $B \to 0$ from fig. 2.6.

(fig. 2.6) is now non-zero and depends strongly on the magnetic field and the concentration used. Secondly, the Curie law is derived from the Brillouin function[6] when $\mu B \ll k_B T$, and hence is valid for all temperatures only when $B \to 0$. For non-zero magnetic fields, the susceptibility of a free spin-1/2 system will level off to a constant value (saturation of magnetization). The relationship between the free spin-1/2 and spin-pair susceptibility in a fixed field then depends on the actual spin-pair distribution function used.

The non-zero field susceptibility converges with the zero-field susceptibility at higher temperatures, with this temperature increasing as the field is increased. For the lower temperatures we see an apparent levelling off of the susceptibility, which occurs at higher temperatures for larger magnetic fields. Closer inspection shows that the non-zero field curves actually go through a very small maximum before levelling off to the asymptotic $T \to 0K$ value $\chi_{T=0K}$ (which can be obtained from fig. 2.6, and is shown in fig. 2.8a by the symbol $\times$ on the y-axis). For the $B = 1T$ curve, this maximum occurs at about $0.1K$ and, at the lowest temperatures shown on this plot, has basically attained its $T \to 0K$ value of $\chi_{T=0K} \simeq 3 \times 10^{-6} mks/m^3$. As inferred from fig. 2.6, the values of $\chi_{T=0K}$ increase as B is decreased to $100G$, and then vanish as $B \to 0$. So we have a crossover of the susceptibility curves in fig. 2.8a as the temperature is reduced even further. The lower magnetic field ($B < 1T$) curves also display a small maximum in χ, which is not visible in the plot, with this maximum moving to lower T as B is reduced. These peaks are very minute, and the non-zero field curves are very close to their asymptotic $T \to 0K$ values at the lowest temperatures shown in the plot.

Figure 2.8b shows the dependence of the susceptibility on a_B^*. Note that we have plotted the $B = 0$ susceptibility for convenience. (The B-field behaviour can be inferred from fig. 2.8a.) We have used values for a_B^* above and below the expected value of $a_B^* \simeq 15\mathring{A}$ for Si:P, and we can see that χ is very sensitive to a_B^*, changing about two orders of magnitude at the lowest temperatures ($\sim 1mK$) in changing a_B^* from $10\mathring{A}$ to $20\mathring{A}$. In the previous section we mentioned that the system should tend towards an isolated spin system as a_B^* vanishes. In this plot we have also included the Curie law, and we see that the susceptibility rapidly converges to this Curie curve as a_B^* is reduced. We note again that, since $\chi_{T=0K} = 0$ for $B = 0$, the curves will display a maximum in the susceptibility, and this is evident from the $a_B^* = 20\mathring{A}$ curve.

[6]The Brillouin function is used to give the general form of the susceptibility for free spins.

Figure 2.8c shows the concentration dependence of the susceptibility (again for $B = 0$, with the B-field dependence inferred from fig. 2.8a). The first feature to note is the curve for $n/n_c = 1$ ($\bar{R}/a_B^* \simeq 2.4$), which has a distinct maximum and clearly shows that $\chi \to 0$ as $T \to 0$, as discussed earlier, for $B = 0$.

As the concentration is reduced, the curvature in the susceptibility on the shown temperature range reduces. For the concentrations $n/n_c = 0.01$ and $n/n_c = 0.001$, there is no visible curvature, and the susceptibility follows a power law form ($\chi \sim T^{-a}$, for some $0 < a < 1$) on the whole temperature range shown ($10mK \to 10K$, representing four orders of magnitude in temperature). Analysis of these two curves shows that $a = 0.971$ and $a = 0.995$ for $n/n_c = 0.01$ and $n/n_c = 0.001$ respectively, converging to and very close to $a = 1$ as n/n_c is reduced. This value of $a = 1$ represents the Curie law and, as expected, the susceptibility tends to the Curie law as the concentration is reduced. So, for concentrations $n/n_c \lesssim 0.01$ and for low magnetic fields, we can clearly use the free spin-1/2 system Curie law for the susceptibility.

2.3.5 Conclusions

Therefore, taking into account the analysis done so far, we conclude that the spin-pair model developed here should be of some use for the Si:P system in the concentration range $0.01 \lesssim n/n_c \lesssim 0.1$. For $n/n_c \lesssim 0.01$, we would expect the system to be well described by the isolated spin-1/2 formalism, and it would be easier to use the simple Schottky and Curie law expressions to explain the thermodynamic quantities. The isolated spin-1/2 behaviour for these low concentrations has been observed experimentally, as was introduced in §1.3.1. For $n/n_c > 0.1$, we have uncertainty in the model as the Herring-Flicker form used could become less valid in describing the exchange couplings, or we may have to take into account the appearance of larger clusters of spins, which is seen experimentally for $n/n_c \gtrsim 0.03$ by probes such as ESR (§1.3.1). The analysis by Andres *et al.*[14] on the susceptibility indicates that the spin pair approximation already fails at $n/n_c \sim 0.2$.

2.4 The Spin-Triad Model

In the previous section we considered a system of randomly distributed, non-interacting spin-pairs. In this section we introduce an extension to the spin-pair model by considering the spin-triad model. We consider a random distribution of clusters containing

three electrons, with no inter-cluster interactions. We choose a very simple specific geometry for the triad, since we want to determine the possible effects of adding a spin to the cluster. The susceptibility is expected to be noticeably affected since all the states are then magnetic, with no non-magnetic states such as the spin-pair singlet ground state present. In the next section we compare the singlet, pair, and triad predictions, which we shall also compare with experimental data.

We start with a cluster of three interacting spins, as shown in fig. 2.9:

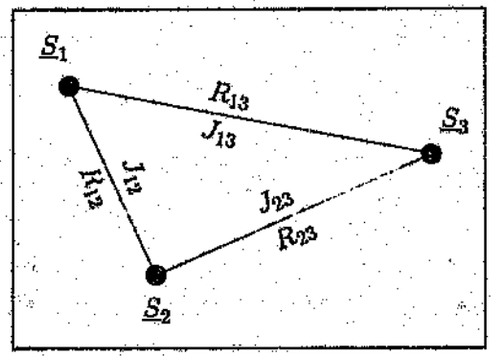


Figure 2.9: A spin-triad, where R_{ij} is the separation and J_{ij} the exchange coupling between spins i and j.

From this triad we choose the nearest neighbour spin-pair S_1 and S_2, separated by R_{12}, with an exchange coupling J_{12}. The formalism of the distribution and exchange coupling for the spin-pair model from the previous sections can also be applied to the spin-pairs present in the triad. So the Poisson distribution in (2.1) is used to describe the distribution of separations R_{12}, while the Herring-Flicker expression in (2.4) describes the exchange couplings $J_{ij} = J(R_{ij})$ between spins. Next we have to consider the couplings J_{13} and J_{23} of the third spin S_3 to the spin-pair.

New and Castner[13] have mentioned that a very probable configuration is the nearly isosceles geometry with $J_{13} \simeq J_{23} \ll J_{12}$, while the equilateral geometry with $J_{13} \simeq J_{23} \simeq J_{12}$ is improbable. The first assumption we make in our model is that each spin-triad in the system has an isosceles geometry with $J_{13} = J_{23} < J_{12}$ (or equivalently $R_{13} = R_{23} > R_{12}$). New and Castner also provide the energy levels for a spin-triad in the isosceles configuration, and the spin-triad together, with its energy spectrum, is shown in fig. 2.10.

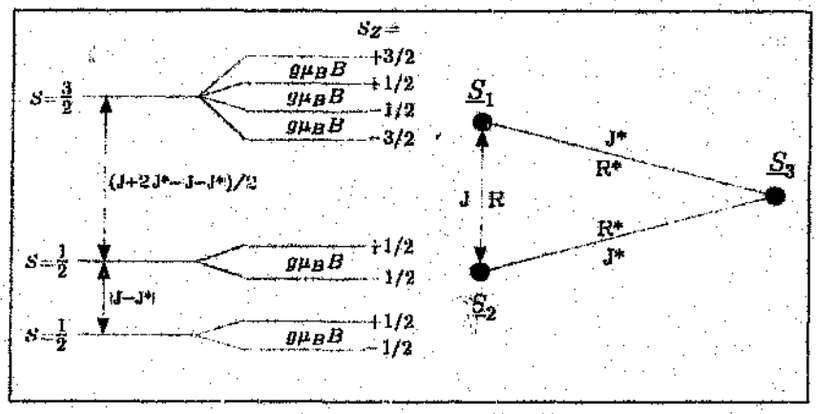


Figure 2.10: The energy level diagram for the spin-triad shown.

The states of the spin-triad are described by the total spin S and z-component S_z. Here J is the spin-pair coupling, while J^* represents the couplings $J_{13} \simeq J_{23}$. The Zeeman splitting in a magnetic field B is clearly present, while it should be noted that all the states, including the doublet ground state, are magnetic states ($S_z \neq 0$).

From the energy spectrum shown in fig. 2.10 we can obtain the partition function $Z_{triad} = \sum_i e^{-\beta E_i}$ for a single spin-triad. The total partition function (App. A.1) is then obtained by taking the product of all spin-triad partition functions, over the distribution of couplings J and J^*. We already have a distribution (§2.3.2) for J and we therefore require a distribution of J^* for the spin-triad system. We, however, simplify the model by taking J^* as being fixed for all spin-triads with a fixed J, i.e. J^* is a function of J only.

One very simple way in which we initially did this was to take $J^* = \alpha J$, where $\alpha \in [0, 1]$ is a fixed parameter describing the triad geometry. We thus assume for each spin-triad in the system that the ratio J^*/J has a constant value of α. Using this very simplified scheme may require us to have an α which is at least concentration-dependent. By reducing the concentration, and thereby reducing the couplings between pairs, we would expect the ratio J^*/J to actually vanish (probably exponentially) as the spins become more isolated from each other. We would not expect J^*/J to remain constant as $n \to 0$.

Another scheme which can be used, and is the one we adopted in this model, is to write $R^* = \alpha R$, where $\alpha \geq 1$ is again a fixed parameter describing the isosceles geometry in real space. We thus assume that the isosceles geometry of all the spin-triads

are mathematically similar, and hence that the ratio $R^*/R \geq 1$ is a constant value. We then take the coupling J^* as described by the Herring-Flicker expression in (2.4), and hence $J^* = J(R_*^*) = J(\alpha R)$. For this scheme, we then have for a spin-triad

$$\frac{J^*}{J} = \alpha^{5/2} e^{-2(\alpha-1)(R/a_B^*)} \quad , \tag{2.21}$$

and this ratio then vanishes exponentially as the concentration is reduced. (Reducing n increases the separation R.) This scheme would be more physically expected than the first scheme introduced above.

For $\alpha = 1$, we have the improbable equilateral geometry, and, by increasing α, with the ratio J^*/J decaying exponentially with respect to α, we shall eventually have the spin-triad equivalent to an isolated spin-pair and spin-singlet. We shall consider the effect of increasing α from 1 in subsequent subsections. At sufficiently low temperatures and magnetic fields, we also expect this spin-triad to behave effectively as an isolated spin-1/2 system, as inferred from fig. 2.10. For sufficiently low T and B the spin-pair is frozen in the singlet state, and the only transitions are then the spin flips of the third spin.

If we now take this very simplified scheme of letting $J^* = J(\alpha R)$, with $\alpha \geq 1$ a fixed parameter, then we only have to consider the distribution of separations R, which we describe using $P(R)$ in (2.1). Z for this spin-triad system is then given by

$$\ln Z = \left(\frac{n}{3}\right) \int_0^\infty dR\, P(R) \ln Z_{triad} \quad , \tag{2.22}$$

and, using (2.9) for the specific heat and susceptibility, we have for the triad system

$$\begin{aligned} C &= \left(\frac{n}{3}\right) k_B \beta^2 \int_0^\infty dR\, P(R) \frac{\partial^2 \ln Z_{triad}}{\partial \beta^2} \\ \chi &= \left(\frac{n}{3}\right) \frac{\mu_0}{\beta B} \int_0^\infty dR\, P(R) \frac{\partial \ln Z_{triad}}{\partial B} \quad . \end{aligned} \tag{2.23}$$

Note that the factor $(n/3)$ gives the concentration of triad clusters. The integrals in the above two expressions have to be evaluated numerically (App. B.3), and depend explicitly on the terms n, T, B, a_B^*, and α.

2.4.1 The Specific Heat

We now consider the properties of the spin-triad specific heat $C = C(T, B, n, a_B^*, \alpha)$ as defined in (2.23). We look at the temperature dependence of C, and consider separately the dependence of C on the parameters B, n, a_B^*, and α. We shall again choose values for

the parameters to reflect the ranges used in the experimental data, and focus particularly on the Si:P system ($a_B^* \simeq 15\mathring{A}$ and $n_c \simeq 3.5 \times 10^{18} cm^{-3}$).

Firstly, we consider the dependence of C on the newly introduced parameter α. Fig. 2.11a shows a plot of C versus T for various values of α.

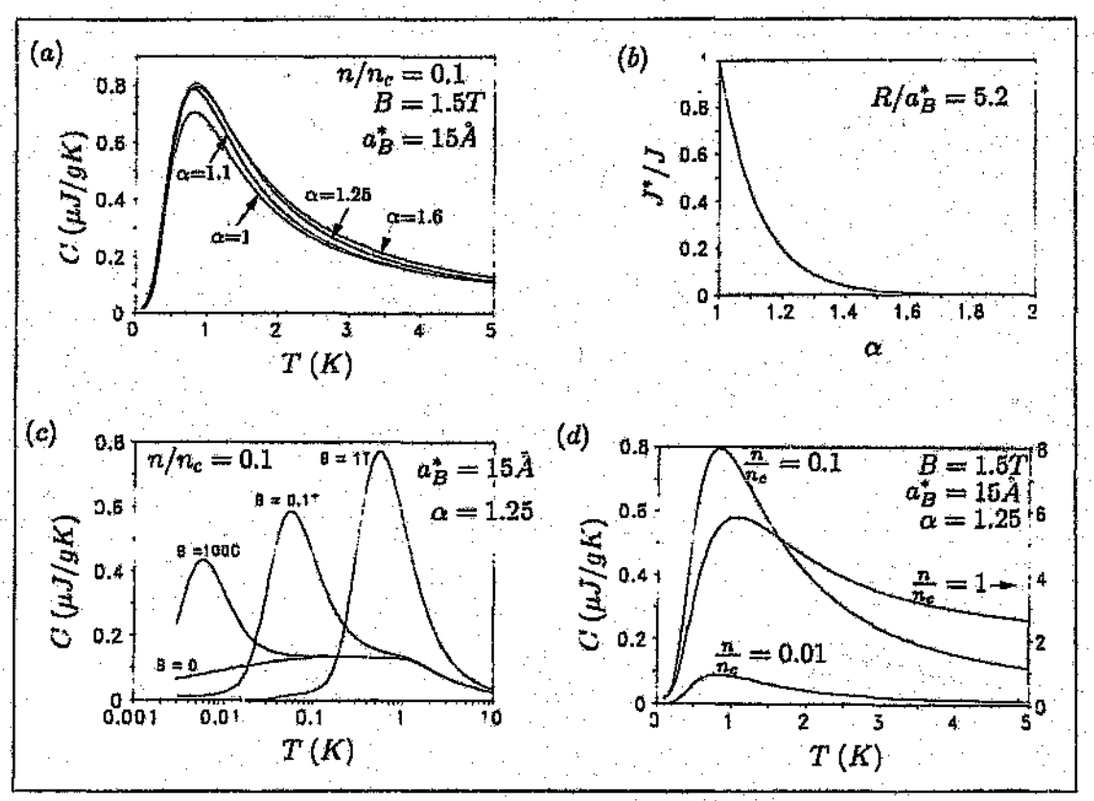


Figure 2.11: Dependence of the spin-triad specific heat C on (a) the parameter α, (c) the magnetic field B, and (d) the concentration n. Figure (b) plots J^*/J versus α as an aid to fig. (a).

We have varied α from $\alpha = 1$, corresponding to an equilateral geometry, to a value of $\alpha = 1.6$. Varying α through these values produces visible changes in the specific heat, although the general form remains the same. For $\alpha > 1.6$, the changes in C are very small, and the different curves are then only distinguishable due to very small deviations at the highest temperatures in the plot. So for $\alpha > 1.6$, the spin-triad predictions are essentially similar to an isolated spin-pair and an isolated spin-1/2 system (letting $\alpha \rightarrow \infty$). This

"convergence" of the specific heat for $\alpha > 1.6$ can be seen from eqn. (2.21) for the relative triad couplings J^*/J. To obtain an estimate of the magnitude of J^*/J for the system with $n/n_c = 0.1$, we can insert $\bar{R}$ into (2.21), and we have from (2.3) that $\bar{R}/a_B^* \simeq 5.2$. A plot of J^*/J versus α is shown in fig. 2.11b, and we can clearly see the exponentially vanishing J^*/J for $\alpha > 1.6$.

For subsequent illustrations of the specific heat, we arbitrarily choose $\alpha = 1.25$ as an intermediate value between $\alpha = 1$ and $\alpha = 1.6$.

The magnetic field dependence of C is plotted in fig. 2.11c. Note again the logarithmic T scale to resolve the expected Schottky type peaks in a magnetic field. We again have a non-zero zero-field contribution which has a broad peak spanning several orders of magnitudes in temperature. The change in curvature above $T = 1K$ can again be attributed to the existence of a maximum exchange coupling $J_{\max} \simeq 17K$ in the distribution. For non-zero magnetic fields, the curves are similar to those of the spin-pair model shown in fig. 2.7a. We have the typical behaviour of the peak moving to higher temperatures as the B-field is increased, while we also have a corresponding increase in the peak height. The quantity $B/T_{\max}$, where $T_{\max}$ is the position of the maximum, also increases as B is increased, similar to the spin-pair model.

The dependence of the specific heat on a_B^* is qualitatively the same as that for the spin-pair model shown in fig. 2.7b.

Finally, fig. 2.11d shows the concentration dependence of the specific heat. Note that we again use a different y-axis for the $n/n_c = 1$ curve which is ten times larger. The peak position for the two lowest concentrations is basically the same at $T \simeq 0.84K$, while, for the largest concentration $n/n_c = 1$, the peak is shifted to larger temperatures ($T \simeq 1.1K$). As for the spin-pair system, the peak height increases as n is increased, but not in proportion to n, and the peaks broaden out as the concentration is increased.

2.4.2 The Suceptibility

We now consider the properties of the spin-triad susceptibility $\chi \equiv \chi(T, B, n, a_B^*, \alpha)$, as defined in (2.23). Again we shall produce the temperature dependence of χ, and consider its dependence on each one of the parameters B, n, a_B^*, and α.

Due to the limits[7] on the numerical evaluation of χ, we were not able to evaluate

[7]The numerical evaluation of the susceptibility only allowed temperatures down to about $3mK$. For temperatures below $3mK$, the orders of magnitudes were too large for the computer to process.

the susceptibility to arbitrarily low temperatures. It is therefore useful to know susceptibility of the spin-triad system at $T = 0K$, since this can give us an indication of the behaviour of χ as $T \rightarrow 0K$. For example, referring to §2.3.4 where we introduced the spin-pair susceptibility, we see that the absolute zero behaviour is essential. Focussing on fig. 2.8c, although it appears that for the lower concentrations the susceptibility increases indefinitely as $T \rightarrow 0K$, we know (fig. 2.6) that $\chi_{T=0K} = 0$, and hence the susceptibility must have a peak structure, attaining its maximum at lower temperatures. This peak structure is evident from the highest concentration curve in this figure. For the spin-pair model, we had to numerically evaluate $M_{T=0K}$ and $\chi_{T=0K}$ from the J-distribution. For the spin-triad system, the results are more easily obtained.

Magnetic Properties at T=0K : From the energy level diagram in fig. 2.10, we see that in a magnetic field, the ground state of every spin-triad has the magnetic moment of a free electron ($\mu = \mu_B$). This is true even for the special case when $J = J^*$, and the ground state is degenerate, even in a magnetic field. So $M_{T=0K}$ of the spin-triad system is given by the simple expression $M_{T=0K} = (n/3)\,\mu_B$, where $n/3$ is the concentration of spin-triads and μ_B is the magnetic moment of each spin-triad at $T = 0K$. Notice that, as for isolated spins, this saturation magnetization is field-independent, unlike the spin-pair magnetization which is strongly field-dependent (§3.2.1). The $T = 0K$ susceptibility ($\chi = \mu_0 M/B$) for Si:P is then

$$\chi_{T=0K} = \frac{\mu_0 \mu_B}{B}\left(\frac{n}{3}\right) = \frac{1.375}{B[T]}\left(\frac{n}{n_c}\right)\ 10^{-5} mks/m^3 \quad , \tag{2.24}$$

and the absolute zero susceptibility of the spin-triad system is reduced by a factor of 3 from the free spin-1/2 susceptibility, due to the freezing out of a spin-pair into the non-magnetic singlet state for every three spins.

We now continue with the susceptibility at finite temperatures and use (2.24) to infer the asymptotic $T \rightarrow 0K$ behaviour. Firstly, we consider the dependence of χ on the parameter α. As for the specific heat shown in fig. 2.11a, χ rapidly converges as α is increased from $\alpha = 1$.

This is shown in fig. 2.12a, where we have plotted χ versus T for the two fields $B = 0$ and $B = 1T$. For each field we varied α from $\alpha = 1$ (the improbable equilateral geometry) to larger values. As can be seen, the sensitivity on α is very small and the curves converge for values as low as $\alpha = 1.25$. So, for $\alpha > 1.25$, the susceptibility is

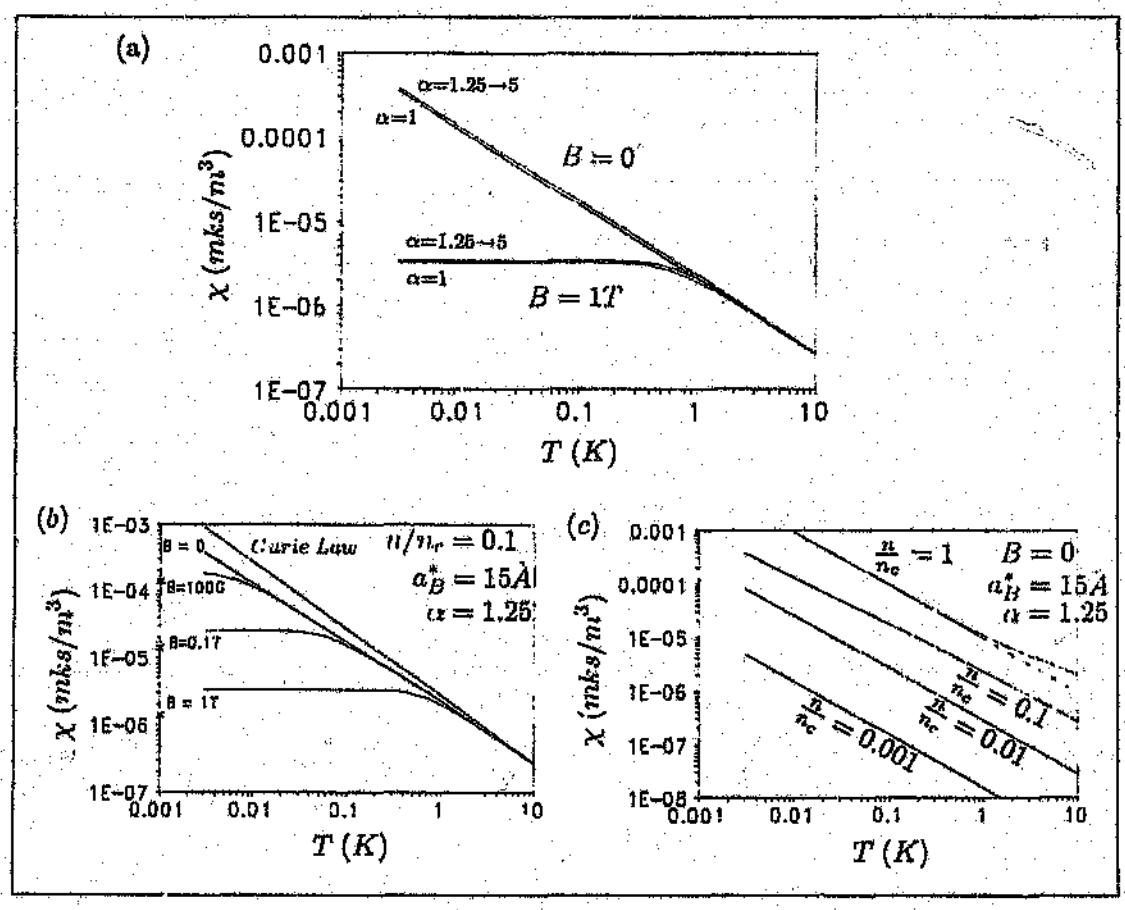


Figure 2.12: Dependence of the spin-triad susceptibility χ on (a) the parameter α, (b) the magnetic field B, and (c) the concentration n.

essentially independent of α. Letting $\alpha \to \infty$, where we then have a decoupled spin-pair and spin-singlet (fig. 2.10 and eqn. (2.21)), we see that, for $\alpha > 1.25$, the susceptibility essentially consists of equal contributions from a spin-pair system and a free-spin system. Subsequently, for the rest of this section we will choose a representative value of $\alpha = 1.25$, as for the specific heat. Larger values of α will not visibly affect the curves, while lower values would not be expected as we would then tend towards the improbable equilateral geometry ($\alpha = 1$).

The magnetic field dependence is shown in fig. 2.12b. Note that we have indicated $\chi_{T=0K}$, obtained from (2.24), in the plot with the symbol '×', and the Curie law is also

included for comparison. The field dependence of the susceptibility is very similar to that of the spin-pair model shown in fig. 2.8a. The curves also show a peak for non-zero fields, evident from the $\chi_{T=0K}$ values. The main difference here is that, whereas the spin-pair susceptibility remains bounded (fig. 2.5) with the zero-field susceptibility $\chi(B=0) \rightarrow 0$ as $T \rightarrow 0K$, $\chi(B=0)$ here diverges as $T \rightarrow 0K$. This is evident from eqn. (2.24). The spin-triad susceptibility is also closer to the indicated Curie law susceptibility, due to the net magnetic moment present in the triad.

The dependence of χ on a_B^* is similar to that of the spin-pair model shown in fig. 2.8b. As expected, by reducing a_B^*, the curves tend to the Curie law, due to the reduction of the antiferromagnetic couplings between the spins.

Finally, we consider the concentration dependence of the susceptibility, which is shown in fig. 2.12c. The $B=0$ susceptibility is shown here with the field dependence inferred from fig. 2.12b. Several points can be obtained from this plot:

1. For the concentration $n/n_c = 1$, we have included a Curie law form ($\chi = c/T$, shown by the dashed curve[8]). We can see that at low temperatures the susceptibility is well described by the Curie law, with a divergence at higher temperatures. This behaviour is expected at higher concentrations. Referring to fig. 2.4b or 2.5, we see that for $n/n_c = 1$, the majority of spin-pairs have a large exchange coupling $0.1K \lesssim J \lesssim 10K$. So, for $T \lesssim 0.1K$, we would have the majority of spin-pairs in a spin-triad frozen in the singlet ground state, with the spin-triad system then behaving as a free spin-1/2 system giving rise to the Curie type behaviour at these low temperatures. The Curie constant for this curve is a third of the free spin-1/2 system value, as expected. The same behaviour would be expected for the lower concentrations, but at much lower temperatures. The enhancement of χ at higher T is due to the breaking ("unfreezing") of the antiferromagnetic coupling in the spin-pairs.

2. For the concentration $n/n_c = 0.1$, we have a near power law form $\chi \sim T^{-a}$, with $a < 1$ ($a \simeq 0.889$, less steep than the Curie law where $a = 1$). Therefore, as a first order approximation, we can use $\chi \sim T^{-a}$ to describe the spin-triad susceptibility at these concentrations. This power law form has been observed in experimental data (§1.3.1).

[8]The Curie constant $c = \left(\mu_0 \mu_B^2 n_c / k_B\right)(n/n_c) \simeq 27.7\,(n/n_c)\ 10^{-6}\ mks/m^3$ for Si:P.

3. As we reduce the concentration even more (from $n/n_c = 0.1$), the power law form $\chi \sim T^{-a}$ becomes more distinct, with $a \rightarrow 1$ (the Curie law). For the concentrations $n/n_c = 0.01$ and $n/n_c = 0.001$, the susceptibility is close to the Curie law, with $a = 0.983$ and $a = 0.993$ respectively. As in the spin-pair model (fig. 2.8c), this behaviour is expected as $n \rightarrow 0$.

2.4.3 The Validity of this Spin-Triad Model

For the spin-triad model we have made two basic assumptions:

1. We first assumed an isosceles geometry for each spin-triad, which was mentioned as being a very probable configuration. For an arbitrary spin-triad, we need two parameters to describe the couplings of the third spin to the other two spins. For an isosceles geometry, we need only one parameter. In our case we have used the parameter α to describe this coupling of the third spin to the spin-pair. For an isosceles geometry, the energy spectrum is also more readily obtained, as shown in fig. 2.10.

2. We take the geometrical parameter α as being fixed for the whole system of spin-triads. This does not seem to be physical and it would be more realistic to introduce a distribution $P(\alpha)$ of α-values to describe the spin-triad geometry.

So far we have used a fixed value of α to determine the specific heat and susceptibility, and we have increased α from 1 to see the evolution of these thermodynamic quantities. The next step would be to average the results over the distribution $P(\alpha)$ of α-values. However, the results from the specific heat and susceptibility calculations so far can be used to make some predictions for an arbitrary distribution of α-values. This is all based on the small changes and rapid convergence of the specific heat and susceptibility curves as α is increased.

We now digress and consider a more general formulation of the spin-triad model. Referring to fig. 2.10, to determine the thermodynamic properties of the spin-triad system we require a distribution $P(R, \alpha)$ of values for R and α (where $R^* = \alpha R$): $P(R, \alpha)dRd\alpha$ is the probability of $R \in (R, R + dR)$ and $\alpha \in (\alpha, \alpha + d\alpha)$. Due to the random spatial distribution of the electrons we do not expect any correlation between the R and α, and

hence we can separate the variables and write $P(R,\alpha) = P(R)P(\alpha)$. For the total specific heat and susceptibility of the spin-triad system, we then have

$$\begin{aligned} C &= \iint P(R,\alpha)dRd\alpha\, C(R,\alpha) = \int d\alpha P(\alpha) \int dR P(R)\, C(R,\alpha) \\ \chi &= \iint P(R,\alpha)dRd\alpha\, \chi(R,\alpha) = \int d\alpha P(\alpha) \int dR P(R)\, \chi(R,\alpha) \quad , \end{aligned} \tag{2.25}$$

where $C(R,\alpha)$ and $\chi(R,\alpha)$ are respectively the specific heat and susceptibility of a spin-triad system with fixed geometrical parameters R and α (with an implicit dependence on T, B, a_B^*, and n). Note that the first integration, which we shall denote $C(\alpha)$ and $\chi(\alpha)$, is the specific heat and susceptibility for a fixed value of α, which we have already analyzed (§2.4.1 and §2.4.2.).

Noting from figs. 2.11a and 2.12a that both $C(\alpha)$ and $\chi(\alpha)$ are bounded from above and below, we can write

$$(C_{\min}, \chi_{\min}) \leq (C(\alpha), \chi(\alpha)) \leq (C_{\max}, \chi_{\max}) \quad . \tag{2.26}$$

Combining (2.25) and (2.26), and using the normalization condition $\int_1^\infty P(\alpha)d\alpha = 1$ for the distribution of α-values, we arrive at the inequalities

$$\begin{aligned} C_{\min} &\leq C \leq C_{\max} \\ \chi_{\min} &\leq \chi \leq \chi_{\max} \quad , \end{aligned} \tag{2.27}$$

for any distribution function $P(\alpha)$. These inequalities tell us that the bounds of the curves $C(\alpha)$ and $\chi(\alpha)$ are also the bounds for C and χ, no matter what the distribution function $P(\alpha)$ is. We therefore have that for any $P(\alpha)$, the specific heat and the susceptibility of the system will lie inbetween these two bounds. The small changes and rapid convergence of the curves $C(\alpha)$ and $\chi(\alpha)$ ensure that these bounds are close together, and we can therefore infer the behaviour of these thermodynamic quantities for an arbitrary spin-triad system.

Since the equilateral geometry ($\alpha = 1$) is improbable, we would expect α not to be too close to $\alpha = 1$. For larger values of α ($\alpha \gtrsim 1.6$ for the specific heat and $\alpha \gtrsim 1.25$ for the susceptibility), the curves become indistinguishable. So, as a first order approximation, we can therefore let $\alpha \to \infty$ to describe this system, which then consists of decoupled spin-pairs and spin-singlets. We can therefore expect that the spin-triad thermodynamic properties lie inbetween those of a free spin-1/2 system and a spin-pair system, with an almost equal admixture.

2.5 Comparisons of the Singlet, Pair, and Triad Models

We now do a comparison of the spin-singlet (free spin-1/2), spin-pair, and spin-triad models, and also compare the predictions of these three models to available experimental specific heat and susceptibility data. These data were obtained from published papers[19, 18, 14], but at the time were limited in availability. The specific heat data are the published excess specific heat attributed to localized moments, with the phonon and itinerant contribution subtracted. Here we do an analysis of these limited data. More data became available subsequently and were used in the analysis of later chapters. For the specific heat, in particular, we discovered inadequacies in using the published excess specific heat data (as used in this chapter) when comparing to the predictions of our models. In view of this, we will, however, return to this model in chapter 5, and consider the predictions with respect to these newer data. The results from this chapter have been published in Physical Review B, and a copy of this article is included in §2.7. Note that, for the spin-triad model, which is the only one with a unknown parameter, we fix $\alpha = 1.25$ as a representative value.

2.5.1 Specific Heat Analysis

We first consider the insulating phase, where we expect the model to be realistic for $n/n_c \sim 0.1$. As mentioned, for larger n/n_c, we do expect a breakdown in the model. The limits of the Herring-Flicker expression may be reached, and the small cluster approach will also become questionable at larger concentrations where we must consider larger cluster formation, inter-cluster interactions, and the formation of itinerant electrons.

Figures 2.13a and 2.13b show the specific heat predictions for the spin-singlet (Schottky), spin-pair, and spin-triad models, together with experimental data for the specific heat in large magnetic fields.

Figure 2.13a shows the results for the concentration $n/n_c = 0.15$, in fields of $B = 0.97T$ and $B = 3.8T$, while fig. 2.13b is at a higher concentration of $n/n_c = 0.23$, in fields of $B = 1.5T$ and $B = 5.7T$. As was noted in the previous section, the spin-triad predictions should be well approximated by the superposition of the free-spin and spin-pair contributions, in roughly equal proportions. This can be seen to be true, in both figs. 2.13a and 2.13b, particularly for the lowest fields.

The quantitative predictions for $n/n_c = 0.15$ in fig. 2.13a are close to the experi-

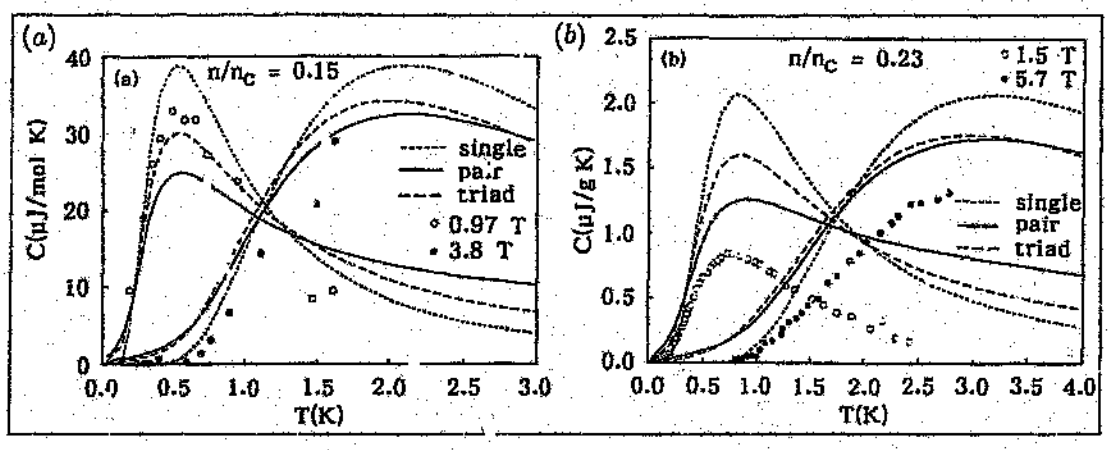


Figure 2.13: Comparisons with the specific heat data in the insulating phase. Reproduced from the publication in §2.7.

mental data, with the triad predictions giving a good account of the peak for $B = 0.97T$. The free-spin prediction overestimates these data, with the spin-pair prediction for the peak too low. Notice also the broader peak structure of the spin-pair curve. For the $B = 3.8T$ data, there are not enough data points to make any conclusions about the predictions, although the magnitudes seem to coincide well. The predictions of all three models for $n/n_c = 0.23$ in fig. 2.13b are larger than the experimental data for both magnetic fields. The shape of the data appears to again follow that of the spin-triad model, if we consider scaling the curves. (We will return to this point of scaling down the concentration in chapter 5.) As expected, the model here is clearly inadequate in describing the data for $n/n_c > 0.1$. To fully test the specific heat predictions in large magnetic fields, we would require data for $n/n_c < 0.1$.

Finally, in fig. 2.14 we plot the specific heat data for a sample in the metallic phase, with $n/n_c = 1.29$, in a magnetic field of $B = 1.5T$. The curves are predictions of the spin-triad model. The percentages next to the curves indicate by how much the actual concentration was scaled down to produce these magnitudes. Although the peak position and peak structure are not well predicted here, the data do indicate the presence of some localized moments, and the predictions do give some indication as to the extent of localization. Paalanen *et al.*[7, 1] have estimated the fraction of electrons appearing to be localized at 2% → 10% for $n/n_c = 1.25$, and the percentages given here compare well to

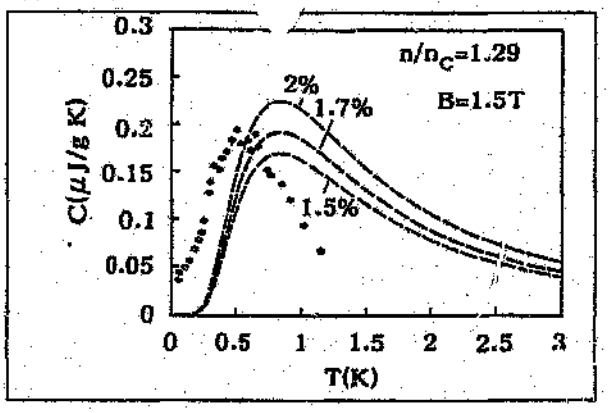


Figure 2.14: Comparisons with the specific heat data in the metallic phase. Reproduced from the publication in §2.7.

the quoted values.

2.5.2 Susceptibility Analysis

For the susceptibility data, we have the concentrations $n/n_c = 0.03$, 0.12, and 0.21, at very low magnetic fields ($10G$ and $50G$). These concentrations are well below the MI transition, and at the concentration values where we expect our model to be valid.

Figure 2.15 shows these susceptibility data, together with the predictions of the spin-singlet (Curie law), spin-pair, and spin-triad models. Again we see that the spin-triad susceptibility lies inbetween those of the spin-singlet and spin-pair, as predicted.

For the lowest concentration $n/n_c = 0.03$, the spin-pair gives the best results, and gives a good account of the susceptibility from about $10mK$ upwards. For the larger two concentrations $n/n_c = 0.12$ and $n/n_c = 0.21$, we see that in this temperature range ($T \gtrsim 10mK$) the data lie between the spin-pair and the spin-triad curves. For the concentration $n/n_c = 0.21$, the spin-pair model underestimates, while the spin-triad model overestimates, the data at the lowest temperatures. These results could indicate that, for the spin-pair model, we need to include more isolated (or very weakly coupled) spin-pairs[9] to enhance the susceptibility.

[9]Referring to fig. 2.5, we see that the distribution of exchange couplings has a peak structure about some average $\log J$. For this type of distribution we therefore have a negligible number of pairs that are very weakly coupled (essentially decoupled to form isolated spins).

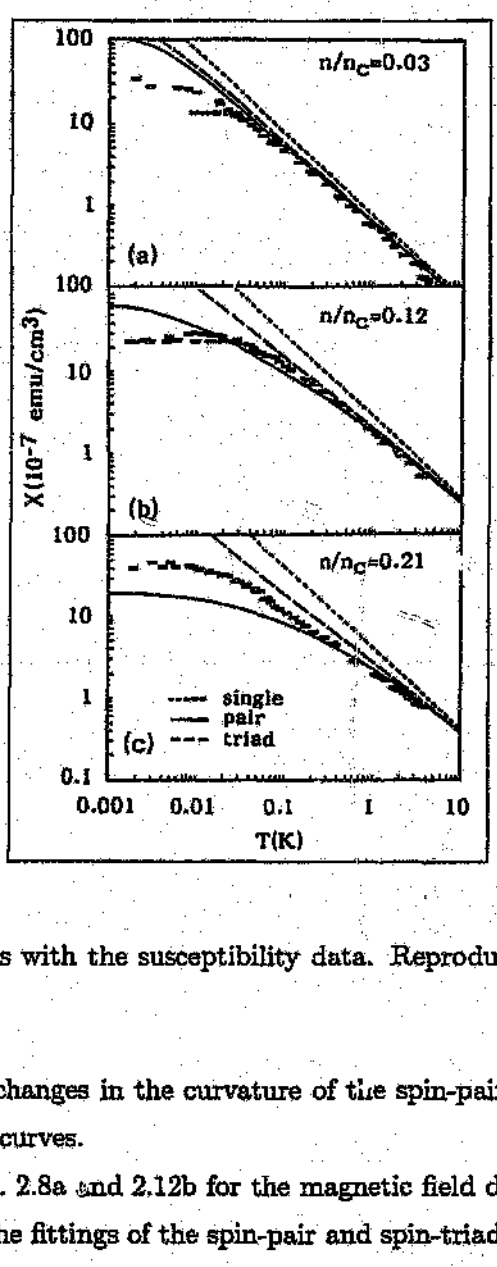


Figure 2.15: Comparisons with the susceptibility data. Reproduced from the publication in §2.7.

Note the rapid changes in the curvature of the spin-pair curve, compared to the spin-singlet or spin-triad curves.

Referring to figs. 2.8a and 2.12b for the magnetic field dependence of the susceptibility, we can improve the fittings of the spin-pair and spin-triad curves by increasing the magnetic field. This will, however, require field values larger than specified for the data.

The data for all three concentrations do lie below the Curie law for isolated spins, and indicate the presence of the antiferromagnetic couplings. For temperatures $T \gtrsim 100mK$, we have a near power law behaviour $\chi \sim T^{-a}$, as observed by Andres *et al.*[14], with $a < 1$ decreasing (tending away from the Curie law slope of $a \doteq 1$) as n/n_c increases. This behaviour is also observed in the predictions for the models.

2.6 Discussion

The lack of experimental data analyzed in this chapter does not enable us to make any definite conclusions about the predictions of the models developed so far. We can, however, make several points on the results:

1. We expected the limits of the models to be reached when $n/n_c \sim 0.1$, due to the validity of the Herring-Flicker form for the exchange couplings. The results show that we are indeed reaching the limits for $n/n_c \sim 0.1$, with the predictions giving good estimates of the magnitudes of the data, but not satisfactorily describing the shapes. The best results we have are for the spin-pair prediction of the susceptibility for $n/n_c = 0.03$, with the data well described for temperatures down to about $T = 10mK$. For the higher concentration, $n/n_c \simeq 0.2$, we see a clear departure of the predictions from the data, in both the specific heat and susceptibility. Already at these low concentrations we may have to introduce a lower effective concentration of localized moments to improve the predictions, or it is possible that the Herring-Flicker form is becoming invalid in describing the exchange couplings. (See point 4.)

2. The results for the metallic phase specific heat indicate that we have to scale down the concentration of localized moments to estimate the specific heat magnitude. The scaling percentages agree well with other estimates of the fraction of localized moments. So, for higher concentrations ($n/n_c \gtrsim 0.2$), even in the metallic phase $n/n_c > 1$, with the use of concentration scaling, we can obtain an indication as to the extent of localization in the system.

3. The models predict a near power law form for the susceptibility at higher temperatures, and this power law form can indeed be observed in the data for $T \gtrsim 100mK$. The slope deviates more from the Curie law as the concentration is increased, due to the stronger antiferromagnetic couplings present as n/n_c increases.

4. The susceptibility data for $n/n_c = 0.21$ lie inbetween the spin-pair and spin-triad predictions. This indicates that we must either introduce an effective concentration of localized moments, or modify the distribution of exchange couplings. For the spin-pair prediction, we need to enhance the susceptibility, which can be done by allowing very weakly coupled spin-pairs in the distribution. We require a significant

number of weakly coupled spin-pairs that are in their excited magnetic triplet state at the temperatures of interest. The Herring-Flicker form, together with the Poisson distribution, produces a peak structure for the distribution of exchange couplings, and does not take into account the possible presence of a significant number of very weakly coupled (nearly free) spins. The model to be introduced in the next chapter does have this property, with the use of the BL distribution of exchange couplings.

The simplicity of the models described here is that for the spin-pair model we do not have any free parameters, while for the spin-triad model we only have the parameter α with which to deal. If we decide to use instead an effective concentration of localized moments to describe the data, we introduce an extra fitting parameter. This may be useful only if the predictions can sufficiently describe the shape of the data. Alternatively, the use of the free spin-1/2 equations (the Scottky specific heat and Curie law susceptibility) can be used, with the use of an effective concentration and effective magnetic field (App. A.2), to make qualitative predictions, such as the fraction of localized moments (determined by the effective concentration) and the strength of the couplings between the spins (determined by the effective magnetic field). This procedure, which has been used in studies to analyze the data in magnetic fields, would then be simpler than using the numerical calculations of the spin-pair model.

In chapter 5 we will revisit the model developed here, and compare the prediction to more recent data. In the next chapter we shall show why the published excess specific heat data used in this chapter is inadequate for our purposes, and in chapter 5 we show that the spin-pair model can indeed give good predictions to the behaviour of the specific heat in a magnetic field, in contrast to the results of figs. 2.13. We also compare the spin-pair model to the extended two-fluid model developed in the next chapter.

2.7 Publication

PHYSICAL REVIEW B VOLUME 49, NUMBER 4 15 JANUARY 1994-II

Small-cluster calculations of the localized-moment contribution to the specific heat of heavily doped Si:P

M. J. R. Hoch and C. Kasl
Condensed Matter Physics Research Unit, Department of Physics, University of the Witwatersrand, P.O. Wits 2050, Johannesburg, South Africa
(Received 5 August 1993)

The localized-moment contribution to the specific heat of Si:P in the vicinity of the metal-insulator transition has been calculated as a function of temperature and magnetic field. The magnetic susceptibility has also been obtained and compared with available experimental data. Small clusters of spins are used in the calculations. The specific-heat predictions are in fairly good agreement with experimental data in fields up to 5.7 T for $n/n_c < 0.2$. At higher concentrations a reduced number of effective spins must be used in order to obtain reasonable agreement with experiment.

INTRODUCTION

Measurements of the thermodynamic response functions, such as low-temperature specific heat[1] and magnetic susceptibility,[2] for systems such as Si:P in the vicinity of the metal-insulator (MI) transition have provided information on the electronic states of these systems. Calculations which attempt to explain the observed properties on both sides of the transition generally do so in terms of localized and delocalized electron states.

Experiments carried out in the presence of high magnetic fields permit additional information to be obtained about the nature of the electronic structure. For Si:P, specific-heat measurements in strong magnetic fields have been made by Kobayashi *et al.*[3] and Lakner and Löhneysen.[4] Schottky-type specific-heat peaks, which are attributed to localized moments, have been observed.

Various approaches have been used in attempting to explain the observed behavior of the thermodynamic response functions. In a scaling approach involving numerical procedures with large arrays of spins, Bhatt and Lee[5] have calculated the low-field magnetic susceptibility χ for Si:P on the insulating side of the transition. Spin pairs with exchange couplings much greater than $k_B T$ become "frozen" in the ground singlet state and are successively discarded with renormalization of the magnetic field as T is lowered. The effective number of free spins at a given temperature and concentration can be found in this way, and hence χ can be obtained.

Fairly recently, Eto and Kamimura[6] have carried out multiconfiguration self-consistent-field calculations for the susceptibility and specific heat of Si:P near the MI transition. Averages were taken for six spins, distributed randomly in a sphere at the appropriate concentration. Both spin-singlet and spin-triplet ground states were shown to occur. The predictions are in general agreement with the specific-heat results of Kobayashi *et al.*[3]

In the present paper a small-cluster model is used to fit the available specific-heat curves as a function of temperature and magnetic field. The approach may be expected to work fairly well in the dilute limit $n/n_c \ll 1$. At higher concentrations, cluster-cluster interactions become important and will lead to failure of the model. In designing more elaborate approaches, it is of interest to know how well the predictions of the simple cluster model agree with the high-field experiments, and to establish the concentration range in which serious discrepancies start to occur. Information of this kind may be obtained from the results presented below.

THEORETICAL CALCULATIONS

For a system of N localized spin $\mathbf{S}_j$, interacting via the exchange interaction, in a magnetic field B, the Hamiltonian is

$$\mathcal{H}=\gamma\hbar B\sum_{j=1}^{N}S_{zj}+\sum_{i>j=1}^{N}J_{ij}\mathbf{S}_i\cdot\mathbf{S}_j\ . \tag{1}$$

The dipolar and hyperfine interactions are regarded as unimportant for the present purposes. J_{ij} is the exchange coupling between spins i and j and, ignoring the many-valley character of Si, is given by the asymptotic Herring-Flicker[7] form

$$J_{ij}(R)\simeq 0.3(R/a_H^*)^{5/2}e^{-2R/a_H^*}\ . \tag{2}$$

a_H^* is the effective hydrogenic radius of the impurity centers, and R is the separation between spins i and j. The distribution of R values for nearest-neighbor spins is given by the Poisson distribution

$$P(R)dR=4\pi R^2 n e^{-(4/3)\pi R^3 n}dR\ , \tag{3}$$

where $n=N/V$, and V is the volume of the sample.

In order to simplify the calculation, clusters of one, two, or three spins have been considered. Figure 1(a) shows the singlet-triplet energy-level diagram for a pair of spins in a magnetic field B. In low fields the ground state is a singlet state, but for high fields the lowest triplet state may cross the ground-state level, depending on the magnitude of the exchange coupling for the particular spin pair. Andres *et al.*[2] have carried out similar susceptibility calculations for the pair model in a somewhat different approach, using an empirical form for the distribution of J values.

 ©1994 The American Physical Society

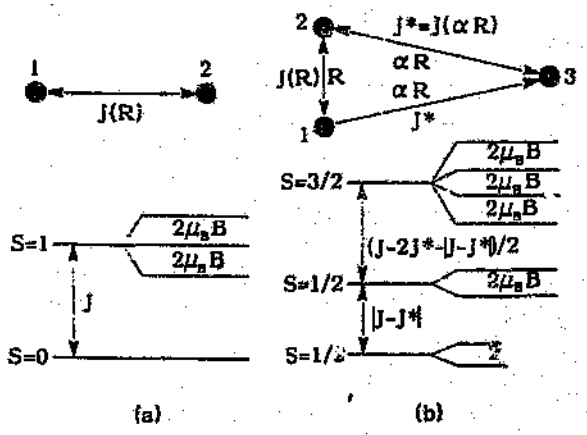


FIG. 1. Energy-level diagram for the (a) spin pair and (b) spin triad in a magnetic field B. J is the exchange coupling between a pair of spins, and α is a parameter which is a little greater than unity.

Figure 1(b) shows the energy-level diagram for three spins in a field B.[6] The ground state is a doublet in contrast to the pair singlet ground state. In calculations related to electron paramagnetic resonance (EPR) spectra, New and Castner[9] have examined the most probable topological arrangement for three spins. They used Monte Carlo calculations for donors on a diamond lattice in a cubic box of volume roughly two orders of magnitude greater than the characteristic volume of a cluster determined using Poisson statistics. Using the pair exchange interaction $J_{ij}(R_{ij},k_0)$ for many-valley semiconductors, the donors were grouped into clusters using a small cutoff exchange coupling J_c, which fixed the mean cluster size (obtained from Poisson statistics) for the particular donor concentration. They identified those triads with $J_{13}\simeq J_{23}\ll J_{12}$ as the most probable ones. In our calculations we have, for simplicity, chosen an isosceles triangle shape for triads, with the ratio of side to base length given by a parameter α, as shown in Fig. 1(b).

Using the energy levels shown in Figs. 1(a) and 1(b) together with Eqs. (2) and (3), we have evaluated the partition function Z for the system of localized spins. Numerical integration procedures are used in the calculation. For spin pairs, we have

$$\ln Z=\frac{N}{2}\int_0^\infty dR\,P(R)\ln Z(R)\,, \tag{4}$$

where $Z(R)$ is the pair partition function for spin separation R. A similar expression applies to the triad case. For the spin pairs there are no adjustable parameters in the model, if we take the effective radius a_H^* as fixed ($\sim$15 Å). In the case of the triad model, there is one adjustable parameter α. From $\ln Z$, the heat capacity C_H and the magnetic susceptibility χ may be calculated in the usual way.

RESULTS AND DISCUSSION

Figure 2 shows the low-field magnetic-susceptibility predictions for the single-spin, pair, and triad models. The experimental results of Andres *et al.*[2] are shown for comparison. The single-spin model, which predicts Curie law behavior over the entire temperature range, shows significant departures from the observation below 1.0 K. The agreement with experiment for the pair and triad models is seen to be acceptable for $n/n_c\leq 0.2$ at temperatures above approximately 100 mK. At higher concentrations the pair and triad calculations show departures from the experimental results. In this region the pair model gives values which are too low, while the triad model gives values which are higher than the measured values. The presence of the doublet ground state for the single-spin and triad models clearly leads to an overestimate of the susceptibility at low temperatures. The more elaborate Bhatt-Lee model is preferable for these higher concentrations. A combination of pair and triad models could be used to obtain better fits to the data at the expense of introducing an additional parameter. In the present calculations, the "freezing out" of spins in the singlet ground state for the pair model is accomplished in a continuous way as T is lowered.

In Figs. 3 and 4 the specific-heat predictions are compared with experimental data for particular n/n_c values as a function of temperature in various fields. The experimental curves are taken from the results of Kobayashi *et al.*[3] and Lakner and Löhneysen.[4] The phonon contri-

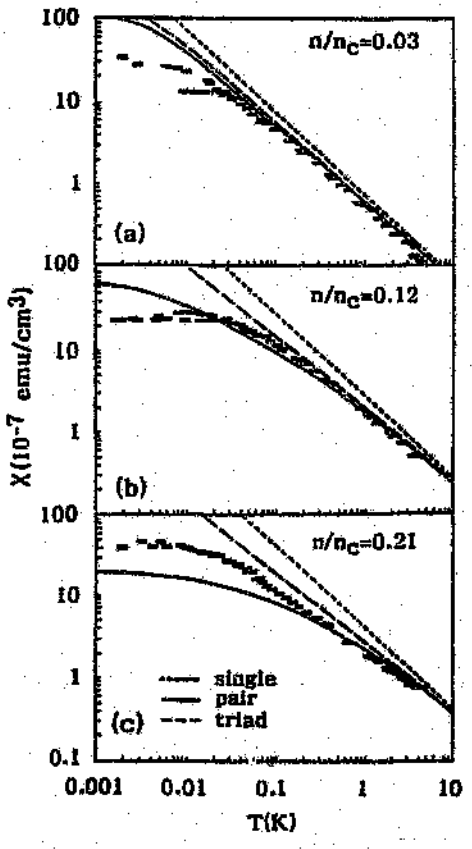


FIG. 2. Low-field magnetic-susceptibility predictions for Si:P as a function of temperature and concentration for the single-spin, pair, and triad models. The experimental data at 50 mK are taken from Andres *et al.* (Ref. 2).

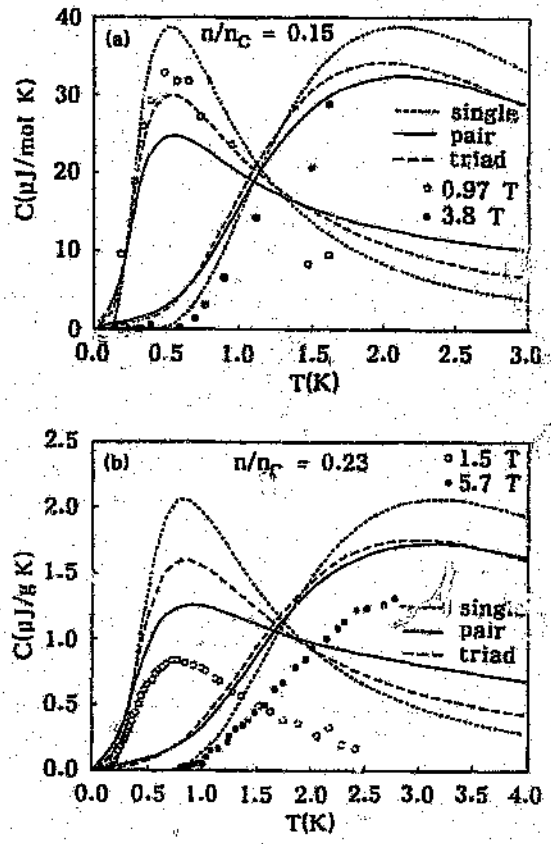


FIG. 3. Specific-heat predictions for Si:P as a function of concentration, temperature, and magnetic field for the single-spin, pair, and triad models. The experimental data of (a) are taken from Kobayashi *et al.* (Ref. 3), while those of (b) are taken from Lakner and Löhneysen (Ref. 4).

bution (γT^3) has been subtracted from the measured specific heats. For $n/n_c=0.15$, the agreement between the triad model, with $\alpha=1.25$, and the experimental results of Kobayashi *et al.* is acceptable at the two field values shown in Fig. 3(a). The pair-model peaks are broader and flatter than the experimental curves.

For the triad model, changing α from 1.0 (equilateral triangle) to 1.1 produces an increase of 15–20 %, depending on n/n_c, in the amplitude of the specific-heat peak. Thereafter, further increases in α produce only fairly small changes ($\lesssim 5\%$) in the peak amplitude. The high-temperature tail of the curves becomes somewhat stretched out, compared to the low-α value curves, but overall the change in shape is not very significant. For $\alpha > 1.6$, the curves effectively correspond to those of a pair of spins and a single spin, averaged over all pair separations. We arbitrarily chose $\alpha=1.25$ for all the triad curves as a reasonable intermediate value between 1.1 and 1.6.

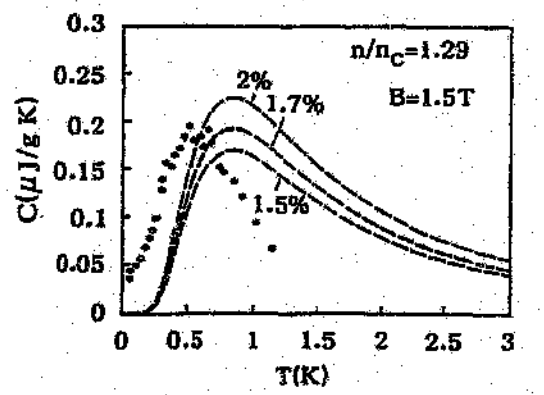


FIG. 4. Specific-heat predictions for the triad model with a reduced number of effective spins compared with the experimental results of Lakner and Löhneysen (Ref. 4) for a sample on the just-metallic side of the transition.

For $n/n_c=0.23$ the theoretical curves, shown in Fig. 3(b), are somewhat higher than the experimental data. As is the case with the susceptibility results, neither the simple pair model with no adjustable parameters nor the triad model with one parameter α is able to provide quantitative fits to the experimental points. The shapes of the triad model plots appear to be closer than the single-spin or pair model shapes to those of the experimental curves. Scaling n by a factor of roughly 0.5 would bring the curves into fairly close agreement with experiment.

Schottky fits for single spins require that the effective number of spins is a function of the applied field[4] in order to fit the experimental observations. The predicted amplitude of the single-spin Schottky specific-heat peak is the same in all fields for a given spin concentration, while the pair and triad models give rise to field-dependent peak amplitudes. This feature supports the cluster-model approach.

Figure 4 shows the experimental results[4] for $n/n_c=1.29$ with $B=1.5$ T. The fitted curve is based on the triad model, with n scaled by the factors shown in the figure for insertion in Eqs. (3) and (4). Neither the shape nor peak position is in very close agreement with experimental points. Nevertheless, it is highly probable that the observed peak is due to the presence of localized moments on the metallic side of the transition. This is consistent with the so-called two-fluid-model ideas[10–12] and the recent work of Bhatt and Fisher.[13] The scaling in the number of effective spins may be explained as being the result of the presence of much larger clusters than those that have been considered here. Alternatively, cluster-cluster interactions may be invoked to justify the scaling that is required for $n/n_c > 0.2$. It should be emphasized that the effective n value is used in obtaining the partition function and hence the plotted curves. If the actual n value is used to obtain the specific heat, followed by scaling in amplitude, the shapes and positions of the curves are in poor agreement with experiment.

More elaborate cluster calculations along the lines of those of Eto and Kamimura[6] should provide a better description for samples with $0.2 < n/n_c \leq 1.0$ than the simple cluster models. The presence of both spin-singlet and spin-triplet ground states appears to be a desirable feature in accounting for the specific-heat observations. With the simple cluster-model approach, a combination of pairs and triads could be used in the calculations. This would, however, involve the introduction of a further parameter, which could be regarded as a fitting parameter. We have not carried out such procedures.

CONCLUSION

Cluster-model calculations, involving spin pairs and spin triads, have been carried out for the low-temperature magnetic susceptibility and specific heat of heavily doped Si:P in the vicinity of the metal-insulator transition. For $n/n_c \lesssim 0.2$, the low-field susceptibility and specific-heat predictions in fields up to 5.7 T are in fair quantitative agreement with experiment. At high concentrations it becomes necessary to introduce a reduced effective number of spins in order to bring the predictions into approximate agreement with experiment. The need for this scaling of n may be interpreted as the result of large clusters and cluster-cluster interactions, which give rise to a reduced susceptibility and specific-heat contribution from regions in the sample in which the localization length is becoming large.

For samples just on the metallic side of the transition, the cluster-model predictions require substantial scaling of n in order to bring them into agreement with experiment. The results are consistent with the presence of a small number of localized spins on the metallic side of the transition.

ACKNOWLEDGMENTS

We gratefully acknowledge the financial support provided by the Foundation for Research Development and the University of the Witwatersrand Research Committee.

[1]M. A. Paalanen, J. E. Graebner, R. N. Bhatt, and S. Sachdev, Phys. Rev. Lett. 61, 597 (1988).
[2]K. Andres, R. N. Bhatt, P. Goalwin, T. M. Rice, and R. E. Walstedt, Phys. Rev. B 24, 244 (1981).
[3]N. Kobayashi, S. Ikehata, S. Kobayashi, and W. Sasaki, Solid State Commun. 32, 1147 (1979).
[4]M. Lakner and H. v. Löhneysen, Phys. Rev. Lett. 63, 648 (1989).
[5]R. N. Bhatt and P. A. Lee, Phys. Rev. Lett. 48, 344 (1982).
[6]M. Eto and H. Kamimura, Phys. Rev. Lett. 61, 2790 (1988).
[7]C. Herring and M. Flicker, Phys. Rev. 134, A362 (1984).
[8]T. Shimizu, J. Phys. Soc. Jpn. 25, 1021 (1968).
[9]D. New and T. G. Castner, Phys. Rev. B 29, 2077 (1984).
[10]H. Alloul and P. Dellouve, Phys. Rev. Lett. 59, 578 (1987).
[11]S. Sachdev, R. N. Bhatt, and M. A. Paalanen, J. Appl. Phys. 63, 4285 (1988).
[12]S. T. Stoddard, M. J. R. Hoch, and U. Thomanschefsky, Phys. Rev. B 46, 10007 (1992).
[13]R. N. Bhatt and D. S. Fisher, Phys. Rev. Lett. 68, 3072 (1992).

Chapter 3

The Extended Two-Fluid Model

3.1 Introduction

In this section we shall develop an extension to the Paalanen two-fluid model[7] (§1.3.3), and consider the effects of finite magnetic fields on this model. The disordered spin subsystem is treated using the Bhatt-Lee (BL) spin-pair model (§1.3.1), which is extended to allow for the presence of a magnetic field. Due to the success of the zero-field two-fluid model in explaining the experimental data at very low magnetic fields ($B \rightarrow 0$), the inclusion of a magnetic field into this model could explain recent data obtained on the thermodynamic properties of Si:P near the metal-insulator transition.

As for the first model in chapter 2, we shall develop expressions for the thermodynamic quantities (the specific heat C, susceptibility χ, and entropy S) using the partition function for the system. The equations relating the thermodynamic quantities to the partition function Z are listed in eqns. (A.3) of App. A.1:

$$C = \frac{\partial E}{\partial T} = k_B \beta^2 \frac{\partial^2 \ln Z}{\partial \beta^2} \tag{3.1}$$

$$\chi = \frac{\mu_0 M}{B} = \frac{\mu_0}{\beta B} \frac{\partial \ln Z}{\partial B} \tag{3.2}$$

$$S = k_B \ln Z - k_B \beta \frac{\partial \ln Z}{\partial \beta} \quad . \tag{3.3}$$

To determine Z it is necessary to know the energy levels of the system. Since we are working in the spin-pair approximation, it is only necessary to find the energy levels of a single spin-pair coupled to an external field. This has already been introduced in §2.3

(fig. 2.2). The partition function Z_{sp} for a single spin-pair[1] is then given by

$$\begin{aligned} Z_{sp} &= 1 + e^{-\beta J} + e^{-\beta(J+g\mu_B B)} + e^{-\beta(J-g\mu_B B)} \\ &= 1 + e^{-x}(1 + 2\cosh(y)) \quad , \end{aligned} \tag{3.4}$$

where we have defined $x = \beta J$ and $y = \beta g\mu_B B$. Note that we shall use this definition for x and y throughout this and the next chapters. Therefore, using (3.4), it is possible to find any one of the thermodynamic quantities shown in eqns. (3.1)→(3.3) for a J-coupled spin-pair.

We shall primarily be concerned with evaluating the specific heat and the susceptibility for our system. There are two reasons for not fully evaluating the entropy. Firstly, there are no direct experimental data for the entropy, and secondly, we can obtain the entropy directly from the specific heat (shown later in §3.6), and hence a study of the specific heat is sufficient to test the model. We shall, however, look at some properties of the entropy in §3.6.

Turning now to the spin-pair specific heat and the susceptibility, we see from eqns. (3.1) and (3.2) that the specific heat C_{sp} and the susceptibility χ_{sp} for a single J-coupled spin-pair are given by

$$C_{sp} = k_B F_C(x, y) \quad , \tag{3.5}$$

where

$$F_C(x, y) = \frac{(x-y)^2 e^{y-x} + (x+y)^2 e^{-y-x} + x^2 e^{-x} + y^2(4 + 2\cosh(y))e^{-2x}}{(1 + (1 + 2\cosh(y))e^{-x})^2} \quad , \tag{3.6}$$

and

$$\chi_{sp} = 2\mu_0 (g\mu_B)^2 \beta F_\chi(x, y) \quad , \tag{3.7}$$

where

$$F_\chi(x, y) = \frac{\sinh(y)}{y} \frac{e^{-x}}{1 + (1 + 2\cosh(y))e^{-x}} \quad . \tag{3.8}$$

The reason for defining the functions $F_C(x, y)$ and $F_\chi(x, y)$ will soon become clear. For $B = 0$ ($y = 0$), the above expressions for C_{sp} and χ_{sp} are identical to eqns. (2.10) for C_0 and χ_0.

[1] In this chapter we use the singlet $|00\rangle$ state as our reference energy.

The total specific heat C and susceptibility χ for the spin-pair system can then be derived using the distribution of exchange couplings $P(J)$, and are given by

$$C = \frac{n_e}{2} \int_0^{J_m} dJ P(J) C_{sp} \tag{3.9}$$

and

$$\chi = \frac{n_e}{2} \int_0^{J_m} dJ P(J) \chi_{sp} \quad , \tag{3.10}$$

where $P(J)dJ$ is the probability of a spin-pair having an exchange coupling J in the interval $(J, J+dJ)$, while $n_e/2$ is the number of spin pairs in our system. (n_e is the effective number of localized moments, and J_m is an upper cutoff to the exchange coupling distribution.) Note that here we explicitly consider J as being an effective exchange coupling (refer to the scaling procedure in §1.3.1). The distribution function $P(J)$ we use is the BL distribution function

$$P(J)dJ = \kappa J^{-\alpha} dJ \quad , \tag{3.11}$$

which is successful in explaining the zero magnetic field data for the specific heat and susceptibility. The constant κ is a normalization constant with dimensions. In the zero-field BL model (§1.3.1), close to the M-I transition, α is found to be roughly constant ($\alpha \simeq 0.62$). There may be a change in α due to a magnetic field but we shall expect the main effect of the magnetic field to be the localization of itinerant electrons, which may produce a change in the relative concentrations of the localized and itinerant electrons. Therefore, using the distribution (3.11), we have, using (3.5) and (3.7), that

$$C = \frac{n_e}{2} \kappa \int_0^{J_m} dJ \; J^{-\alpha} \; k_B F_C(x, y) \tag{3.12}$$

and

$$\chi = \frac{n_e}{2} \kappa \int_0^{J_m} dJ \; J^{-\alpha} \, 2\mu_0 (g\mu_B)^2 \beta F_\chi(x, y) \quad . \tag{3.13}$$

Using the transformation $x = \beta J$, and defining

$$I_\delta(y) \doteq \int_0^{X_m} dx \; x^{-\alpha} F_C(x, y) \tag{3.14}$$

and

$$I_\varepsilon(y) = \int_0^{X_m} dx \; x^{-\alpha} F_\chi(x, y) \quad , \tag{3.15}$$

where $X_m = \beta J_m = J_m/k_B T$ is the upper cutoff for the integral, we have the final expressions for the specific heat and susceptibility of the localized system:

$$C = \frac{n_e}{2}\left(\kappa k_B^{2-\alpha}\right) I_\delta(y)\, T^{1-\alpha} \tag{3.16}$$

$$\chi = \frac{n_e}{2}\left(2\kappa\mu_0(g\mu_B)^2 k_B^{-\alpha}\right) I_\varepsilon(y)\, T^{-\alpha}. \tag{3.17}$$

So in order to evaluate C and χ, we need only evaluate the integrals $I_\delta(y)$ and $I_\varepsilon(y)$.

We shall now cast the equations in the same form as the two-fluid model equations in (1.10).

3.2 The Extended Two-Fluid Model Equations

From eqns. (1.10), the zero-field two-fluid model equations are given by

$$\frac{\gamma}{\gamma_0} = \frac{m^*}{m_0^*} + \left(\frac{T}{T_0}\right)^{-\alpha} \tag{3.18}$$

$$\frac{\chi}{\chi_0} = \frac{m^*}{m_0^*} + \beta_0\left(\frac{T}{T_0}\right)^{-\alpha} \quad . \tag{3.19}$$

where the specific heat coefficient[2] γ and susceptibility χ are expressed as the sum of the itinerant and localized contributions.

Our assumption is that the dominant effect of a magnetic field is on the localized subsystem, with negligible effect on the thermodynamics of the itinerant subsystem. The itinerant contribution to γ/γ_0 and χ/χ_0 in the extended two-fluid model therefore remains unchanged, and equals the constant m^*/m_0^*.

We need therefore only evaluate γ/γ_0 and χ/χ_0 for the localized subsystem. γ_0 and χ_0, the Fermi liquid values for the Si conduction band, are given by eqns. (A.8) and (A.9) in App. A.2:

$$C_0 = \gamma_0 T = \left(\frac{\pi^2}{2}\frac{k_B n_i}{T_f}\right) T \tag{3.20}$$

$$\chi_0 = \frac{3}{2}\frac{\mu_0\mu_B^2}{k_B T_f} n_i \quad , \tag{3.21}$$

[2]The reason for using the specific heat coefficient γ instead of the specific heat $C = \gamma T$ is that in the two-fluid equations γ has the same form as χ.

where n_i represents the number of itinerant electrons. The specific heat $C = \gamma T$ and susceptibility χ of the localized system are given by (3.16) and (3.17).

The localized contribution to (3.18) is found by using (3.14), (3.16), and (3.20). By defining

$$\delta(y) = \frac{I_\delta(y)}{I_1} \quad ; \quad I_1 = I_\delta(0) \tag{3.22}$$

and

$$\left(\frac{1}{T_0}\right)^{-\alpha} = \left(\frac{\kappa I_1}{\pi^2}\right)\left(\frac{n_e}{n_i}\right) k_B^{1-\alpha} T_f \quad , \tag{3.23}$$

we have that

$$\frac{\gamma}{\gamma_0} = \delta(y)\left(\frac{T}{T_0}\right)^{-\alpha} \quad . \tag{3.24}$$

The parameter T_0, which has the dimensions of temperature, contains the ratio (n_e/n) of localized and itinerant electrons, and gives us an indication of the extent of localization in the system. The coefficient $\delta(y)$ in (3.24) is defined so as to cast the equations into the same form as the zero-field two-fluid equation. For a zero magnetic field, we have that $y = g\mu_B B/k_B T = 0$, and from (3.22) we can see that $\delta(y) = 1$. Hence the localized contribution given by (3.24) becomes

$$\frac{\gamma}{\gamma_0} = \left(\frac{T}{T_0}\right)^{-\alpha}$$

and has exactly the same form as the localized contribution in the zero-field two-fluid equations. The parameter T_0, defined in (3.23), therefore has the same meaning.

Next we consider the localized contribution to (3.19), which is found by using (3.15), (3.17), and (3.21). By defining

$$\varepsilon(y) = \beta_0 \frac{I_\varepsilon(y)}{I_2} \quad ; \quad I_2 = I_\varepsilon(0) \quad , \tag{3.25}$$

where

$$\beta_0 = \left(\frac{2}{3}\pi^2 g^2\right)\left(\frac{I_2}{I_1}\right) \quad , \tag{3.26}$$

we obtain, using the definition of T_0 in (3.23),

$$\frac{\chi}{\chi_0} = \varepsilon(y)\left(\frac{T}{T_0}\right)^{-\alpha} \quad . \tag{3.27}$$

Again, we have defined the coefficient $\varepsilon(y)$ so as to cast (3.27) in the same form as the two-fluid model equation in the zero field limit. For $B = 0$, we have $y = g\mu_B B/k_B T = 0$, and hence $\varepsilon(y) = \beta_0$, and eqn. (3.27) reduces to

$$\frac{\chi_L}{\chi_0} = \beta_0\left(\frac{T}{T_0}\right)^{-\alpha} \quad , \tag{3.28}$$

which is the same as the zero-field two-fluid model equation for the localized contribution to the susceptibility. For $\alpha \simeq 0.62$, we find that $\beta_0 \simeq 10.3$, in close agreement with the value given by Paalanen *et al.*[7].

Therefore, by using (3.24) and (3.27) for the specific heat and susceptibility of the localized contributions, we arrive at the extended two-fluid model equations:

$$\frac{\gamma}{\gamma_0} = \frac{m^*}{m_0^*} + \delta(y)\left(\frac{T}{T_0}\right)^{-\alpha} \tag{3.29}$$

and

$$\frac{\chi}{\chi_0} = \frac{m^*}{m_0^*} + \varepsilon(y)\left(\frac{T}{T_0}\right)^{-\alpha} . \tag{3.30}$$

Both equations reduce to the zero-field two-fluid equations in the zero-field limit ($B \rightarrow 0$) and so we can see that the terms $\delta(y)$ and $\varepsilon(y)$ basically contain the effects a magnetic field will have on the localized system. The effect of a magnetic field on the itinerant system may be to induce localization and hence change the relative concentrations of itinerant and localized electrons. This effect should appear as a change in the parameter T_0 through its dependence on (n_e/n_i).

Before looking at the theoretical predictions that the extended equations give for the specific heat and susceptibility, we will first need to evaluate $\delta(y)$ and $\varepsilon(y)$. For this purpose we need to numerically evaluate (see (3.22) and (3.25)) the integrals $I_\delta(y)$ and $I_\varepsilon(y)$ defined in (3.14) and (3.15). App. C contains the details on the numerical evaluation of the integrals $I_\delta(y)$ and $I_\varepsilon(y)$.[3] Note that for our analysis we use the assumptions

$$T \ll j_m = \frac{J_m}{k_B}$$

and

$$g\mu_B B \ll J_m \tag{3.31}$$

introduced in App. C.1 (expressions (C.3) and (C.5)).

We can now look at the theoretical predictions made by the extended equations (3.29) and (3.30). We shall first consider the specific heat behaviour and then look at the predictions for the susceptibility and entropy. Also to be introduced is the Wilson ratio, which is useful in testing the models made on the M-I transition in Si:P. Lastly, we consider

[3]See expression (C.11) in App. C.1 for the final forms used in the numerical integration.

the case when the conditions in (3.31) are not valid, and introduce some of the corrections that are necessary.

3.3 The Specific Heat

The specific heat is given by (3.29) and consists of the itinerant and localized contributions. The itinerant contribution leads to a specific heat linear in T,

$$\begin{aligned} C &= \left(\frac{m_i^*}{m_0^*}\right)\gamma_0 T \\ &= \left(\frac{m^*}{m_0^*}\right)C_0 \quad . \end{aligned} \tag{3.32}$$

This shows that the itinerant electron specific heat is enhanced by a factor of $m^*/m_0^* \simeq 1.3$ (App. A.2), over the Si conduction band specific heat C_0 given by (3.20).

The localized contribution to the electronic specific heat is then given by

$$C = \gamma_0 \left(\frac{1}{T_0}\right)^{-\alpha} \delta(y)\, T^{1-\alpha} \quad . \tag{3.33}$$

Equations (3.32) and (3.33) are the expressions we use to compare to the experimental data and so we have

$$C = \gamma T + \sigma\delta(y)T^{1-\alpha} \quad , \tag{3.34}$$

for the total impurity electron specific heat, where $\gamma = (m^*/m_0^*)\gamma_0$ and $\sigma = \gamma_0(1/T_0)^{-\alpha}$ are introduced since these terms will be produced by the experimental analysis. Using eqns. (3.20), (3.23), and (A.10) in App. A.2, we find that (using $\nu = 6$ for Si)

$$\gamma = \left[\frac{k_B}{\hbar}(2\pi)^{1/3}\right]^2 m^* n_i^{1/3}$$

and

$$\sigma = \left[\frac{1}{2}\kappa k_B^{2-\alpha} I_1\right] n_e \quad . \tag{3.35}$$

Hence we see that both γ and σ are constants depending only on the concentrations n_i and n_e of itinerant and localized electrons. It should be noted that γ and σ may have a magnetic field dependence due to the localizing effects produced by a magnetic field. Recent

studies[20] have shown, however, that observable localizing effects may only be occurring for larger magnetic fields (for $B \gtrsim 3\ T$).

A plot of $\delta(y)$ is shown in fig. 3.1a. For convenience δ is plotted as a function of $1/y = k_B T/g\mu_B B$. For this plot α was chosen as 0.63 to correspond closely to the value close to the MI transition. In fig. 3.1b we can see a plot of $\delta(y)$ versus y, showing the dependence on the parameter α. The form of the function stays the same and the peak position appears to remain constant. This peak in the curve, which occurs at $y \simeq 2.6$ and is clearly sensitive on α, leads to the Schottky-type anomaly which is clearly seen in the presence of a magnetic field (fig. 1.2a).

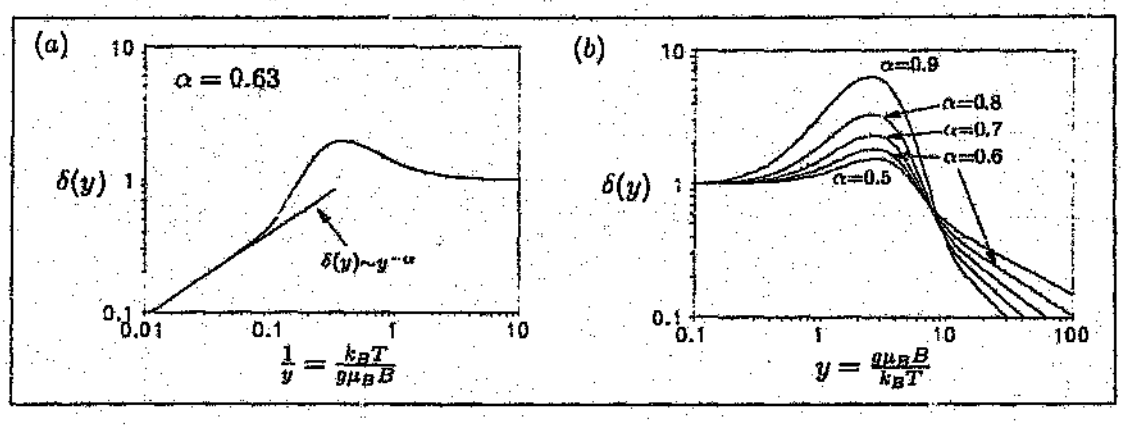


Figure 3.1: A plot of (a) the function $\delta(y)$ versus $1/y$, for $\alpha = 0.63$, with (b) showing its dependence on the parameter α.

The asymptotic behaviour of $\delta(y)$ is also of interest. For the larger values of y ($y \gtrsim 15$), we have $\delta(y) \sim 1.683 y^{-0.630} = 1.683 y^{-\alpha}$. (The asymptotic form is included in fig. 3.1a.) App. D contains a detailed analysis of the asymptotic form of $\delta(y)$ as y becomes large. We find that

$$\delta(y) \simeq \left(\frac{\pi^2}{3I_1}\right) y^{-\alpha} \quad for \quad y \gtrsim 15 \ . \tag{3.36}$$

This asymptotic behaviour describes the specific heat as $T \to 0K$ (since $y \to \infty$) in a non-zero magnetic field (since for $B = 0$ we would have $y = 0$ for all T). The condition $y \gtrsim 15$ translates into $T[mK] \lesssim 100\ B[T]$. Inserting (3.36) into the localized contribution

of (3.34), we arrive at the low temperature behaviour for the localized system:

$$\begin{aligned} C &= \sigma \frac{\pi^2}{3l_1} \left(\frac{k_B T}{g\mu_B B}\right)^{\alpha} T^{1-\alpha} \\ &\propto \frac{T}{B^{\alpha}} \quad for \quad T[mK] \lesssim 100\, B[T] \ . \end{aligned} \tag{3.37}$$

Hence we see that the localized electronic specific heat behaves linearly in T as $T \to 0K$. Since the itinerant part is also linear in T, we expect that the total electronic specific heat converges linearly in T towards absolute zero. However, verification of this linear behaviour is made difficult by the presence of a nuclear specific heat which appears to have a contribution to the total specific heat at the temperatures required for the verification of (3.37). The low temperature experimental data and the appearance of the nuclear specific heat are examined in the next chapter.

For $y \lesssim 0.1$, we have that $\delta(y) \equiv 1$. The condition $y \lesssim 0.1$ translates into $B[T] \lesssim 0.074\, T[K]$ and relates to the asymptotic behaviours for small fields or large temperatures. As expected, we obtain the localized moment contribution in the zero-field equation:

$$C \equiv \sigma T^{1-\alpha} \quad for \quad B[T] \lesssim 0.074\, T[K] \tag{3.38}$$

and so for magnetic fields and temperatures, such that $B[T] \lesssim 0.074T[K]$, we can ignore the effects of the field and use the zero field two-fluid model equations.

3.4 The Susceptibility

The predictions for the electronic susceptibility are given by eqn. (3.30). The itinerant electron contribution

$$\frac{\chi}{\chi_0} = \frac{m^*}{m_0^*} \tag{3.39}$$

shows an enhancement ((A.12) in App. A.2) over the Si conduction band Pauli susceptibility. This leads to a temperature-independent contribution to the electronic susceptibility.

The localized contribution to the electronic susceptibility is then given by

$$\frac{\chi}{\chi_0} = \varepsilon(y) \left(\frac{T}{T_0}\right)^{-\alpha} \tag{3.40}$$

and is therefore clearly temperature and magnetic field dependent. For the susceptibility we need only focus on the localized contribution (3.40). The reason for this is that the itinerant contribution in (3.39) is temperature independent, and the diamagnetic contribution from

the Si lattice (App. A.3) is also temperature independent. These contributions therefore do not have any T-dependence and this background can easily be subtracted from the total susceptibility to produce the localized contribution. When referring to the susceptibility, we shall mean the temperature dependent part of the susceptibility, unless specified otherwise. The susceptibility prediction of this model is then

$$\begin{aligned} \chi &= \chi_0 \varepsilon(y) \left(\frac{T}{T_0}\right)^{-\alpha} \\ &= \rho \varepsilon(y) T^{-\alpha} \quad , \end{aligned} \tag{3.41}$$

where, using (3.21) and (3.23),

$$\rho = \left(\frac{3}{2}\frac{1}{\pi^2}\mu_0 \mu_B^2 k_B^{-\alpha} \kappa I_1\right) n_e \tag{3.42}$$

is a constant depending only on the effective concentration of localized moments.

A plot of the factor $\varepsilon(y)$, as a function of $1/y = k_B T/g\mu_B B$, is shown in fig. 3.2a. Again we have chosen the value of $\alpha = 0.63$. Fig. 3.2b shows the form of $\varepsilon(y)$ versus y, for various values of the parameter α.

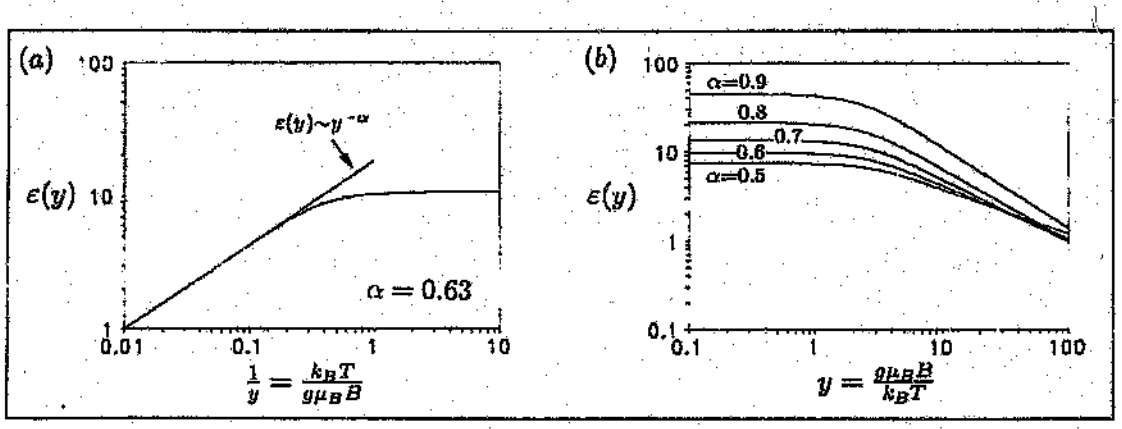


Figure 3.2: A plot of (a) the function $\varepsilon(y)$ versus $1/y$, for $\alpha = 0.63$, with (b) showing its dependence on the parameter α.

As can be seen from the plots, the factor $\varepsilon(y)$ has much less structure than the factor $\delta(y)$ discussed in the previous section. $\varepsilon(y)$ is a strictly decreasing function of y. For $y = 0$, we have $\varepsilon(y) = \varepsilon(0) = \beta_0$, and $\varepsilon(y)$ then decreases to zero for increasing y. The asymptotic behaviour, for both small and large values of y, is all that is needed for a detailed summary of the properties of the term $\varepsilon(y)$.

We first look at the asymptotic form for large values of y (small T). App. D contains a detailed analysis for the asymptotic ($y \to \infty$) behaviour of $\varepsilon(y)$ (included in fig. 3.2a). and the results show that

$$\varepsilon(y) \equiv \left(\frac{2}{3}\pi^2 g^2 \frac{1}{2(1-\alpha)I_1}\right) y^{-\alpha} \quad , \quad y \gtrsim 5 \quad . \tag{3.43}$$

The condition $y \gtrsim 5$ translates into $T[mK] \lesssim 0.027B[G]$. Inserting the above form into (3.41), we obtain for the low T behaviour of the susceptibility (in a non-zero magnetic field)

$$\chi = \left(\frac{n_e}{2}\right) \frac{\kappa}{1-\alpha} \mu_0 (g\mu_B)^{2-\alpha} B^{-\alpha} \quad , \quad T[mK] \lesssim 0.027B[G] \quad , \tag{3.44}$$

which is temperature independent. So the susceptibility converges to a constant value as $T \to 0K$. Also note the field dependence of the above asymptotic behaviour. The magnetization is then

$$M \propto B^{1-\alpha} \quad , \quad T \to 0K \quad , \tag{3.45}$$

which increases with increasing magnetic field. This form of the magnetization, at absolute zero, is a direct consequence of the BL distribution function $J^{-\alpha}$ in (3.11).

By noting that at $T = 0K$ only the ground state is occupied and by referring to the level diagram in fig. 2.2, we can find a simple expression for the magnetization at absolute zero[4]:

$$M_{T=0K} = g\mu_B \frac{n_e}{2} \int_0^{g\mu_B B} dJ\, P(J) \quad , \tag{3.46}$$

where $P(J)$ is any distribution function for the exchange couplings J. The integral in eqn. (3.46) gives the fraction of spin-pairs with a triplet ground state. This form follows directly from the fact that pairs with $J > g\mu_B B$ have the singlet, non-magnetic ground state, while pairs with $J < g\mu_B B$ have a triplet, magnetic ground state. For the BL distribution (3.11), eqn. (3.46) leads directly to (3.44) and (3.45).

Another interesting observation to be made from eqn. (3.46) is the integral expression $\int_0^{g\mu_B B} dJ P(J)$. Since $P(J)$ is non-negative and is a probability density, we see that the integral is a strictly increasing function of the magnetic field B, ranging from 0 (for $B = 0$) to 1 (for $B \to \infty$), since the distribution is normalized. So we can see that, for sufficiently large B, such that $g\mu_B B \gtrsim J_m$, where J_m is the maximum exchange coupling[5], the magnetization will converge to its saturation value $g\mu_B(n_e/2)$ where all pairs are in the

[4] Refer to §2.3.2 with a similar discussion of $M_{T=0K}$ and $\chi_{T=0K}$.
[5] $P(J) \equiv 0$ for $J > J_m$.

magnetic triplet state. Notice that up to now we have assumed that $g\mu_B B \ll J_m$ (refer to (3.31)), while eqn. (3.46) is a general equation holding for any distribution with no restrictions on B. So low temperature susceptibility studies for large magnetic fields can give an indication of the strengths of exchange couplings present in the system by looking at the onset of magnetization saturation.

For $y < 1$, the factor $\varepsilon(y)$ has a constant asymptotic behaviour equal to $\varepsilon(0) = \beta_0$. This condition $y < 1$ translates into $T[K] > 1.34\ B[T]$, and so we have for the higher T behaviour, using (3.26), (3.41), and (3.42),

$$\begin{aligned} \chi &= \rho\beta_0 T^{-\alpha} \\ &= n_i\left(\mu_0(g\mu_B)^2 k_B^{-\alpha}\kappa I_2\right) T^{-\alpha} \quad , \quad T[K] > 1.34\ B[T] \ , \end{aligned} \tag{3.47}$$

which has the same T-dependence as the zero-field expression in (3.19). At higher T we therefore expect the $B = 0$ and $B \neq 0$ predictions to converge.

Summarizing, for a fixed field B, we have

$$\begin{aligned} T[K] &< 0.27\ B[T] \quad \Rightarrow \quad \chi \equiv constant \\ T[K] &> 1.34\ B \quad \Rightarrow \quad \chi \equiv T^{-\alpha} \quad . \end{aligned} \tag{3.48}$$

For $0.27B < T < 1.34B$, the susceptibility χ changes smoothly from a constant behaviour to the $T^{-\alpha}$ behaviour.

3.5 The Entropy

The entropy S of a spin pair can be obtained from the partition function with the use of (A.3) in App. A.1:

$$S = k_B \ln Z - k_B\beta\frac{\partial \ln Z}{\partial \beta} \quad . \tag{3.49}$$

Using the BL distribution function in (3.11) for the exchange couplings, we could follow similar procedures to that of the specific heat and susceptibility analysis. However, an alternative way would be to obtain the entropy directly from the specific heat by using the defining equation for the entropy:

$$dS = \frac{dQ}{T} \quad , \tag{3.50}$$

where dS is the change in entropy when an amount of heat dQ is added to the system. Since $dQ = CdT$ by definition, we arrive at an alternative expression for the entropy:

$$S = \int_0^T C\frac{dT}{T} \quad , \tag{3.51}$$

where the absolute zero entropy is arbitrarily chosen as $S(0) = 0$. So we see that the knowledge of the specific heat completely determines the entropy via eqn. (3.51).

For $B = 0$, where we have the specific heat $C_0 = \sigma T^{1-\alpha}$ (3.38), the entropy S_0 has the simple form of

$$S_0 = \frac{\sigma}{1-\alpha}T^{1-\alpha} \quad , \tag{3.52}$$

and hence also has the power law form for all temperatures.

Inserting (3.37) for the low T behaviour of the specific heat in a magnetic field into (3.51), we arrive at the low temperature (or high field) behaviour for the spin-pair entropy:

$$S \equiv \frac{T}{B^\alpha} \qquad T[K] \lesssim 0.10\, B[T] \tag{3.53}$$

which has a similar form to the specific heat, and hence we can see that $S \rightarrow 0$ linearly in T as $T \rightarrow 0K$. Fig. 3.3 shows a representative plot of the entropy, evaluated using (3.49), as a function of temperature, to indicate the general form and also to emphasize the asymptotic behaviour. The $B = 0$ power law form shown in eqn. (3.52) is clearly visible. Note the convergence with the zero-field curve for higher temperatures and also the asymptotic low T form indicated by the straight line for $B = 1000G$.

3.6 The Wilson Ratio

Paalanen *et al.* have used the Wilson ratio to test their two fluid model predictions (fig. 1.7a in chapter 1). This ratio provides a yardstick to test other models pertaining to these metal-insulator systems. From a primary point of view, models that are developed should at least, as a first criterion, give a sufficient account of the Wilson ratio W, which is defined as

$$W = \frac{\chi/\chi_0}{\gamma/\gamma_0} \quad , \tag{3.54}$$

where χ and γ are, as previously defined, the susceptibility and the specific heat coefficient, while χ_0 and γ_0 are the corresponding Si conduction band quantities.

There are several reasons which make W a useful, if not essential, quantity. The experimental determination of the quantities χ/χ_0 and γ/γ_0 requires the knowledge of

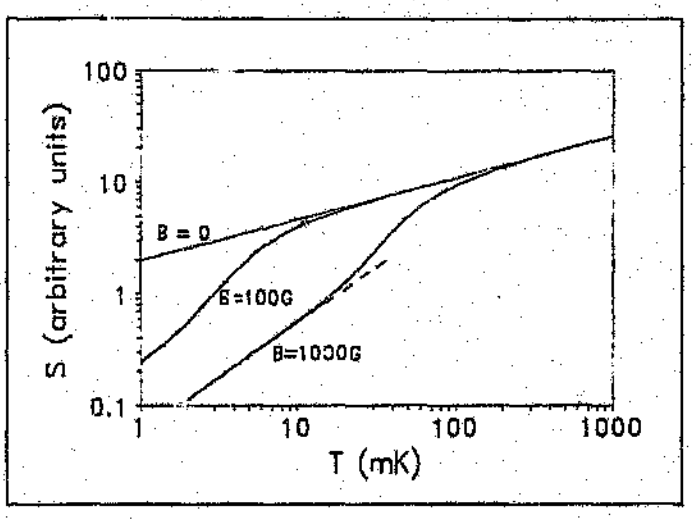


Figure 3.3: The entropy S, in arbitrary units, for various magnetic fields.

several unknown quantities such as the Fermi temperature and the concentration of itinerant electrons. By using the Wilson ratio, the need for these unknowns is removed. This can be seen by observing that

$$W = \left(\frac{\chi}{\gamma}\right)\left[\frac{\pi^2}{3}\frac{k_B^2}{\mu_0\mu_B^2}\right] \quad , \tag{3.55}$$

where we have used (3.20) and (3.21) to evaluate γ_0/χ_0. So W is determined, apart from a known constant, by taking the ratio of experimental values for χ and γ, and is easily obtained. Using the extended equations (3.29) and (3.30), we predict that

$$W = \frac{\frac{m^*}{m_0^*} + \varepsilon(y)\left(\frac{T}{T_0}\right)^{-\alpha}}{\frac{m^*}{m_0^*} + \delta(y)\left(\frac{T}{T_0}\right)^{-\alpha}} \tag{3.56}$$

and, since $m^*/m_0^* \simeq 1.3$ (A.12), we see that we have a one-parameter expression in T_0, which contains the fraction of localized spins. The parameter $\alpha \sim 0.6$ close to the MI transition, or α can be treated as a second fitting parameter in eqn. (3.56).

Figure 1.7a in chapter 1 shows a plot of the Wilson ratio versus the temperature for various concentrations in zero magnetic field. As can be seen, the one-parameter fits of (3.56) are satisfactory. In fig. 3.4 we have reproduced the zero field data of the Wilson ratio for $n/n_c = 1.09$. Included are the predictions of (3.56) showing the expected evolution of the Wilson ratio in a magnetic field. The minima in the curves arise from the maximum

observed in the plot of the factor $\delta(y)$ shown in fig. 3.1a.

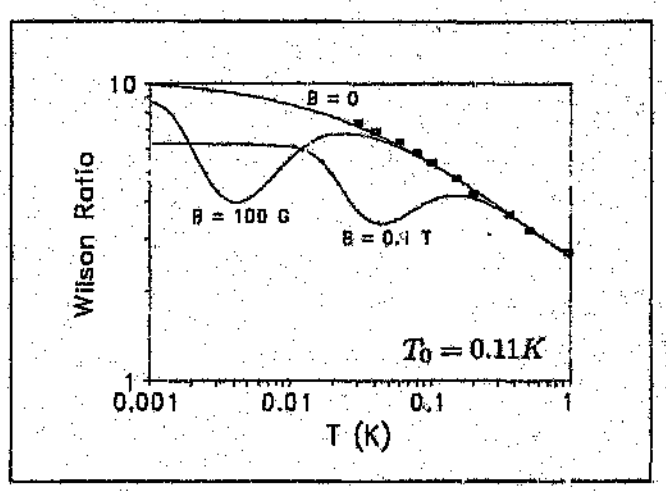


Figure 3.4: The magnetic field dependence of the Wilson Ratio.

Comparisons of the Wilson ratio in a magnetic field could not be done since there were no measurements available of the susceptibility and specific heat in the same magnetic field. Susceptibility measurements were all done in low magnetic fields (the highest available data being for $B = 3000G$), while the specific heat was done for much higher field values (the lowest field value being $0.4T$). Measurements of the susceptibility and specific heat on the same sample in high magnetic fields will be very useful, and would be ideal for testing the model predictions using the Wilson ratio.

Another useful technique is to generate a plot of the quantities χ/χ_0 versus γ/γ_0. Since the susceptibility and specific heat for this system are linked (such as through the partition function, as shown in (3.1) and (3.2)), the set of points $(\chi/\chi_0, \gamma/\gamma_0)$ will lie in a predefined subset on the $\chi/\chi_0 - \gamma/\gamma_0$ plane. Figure 1.7b in chapter 1 shows this type of plot for $B = 0$.

With the extended two-fluid equations (3.29) and (3.30) we can derive the relationship between χ/χ_0 and γ/γ_0 in this model. Combining these two equations we find the relationship

$$\frac{\chi}{\chi_0} = \frac{m^*}{m_0^*} + \frac{\epsilon(y)}{\delta(y)}\left(\frac{\gamma}{\gamma_0} - \frac{m^*}{m_0^*}\right) \quad . \tag{3.57}$$

For $B = 0$, since $\delta(0) = 1$ and $\epsilon(0) = \beta_0$, (3.57) reduces to

$$\frac{\chi}{\chi_0} = \frac{m^*}{m_0^*} + \beta_0 \left(\frac{\gamma}{\gamma_0} - \frac{m^*}{m_0^*} \right) \quad , \tag{3.58}$$

indicating a linear form between χ/χ_0 and γ/γ_0. This expression represents the BL+FL curve shown in fig. 1.7b. For non-zero magnetic fields, since $y \neq 0$, eqn. (3.57) represents different curves on the $\chi/\chi_0 - \gamma/\gamma_0$ plane, depending on the value of y. Varying y continuously through its allowed values ($0 \leq y \leq \infty$), we obtain a family of curves which represent a surface (subset) on the $\chi/\chi_0 - \gamma/\gamma_0$ plane, and gives the allowed values which $(\chi/\chi_0, \gamma/\gamma_0)$ can take in the extended two-fluid model.

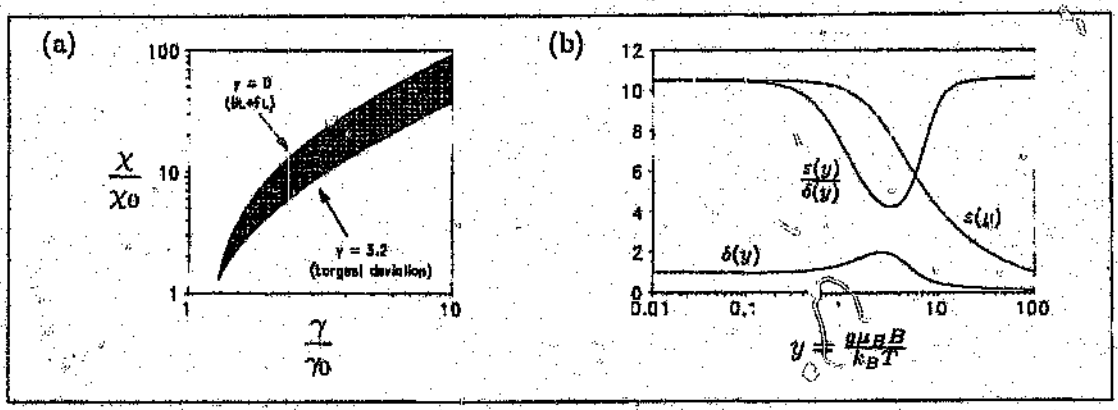


Figure 3.5: The (a) surface of allowed $(\gamma/\gamma_0, \chi/\chi_0)$ values predicted by the extended two fluid model, and (b) a plot of $\varepsilon(y)/\delta(y)$, which determines this surface.

Figure 3.5a shows a plot of this surface obtained from eqn. (3.57). Note that, although there is a linear relationship between χ/χ_0 and γ/γ_0 according to this equation, we have used the logarithmic scale in fig. 3.5a to match the published fig. 1.7b. Fig. 3.5b shows a plot of the term $\varepsilon(y)/\delta(y)$ in eqn. (3.57), and it is this term that determines the form of the surface. The zero field curve ($y = 0$) is shown as one boundary in fig. 3.5a. The other boundary of this surface corresponds to the minimum of $\varepsilon(y)/\delta(y)$, as seen in fig. 3.5b.

3.7 Corrections to the Extended Two-Fluid Model Equations

We will now consider the required corrections that have to be made to the extended equations (3.29) and (3.30) when the conditions

$$T \ll j_m = \frac{J_m}{k_B T} \quad and \quad g\mu_B B \ll J_m \quad , \tag{3.59}$$

given by (3.31), are not satisfied. We will consider the corrections to the expressions we have so far developed, for the case of a small maximum exchange coupling j_m. With these corrections we then have the general extended two-fluid equations. The assumptions in (3.59) simplify the form of the equations and make their use easier.

Section C.6 in App. C contains the mathematical details of adding the corrections to the equations, and we find that a breakdown in the conditions above can be simply taken account of by the replacement

$$\begin{aligned} \delta(y) &\longrightarrow \delta(y) + \Delta_\delta \\ \varepsilon(y) &\longrightarrow \varepsilon(y) + \Delta_\varepsilon \end{aligned} \tag{3.60}$$

in the extended two-fluid equations (3.29) and (3.30) to yield the complete extended two-fluid expressions

$$\begin{aligned} \frac{\gamma}{\gamma_0} &= \frac{m^*}{m_0^*} + [\delta(y) + \Delta_\delta] \left(\frac{T}{T_0}\right)^{-n} \\ \frac{\chi}{\chi_0} &= \frac{m^*}{m_0^*} + [\varepsilon(y) + \Delta_\varepsilon] \left(\frac{T}{T_0}\right)^{-\alpha} \quad . \end{aligned} \tag{3.61}$$

The corrections Δ_δ and Δ_ε, to $\delta(y)$ and $\varepsilon(y)$ respectively, are given by

$$\begin{aligned} \Delta_\delta &= \Delta_\delta(T, B, j_m) = -\frac{1}{I_1} \int_{j_m/T}^{\infty} dx\, x^{-\alpha}\, F_C(x, 1.34B/T) \\ \Delta_\varepsilon &= \Delta_\varepsilon(T, B, j_m) = -\frac{2}{3}\pi^2 g^2 \frac{1}{I_1} \int_{j_m/T}^{\infty} dx\, x^{-\alpha}\, F_\chi(x, 1.34B/T) \quad . \end{aligned} \tag{3.62}$$

Section C.6 in App. C also contains a detailed look at these corrections Δ_δ and Δ_ε and derives some interesting features regarding these correction functions.

The correction can produce quite drastic changes to the specific heat predictions. For the susceptibility χ, the changes are more subtle, since χ decreases to zero with increasing temperature (as $T^{-\alpha}$) and the correction, which is negative and reduces the susceptibility, may not be noticeable at higher temperatures where χ vanishes anyway. The specific

heat, however, increases indefinitely as $T^{1-\alpha}$, and the correction will reduce the specific heat to zero as the temperature is increased. This fact is demonstrated in figs. 3.6a and 3.6b, where we have shown the corrected and uncorrected specific heat curves for a zero and non-zero magnetic field. The parameter values used are shown in the figures.

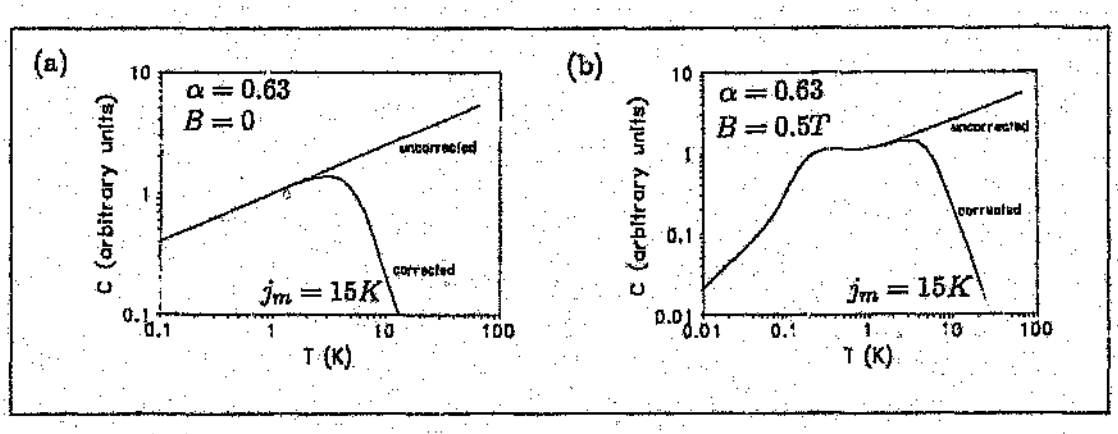


Figure 3.6: Plots of the specific heat C for a (a) zero, and (b) non-zero magnetic field, showing the effects of introducing the corrections to the extended two-fluid model.

When using the correction, we take an upper cutoff to the exchange coupling, and hence the total energy of the system becomes bounded above. The vanishing specific heat at higher T is therefore the result of the saturation of the energy, which does not occur if the finiteness of j_m is not taken into account. This correction therefore produces a peak at higher temperatures (in addition to the Schottky-type peak produced by a magnetic field), the position of which depends on the maximum exchange coupling j_m.

As a final note, referring to §2.3.1 of chapter 2, we also have for the zero-field specific heat that

$$C \sim \frac{1}{T^2} \quad for \quad T \gg j_m \ . \tag{3.63}$$

With reference to the analysis done in §C.6 of App. C, we can summarize the results as follows :

1. When we have

$$B[T] \lesssim \frac{1}{10} j_m[K] \ , \tag{3.64}$$

we can use the simpler zero-field correction. The zero-field correction for the specific

heat can be approximated by the simple analytical expression

$$\Delta_6 \simeq \frac{-1}{1 + 0.0245\,(T/j_m)^{-3.62}} \quad . \tag{3.65}$$

2. The corrections can be ignored if the following two conditions are satisfied:

$$B[T] < \frac{1}{10} j_m \quad \textit{and} \quad T[K] < \frac{1}{10} j_m \quad . \tag{3.66}$$

This to some extent quantifies the conditions $g\mu_B B \ll J_m$ and $T \ll j_m$, shown in (3.59).

As mentioned in §C.1 of App. C, we expect that the maximum exchange coupling j_m is at least of the order of $100K$. So, from condition (3.66) above, we can expect to ignore the corrections for $B \lesssim 10T$ and $T \lesssim 10K$. The temperatures and magnetic fields that we are concerned with do fall in this range, and so, unless j_m is much smaller than expected, we need not be concerned with the corrections when doing comparisons to experimental data.

Chapter 4

Testing the Extended Two-Fluid Model

4.1 Introduction

In this chapter we apply the extended two-fluid model, which was developed in the previous chapter, to available experimental data for the specific heat C and susceptibility χ. We will be mainly interested in the experimental data for non-zero magnetic fields, as this is the basis for the development of the extended two-fluid model in the first place. We will, however, review the zero-field data as well.

Although the zero-field two-fluid model has been successfully applied to experimental data, we will look at alternative ways to analyze the zero-field data, which lead to some discrepancies, particularly in the specific heat. These different approaches to the data and the analysis thereof lead to similar, but quantitatively very different results, both in the zero and non-zero magnetic field analysis.

We will see in this section, as was mentioned in the previous chapter, that the analysis of the specific heat data can be more difficult than the susceptibility analysis. For the specific heat we have additional contributions (apart from the electronic specific heat) both at high and low temperatures. At higher temperatures ($T \gtrsim 1K$) the phonon contribution ($\propto T^3$) dominates the specific heat, while at lower temperatures ($T \lesssim 100mK$) an anomaly in the specific heat, which is believed to be nuclear in origin, appears and casts uncertainty on the form of the electronic specific heat at these low temperatures. So, for

the specific heat, we only have a small temperature window ($100mK \lesssim T \lesssim 1K$) on which we can test the model for the electronic specific heat reliably.

The susceptibility is a much better thermodynamic quantity to analyze . The nuclear susceptibility is about three orders of magnitude smaller than the electronic contribution and is hence negligible. Also, the diamagnetic contribution from the host Si lattice is temperature-independent, and can be easily removed from the susceptibility. The itinerant electron susceptibility contribution is also temperature-independent (Pauli susceptibility) and hence simplifies the extraction of the localized electron susceptibility contribution. There are, however, not as many experimental data on the susceptibility as there are on the specific heat. Also, whereas high magnetic field specific heat data are readily available, we found only one set of data for the susceptibility in higher magnetic fields. So the susceptibility analysis for our model was limited, although, as will be seen in this chapter, quite successful.

The ideal quantity for testing our model is the Wilson ratio $W = (\chi/\chi_0)/(\gamma/\gamma_0)$. This ratio is particularly useful in testing models in that the knowledge of several physical parameters, which are unknown, is removed from its definition (§3.6). The zero-field two-fluid model has been very successfully applied to the Wilson ratio and it would be ideal to test the extended two-fluid model using this ratio as well. However, due to the lack of susceptibility data, this can as yet not be done. Simultaneous experimental analysis on both the susceptibility and specific heat in magnetic fields would need to be done and would be of great value, not only for testing this model, but other models as well.

Some of the specific heat data were kindly provided by H. von Löhneysen and S. Wagner from the University of Karlsruhe, Germany. However, some of the data had to be digitized from published papers, and the origins of these data are mentioned. App. E gives an overview of the digitizing procedures used, and also explains some of the disadvantages that arose.

In §4.7 we include a paper published in Physical Review B, which contains a summary of the extended two-fluid model and some of the important results.

4.1.1 The Specific Heat

The electronic specific heat, in the extended two-fluid model, consists of the itinerant and localized contributions, and is given by eqn. (3.34):

$$C = \gamma T + \sigma \delta(y) T^{1-\alpha} \quad . \tag{4.1}$$

The parameters γ and σ are defined in (3.35) and are clearly dependent on the effective concentrations of itinerant and localized electrons respectively. We will, however, consider γ and σ as fitting parameters to the experimental data, and from the results obtain instead an indication of the relative concentrations of itinerant and localized electrons for the Si:P MI system. The parameter α, which determines the distribution of exchange couplings in (3.11), is also determined from the experimental data, while the factor $\delta(y)$ is plotted in fig. 3.1 of the previous chapter.

The asymptotic behaviours of the localized electron specific heat are given by (3.37) and (3.38):

$$\begin{aligned} C &\propto \frac{T}{B^{\alpha}} \qquad T[K] \lesssim 0.1B[T] \\ C &\propto T^{1-\alpha} \qquad T[K] \gtrsim 13.5B[T] \quad . \end{aligned} \tag{4.2}$$

At low temperatures, both the itinerant and localized contributions are linear in T and so we expect that the total electronic specific heat will tend to zero linearly in T as $T \to 0$. This prediction is difficult to verify, due to the nuclear contribution which is expected to appear at the lowest temperatures. In §4.7 we analyze the low T specific heat to see whether this predicted linear form is present, and also whether the anomaly is a nuclear specific heat.

For $B = 0$, since $\delta(y) = 1$, we have the simple expression of

$$C = \gamma T + \sigma T^{1-\alpha} \quad . \tag{4.3}$$

The phonon contribution (App. A.3), due to the host Si lattice, must also be taken into account. At the low temperatures which are of interest to us, the phonon specific heat has the form

$$C_{phonon} = \beta T^3 \quad , \tag{4.4}$$

where $\beta = 0.241 \pm 0.022\ \mu J/gK^4$. We can use this value for β, or treat it as another fitting parameter. Due to the cubic dependence in T, the phonon contribution becomes dominant at higher temperatures ($T \gtrsim 1K$), and the extraction of the electronic specific heat becomes

more uncertain. However, due to this cubic behaviour, the phonon contribution also vanishes very rapidly as the temperature is lowered, and becomes negligible at ..peratures well below $1K$.

Lastly, the corrections to the extended equations which have to be made when considering the finite size of the maximum exchange coupling J_m (when the conditions in (3.31) are not satisfied) must be considered. From (3.61) we can take the correction in b account by simply replacing $\delta(y)$ in eqn. (4.1) with $\delta(y) + \Delta_\delta$, where Δ_δ is the correction defined in (3.62). We shall use this approach for the low magnetic field data where we can use the zero-field correction as a first order correction to the fitting (point 1 of §3.7). The reason for this is that the zero-field correction can be analytically approximated by the simple expression in (3.65):

$$\Delta_\delta \simeq \frac{-1}{1 + 0.0245\,(T/j_m)^{-3.62}} \quad . \tag{4.5}$$

4.1.2 The Susceptibility

The susceptibility ca ı be expressed in the following way (§3.5) for the purpose of experimental comparison:

$$\chi = \chi^* + \rho\varepsilon(y)T^{-\alpha} \quad . \tag{4.6}$$

The physical parameters χ^*, ρ and α are determined from experimental data. The factor $\varepsilon(y)$ is plotted in fig. 3.2. The term χ^* consists of the temperature-independent contributions to the susceptibility (the Si lattice diamagnetic susceptibility and the Pauli susceptibility of the itinerant electrons).

Generally, the constant background to the experimentally determined susceptibility data is subtracted, and analysis is focused on the temperature-dependent part of the susceptibility, which is attributed to the localized moments. When the total susceptibility is considered, we shall make use of (4.6) and determine the constant background χ^*. When the background has been subtracted from the data, our model predicts a temperature-dependent behaviour

$$\chi = \rho\varepsilon(y)T^{-\alpha} \quad . \tag{4.7}$$

Here ρ is a constant, given by (3.42), which is proportional to the effective concentration of localized moments. The parameter α, which governs the distribution of exchange couplings in (3.11), is determined by the high T data. Referring to (3.47), the susceptibility

is predicted to follow the power law behaviour at higher temperatures

$$\chi = \rho\beta_0 T^{-\alpha} \quad . \tag{4.8}$$

Lastly, the model predicts that the susceptibility tends to a constant value as $T \to 0$, and the magnetic field dependence of this asymptotic value is given by eqn. (3.44).

With regards to the extended two-fluid model, the susceptibility provides one with a better thermodynamic quantity to study than the specific heat. The model can be tested over the whole temperature range, since we do not expect unwanted additional contributions such as in the specific heat. There is, however, as was mentioned, a lack of sufficient experimental data on the susceptibility to test the extended two-fluid model comprehensively.

4.2 Determination of the Excess Specific Heat

The excess specific heat ΔC is defined in the following expansion of the total specific heat C:

$$C = \Delta C + \gamma T + \beta T^3 \quad . \tag{4.9}$$

Here βT^3 is the phonon contribution, while γT is the contribution from the impurity itinerant electrons. The term ΔC is the excess specific heat which is attributed to the localized moments. It also contains, however, the anomaly which appears at the lowest temperatures, but this anomaly is expected to only have a significant contribution at temperatures below $100mK$, and so we expect that, in the range of about $100mK$ to $3K$, the term ΔC is mainly due to the localized moments.

The main problem is the extraction of the term ΔC from the specific heat data. What follows is a standard procedure which has been used to determine ΔC, which we shall refer to as the "standard method".

4.2.1 Standard Method

In normal metals, where we only have the electronic (γT) and phonon (βT^3) terms, the standard way for determining the coefficients γ and β are through a plot of C/T versus T^2. From this plot we expect the data to be linear, and to be given by the expression

$$C/T = \gamma + \beta\left(T^2\right) \quad . \tag{4.10}$$

The coefficients γ and β are obtained from the intercept and slope of the data respectively.

Figure 1.6a in chapter 1 shows a plot of C/T versus T^2, where C is the zero-field specific heat of Si:P for various concentrations ranging through the MI transition. This figure shows the apparent linear behaviour at higher temperatures which is indicative of a metallic system. Also shown are fits of 4.10 to the high T data. From the intercept and slope, the values of γ and β are obtained (with γ being attributed to the impurity itinerant electrons), and from these values the excess specific heat ΔC is determined using (1.7). Fig. 1.6b shows these values obtained for γ as a function of the P concentration N, while fig. 1.6c shows the corresponding excess specific heat ΔC obtained for several concentrations. The solid lines indicate the power law fits, which are predicted by the zero-field two-fluid model (eqn. (4.3)), and fit the data up to temperatures of about $0.4K$. In §4.4.1 we do our own analysis on these $B = 0$ data.

To obtain the excess specific heat in a magnetic field, eqn. (1.6) is used:

$$C(B,T) = C_{Schottky}(B,T) + \gamma(B)T + \beta T^3 \quad , \tag{4.11}$$

where the itinerant contribution $\gamma(B)$ now has an explicit field dependence, while $C_{Schottky}$ is used to describe the Schottky-type excess specific heat attributed to the localized moments. An effective magnetic field and effective concentration are used for $C_{Schottky}$ to fit the above expression to the data. (Refer to point 5 of App. A.2.) The field dependence of γ, obtained in this way for two particular P concentrations ($n = 0.79 \times 10^{18} cm^{-3}$ and $n = 4.5 \times 10^{18} cm^{-3}$), is shown in fig. 4.1a. The figure shows that a significant change in γ starts to occurs only at a magnetic field of about $3T$. This reduction in $\gamma(B)$ is explained as a localization effect on the itinerant electrons, with the high magnetic fields driving the system to the insulating phase. As an example, fig. 4.1b shows the excess specific heat obtained in this way for two magnetic fields in the metallic phase ($n/n_c \simeq 1.3$). Note the Schottky-type form of the specific heat (the fits being Schottky fits), indicating the presence of localized moments even in the metallic phase.

4.2.2 Alternative Method

In our analysis of the excess specific heat ΔC obtained using the "standard method" described in §4.2.1, we obtained several discrepancies[1] in our results. We therefore

[1] Refer to §4.4.3 for a review of the results.

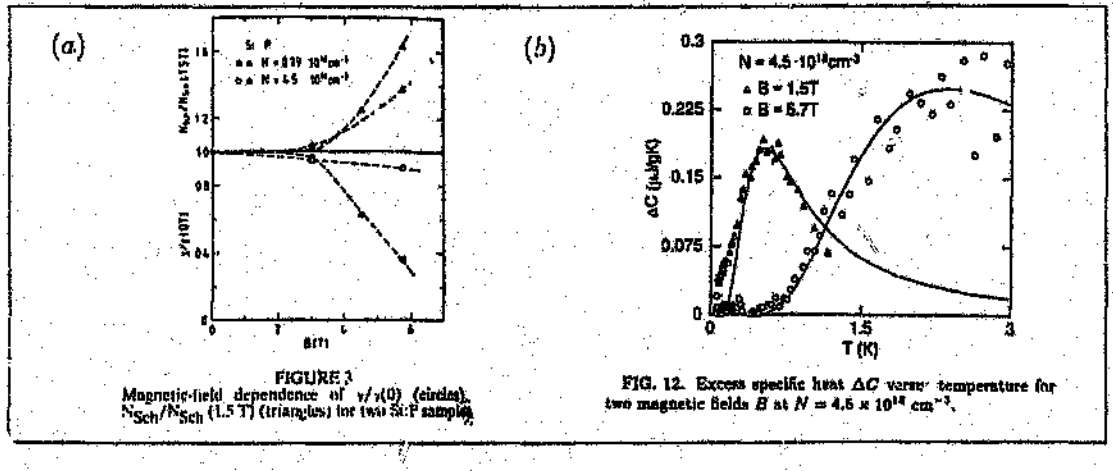


FIGURE 3
Magnetic-field dependence of $\gamma/\gamma(0)$ (circles), N_{Sch}/N_{Sch} (1.5 T) (triangles) for two Si:P samples.

FIG. 12. Excess specific heat ΔC versus temperature for two magnetic fields B at $N = 4.5 \times 10^{18}$ cm^{-3}.

Figure 4.1: Plots showing (a) the field-dependence of the effective localized moment concentration N_{Sch} and itinerant contribution $\gamma(B)$, and (b) the excess specific heat ΔC in non-zero fields for a metallic sample. Reproduced from (a) [20] and (b) [5].

used an alternative method to obtain the ΔC, which appears to be more successful. We do instead a direct fitting of the predicted behaviour of the total specific heat using (4.1), where, including the phonon term (4.4), we have the predicted form

$$C = \sigma\delta(y)T^{1-\alpha} + \gamma T + \beta T^3 \quad . \tag{4.12}$$

Hence we explicitly assume that the excess specific heat has the predicted form $\Delta C = \sigma\delta(y)T^{1-\alpha}$. We ignore the low temperature anomaly by just considering the higher temperature data ($T \gtrsim 100mK$), where we expect the anomaly to be negligible. For the phonon term βT^3 we can consider β as a fitting parameter, or use the experimentally determined value of $\beta \simeq 0.241\mu J/\rho K^4$. The phonon contribution can then be subtracted, and only the electronic contribution is fitted, to determine the values of σ, α, and γ. With this determined γ we can then obtain the excess specific heat by subtracting the term $\gamma T + \beta T^3$ from the total specific heat.

The reasoning for using this alternative method is as follows. Since the excess specific heat ΔC is positive, we conclude that $\gamma T + \beta T^3 \leq C$, and hence

$$\gamma + \beta\left(T^2\right) \leq \frac{C}{T} \quad . \tag{4.13}$$

In the plot of C/T versus T^2, the itinerant and phonon contribution ($\gamma + \beta T^2$,

which appears as a straight line in this plot) lies below the experimental points. So, referring to fig. 1.6a in chapter 1, the straight lines fitted through the higher temperature points give at best an upper bound to the itinerant contribution γ (since γ is the intercept of this straight line, and $\beta \simeq 0.241 \mu J/gK^4$ is predetermined). If the predicted power law form for the localized moments is valid for the higher temperatures (which we expect), then the higher temperature data points in fig. 1.6a will have contributions from the localized subsystem too, and it would be incorrect to attribute this apparent linearity in the data only to the itinerant and phonon contributions.

4.3 A Note on the Experimental Data Analysis

According to eqn. (4.1), the localized contribution to the electronic specific heat is

$$\Delta C = \sigma \delta(y) T^{1-\alpha} \quad , \tag{4.14}$$

where we associate the excess specific heat ΔC with the localized moment contribution. Eqn. (4.14) is the prediction of the extended two-fluid model and is used in the comparisons with the experimental data. Instead of a direct fitting of (4.14) with the data, we can simplify matters by dividing the excess specific heat by $T^{1-\alpha}$. Then

$$\frac{\Delta C}{T^{1-\alpha}} = \sigma \delta(y) \tag{4.15}$$

and we can see that a plot of $\Delta C/T^{1-\alpha}$ versus $y \simeq 1.34 B/T$ should yield a universal curve, independent of the magnetic field B. This method of analysis would be very useful in determining the universality of the magnetic field behaviour of the data, and also in comparing the model predictions of the term $\delta(y)$, which determines the shape of the specific heat.

Our initial analysis on the specific heat data involved plots of $\Delta C/T^{1-\alpha}$ versus y, and comparing the results to the expected behaviour in (4.15). This method we found was not very successful. Also, when considering the corrections (§3.7), the universal aspect in (4.15) is destroyed. Using eqn. (4.15) to find a universal curve, there were several complications which appeared in the data analysis.

1. The first was the choice of α in the non-zero magnetic field analysis. The value of α has to be known beforehand to determine $\Delta C/T^{1-\alpha}$ from the experimental data.

If the assumption is made that α is magnetic field-independent, which implies that the exchange coupling distribution in (3.11) is field-independent, then we can use the value for α determined from the zero-field analysis. The zero-field data provide a way to determine α from the slope in a log-log plot. (Refer to (4.3)). Matsunaga and Ootuka [17] do claim that the effect of a magnetic field on the distribution function is minute in their calculations of the magnetization. Their results, however, are only for fields up to $0.5T$, and larger fields could have a significant effect on this distribution.

2. Choosing the zero-field value for α can introduce additional problems, particularly for the low concentration data. The extended two-fluid model has as its main foundation the distribution of exchange couplings given in (3.11). The term α, which determines the exponent of this distribution and appears in all derived equations, is limited to values in the interval $(0,1)$. The upper bound of 1 is required for normalization purposes[2]. However, when the concentration is reduced to below $n = 1 \times 10^{18} cm^{-3}$, the zero-field analysis produces values of α larger than 1. As an example, refer to fig. 1.6c where we can see the negative slope in the $n = 0.34$ data, corresponding to $\alpha > 1$ (since the slope is $1 - \alpha$).

3. Another problem was the implicit dependence of the term $\delta(y)$ on α, as shown in fig. 3.1b of the previous chapter, and we can see that $\delta(y)$ is quite sensitive to the value of α. The problem that arose in the analysis using eqn. (4.15) was as follows: on choosing a value for α to determine the quantity $\Delta C/T^{1-\alpha}$, we proceeded by fitting the term $\sigma\delta(y)$ in (4.15) to the experimental data. What was generally required, however, was to choose a different value of α for the term $\delta(y)$ to get a sufficient fitting. So, in many cases, in particular when choosing the zero-field value for α to determine $\Delta C/T^{1-\alpha}$, it was necessary to use a different value of α for the term $\delta(y)$. This is not acceptable since the values of α in both $T^{1-\alpha}$ and $\delta(y)$ have to be the same.

4. This discrepancy in point 3 does provide us with a way to determine α directly without involving the zero-field values. This involves an iterative method in which the value of α is adjusted until the values in $T^{1-\alpha}$ and $\delta(y)$ match. This method is, however, very tedious and destroys the advantages of using the form in eqn. (4.15) to find a universal behaviour. It is then more useful to do a direct fitting of eqn. (4.14) for each

[2]Refer to App. C.7 for more on the limits imposed on α.

magnetic field.

4.4 Analysis on the Experimental Specific Heat Data

A Note on Units used in the Section

The specific heat data used in this section are specified in units of $\mu J/gK$. From the fitting of eqn. (4.1) we obtain the values for γ and σ. Since we are primarily interested in the relative magnitudes of γ and σ in the fittings, we will only specify these magnitudes obtained in this section. From eqn. (4.1), the units of γ and σ will be in $\mu J/gK^2$ and $\mu J/gK^{2-\alpha}$ respectively, since we use the Kelvin (K) units for the temperature T.

The units of $\mu J/gK^{2-\alpha}$ for σ may not be acceptable to some. due to the appearance of the power $(2-\alpha)$. The units of γ and σ, however, are in some sense arbitrary. For example, we can express eqn. (4.1) equivalently as

$$C = \gamma^* \left(\frac{T}{1K}\right) + \sigma^* \delta(y) \left(\frac{T}{1K}\right)^{1-\alpha} \quad , \tag{4.16}$$

where the term $(T/1K)$ now explicitly gives the temperature in Kelvin units. We now therefore have both γ^* and σ^* in the same units as C. The magnitudes of γ^* and σ^*, however, are the same as the magnitudes of γ and σ (since $\sigma^* = \sigma \cdot (1K)^{1-\alpha}$ and $\gamma^* = \gamma \cdot (1K)$). We could therefore replace all occurrences of γ and σ in this chapter with γ^* and σ^* with an explicit reference to the form in eqn. (4.16).

For convenience we maintain the form shown in eqn. (4.1) and do not explicitly specify the units of the fitting parameters γ and σ. If required. the reader can choose which units are more convenient. The same applies to the parameter ρ in eqn. (4.6) for the susceptibility, and in §4.5 we only specify the value obtained from the fittings. (The units of ρ can be inferred from the corresponding plots.)

4.4.1 Zero-Field Analysis on "Standard" Excess Specific Heat

Here we review the zero-field excess specific heat as given in fig. 1.6c of chapter 1. This excess specific heat ΔC was obtained by subtracting the linear (γT) and cubic (βT^3) terms (eqn. 4.9), where the coefficients γ and β were obtained from the standard method (§4.2.1).

In the two-fluid model, the excess specific heat ΔC is predicted to follow a power law behaviour

$$\Delta C = \sigma T^{1-\alpha} \quad . \tag{4.17}$$

This behaviour is also indicated on fig. 1.6c with the solid lines. This power law form appears in the data up to about $0.4K$, after which there is a rapid decrease in magnitude, well below the predicted power law form. In this section we also look at the possibility of attributing this rapid decrease to a maximum exchange coupling J_m in the system, by examining the effects of introducing the corrections to the model (§3.7 and fig. 3.6a).

The parameter α clearly has a magnitude depending on the P concentration. This concentration dependence of α, which is to be expected, can readily be seen by the varying slopes of the fits in fig. 1.6c.

We now look at the results we have obtained from our own analysis on this excess specific heat.

The power law expression in (4.17) was fitted to the excess specific heat ΔC to determine the concentration dependence of the parameters α and σ. The parameter σ gives us an indication as to the effective concentration of localized moments in the system.

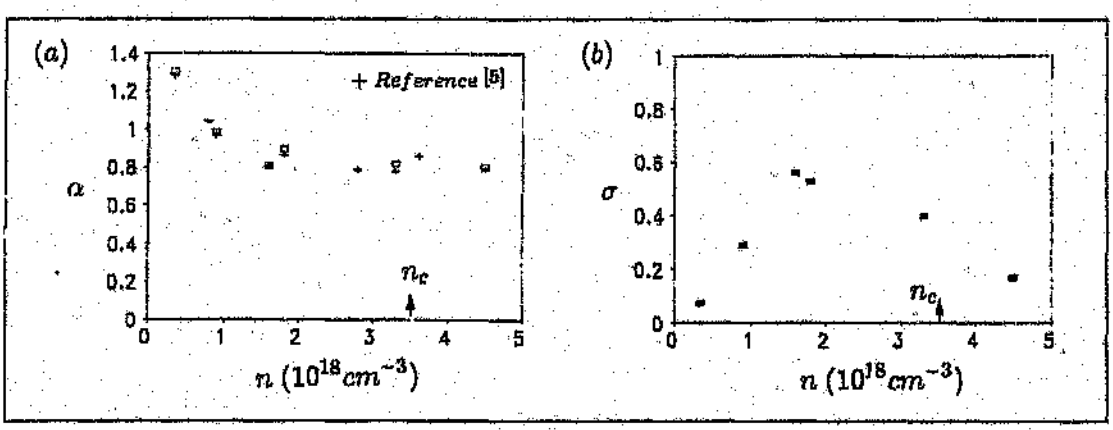


Figure 4.2: Values obtained for α and σ from fitting the zero-field data of various donor concentrations n.

Figures 4.2a and 4.2b respectively show the dependence of α and σ on the P concentration n, obtained from the fitting. The results were basically identical to that in

fig. 1.6c, and so the graphs are not reproduced. Refer to fig. 1.6c in future discussions on the fittings.

The values of α that we obtained in our analysis ($\Box$ in fig. 4.2a) are very close to the values shown in reference [5] (+ in fig. 4.2a).

The value of α appears to converge to a value of about 0.8 for concentrations close to and above the MI transition ($n_c \simeq 3.54 \times 10^{18} cm^{-3}$, indicated by the arrow). This is somewhat higher than the value of $\alpha \simeq 0.63$ expected near the MI transition (§1.3). Another point which needs explanation is the value of α for concentrations below $1 \times 10^{18} cm^{-3}$ where the magnitude of α exceeds 1. This leads to some physical problems, especially with regards to the distribution function in (3.11), where we require that $\alpha < 1$. As we reduce the concentration, we do expect α to tend to 1, but always to remain less than 1 (App. C.7). The two-fluid model was developed to account for the behaviour of the electronic system near the MI transition and so it is possible that the model (in particular the exchange coupling distribution in (3.11)) breaks down for smaller concentrations. Another possibility is that at these low concentrations the localized moment contribution, which vanishes in proportion to the P concentration, becomes so small in magnitude that the anomaly, which was discussed earlier, starts to have a comparable contribution and has to be taken account of. (This anomaly could distort the actual α values.)

Figure 4.2b shows the determined values for the parameter σ, which in the two-fluid model is defined by eqn. (3.35), and gives us an indication as to the behaviour of the effective concentration of localized moments as a function of the P concentration. For the lowest concentrations we see an increase in σ which appears to be almost a linear behaviour. At these low concentrations, well below the MI transition, we can expect almost 100% localization and therefore σ to be proportional to n. (See (3.35), with $n_e \equiv n$.) As the concentration is increased through the MI transition, there is a decrease in σ, where the impurity electrons start becoming delocalized. It can be clearly seen that even in the metallic phase there appear to be localized electrons ($\sigma \neq 0$). It is expected that the system becomes fully metallic (100% delocalization) only for $n \gtrsim 2n_c$, as discussed in §1.3.

Next we see if the correction to the two-fluid equation can explain the deviations (fig. 1.6c) from the power law predictions which occur for temperatures above $0.4K$. To introduce this correction we need only do the transformation shown in (3.60). Referring to

eqn. (4.14), we therefore have the predicted form for the excess specific heat given by

$$\begin{aligned} \Delta C &= \sigma \left[\delta(y) + \Delta_\delta\right] T^{1-\alpha} \\ &= \sigma \left[1 + \Delta_\delta\right] T^{1-\alpha} \quad , \end{aligned} \tag{4.18}$$

where $\delta(y) = 1$ for $B = 0$. For a zero field we can also use the approximation in (4.5) for the correction Δ_δ, which contains the single parameter j_m, the maximum exchange coupling ($j_m = J_m/k_B$) present in the system. For $T < 0.1 j_m$ the term Δ_δ becomes negligible, and (4.18) reverts back to the power law form $\sigma T^{1-\alpha}$. Since we can see the power law form up to about $0.4K$ in the data, we can see that $0.1 j_m \sim 0.4K$, and hence we can expect that $j_m \sim 4K$, provided that this higher temperature deviation is due to a maximum exchange coupling.

Dividing (4.18) by $\sigma T^{1-\alpha}$, we arrive at

$$\frac{\Delta C}{\sigma T^{1-\alpha}} = 1 + \Delta_\delta \quad . \tag{4.19}$$

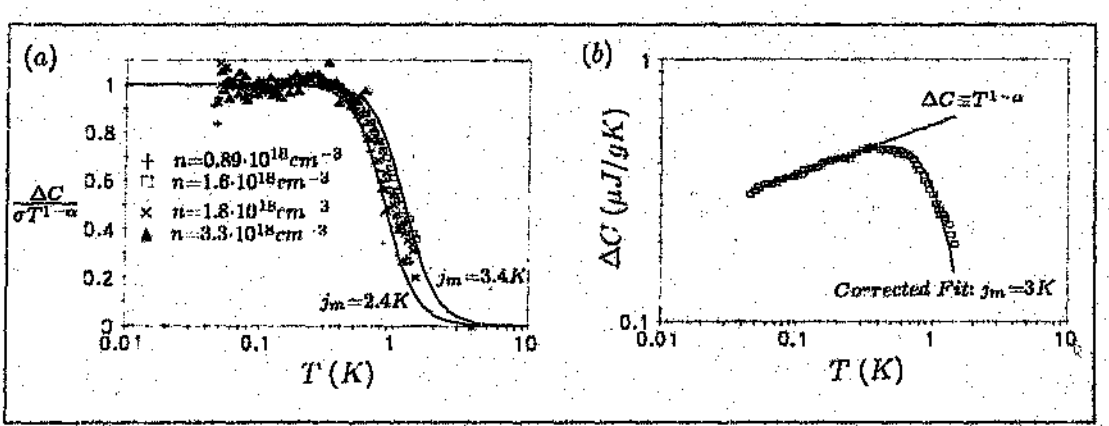


Figure 4.3: The excess specific heat ΔC for $B = 0$, with (a) a plot of $\Delta C/\sigma T^{1-\alpha}$ versus T, together with fits of eqn. (4.19), while (b) shows a plot of ΔC for $n = 1.6 \times 10^{18} cm^{-3}$, indicating the power law form as well as the corrected fit given by eqn. (4.18).

Figure 4.3a shows a plot of $\Delta C/\sigma T^{1-\alpha}$ versus the temperature T, for various concentrations ($n = 0.89$, 1.8, 3.3, and $4.5 \times 10^{18} cm^{-3}$). The values of α and σ used are those from figs. 4.2a and 4.2b. From fig. 4.3a we can see the common behaviour for the various P concentrations. The solid lines are fits of the expression $1+\Delta_\delta$ appearing in (4.19).

Instead of a single curve to fit to the data, we show two extreme fits to give an indication of the range of j_m values corresponding to the scatter of the data points. The values used in these fits are $j_m = 2.4K$ and $j_m = 3.4K$, showing quite a small variation in the parameter j_m. Fig. 4.3b shows an example plot of the excess specific heat for $n = 1.6 \times 10^{18} cm^{-3}$. Included is the power law fit, together with the correction using a value of $j_m = 3K$. The fits to the data are satisfactory and show that this rapid deviation of the data from the power form could be attributed to a finite maximum exchange coupling j_m. However, the magnitude of j_m ($\sim 3K$) obtained from this analysis is much lower than expected (App. C.1).

4.4.2 Analysis on "Standard" Excess Specific Heat in a Magnetic Field

Next we look at the excess specific heat in a non-zero magnetic field as obtained using the "standard method" described in §4.2.1. The predictions of the extended two-fluid model in (4.1) are compared to the experimental data. Published excess specific heat data were available for the donor concentrations $n = 0.79 \times 10^{18} cm^{-3}$ (insulating) and $n = 4.5 \times 10^{18} cm^{-3}$ (metallic).

The data for $n = 4.5 \times 10^{18} cm^{-3}$ have already been introduced in fig. 4.1b, for magnetic fields $B = 1.5T$ and $5.7T$. We focus first on the $n = 0.79 \times 10^{18} cm^{-3}$ data.

Figure 4.4a shows the total specific heat for $n = 0.79 \times 10^{18} cm^{-3}$, for several magnetic fields. Fig. 4.4b shows the corresponding excess specific heat, together with Schottky fittings to the data, as determined using (4.11) in §4.2.1. (Also refer to fig. 4.1a.) With an increasing magnetic field the peak position shifts to the right, while the peak height increases. In the Schottky expression there are two fitting parameters, the effective field and the effective concentration of localized moments. The position of the peak determines the effective magnetic field, which in this case is smaller than the applied field, showing that the electron interactions are antiferromagnetic in nature. The peak height determines the effective concentration, and the increase can be interpreted as field-induced localization effects (fig. 4.1a).

As an example to the use of eqn. (4.15) for data analysis, we plotted $\Delta C/T^{1-\alpha}$ versus T/B, which, according to the extended two-fluid model, should produce the universal curve $\sigma\delta(1.34B/T)$. Fig. 4.5a shows the results of this analysis. We used a value of $\alpha = 0.85$ which appeared to give the best results, particularly fitting the data below the peak. The

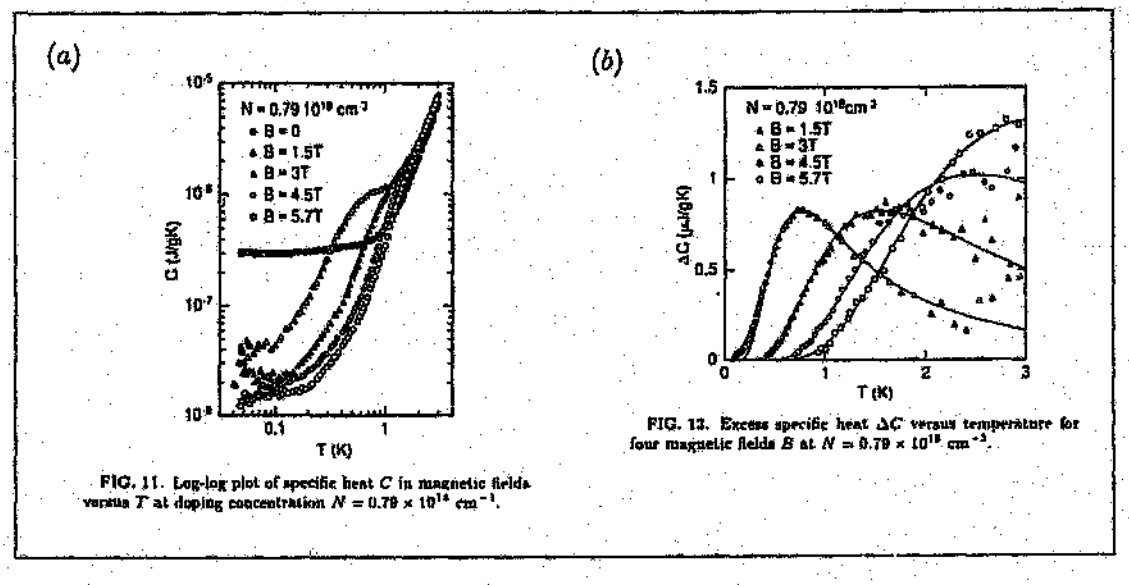


FIG. 11. Log-log plot of specific heat C in magnetic fields versus T at doping concentration $N = 0.79 \times 10^{18}$ cm^{-3}.

FIG. 12. Excess specific heat ΔC versus temperature for four magnetic fields B at $N = 0.79 \times 10^{18}$ cm^{-3}.

Figure 4.4: Plots of (a) the total specific heat C of an insulating sample in various magnetic fields, with (b) showing the corresponding excess specific heat ΔC obtained with the use of eqn. (4.11). Reproduced from [5].

large scattering of the rightmost data points for each field is due to the high temperature data points where measurements became more uncertain[5]. It is difficult to say whether a universal curve has been achieved, since for the two highest fields we do not have the full details of the peak. For the two lowest fields, where the peak is well defined, we do have a correspondence in the peak position, and the low temperature data appear to coincide for all fields. The peak heights for the data do not appear to be the same, indicating a possible field-dependent σ, or scatter in the data (fig. 4.4b).

The upper curve is a fit of eqn. (4.15), particularly fitted to the $B = 1.5T$ data which are the most pronounced. Below the peak, the fitting is very good and also describes the feature in the data at the lowest temperatures ($T/B < 0.2$). Above the peak the predicted behaviour deviates from the data. The lower curve, which shows a marked improvement in fitting the data, is the predicted form using the corrections to the extended two-fluid equations. For this low field ($B = 1.5T$), we used the analytical approximation in (4.5) as a first order correction. The value of $j_m = 3K$ is used for the maximum exchange coupling appearing in this expression for the correction.

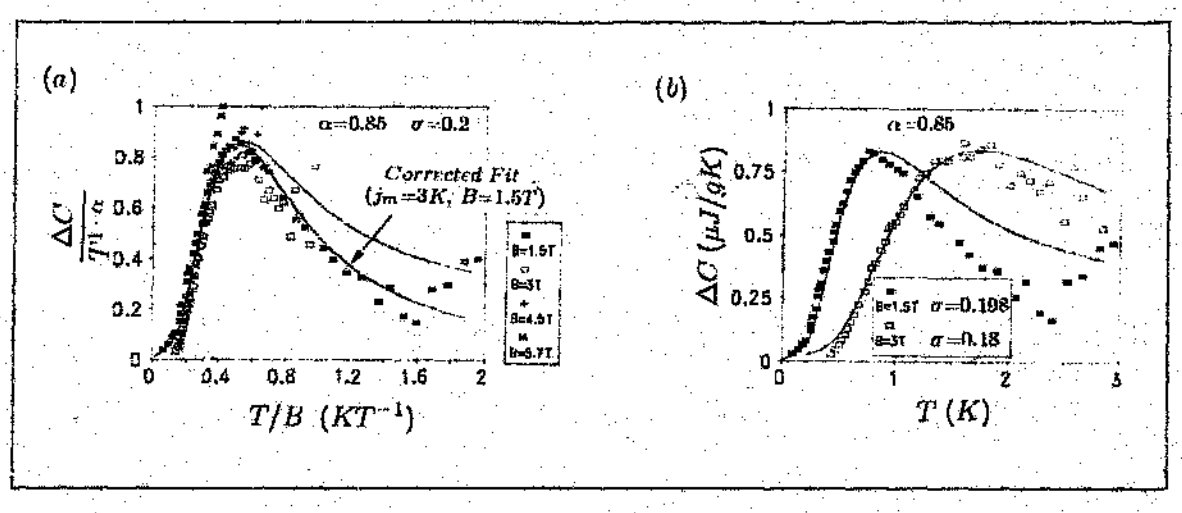


Figure 4.5: The specific heat data for $n = 0.79 \times 10^{18} cm^{-3}$ from fig. 4.4b, together with the predictions of the extended two-fluid model.

In fig. 4.5b we do a direct fitting, using eqn. (4.14), to the excess specific heat for the fields $B = 1.5T$ and $B = 3T$. In this figure we can see the same features as in the fig. 4.5a. The prediction is good below the peak, but, as the temperature is increased above the peak, the prediction diverges from the data. This can also be seen in the $B = 3T$ data, even with the high temperature scattering of points. As shown in fig. 4.5a, this deviation can be corrected with the use of the correction function in (4.5).

Finally we show the results for the data shown in fig. 4.1b. The data are reproduced in fig. 4.6, together with the predicted behaviour of eqn. (4.14). The value of $\alpha = 0.80$ was used for both fields, and was chosen to correspond to the zero-field value (fig. 4.2a). Although the fit for the $B = 5.7T$ data appears to be acceptable, we cannot make any conclusions since we do not have sufficient data for the complete peak structure. For the $B = 1.5T$ data we can clearly see a shift in the peak from the predicted position ($\Delta B \sim 0.1T$). Even when taking into account the magnetic field shift of the peak position, we still see that the tail of the curve diverges from the data as the temperature is increased, similar to the curve in fig. 4.5b. This deviation can also be eliminated by use of the correction functions, with a maximum exchange coupling $j_m \sim 2K$.

Similar analysis was done for other concentrations, both on the insulating and metallic phase, and the excess specific heat ΔC was determined in a similar fashion. As

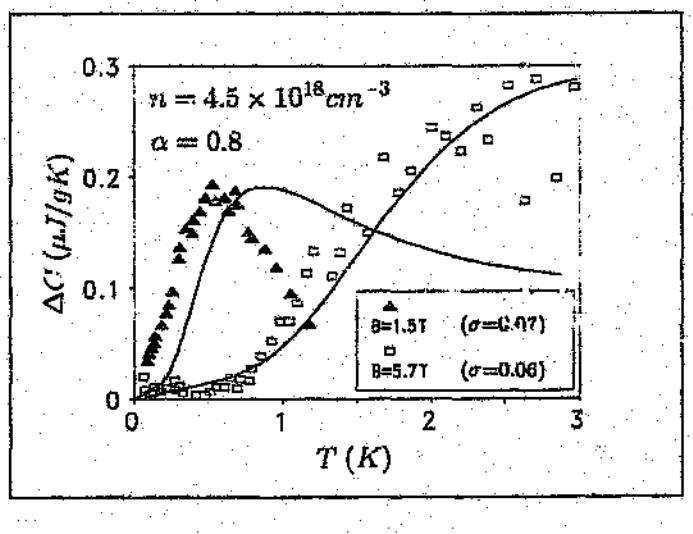


Figure 4.6: Predictions of the extended two-fluid model to the $n = 4.5 \times 10^{18} cm^{-3}$ specific heat data in fig. 4.1b.

for the $n = 0.79 \times 10^{18} cm^{-3}$ and $n = 4.5 \times 10^{18} cm^{-3}$ data in figs. 4.5a and 4.6, our model predictions give a poor account of the data.

4.4.3 Review of the Results

We now review the results obtained from §4.4.1 and §4.4.2, and show why we decided to look for alternative ways to analyze the data.

$B = 0$ Results

The zero-field analysis shows that the power law form prediction for the specific heat is present in the data in a certain temperature range, for all concentrations, as can be seen in fig. 1.6c in chapter 1. There are, however, several points that need attention with regard to the results obtained so far for the zero-field specific heat data.

1. The first point to consider is the method used in extracting the excess specific heat as shown in fig. 1.6a. As was mentioned (§4.2.2), the fitting of the linear and cubic terms $(\gamma T + \beta T^3)$ to the data in the C/T versus T^2 plot at best gives us an upper bound to the itinerant contribution γT (where γ is the intercept in this plot). So the actual

excess specific heat will be greater than that obtained using the "standard method" in §4.2.1.

2. Referring to fig. 4.3 and the rapid deviation of the data from the predicted power law fit above $0.4K$, our analysis shows that in the extended two-fluid model this deviation can be explained by using a maximum exchange coupling $j_m \sim 3K$. This is much lower than expected. This small value of j_m is actually a direct consequence of the method of extracting the excess specific heat (point 1 above). By fitting the straight line through the higher temperature data points, the excess specific heat is in fact minimized, by choosing a value of γ as large as possible. This forcing of the straight line through the data points actually forces the excess specific heat ΔC to vanish rapidly near the point where the straight line fitting starts to match the data (fig. 1.6a), leading to the unusually small term j_m. If the power law form does hold for higher temperatures (as expected), then in fig. 1.6a the localized moment contribution will be $C/T \sim (T^2)^{-\alpha/2}$ (from (4.3)), which at higher T is slow-varying and could be mistaken as a constant contribution, being added to the itinerant term γ.

3. The determined values of α, as shown in fig. 4.2a, are not as expected. Near the MI transition, the expected value is $\alpha \sim 0.6$, whereas here we have $\alpha \sim 0.8$.

$B \neq 0$ Results

Section 4.4.2 shows the analysis done on the specific heat in a magnetic field, and the results are not satisfactory. As for the $B = 0$ specific heat, the fittings can be improved by introducing the corrections to the model equations, by using a maximum exchange coupling of $j_m \sim 3K$. This value of j_m is similar to that used in the zero-field analysis, and again is much smaller than expected. The reason for the failure of the predictions of our model, is, however, easily obtained, and is not due to inadequacies in the model, but again due to the method in which the excess specific heat data are extracted.

Conclusions

For the zero-field analysis, the major discrepancy arises from the extraction of the itinerant contribution using the C/T versus T^2 plots. To eliminate the need for this method, we can instead use the "alternative" method (§4.2.2) by doing a direct fitting of

the theoretical prediction to the data.

The next question is to review the extraction of the excess specific heat in a magnetic field. The answer to the failure of the extended two-fluid model is actually very simple, and tells us why the Schottky fits to the data in figs. 4.1b and 4.4b are superior to the extended two-fluid predictions.

The method used to obtain the excess specific heat is to fit eqn. (4.11) in §4.2.1 to the total specific heat data, and is the reason why the excess specific heat data provided resemble Schottky peaks. In fitting the data with (4.11), the terms $\gamma(B)$ and β are obtained to best match the remaining contribution to the term C_{Sch}, and in essence force the excess specific heat to be as close to a Schottky peak as possible. This is the reason for the good fits of the Schottky expression to the data.

This method of analysis can produce qualitative results such as the behaviour of the effective concentration of localized moments in going through the MI transition, and can give indications as to the magnitude and antiferromagnetic nature of the electron interactions. (Refer to point 5 in App. A.2.) The excess specific heat produced in this way is, however, inadequate for testing the specific heat predictions of other models.

4.4.4 Alternative Analysis on Zero-Field Specific Heat

In this section we analyze the zero-field specific heat data using the "alternative method" (§4.2.2). Here we do a direct fitting of the predicted total specific heat

$$C = \sigma T^{1-\alpha} + \gamma T + \beta T^3 \tag{4.20}$$

to the experimental data. Three different procedures were used to get results:

1. All four quantities σ, α, γ, and β were considered as fitting parameters, and (4.20) was fitted on the whole range of data.

2. All four quantities σ, α, γ, and β were considered as fitting parameters, but eqn. (4.20) was only fitted for temperatures $T \geq 100mK$. The reason for ignoring temperatures below $100mK$ was that there appeared to be an anomaly (an upturn in the data) present at these low temperatures even in the absence of an applied magnetic field. Taking only into account the data above $100mK$ could reduce the effect of this possible anomaly in the data.

3. The third procedure, which is preferred, used the experimentally determined value of $\beta = 0.241\mu J/gK^4$ (App. A.3) for the phonon contribution in (4.20). This reduces the number of fitting parameters to σ, α, and γ. This value of β was used for all concentrations, and since it is determined by the Si lattice dynamics, we do not expect it to be very sensitive to the impurity concentration.

The results for β, α, σ, and γ using the above three procedures are shown in figs. 4.7a, 4.7b, 4.7c, and 4.7d respectively. The symbols used for all four figures are: Procedure 1 (□), Procedure 2 (+), and Procedure 3 (▲), . The vertical line indicates the MI transition with $n_c \simeq 3.5 \times 10^{18} cm^{-3}$. The concentrations used are: $n[10^{18} cm^{-3}] = 0.34$, 0.79, 0.89, 1.6, 1.8, 2.8, 3.3, 3.6, 4.5, 5.1, and 7.3. Note that for the concentrations $n = 2.8 \times 10^{18} cm^{-3}$ and $5.1 \times 10^{18} cm^{-3}$ we did not have the original zero-field data, and these data had to be digitized from published figures in reference [5]. We will refer to the results of these two concentrations as we proceed.

1. Figure 4.7a shows the values of β obtained using procedures 1 and 2. The value of $\beta = 0.241\mu J/gK^4$ used in procedure 3 is indicated in the plot. The two vertical lines indicate the uncertainty $\Delta\beta \simeq 0.022\mu J/gK^4$ obtained for β (App. A.3). The β values obtained from the fittings are scattered about this experimentally determined value, with an average value of $\beta \simeq 0.245\mu J/gK^4$. This scattering of the β values could be attributed to the increased uncertainty in the data points occurring at the higher temperatures ($T \gtrsim 2K$) [5]. Since the phonon contribution becomes dominant at these temperatures, the magnitude of β is essentially determined by these higher temperature data points, with the experimental uncertainty manifesting itself in the values of β.

2. Figure 4.7b shows the results obtained for α. The arrow indicates the expected $\alpha \simeq 0.63$ near the MI transition. For the two concentrations, $n = 2.8$ and $n = 5.1$, the digitizing of the data from published figures was the least successful and not very accurate, and this could account for the deviation of these two α values from the average results where original data were available. The result for $n = 7.3$ is not shown, since for this high concentration the meaning of α is arbitrary because the localized contribution has become negligibly small, and the itinerant contribution dominates the electronic specific heat. (See next two points.) The results here can be compared

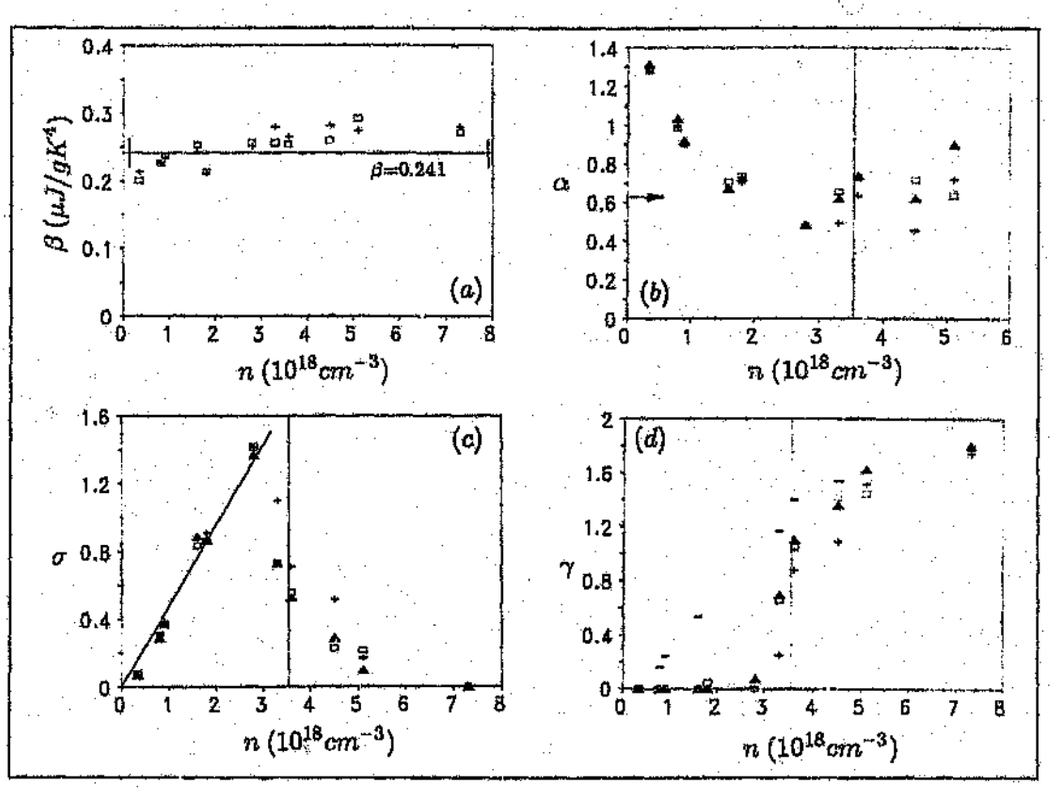


Figure 4.7: Plots of the values obtained for β, α, σ, and γ from the fitting of eqn. (4.20) to the zero-field specific heat data.

to those in fig. 4.2a. The behaviour of the data is similar, but, whereas α in fig. 4.2a converges to about 0.8 at higher concentrations, the α values in fig. 4.7b are lower, and, near the MI transition, are closer to the expected value of $\alpha \simeq 0.63$.

3. Figure 4.7c shows the results obtained for σ, and gives us an indication as to the effective concentration of localized moments. The solid line is only a guide to the low concentration behaviour. As the concentration is increased from zero, σ systematically increases, as would be expected. Close to the MI transition we then have a change in this trend, and σ gradually decreases through the MI transition, and vanishes at the concentration $n = 7.3 \times 10^{18} cm^{-3}$. For $n \gtrsim 2n_c$ the system is expected to be fully metallic, and so the vanishing of σ at $n = 7.3 \times 10^{18} cm^{-3}$ ($n/n_c \simeq 2.1$) would be

expected. The important point to notice is the presence of localized moments even in the metallic phase, which persists even up to $n = 5.1 \times 10^{18} cm^{-3}$ ($n/n_c \simeq 1.44$). The decrease in σ below the MI transition could be attributed to the formation of larger spin clusters (possibly metallic islands). For sufficiently large clusters, the local concentration could be larger than n_c and these clusters could be in the metallic phase, giving rise to metallic islands in the insulating phase. Comparing the results to those in fig. 4.2b, we see that the behaviour is similar, but the values of σ in fig. 4.2b are lower. This is a consequence of the "standard method" minimizing the excess specific heat (§4.2.2).

4. Figure 4.7d shows the results obtained for the itinerant contribution γ. The horizontal bars indicate the values shown in fig. 1.6b. The itinerant contribution determined in this section differs quite dramatically from the previous values. Whereas the previous values decrease smoothly through the MI transition (on decreasing the concentration from the metallic phase) and have a significant contribution even at the lowest concentrations, the values obtained here decrease more rapidly through the MI transition, and essentially vanish below $n = 3 \times 10^{18} cm^{-3}$. This is a more expected behaviour for γ, following from the form of the absolute zero conductivity (fig. 1.1). However, from the conductivity we would expect γ to vanish at the MI transition ($n = n_c$). One possibility is that the itinerant contribution γT to the specific heat should not be strictly interpreted as being due to itinerant electrons. This linear contribution could arise from itinerant electrons, and also from the additional interactions that localized moments would experience as the impurity concentration is increased towards the MI transition.

In fig. 4.8 we plot the average values of σ and γ to show the combined behaviour of these quantities. Just below the MI transition the itinerant contribution γ appears at the same concentration where the localized contribution σ starts to decrease. The inset in fig. 4.8 shows the itinerant contribution γ in a logarithmic plot. (The minimum and maximum values obtained are indicated.) The curves show the predictions of the nearly-free-electron model (App. A.2), given by

$$\gamma = 2.283 \left(\frac{m^*}{m_0}\right) n^{1/3} \quad , \tag{4.21}$$

where m^* is the effective mass of the impurity electrons. The upper curve uses the experimentally determined $m^*/m_0 = 0.44$ (A.12), while the lower curve uses the silicon conduc-

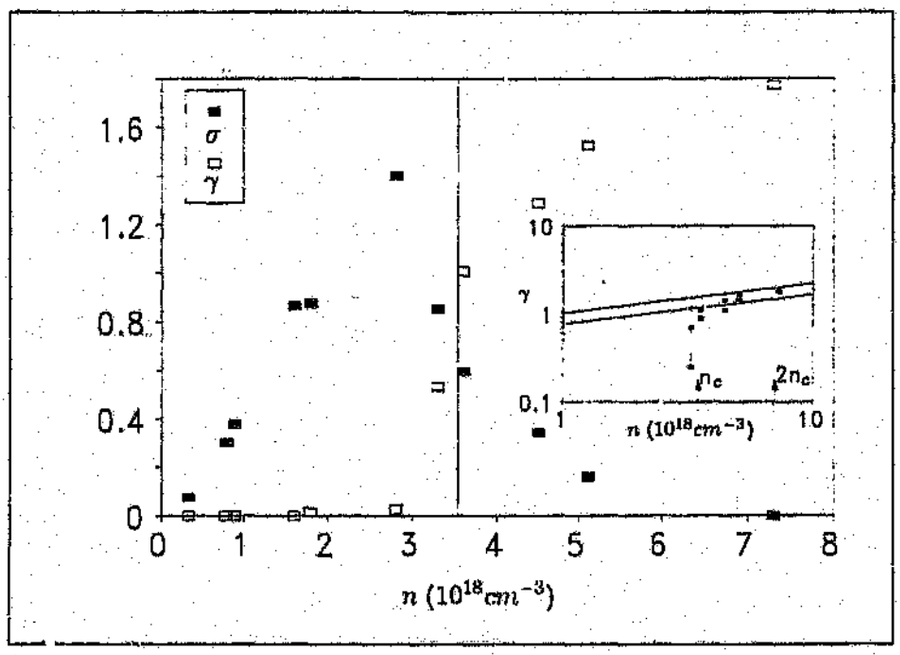


Figure 4.8: The average values of σ and γ, from figs. 4.7, in a single plot to compare the relative behaviour. The insert shows γ in the metallic phase, together with predictions of the free-electron model with two different effective masses.

tion band effective mass of $m^*/m_0 = 0.34$ (A.11). The arrows indicate the MI transition ($n = n_c$), and the concentration $n = 2n_c$ above which it is predicted that the system will be fully metallic and well described by the nearly-free-electron model. The data do appear to converge with the upper curve at $n \sim 2n_c$, supporting this prediction, and also the results of a mass enhancement over the silicon conduction band effective mass (although a slightly smaller value might give better convergence).

Figure 4.9a shows the excess specific heat obtained using procedure 1, together with the power law fits, for $n = 1.8 \times 10^{18} cm^{-3}$ (□), $n = 3.3 \times 10^{18} cm^{-3}$ (▲), and $n = 4.5 \times 10^{18} cm^{-3}$ (×). The results obtained using procedure 2 are shown in fig. 4.9b, and we can see marked improvements in this figure. Firstly, the theoretical curves fit the data much better above $100mK$, and there is particularly the removal of the scattering of data points observed above $T = 1K$ in fig. 4.9a . The power law behaviour above $100mK$ is more pronounced, while the possible upturn in the data below $100mK$ is now more visible.

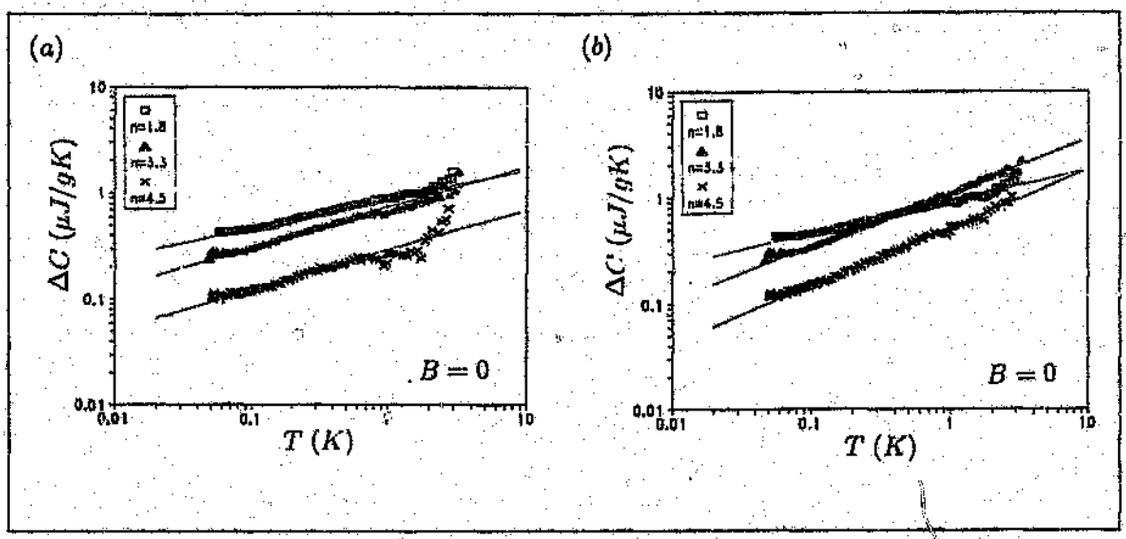


Figure 4.9: The excess specific heat ΔC obtained using (a) procedure 1, and (b) procedure (2). The power law form predicted by the model is shown by the straight lines.

Comparing fig. 4.9b with the excess specific heat shown in fig. 1.6c, we see that the power law form is present over the whole temperature range, and we need not introduce a correction. Referring to the inequalities in (3.66), the data in this figure would imply a maximum exchange coupling $j_m > 30K$.

All the results obtained so far in this section are based on the fitting of eqn. (4.20), where we have predicted the excess specific heat ΔC to go as $\sigma T^{1-\alpha}$, and using four fitting parameters (β, α, σ, and γ).

In procedure 3, where we use the experimentally determined phonon contribution of β, we do have an improvement by the removal of a fitting parameter. We are, however, still left with three fitting parameters (σ, α, and γ). The results of these fittings can, however, be used to show some of the data behaviour, without the need to fit (4.20). For example, referring to fig. 4.8, the results indicate that γ vanishes for concentrations $n < 3\times10^{18}cm^{-3}$, while σ vanishes for concentrations $n > 7 \times 10^{18}cm^{-3}$. These two extremes ($\gamma \to 0$ and $\sigma \to 0$) inferred from the plot can be shown directly, without the need to do any fittings with unknown parameters.

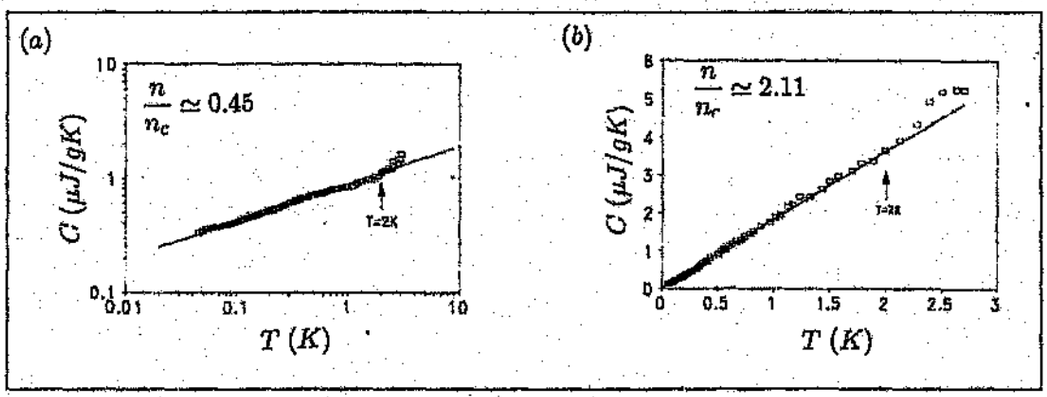
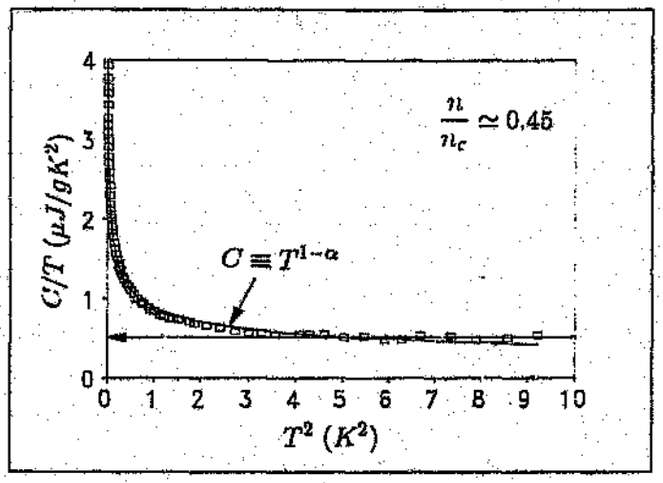


Figure 4.10: The zero-field specific heat, with the phonon contribution subtracted from the data, for an (a) insulating, and (b) metallic sample. The straight lines indicate the form of the data.

Using the predetermined value of $\beta = 0.241 \mu J/gK^4$ for the phonon contribution, we can subtract the phonon contribution from the total specific heat. Figs. 4.10a and 4.10b show these data for the concentrations $n = 1.6 \times 10^{18} cm^{-3}$ and $n = 7.3 \times 10^{18} cm^{-3}$ respectively. The straight lines indicate the form of these data. For $n = 1.6 \times 10^{18} cm^{-3}$, noting the logarithmic scale, the straight line implies directly the form $\sigma T^{1-\alpha}$ ($\sigma = 0.89$ and $\alpha = 0.67$), indicating the expected power law form, while for $n = 7.3 \times 10^{18} cm^{-3}$ the line shows the linear form of the data. So, without the need for fitting parameters, we can see that the itinerant and localized contributions (γ and σ) vanish, or become negligibly small, for the concentrations $n = 1.6$ and $n = 7.3$ respectively, giving validity to the results in fig. 4.8, particularly away from the MI transition. Note that above $T = 2K$ (indicated by the arrows) the data could be questionable, due to the uncertainty in the experimental measurements at these higher temperatures[5].

Lastly, we give an example of the difference between the "standard" and "alternative" method used (§4.2.1 and §4.2.2), particularly in the use of the C/T versus T^2 plots to extract the itinerant contribution γ from the intercept. Fig. 4.11 shows the electronic specific heat for $n = 1.6 \times 10^{18} cm^{-3}$ (fig. 4.10a) in a C/T versus T^2 plot. The curve is a power law fit ($C/T \sim T^{-\alpha}$) obtainable from the fit in fig. 4.10a. Note that the expression $T^{-\alpha}$ falls off slowly at higher temperatures. The data that follow this behaviour may appear to be



ure 4.11: The zero-field specific heat data for $n = 1.6 \times 10^{18} cm^{-3}$, as shown in fig. 4.10a, plotted as C/T versus T^2. This plot shows the apparent constant contribution at high T attributed to the itinerant component in the "standard" method (§4.2.1).

constant in value at these higher temperatures, particularly when there is significant scatter in the points. This apparent higher temperature constant contribution ($C/T \sim constant$) could then be wrongly attributed to the itinerant contribution ($C/T = \gamma$, as indicated by the horizontal line).

4.4.5 Alternative Analysis on Specific Heat in a Magnetic Field

Next we look at the specific heat in the presence of a magnetic field. The extended two-fluid model is applied to the electronic specific heat, and, as will be mentioned, some ambiguities arise, particularly close to and above the MI transition. However, the success of the extended two-fluid model will become evident, particularly in explaining the data in the insulating phase.

The predicted specific heat is given by eqn. (4.12), and the phonon contribution is subtracted from the total specific heat data., with a value $\beta = 0.241 \mu J/gK^4$. This leaves the predominantly electronic specific heat, which in the extended two-fluid model is predicted to go as

$$C = \sigma\delta(y)T^{1-\alpha} + \gamma T \quad , \tag{4.22}$$

consisting of the localized and itinerant contributions. The parameters σ, α, and γ are chosen to fit the data. Although σ, α, and γ are free parameters here, we do expect some correspondence to the values obtained in the zero-field analysis of the previous section.

Firstly we shall look at the specific heat near the MI transition. For this purpose we look at the $n = 3.3 \times 10^{18} cm^{-3}$ (just-insulating) and $n = 3.6 \times 10^{18} cm^{-3}$ (just-metallic) data for several magnetic fields. We choose a fixed value of $\alpha = 0.63$ which is the predicted value near the MI transition This is also close to the average values of α obtained in the zero-field analysis (fig. 4.7b). The parameters σ and γ are then chosen to fit the data.

Figures 4.12 and 4.13 show the localized moment contribution together with a fit of the expression $\sigma\delta(y)T^{1-\alpha}$ for the concentrations $n = 3.3$ and $n = 3.6$ respectively. The itinerant contribution γT has been subtracted from the electronic specific heat, with the value of γ obtained from the fitting of (4.22). The fittings are acceptable, and, particularly for the lowest magnetic field ($B = 0.7T$), we have an excellent agreement between theory and experimental data. Note the broad peak and the upturn at higher temperature. This is because our model predicts that $C \sim T^{1-\alpha}$ for higher temperatures (eqn. (4.2)).

Also note the anomaly (upturn) in the data at the lowest temperatures in both figures. This anomaly is field-dependent, and is believed to be nuclear in nature. From eqn. (4.2), the localized moment contribution is predicted to be linear in T for sufficiently low temperatures (and hence a linear electronic specific heat, since the itinerant contribution is also linear in T). A more detailed study of this predicted low T linear form, and the possibility of attributing this anomaly to a nuclear specific heat, is done in the next section.

The values of σ and γ obtained from the fittings are close to the values obtained in the zero-field analysis, particularly when considering the spread in values obtained from the three procedures (figs. 4.7c and 4.7d). What should be noted is the large change in σ and γ in the $B = 5.7T$ data for $n = 3.3 \times 10^{18} cm^{-3}$ (fig. 4.12). This could support the idea of field-induced localization, as inferred from the results in fig. 4.1. However, this feature does not appear for $n = 3.6$, although there is a gradual increase in σ. Since the peak position and peak height for $B = 5.7T$ are unknown from these data, with the extended two-fluid model predicting a peak position at $T > 2.85K$ (App. C.9), there is more uncertainty in these values of σ and γ, and the field-induced localization cannot be confirmed.

Also note that the values of σ and γ were not unique. There was a range of values for γ and σ which gave equivalent fits, particularly for the two higher fields where the prediction is not as good as for the lowest field. This range is similar to the range of

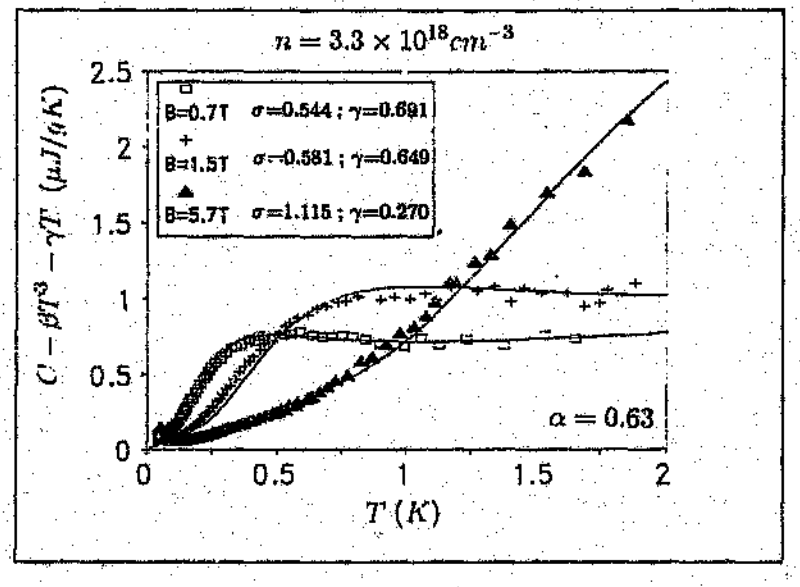


Figure 4.12: The excess specific heat ΔC for a just-insulating sample. The curves are fits of $\sigma\delta(y)T^{1-\alpha}$, with the parameters used shown in the figure.

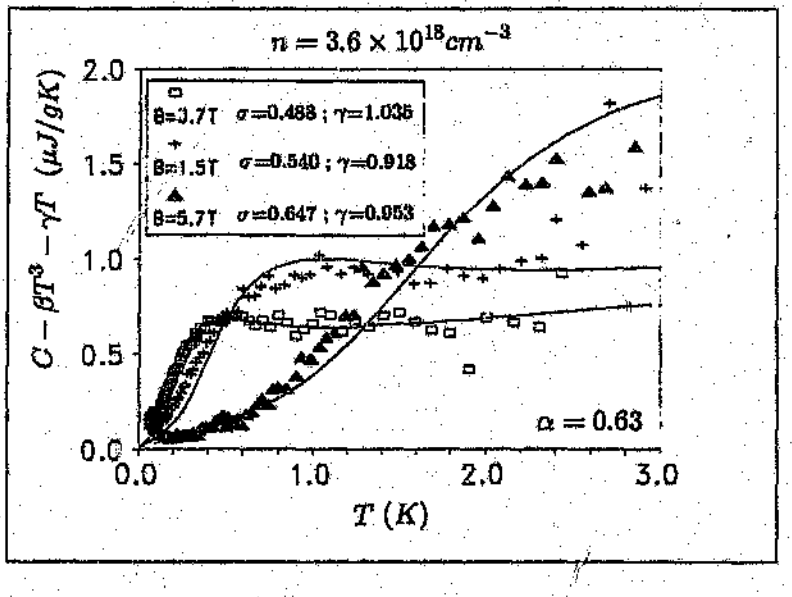


Figure 4.13: The excess specific heat ΔC for a just-metallic sample. The curves are fits of $\sigma\delta(y)T^{1-\alpha}$, with the parameters used shown in the figure.

σ and γ values obtained in the zero-field analysis of the previous section (figs. 4.7). This ambiguity in the values, particularly for the two higher fields, could be due to the fact that most of the important features of the data (such as the peak position, peak height, and tail) are less defined and are at higher temperatures where the experimental measurements become more uncertain[5], and we have a larger scatter of data. However, with some choice of σ and γ, the extended two-fluid model can explain the specific heat data both in a zero and non-zero magnetic field; above and below the MI transition.

Choosing the phonon coefficient β as a fitting parameter, and fitting to the total specific heat, can greatly improve the fittings shown in figs. 4.12 and 4.13, but we prefer to use the quoted value and reduce the amount of fitting parameters.

The value of $\alpha = 0.63$ was chosen for figs. 4.12 and 4.13 to coincide with the zero-field results and also the expected value quoted in literature. By fixing this value of α, we only have σ and γ as fitting parameters. By freeing the parameter α, we can get drastically different results.

For the $n = 3.3$ sample, which is in the insulating phase, the conductivity measurements would imply an absence of an itinerant contribution ($\gamma = 0$). We can explain the electronic specific heat for this sample in terms of a localized moment contribution $\sigma\delta(y)T^{1-\alpha}$ only. Fig. 4.14 shows this with a fit of eqn. (4.22), using a value of $\gamma = 0$ (no itinerant contribution).

The fits are good for all the magnetic fields, on the entire temperature range (except of course for the low temperature anomaly). The only drawback to this figure is the unusually low value of $\alpha = 0.4$ used in the theoretical curve, much lower than the expected magnitude near the MI transition. This is also an example of the absence of a peak in the theoretical curve for low α values, as introduced in App. C.9.

Next we look at the specific heat deeper into the insulating phase. It is here that the predictions of the extended two-fluid model manifest themselves, and justify the use of this model in explaining properties of this MI system. We look at the concentrations $n[10^{18}cm^{-3}] = 0.79$, 0.89, and 1.6 in the insulating phase (with $n/n_c \simeq 0.22$, 0.25, and 0.45 respectively). Figs. 4.15,4.16, and 4.17 show the results for these concentrations.

The data in all three figures are the total electronic specific heat, with the curves being fits of eqn. (4.22), using a value of $\gamma = 0$. The fits are good for all concentrations, and for all magnetic fields. The results show that at these concentrations the electronic specific heat can be explained in terms of only localized moments, without the need to introduce an

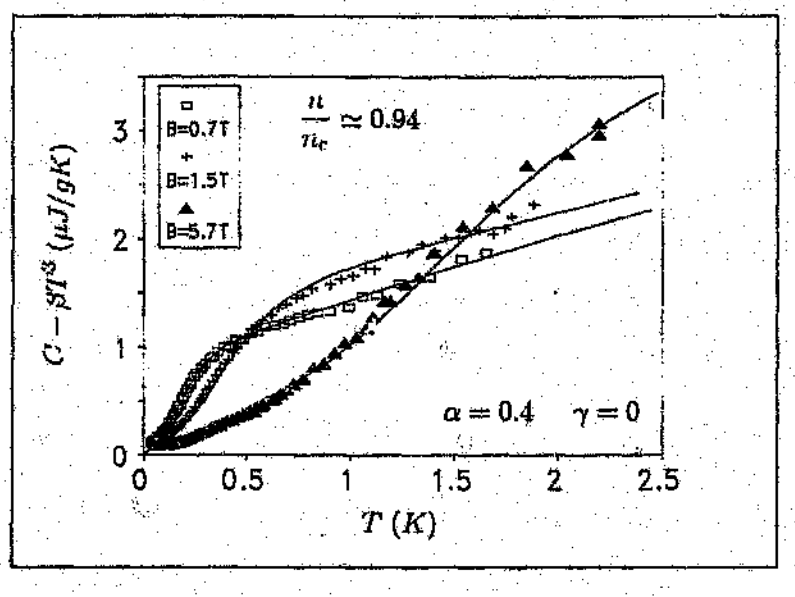


Figure 4.14: The electronic specific heat for $n = 3.3 \times 10^{18} cm^{-3}$ (refer to fig. 4.12). The curves are fits of eqn. (4.22) with $\gamma = 0$. The value of $\alpha = 0.4$ is much lower than expected.

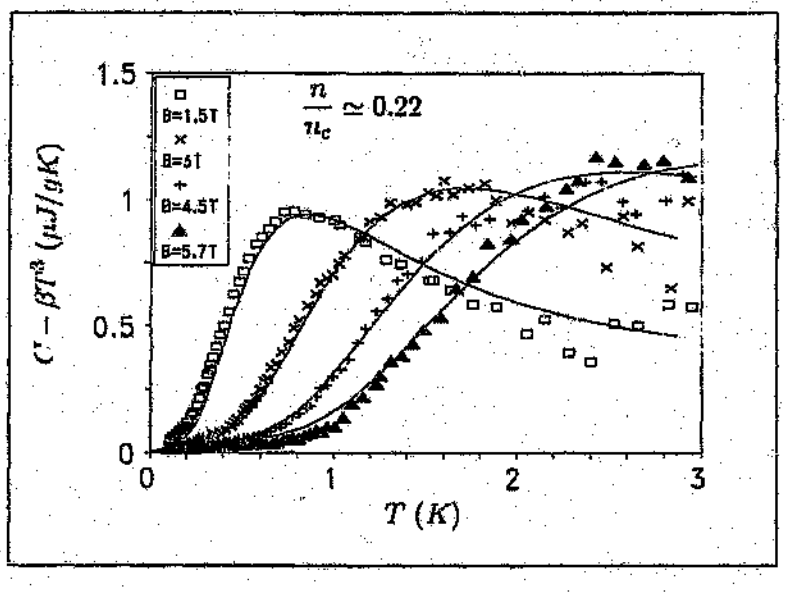


Figure 4.15: The electronic specific heat for $n = 0.79 \times 10^{18} cm^{-3}$. The curves are fits of (4.22), with no itinerant contribution ($\gamma = 0$), and $\alpha = 0.85$. The value of $\sigma = 0.225$ was used for all fields.

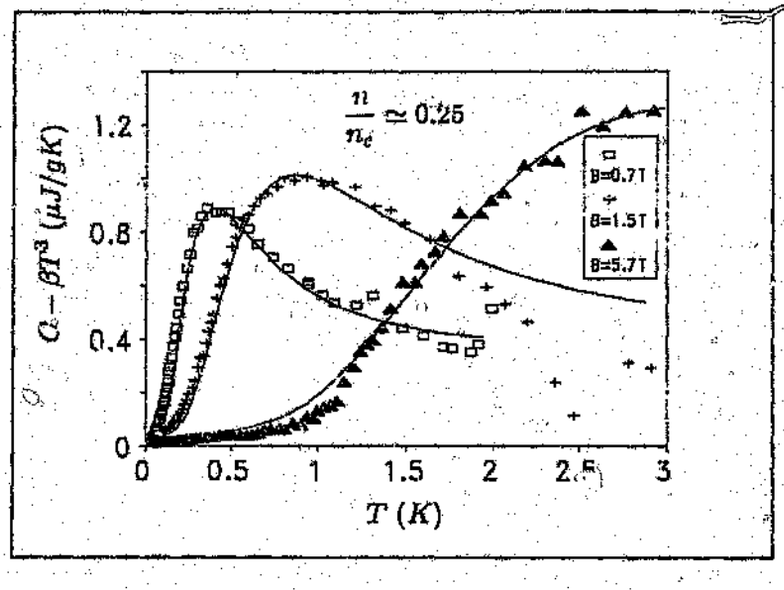


Figure 4.16: The k ·onic specific heat for $n = 0.89 \times 1.^{18} cm^{-3}$. The curves are fits of (4.22), with no itinerant contribution ($\gamma = 0$), and $\alpha = 0.83$. The value of $\sigma = 0.275$ was used for all fields. The $B = 1.5T$ deviation for $T \gtrsim 2.$ could be attributed to the larger uncertainties in the data occurring at these temperatures [5].

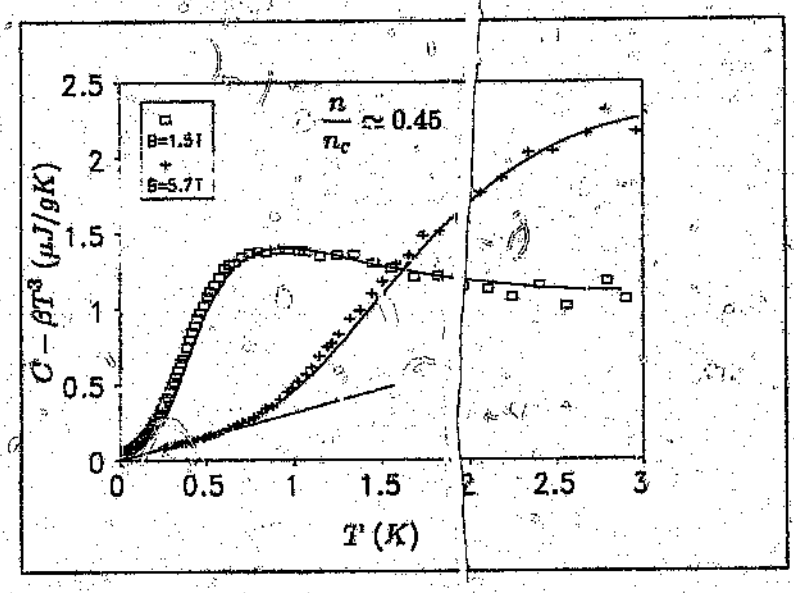


Figure 4.17: The electronic specific heat for $n = 1.6 \times 10^{18} cm^{-3}$. The curves are fits of (4.22), with no itinerant contribution ($\gamma = 0$), and $\alpha = 0.7$. The values of $\sigma = 0.64$ and 0.71 were used for $B = 1.5T$ and $5.7T$. The low temperature behaviour, predicted by (4.12), is also shown.

itinerant contribution. This result of 100% localization supports the zero-field results shown in fig. 4.7d, where we also have a vanishing itinerant contribution for these concentrations.

For $n = 1.6 \times 10^{18} cm^{-3}$, we have $\alpha = 0.7$, close to the zero-field value (fig. 4.7b). As the concentration is reduced to $n = 0.79$, α increases, as expected, to the value $\alpha = 0.85$, which is lower than the zero-field value. The zero-field results in fig. 4.7b show that α crosses the value $\alpha = 1$, which is not allowed in this formalism of the model, at these low concentrations ($n \leq 0.79 \times 10^{18} cm^{-3}$). The results in figs. 4.15 to 4.17 give a more expected behaviour, with α increasing towards 1, but remaining strictly less, as the concentration is reduced.

Also note that σ is essentially field independent, and does not support the results in fig. 4.1a.

In fig. 4.17 we have also indicated the asymptotic linear form predicted by the model. The anomaly is not present as the data do not go to sufficiently low temperatures.

Finally, we consider the magnetic field dependence of the specific heat for the concentration $n = 7.3 \times 10^{18} cm^{-3}$ (well into the metallic phase with $n/n_c = 2.1$). As the zero-field analysis has shown, the itinerant contribution γT dominates the electronic specific heat with the localized contribution being essentially negligible (or not present). So for this concentration we consider instead the field dependence of the total electronic specific heat.

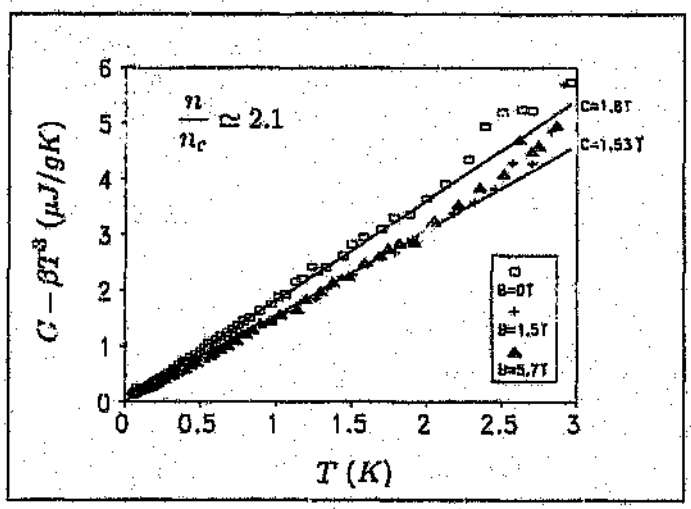


Figure 4.18: The electronic specific heat for $n = 7.3 \times 10^{18} cm^{-3}$ in various magnetic fields. The curves are linear fits to the data.

Figure 4.18 shows the specific heat for $n = 7.3 \times 10^{18} cm^{-3}$ with the phonon contribution subtracted. Note that the zero-field data have also been included, with a linear fit ($C = \gamma T$) corresponding to fig. 4.10b. Also shown are the data for the fields $B = 1.5T$ and $B = 5.7T$. The data for these two fields can also be described by a linear curve, as shown in the figure, indicating the dominant itinerant contribution. For $B = 1.5T$, we have $\gamma \simeq 1.55$ and for $B = 5.7T$, $\gamma \simeq 1.52$, showing a significant reduction in γ from the zero-field value ($\gamma \simeq 1.8$) on switching on a magnetic field ($\Delta\gamma/\gamma \simeq 15\%$). This could be due to field-induced localization, but the localized contribution could be small and indistinguishable from the scatter in the data. An interesting question here is the almost identical data for the two magnetic fields: there is a significant difference between the zero and non-zero field data, but an almost indistinguishable change in going from $1.5T$ to $5.7T$. This is contrary to the behaviour in a magnetic field for the lower concentrations where a significant change in γ only occurs for the largest fields. This requires more investigation, and possibly measurements for larger concentrations to determine whether there is localization or whether this is a property of the itinerant subsystem alone.

4.4.6 Low Temperature Behaviour and the Nuclear Contribution

We now look at the lowest temperature behaviour of the specific heat and the predictions of the extended two-fluid model at these low temperatures. We also consider the nuclear contributions to explain the anomalies.

The extended two-fluid model predicts that the localized moment contribution vanishes linearly in temperature as $T \to 0K$. This is shown in eqn. (4.2) and is also indicated in the data fitting of fig. 4.17. The itinerant contribution γT is also linear in temperature, and so at sufficiently low temperatures we predict for the electronic specific heat

$$C_{Elec} = \gamma^* T \quad , \quad T[K] \lesssim 0.1\ B[T] \quad , \tag{4.23}$$

where γ^* now represents both the localized and itinerant contributions. The verification of this form is made difficult by the anomaly, as seen in fig. 4.12 and 4.13, which we attribute to the nuclear system.

For the nuclear contribution we use the Schottky expression (App. A.2) and write

$$C_{Nuc} = \frac{\eta}{T^2} \quad , \tag{4.24}$$

which is a good approximation to the full Schottky expression for the temperatures we are dealing with ($T \gtrsim 50mK$). The parameter η is given by

$$\eta = \frac{g_N^2 \mu_N^2 B^2}{4k_B} n_N \quad , \tag{4.25}$$

where g_N is the nuclear g-factor, μ_N the nuclear magneton, and n_N the concentration of nuclei contributing to the specific heat.

For the analysis in this section we use the data for the highest field $B = 5.7T$. The first reason for this, as (4.23) indicates, is that the temperature interval in which the prediction should hold is the largest ($T \lesssim 0.57K$). The $5.7T$ data allow for the largest temperature range and hence more data points to test the predictions. The second reason is that the anomaly is most pronounced for this field, and hence preferable for comparison to (4.24).

The phonon contribution βT^3 (with $\beta = 0.241 \mu J/gK^4$) is subtracted from the total specific heat data, and combining eqns. (4.23) and (4.24), we have the predicted form for the low temperature data given by

$$C = \gamma^* T + \frac{\eta}{T^2} \quad , \quad T[K] \lesssim 0.1\ B[T] \quad , \tag{4.26}$$

which can also conveniently be expressed as

$$\frac{C}{T} = \gamma^* + \frac{\eta}{T^3} \quad , \quad T[K] \lesssim 0.1\ B[T] \quad , \tag{4.27}$$

where we treat γ^* and η as fitting parameters.

Firstly, we consider the concentration $n = 7.3 \times 10^{18} cm^{-3}$. As the zero and non-zero field analysis in §4.4.4 and §4.4.5 has shown, the localized moment contribution is negligible at this concentration and the electronic specific heat is linear in T in the whole temperature range. So here we have the special case where eqn. (4.23) holds for all T and the above two expressions should describe the data in the whole temperature range.

Figures 4.19a and 4.19b show the data for $n = 7.3 \times 10^{18} cm^{-3}$, with $B = 5.7T$ and $B = 1.5T$. We have plotted the electronic specific heat C, and C/T (to emphasize the anomaly), versus T. The curves are the corresponding fits of eqns. (4.26) and (4.27), and give excellent fits to the data.

The magnitude of the parameter η obtained from the fitting also gives us an interesting result. For $B = 5.7T$, eqn. (4.25) can be written as

$$n_N[10^{18} cm^{-3}] = 1.5 \times 10^{11} \left(\frac{\eta[JKg^{-1}]}{g_N^2} \right) \quad , \tag{4.28}$$

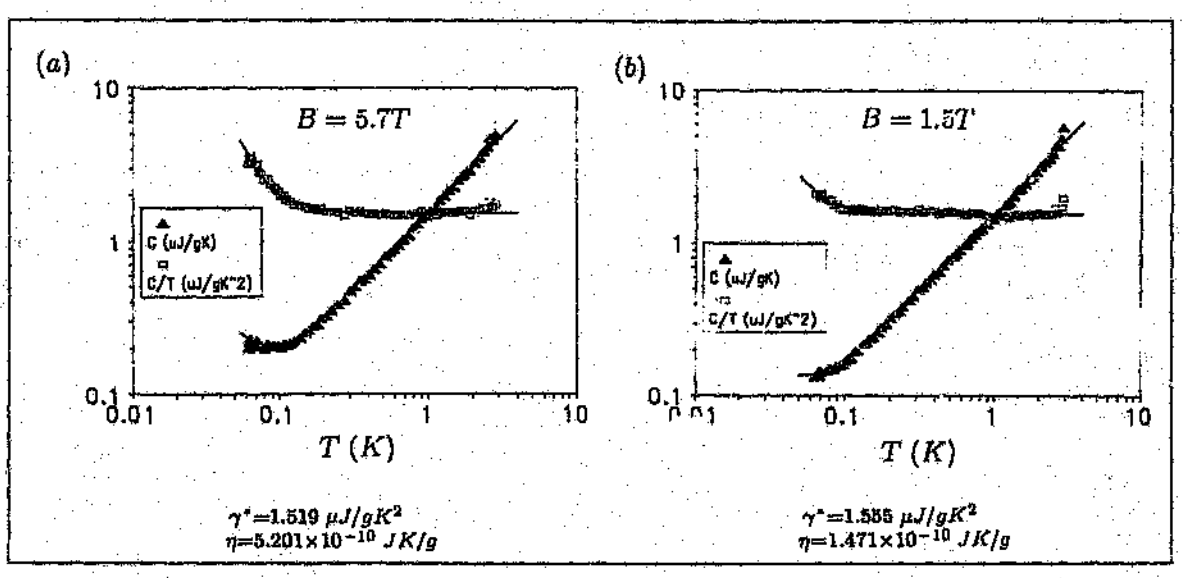


Figure 4.19: Plots of C and C/T versus T for $n = 7.3 \times 10^{18} cm^{-3}$, in two magnetic fields. The curves are fits of (4.26) and (4.27). The low T anomaly is clearly visible as the upturn in the data.

and from an order of magnitude analysis ($\eta \sim 10^{-10}$ and $g_N \sim 1$), we have that $n_N \sim 10^{19} cm^{-3}$, which is of the order of the impurity concentration ($7.3 \times 10^{18} cm^{-3}$). This supports the remarks that the nuclear contribution is due mainly to P nuclei, with the Si nuclei having too long a relaxation time to significantly contribute to the specific heat [18, 5].

Figures 4.20a to 4.20c show plots of C_i/T versus T, for lower concentrations, together with fits of eqn. (4.27). The first two figures show the results for concentrations in the metallic phase, while the third figure shows the results for insulating samples. For fig. 4.20b, with $n = 3.6 \times 10^{18} cm^{-3}$, $B = 6T$, while for the rest of the figures $B = 5.7T$. The arrows show the temperatures up to which we predict (4.27) to hold. For the metallic phase samples this prediction, and the fittings, are excellent, while, for the insulating samples shown in fig. 4.20c, the fittings are less convincing. In particular, for the $n = 3.3$ sample, the data deviate from the curve at lower temperatures than indicated by the arrow.

The details of figs. 4.20a, 4.20b, and 4.20c are shown below:

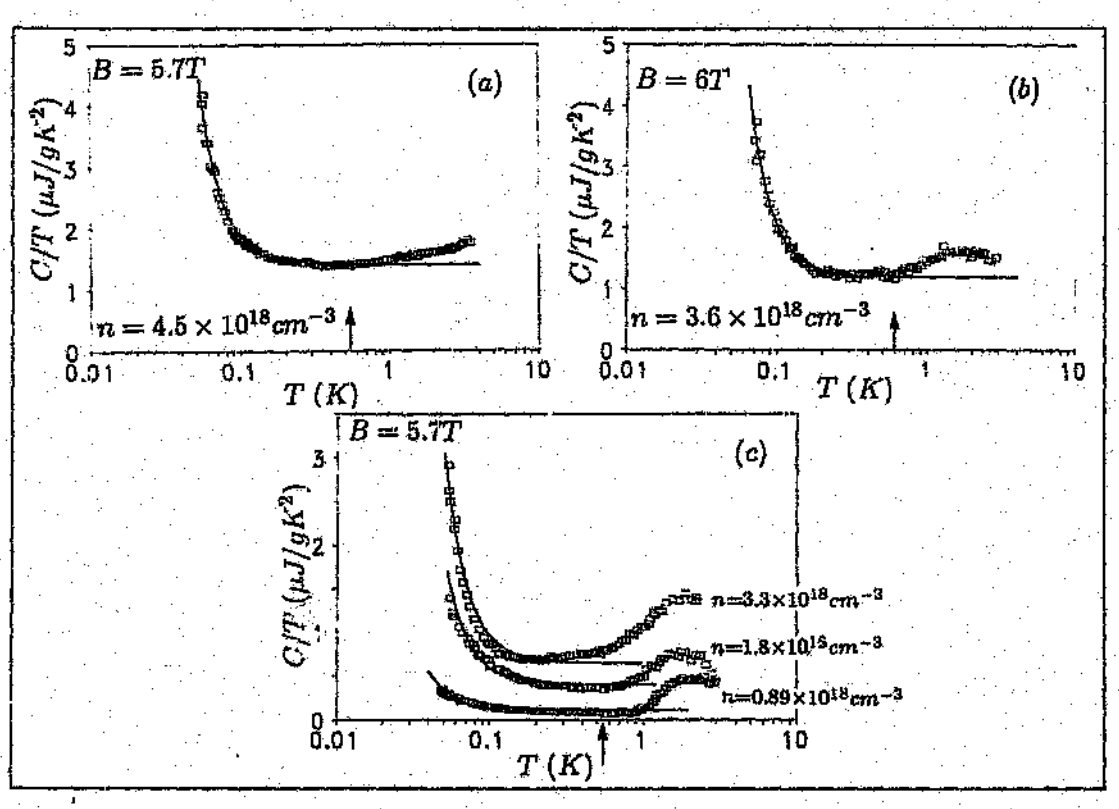


Figure 4.20: Plots of C/T versus T for various concentrations, with the curves being fits of eqn. (4.27). The arrows indicate the predicted temperature up to which this expression should describe the data.

Figure	n $(10^{18}cm^{-3})$	B (T)	η $(10^{-10}JK/g)$	γ^* $(\mu J/gK^2)$
4.20a	4.5	5.7	4.604	1.394
4.20b	3.6	6	8.56	1.189
4.20c	3.3	5.7	3.193	0.648
	1.8	5.7	1.940	0.403
	0.89	5.7	0.289	0.105

Notice the large value of $\eta = 8.56$ for the $n = 3.6$ sample, even when taking into account the slightly larger field. This jump can be clearly seen in fig. 4.21 where we have plotted η versus the donor concentration n. The straight line is a plot of eqn. (4.25) using $B = 5.7T$ and the ^{31}P nuclear g-factor $g_N = 2.26$. This line gives the P nuclear specific

heat contribution, ignoring couplings of the nucleus to the surrounding system.

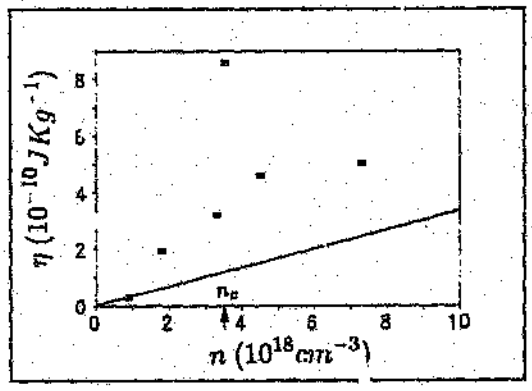


Figure 4.21: Plot of the nuclear contribution η versus the donor concentration n. The curve gives the expected value (eqn. (4.25)) for a non-interacting ^{31}P nuclear system.

The enhancement of η over the bare P nucleus contribution is clearly visible. The deviation from the curve increases as the concentration increases, and then the data appear to reduce towards the curve, as inferred from the $n = 7.3$ datum. Well into the metallic phase we would expect only the Knight shift to affect the nuclei, and since this shift is small, we would expect the data to converge with this curve as the concentration is increased. The enhancement for the lower concentrations near the MI transition could be due to the localized electrons, with a possible hyperfine coupling or the possible detection of some Si nuclei in the measurement. Taking into account the g-factor of the Si nucleus ($g_{Si} \simeq 1.1$), we would require between about 5 to 10 Si nuclei to be detected for every P nucleus to explain the enhancement.

Another point to consider is the unusually large value for the $n = 3.6 \times 10^{18} cm^{-3}$ sample. Is this enhancement a feature at the critical concentration? However, what should be noted is that we are only dealing with a small temperature range of the nuclear contribution (the tail of the nuclear specific heat at higher temperatures), and this value could just be an indication as to the uncertainties we are dealing with when analyzing only a small portion of the nuclear specific heat structure. If this is the case, then not much can be inferred from fig. 4.21, except the order of magnitudes indicating that the low temperature anomaly is nuclear in nature and predominantly due to the ^{31}P donors. Measurements at even lower temperatures have to be done to get more information on the anomaly's complete

structure and to confirm the validity of the data in fig. 4.21.

4.5 Analysis on the Experimental Susceptibility Data

Here we look at the predictions of the susceptibility in the extended two-fluid model and compare to available data. Eqn. (4.6) gives the expression for the susceptibility:

$$\chi = \chi^* + \rho\varepsilon(y)T^{-\alpha} \quad . \tag{4.29}$$

In the next section (§4.5.1) we look at the low magnetic field ($B \leq 300G$) susceptibility data, while in the following section (§4.5.2) we consider susceptibility data for larger fields (up to $B = 3000G = 0.3T$).

4.5.1 Low B-Field Susceptibility

Susceptibility data were digitized from reference [14] for several concentrations ($n[10^{18}cm^{-3}] = 0.11$, 0.43, 0.72, 1.2, and 3.7) in a range of magnetic fields ($B = 10G$, $50G$, $100G$, and $300G$). These data were also used in testing the susceptibility predictions of the spin-pair model in chapter 1 (§2.5) with the corresponding results shown in fig. 2.15. The constant background contribution χ^* has been subtracted, with the data giving only the temperature-dependent form attributed to impurity donors. Our model then predicts (eqn. 4.7) that the susceptibility goes as

$$\chi = \rho\varepsilon(y)T^{-\alpha} \quad ; \tag{4.30}$$

where ρ and α are considered as fitting parameters. These two parameters will be primarily determined by the higher temperature data where $\chi \sim T^{-\alpha}$.

According to eqn. (4.8), for $T[K] \gtrsim 1.34B[T]$, the susceptibility is then

$$\chi = \rho\beta_0 T^{-\alpha} \quad . \tag{4.31}$$

For these data, where the highest field is $B = 300G = 0.03T$, we predict eqn. (4.31) to hold for $T > 40mK$ for all the data. (For the lower fields the temperature up to which (4.31) should hold will obviously be lower than $40mK$.) The data are presented up to about $4K$, and so there are about two orders of magnitude in temperature in which eqn. (4.31) is predicted to hold. It is this power law region, $40mK < T < 4K$, which will then

primarily determine the values of the fitting parameters ρ and α through the form in eqn. (4.31).

Figures 4.22a to 4.22e show the susceptibility data together with fits of eqn. (4.30). Note that we only distinguish the field dependence at the lowest temperatures, where we use the symbol ■ for the $B = 10G$ data, and the symbol ▲ for the $B = 50G$ data. For the higher temperatures, where the data for the different fields converge, we use a single symbol ■ to collectively represent these data. Reference [14] can be consulted for the explicit magnetic field for each datum. For $T > 40mK$ (indicated by the arrow), the prediction (4.31) is the same for each of the fields.

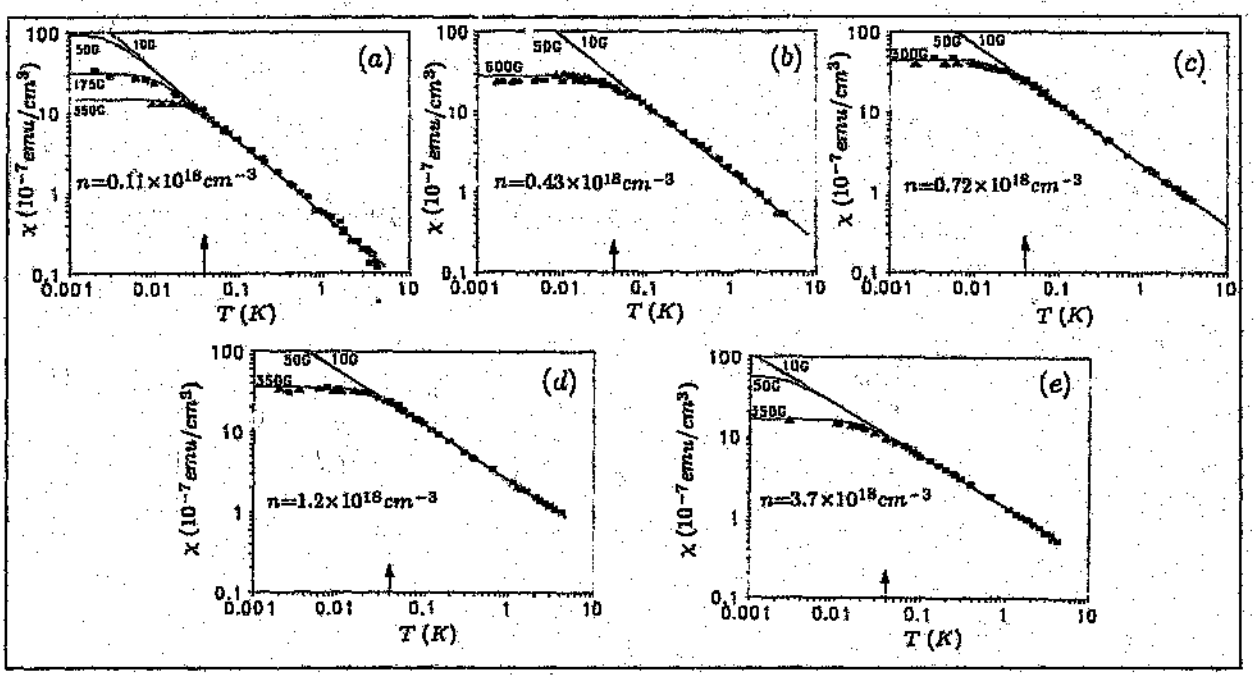


Figure 4.22: Fits of the prediction in eqn. (4.30) to the low magnetic field susceptibility χ, for various concentrations in the insulating phase. The arrows indicate the temperature above which we predict the $T^{-\alpha}$ power law form. The magnetic fields used for each curve are shown. For the data we use "■" and "▲" for $B = 10G$ and $50G$ respectively.

The curves show the fits of eqn. (4.30), and the details of these figures are shown below:

Figure	$n\ (10^{18}cm^{-3})$	α	$\Delta\alpha \sim$	ρ
29a	0.11	0.90	0.05	0.012
29b	0.43	0.85	0.035	0.059
29c	0.72	0.75	0.025	0.13
29d	1.2	0.685	0.02	0.19
29e	3.7	0.64	0.04	0.12

Notice that the curves which fit the data much in the whole temperature range are fits using fields much larger than the fields corresponding to the data. The same values of ρ and α shown in the above table were used, with the magnetic fields shown in the figures. This feature remains as yet unexplained.

Also notice the power law form predicted for $T > 40mK$, which gives acceptable fits to the data (except possibly for $n = 0.43 \times 10^{18}cm^{-3}$). As expected, the parameter α increases towards 1 as the concentration is reduced, and is around the expected value of $\alpha \simeq 0.63$ near the MI transition. Fig. 4.23 gives a graphical presentation of the table above, with a plot of ρ and α versus n.

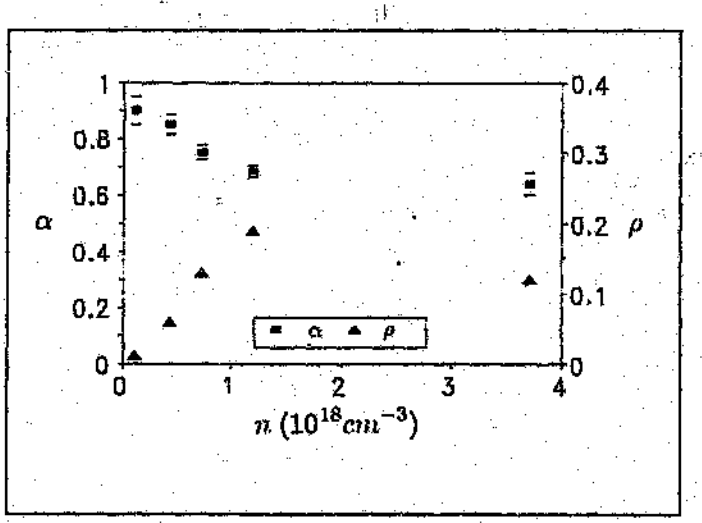


Figure 4.23: Plot of the values of α and ρ obtained from the fittings in figs. 4.22.

The behaviour of α is more of what is expected than that shown in figs. 4.2a and 4.7b from the specific heat analysis. Near the MI transition $\alpha \sim 0.63$ as expected, and increases towards 1 as the concentration is reduced, but is never larger than 1. This is to be expected as the system tends to an isolated spin system (App. A.2) with the Curie law

then describing the susceptibility. We do not have the discrepancy of $\alpha \geq 1$ as we have in the zero-field specific heat (figs. 4.2a and 4.7b), and the α values here are close to the α values obtained from the $B \neq 0$ specific heat analysis of §4.4.5 (figs. 4.15 to 4.17).

The form of the parameter ρ is similar to the corresponding specific heat parameter σ, shown in fig. 4.8, as expected.

4.5.2 High B-Field Susceptibility

More recent susceptibility data were digitized from reference [17] for the concentration $n = 3.3 \times 10^{18} cm^{-3}$, in larger magnetic fields ($B = 50G$, $500G$, $1000G$, $2000G$ and $3000G$). This reference quotes $n/n_c = 1.1$, showing this sample to be in the metallic phase, indicating the use of a different concentration scale. These susceptibility data for the various magnetic fields are shown in fig. 4.24.

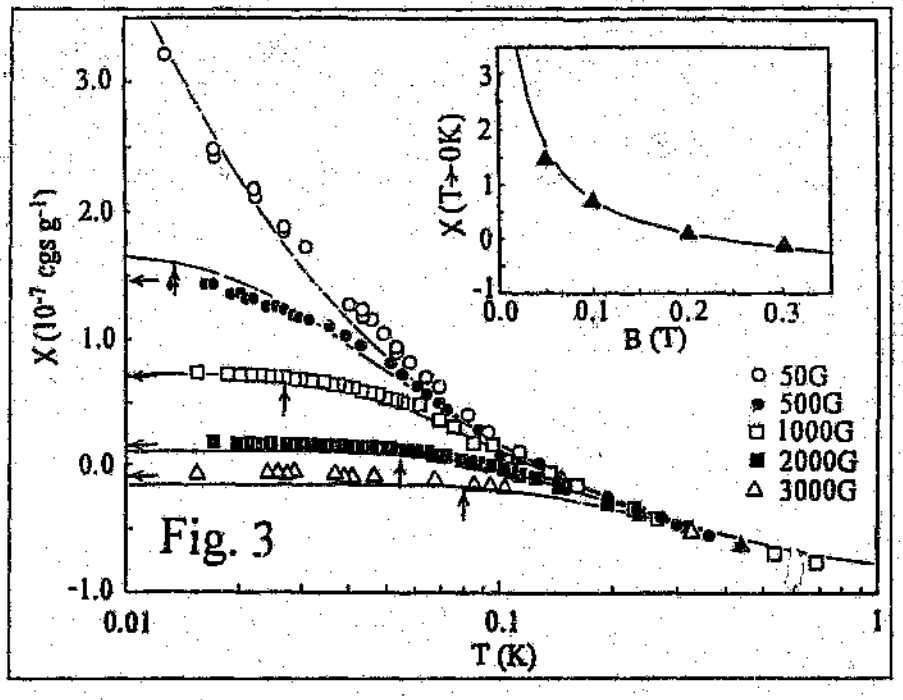


Figure 4.24: Comparisons to the susceptibility data in higher fields for a just-metallic sample. Reproduced from the publication in §4.7.

These data correspond to the total susceptibility, including the Si diamagnetic

susceptibility (evident from the negative magnitudes). The solid curves are fits of eqn. (4.29), with χ^*, ρ, and α as fitting parameters. The value $\alpha = 0.60$ was chosen, close to the expected value near the MI transition. The value $\chi^* = -1.1 \times 10^{-7} cgs/g$ is close to the experimentally determined diamagnetic contribution (App. A.3). The predictions of the model are good, and also give a good account of the strong magnetic field dependence. Note that in this figure we fixed all the parameters (χ^*,ρ, and α), and varied only the magnetic field B to get the fits. We could obtain much better fits by varying the term ρ, which could have a possible field-dependence.

As eqn. (3.44) indicates, for temperatures $T[K] \lesssim 0.27B[T]$, the susceptibility is predicted to level off to its asymptotic low temperature value $\chi_{T=0K}$, with $\chi_{T=0K} \propto B^{-\alpha}$. Hence we expect

$$\chi \equiv \chi^* + cB^{-\alpha} \quad , \quad T[K] \lesssim 0.27\ B[T] \quad , \tag{4.32}$$

where we include the diamagnetic and Pauli susceptibility, with c a constant, defined in eqn. (3.44).

In fig. 4.24, the vertical arrows indicate the temperature $T = 0.27B$ below which we predict the data should start leveling off. For the $B = 50G$ data this occurs at $T = 35mK$, well below the range of temperatures in the figure. The horizontal arrows show the apparent limiting values χ. The inset to fig. 4.24 shows these values together with a fit of (4.32) to explicitly show the B-field dependence of $\chi_{T=0K}$.

Also note the convergence of the data for larger T. The susceptibility in magnetic fields can therefore be described by the $B = 0$ predictions at sufficiently large temperatures. This is also predicted in §3.4 by the extended two-fluid model.

4.6 Discussion

1. In §4.4.5 and §4.4.6 we used a predetermined value for β to remove the phonon contribution. Taking into account the uncertainty in β of around 10% (App. B.3), we could to some extent regard β as a fitting parameter, which does greatly improve the predicted behaviour.

2. The alternative analysis on the $B = 0$ and $B \neq 0$ specific heat showed good results. In particular, we have shown that the use of the "standard" method (§4.2.1) to extract the excess specific heat data should not be used if a quantitative analysis of the data

is required.

3. The power law form ($C \sim T^{1-\alpha}$) for the zero-field specific heat appears to be present on the whole temperature range (figs. 4.9 and fig. 4.10b), and we do not require any corrections due to the finite maximum exchange coupling (§3.7). The non-zero field results for the specific heat also do not use any of the corrections to the extended two-fluid equations. The results therefore indicate that the maximum exchange coupling is indeed sufficiently large so as not to require corrections to the extended two-fluid model.

4. The alternative analysis on the $B = 0$ specific heat data, with the results summarized in figs. 4.7 and fig. 4.8, show similar results to previous work, with one exception. The itinerant contribution γ to the specific heat does not vanish gradually through the MI transition as the donor concentration is reduced (fig. 1.6b and fig. 4.7d), but instead shows a rapid decrease in magnitude near the critical concentration. This is a more expected behaviour. For $n/n_c \lesssim 0.8$, the itinerant contribution becomes negligible, and the data are described in terms of only localized moments. This vanishing γ in the insulating phase is also supported by the $B \neq 0$ specific heat results, where we have $\gamma = 0$ for $n/n_c \leq 0.45$.

5. The values of α (which determines the distribution of exchange couplings) determined from the susceptibility and the $B \neq 0$ specific heat analysis are as expected. Near the MI transition $\alpha \sim 0.6$ is roughly constant, and then increases towards 1 as the donor concentration is reduced. The $B = 0$ specific heat results, however, produce values of α that are larger than 1 (fig. 4.7b) for concentrations $n/n_c \lesssim 0.2$. These values of $\alpha > 1$ are not allowed in the extended two-fluid model (App. C.7).

6. These unexpected values of $\alpha > 1$ could be caused by a low temperature anomaly which distorts the actual values. We did consider this possibility in procedure 2 of §4.4.4 when we analyzed the $B = 0$ specific heat data. Referring to fig. 1.6c, and in particular the data for $n = 0.34 \times 10^{18} cm^{-3}$, we can clearly see the negative slope in the data. We analyzed the original data for this concentration and found that there is a sharp upturn in the data for $T \lesssim 100mK$. This upturn, which is more pronounced in a linear plot than in the log-log plot of fig. 1.6c, appears to have a $1/T^2$ behaviour, hinting at a possible nuclear contribution.

7. In the $B \neq 0$ specific heat analysis we took α as being field-independent. Referring to figs. 4.15 and 4.16, we see that, for the highest field $B = 5.7T$, there is a visible deviation from the data around $T = 1K$ which is not present for the lower magnetic fields. This feature is also absent from the higher concentration data in fig. 4.17. For the $n = 0.89 \times 10^{18} cm^{-3}$ data in fig. 4.16 we were able to remove this deviation by using a larger value of $\alpha = 0.90$ for the $B = 5.7T$ curve. This result could indicate a possible magnetic field dependence in α for sufficiently large fields, which could be expected.

8. The low temperature analysis in §4.4.6 was not fully conclusive. The results support the idea that the low T anomaly could be the nuclear specific heat. Our prediction of a linear electronic specific heat at sufficiently low temperatures (also indicated in fig. 4.17) is also supported, but cannot be confirmed.

9. The susceptibility analysis was also successful, and in particular we have a good prediction of the behaviour in larger magnetic fields, as shown in fig. 4.24.

10. As a final point, we introduce a very useful expression which was obtained after all the analysis was completed. In App. C.9 we include some analysis on the specific heat peak as predicted by the extended two-fluid model. Equation (C.57) in this appendix relates the specific heat peak heights C_1 and C_2 in the magnetic fields B_1 and B_2 respectively, by the expression

$$\frac{C_1}{C_2} = \left(\frac{B_1}{B_2}\right)^{1-\alpha} \qquad (4.33)$$

This relation shows directly that the peak amplitude increases as the magnetic field is increased. This increasing peak height with B is evident in the specific heat data (§4.4.5), and is also predicted by the spin-pair model of chapter 2 (fig. 2.7a). On the other hand, the analysis using the Schottky expression to describe the data (§4.2.1) has to consider an increasing effective concentration of localized moments, as indicated in fig. 4.1a. Although in §4.4.5 we used α as a fitting parameter, we can obtain α directly, using eqn. (4.33), from only a knowledge of the peak heights (with no need to do curve fitting). Applying eqn. (4.33) to the data in figs. 4.15, 4.16, and 4.17 we obtained almost identical values for α as were used for the curves.

In conclusion, we now have a two-fluid model for both zero and non-zero magnetic

fields, which can explain the thermodynamic properties on the insulating and metallic sides of the metal-insulator transition. More experimental measurements, such as the determination of the Wilson ratio and data for much lower temperatures, are required to fully test the prediction of the extended two-fluid model. The analyses, however, done on the available data are gratifying, and show that the extended two-fluid model is a useful tool.

4.7 Publication

PHYSICAL REVIEW B VOLUME 53, NUMBER 24 15 JUNE 1996-II

Thermodynamics of metal-insulator systems: The two-fluid model in the presence of a magnetic field

M. J. R. Hoch and C. Kasl
Department of Physics, University of the Witwatersrand, P.O. Wits 2050, South Africa
(Received 13 February 1996)

The two-fluid model for metal-insulator systems such as Si:P, involving localized and delocalized electrons, is extended to allow for magnetic field effects. Specific-heat and spin susceptibility expressions are given for the extended model and the predictions are compared with available experimental results. The agreement is satisfactory but further measurements of, for example, the Wilson ratio are needed in order to provide a more stringent test of the model. [S0163-1829(96)02124-8]

PACS number(s): 71.30.+h, 65.50.+m, 71.55.Jv

For metal-insulator (MI) systems, such as heavily doped semiconductors, there are important differences in character between transport properties and thermodynamic properties in the vicinity of the MI transition. The transport properties, in general, exhibit critical behavior near the critical concentration n_c, while the thermodynamic properties vary smoothly across the transition even at very low temperatures. A recent review[1] gives a comprehensive account of developments related to the Anderson-Mott transition, with emphasis on the transport phenomena and an effective field theory approach.

Paalanen *et al.*[2,3] have developed a phenomenological two-fluid model for MI systems, which allows for both localized and delocalized moments in systems close to the MI transition. Localized moments can play an important role in determining properties such as the magnetic susceptibility and the specific heat. These moments are also believed to play a dominant role in the nuclear relaxation processes near the transition.[4,5] The delocalized electrons, on the other hand, determine the measured NMR Knight shift[6,7] and the transport properties.[8]

While the two-fluid model is phenomenological, some progress has been made in placing it on a theoretical basis using an effective Hubbard model Hamiltonian.[9] Bhatt and Fisher[10] have argued on the basis of a positionally disordered Anderson-Hubbard model where the low-temperature thermodynamics of the disordered metallic phase is dominated by spin excitations in regions of low impurity concentration where the Kondo temperature is extremely low. The basic ideas are related to those of Bhatt and Lee[11] (BL) on the insulating side of the transition. Lakner *et al.*[12] have recently put forward a theoretical model that allows for a distribution of Kondo temperatures and that gives a quantitative description of the concentration of local moments. Related ideas have been put forward by Dobrosavljevic *et al.*[13,14]

Local moments are important in other highly correlated electron systems including heavy fermions such as UPd_2Al_3 and $CeCu_{2.2}Si_2$, which exhibit local moment antiferromagnetism and superconductivity at low temperatures.[15] Magnetic order and superconductivity are competing temperature-dependent effects.[16,17]

The application of a magnetic field can produce changes in the behavior of the MI systems such as the universality class in which a given system falls. Marked changes in the behavior of thermodynamic properties such as the specific heat,[18] which develops Schottky type peaks,[19] may also be brought about in this way.

This paper is concerned with generalizing the two-fluid model of Paalanen *et al.*[2,3] to allow for magnetic field effects. The dominant contribution to such effects is believed to be due to the localized moments and this is the basis for extending the model.

The thermodynamic two-fluid predictions for $B=0$ are expressed in the following equations for the specific-heat coefficient γ and the magnetic susceptibility χ:

$$\frac{\gamma}{\gamma_0}=\frac{m^*}{m_0^*}+\left(\frac{T}{T_0}\right)^{-\alpha}, \tag{1}$$

$$\frac{\chi}{\chi_0}=\frac{m^*}{m_0^*}+\beta_0\left(\frac{T}{T_0}\right)^{-\alpha}. \tag{2}$$

γ_0 and χ_0 are Fermi-liquid values, with m^* the Fermi-liquid effective mass and $m_0^*=0.34m_0$ the Si conduction-band mass.[2] T_0 is a parameter that includes the fraction of localized moments and β_0 is a constant. The exponent α is discussed below.

The local moment contributions to γ and χ contained in the second terms in Eqs. (1) and (2) are obtained using ideas put forward by BL to explain the low-field ($B\rightarrow 0$) behavior of χ for MI systems on the insulating side of the transition. The exchange coupling between the randomly positioned local moments is assumed to follow the distribution

$$P(J)dJ=\kappa J^{-\alpha}dJ, \tag{3}$$

where the exponent $\alpha\sim 0.62$ for Si:P and other similar systems[3] for $n=n_c$. κ is a normalization constant. A maximum cutoff value J_0 may be assumed for the distribution[2] but this is sufficiently high that for many purposes integrals containing J_0 as an upper limit may be extended to infinity.

The local moment contribution to Eqs. (1) and (2) may be obtained readily. For $B=0$, the exchange Hamiltonian H_e is of dominant importance for the local moments, with $H_e=\Sigma_{i<j}J_{ij}\mathbf{S}_i\cdot\mathbf{S}_j$. J_{ij} is the exchange coupling between spins i and j. The partition function for a pair of localized spins with exchange coupling J may be written as $Z=1+3e^{-\beta J}$, where $\beta=1/k_BT$. Using the distribution func-

 © 1996 The American Physical Society

tion given in Eq. (3), one can then obtain the localized contributions shown in Eqs. (1) and (2). The parameter T_0 is then defined as

$$\left(\frac{1}{T_0}\right)^{-\alpha}=\frac{1}{\pi^2}\left(\kappa\int_0^\infty dx\frac{3x^{2-\alpha}e^{-x}}{(1+3e^{-x})^2}\right)k_B^{1-\alpha}T_F\left(\frac{n_e}{n}\right),$$

where $x=\beta J$ and T_F is the Fermi temperature; n_e and n are the localized and itinerant electron concentrations, respectively. Numerical evaluation gives $\beta_0=10.3$, for $\alpha=0.62$, in close agreement with the value given by Paalanen *et al.*[2]

When a magnetic field B is applied to the system, a Zeeman term must be included in the Hamiltonian for the local moment subsystem. The partition function for a spin pair is then $Z=1+e^{-\beta J}+e^{-\beta(J+g\mu_B B)}+e^{-\beta(J-g\mu_B B)}$, where μ_B is the Bohr magneton and g is the g factor. Again using the distribution function in Eq. (3), the modified two-fluid model equations for $B\neq 0$ may be written as

$$\frac{\gamma}{\gamma_0}=\frac{m^*}{m_0^*}+\delta(y)\left(\frac{T}{T_0}\right)^{-\alpha}, \tag{4}$$

$$\frac{\chi}{\chi_0}=\frac{m^*}{m_0^*}+\varepsilon(y)\left(\frac{T}{T_0}\right)^{-\alpha}, \tag{5}$$

where the factors $\delta(y)$ and $\varepsilon(y)$, using $y=g\mu_B B/k_B T$, are given by

$$\delta(y)=\frac{I_\delta(y)}{I_\delta(0)},\quad \varepsilon(y)=\beta_0\frac{I_\varepsilon(y)}{I_\varepsilon(0)}, \tag{6}$$

with the integrals $I_\delta(y)$ and $I_\varepsilon(y)$, which have to be evaluated numerically, defined as

$$I_\delta(y)=\int_0^\infty dx\left(x^2\frac{\partial^2\ln Z}{\partial x^2}+2xy\frac{\partial^2\ln Z}{\partial x\partial y}+y^2\frac{\partial^2\ln Z}{\partial y^2}\right)x^{-\alpha}, \tag{7}$$

$$I_\varepsilon(y)=\int_0^\infty dx\left(\frac{1}{2y}\frac{\partial\ln Z}{\partial y}\right)x^{-\alpha}. \tag{8}$$

The behavior of the coefficients δ and ε is shown as a function of $1/y$ in Fig. 1. The specific-heat coefficient δ shows a peak for $y=2.6$, which leads to the Schottky-type peak observed in the specific heat. Sarachik *et al.*[20] have previously obtained a similar expression for χ for the localized moments in a magnetic field.

Equations (4) and (5) reduce to Eqs. (1) and (2) in the $B=0$ limit. It is to be expected that the extended two-fluid model equations will be of some value in accounting for the effects of magnetic fields.

In making comparisons of the two-fluid model predictions with experiment, one is faced with choosing the parameters α and T_0. It is possible that T_0 (Ref. 21) and, to a lesser extent, α will depend on the field B. We allow for a slight field dependence of T_0, due to an enhanced localization of spins, but, for simplicity, fix α for a given n/n_c value.

As a test of the model Paalanen *et al.*[2] have plotted experimental values of the Wilson ratio $(\chi/\chi_0)/(\gamma/\gamma_0)$ versus T for three samples on which they made low-field heat capacity and susceptibility measurements. The $B=0$, two-fluid

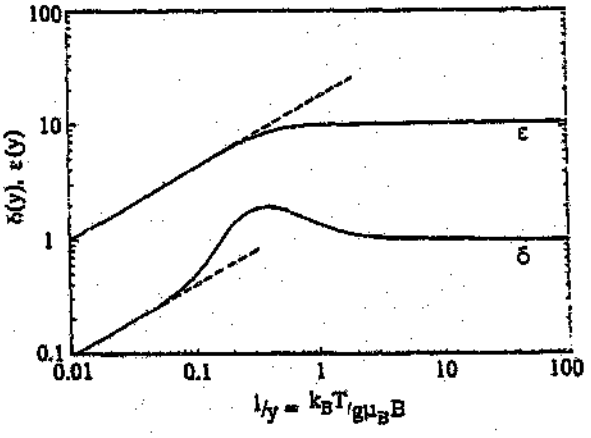


FIG. 1. The coefficients δ and ε, as defined in Eqs. (6), vs $k_BT/g\mu_BB$. The dashed lines show the low-temperature asymptotic behavior where $\delta,\varepsilon\sim y^{-\alpha}$.

model predictions give good one-parameter fits to the experimental results. The present extended two-fluid model provides Wilson ratio values as a function of temperature for nonzero magnetic fields. Figure 2 gives plots of this kind. The minimum feature corresponds to the maximum in the plot of $\delta(y)$ shown in Fig. 1. Unfortunately, no sufficiently complete measurements of the field dependence of the specific heat and magnetic susceptibility for a given sample near the MI transition appear to have been made. It is therefore not possible for us to make a comparison of experimentally determined Wilson ratio values for nonzero magnetic fields with the extended two-fluid model predictions. Measurements that permit such a comparison to be made would be of great interest.

The asymptotic $T\to 0$ forms of the specific heat and susceptibility can be directly inferred from the asymptotic forms of $\delta(y)$ and $\varepsilon(y)$, as shown in Fig. 1, using Eqs. (4) and (5). At low temperatures (T [mK]$\lesssim 100B$ [T]) the model predicts that the total electronic specific heat will be linear in T. Accurate verification of this prediction is made difficult by the presence at low temperatures of what is believed to be a nuclear contribution.[18] The susceptibility tends to a constant

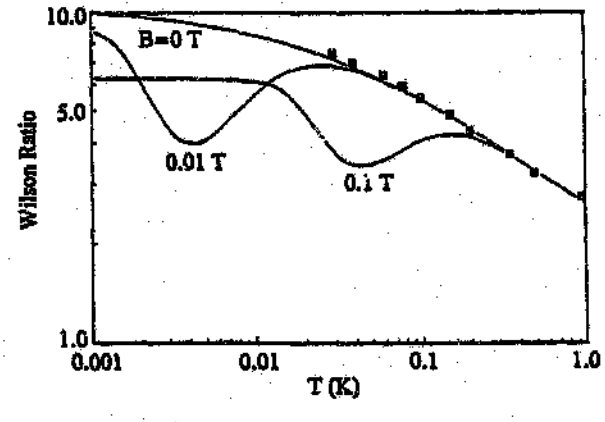


FIG. 2. Two-fluid model predictions of the Wilson ratio vs temperature for $n/n_c=1.09$. The zero-field experimental points shown are from Ref. 2.

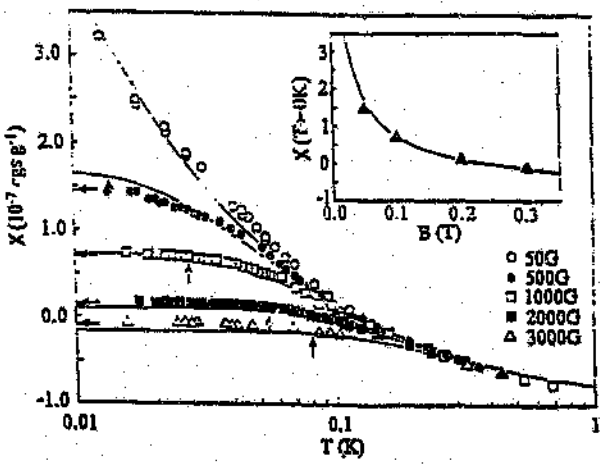


FIG. 3. Fits of Eq. (10) to the susceptibility (Ref. 22) for various magnetic fields, for $n=3.3\times10^{18}$ cm^{-3} ($n/n_c=1.1$ according to Ref. 22). Values used were $\chi^*=-1.1$ and $\rho=0.44$. The insert shows the asymptotic low-temperature behavior (indicated by the horizontal arrows) as a function of the applied field. The vertical arrows show the predicted temperatures where the susceptibility should start levelling off.

value, in this model, as $T\to0$. For T [K]$\lesssim0.27B$ [T] the localized contribution to the susceptibility has the field-dependent form

$$\chi=\left[\frac{\kappa\mu_0(g\mu_B)^{2-\alpha}}{2(1-\alpha)}n_e\right]B^{-\alpha}. \tag{9}$$

From Eq. (5) the total susceptibility χ can be written as

$$\chi=\chi^*+\rho I_s(y)T^{-\alpha}, \tag{10}$$

where χ^* now also includes the constant diamagnetic Si host susceptibility, and ρ is a constant. Matsunage and Oonuka[22] have measured the magnetic susceptibility for a Si:P sample very close to the MI transition as a function of temperature and applied magnetic field. Their results are shown in Fig. 3. The fitted curves are obtained using Eq. (10) above, with $\alpha=0.6$. The constant $\chi^*=-1.1\times10^{-7}$ cgs/g is consistent with estimates of the diamagnetic Si susceptibility[23] and the Pauli-Landau susceptibility of itinerant electrons. ρ is treated as a parameter, depending on several unknowns. The inset in Fig. 3 shows the field dependence of the asymptotic low-temperature behavior, which can be read for four values of B. The fitted curve is based on Eq. (9). For the lowest field (50 G), the model predicts that convergence will only occur for temperatures around 1 mK.

Lakner and Löhneysen[12,18] have measured the specific heat for a number of MI systems in fields up to 6 T. We have used Eq. (4) to make comparisons of theory with their results for Si:P. In zero magnetic field, the total specific heat may be written as a function of temperature in the form

$$C(T)=\sigma T^{1-\alpha}+\gamma_l T+\beta T^3, \tag{11}$$

where σ is a constant, involving the parameter T_0, which is proportional to n_e. $\gamma_l=\gamma_0 m^*/m_0^*$ is the itinerant electron specific-heat coefficient and β is the phonon coefficient. We have used the Debye temperature of 660 K for silicon[18] to determine β. This reduces the number of fitting parameters. σ and γ_l for a particular specimen may be determined by fitting the zero field data. We take $n_c=3.52\times10^{18}$ cm^{-3}.[24] σ, which gives a measure of the localized moment contribution, increases with n and then decreases smoothly through the transition. γ_l increases from a value close to zero for $n<n_c$ to finite values fairly abruptly at the transition. For $n/n_c>1$, γ_l tends to the value expected for the multivalley system,[12,25] with an effective mass m^* close to the band effective mass.[2]

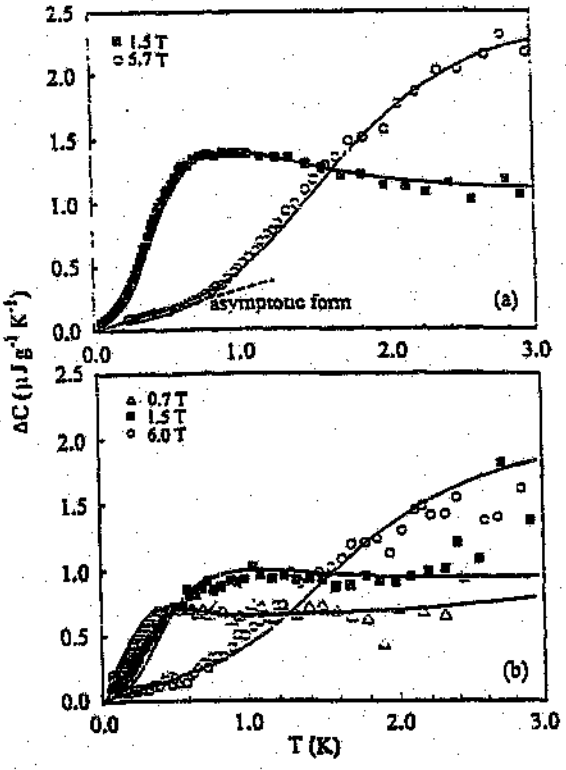


FIG. 4. Fits of Eq. (12) to the experimental ΔC values in various magnetic fields (Ref. 12) for (a) $n/n_c=0.45$ and (b) $n/n_c=1.02$. For the insulating side (a), using $\alpha=0.7$, we find $(\sigma,\gamma_l)=(0.64,0)$ and $(0.70,0)$ for $B=1.5$ and 6 T, respectively. For the metallic sample (b), using $\alpha=0.63$, we find $(\sigma,\gamma_l)=(0.49,1.04)$, $(0.55,0.92)$, and $(0.63,0.94)$ for $B=0.7$, 1.5, and 6 T, respectively.

For the heat capacity data $C(B,T)$ obtained with an applied magnetic field present, it is convenient to introduce the excess specific heat ΔC, defined as $C(B,T)=\Delta C+\gamma_l T+\beta T^3$. This quantity may be compared with the theoretical prediction based on Eq. (4):

$$\Delta C=\sigma\delta(y)T^{1-\alpha}. \tag{12}$$

Figures 4(a) and 4(b) show plots of experimental ΔC values, obtained from the data of Lakner *et al.*,[12] for $n/n_c=0.45$ and 1.02. The theoretical predictions of the extended two-fluid model are shown as the fitted curves. σ and γ_l values are given in the captions for each figure. Note the absence of an itinerant contribution for $n/n_c<1$. While there

may be a slight field dependence of σ obtained from the fits, it is not possible to draw any firm conclusions on field-induced localization effects.[21]

Nuclear moment contributions to the specific heat have been ignored but it is clear that at the lowest temperatures and for high fields these effects are becoming important. A nuclear Schottky term can be added to Eq. (11) to account for the upturn in ΔC observed below 100 mK.

The entropy of the system can be directly obtained by using the specific heat expression in Eq. (4). At sufficiently low temperatures the nuclear spin entropy contribution will dominate, as has been pointed out by Lakner and Löhneysen.[18]

In summary, the two-fluid model[2] has been generalized to include the effects of an applied magnetic field. The predictions of the modified equations are compared with the limited number of measurements of thermodynamic response functions made on MI systems in the presence of a magnetic field. The agreement of the present model with both the experimental ΔC and χ values is gratifying. Further experiments are needed to test the model in greater detail.

M.J.F.H. wishes to thank Don Holcomb and other members of the Laboratory of Atomic and Solid State Physics at Cornell University for the advice and great hospitality which they extended during a three month visit. We are grateful to H. von Löhneysen and S. Wagner for supplying some heat capacity data. Financial support was provided by the Foundation for Research Development and the University of the Witwatersrand.

[1] D. Belitz and T. R. Kirkpatrick, Rev. Mod. Phys. 66, 261 (1994).
[2] M. A. Paalanen, J. E. Graebner, R. N. Bhatt, and S. Sachdev, Phys. Rev. Lett. 61, 597 (1988).
[3] M. A. Paalanen and R. N. Bhatt, Physica B169, 223 (1991).
[4] M. A. Paalanen, A. E. Ruckenstein, and G. A. Thomas, Phys. Rev. Lett. 54, 1295 (1985).
[5] M.J.R. Hoch and D.F. Holcomb, Phys. Rev. B 38, 10 550 (1988).
[6] H. Alloul and P. Dellouve, Phys. Rev. Lett. 59, 578 (1987).
[7] S. T. Stoddart, M. J. R. Hoch, and U. Thomanschefsky, Phys. Rev. B 46, 10 007 (1992).
[8] M. Sarachik, in The Metal-Nonmetal Transition Revisited, edited by P. P. Edwards and C. N. R. Rao, in honor of Sir Nevill Mott's 90th birthday (Publisher, City, in press).
[9] M. Milanovic, S. Sachdev, and R. N. Bhatt, Phys. Rev. Lett. 63, 82 (1989).
[10] R. N. Bhatt and D. S. Fisher, Phys. Rev. Lett. 68, 3072 (1992).
[11] R. N. Bhatt and P. A. Lee, Phys. Rev. Lett. 48, 344 (1982).
[12] M. Lakner, H. von Löhneysen, A. Langenfeld, and P. Wölfle, Phys. Rev. B 50, 17 064 (1994).
[13] V. Dobrosavljević, T. R. Kirkpatrick, and G. Kotliar, Phys. Rev. Lett. 69, 1113 (1992).
[14] V. Dobrosavljević and G. Kotliar, Phys. Rev. B 50, 1430 (1994).
[15] R. Caspary, P. Hellmann, M. Keller, G. Sparn, C. Wassilew, R. Köhler, C. Geibel, C. Schank, and F. Steglich, Phys. Rev. Lett. 71, 2146 (1993).
[16] R. Feyerherm, A. Amato, F. N. Gygax, A. Schenk, C. Geibel, F. Steglich, N. Sato, and T. Komatsubara, Phys. Rev. Lett. 73, 1849 (1994).
[17] G. M. Luke, A. Keren, K. Kojima, L. P. Le, B. J. Sternlieb, W. D. Wu, and Y. J. Uemura, Phys. Rev. Lett. 73, 1853 (1994).
[18] M. Lakner and H. von Löhneysen, Phys. Rev. Lett. 63, 648 (1989).
[19] M. J. R. Hoch and C. Kasi, Phys. Rev. B 49, 2331 (1994).
[20] M. P. Sarachik, A. Roy, M. Turner, M. Levy, and D. He, Phys. Rev. B 34, 387 (1986).
[21] H. von Löhneysen and M. Lakner, Physica B 165–166, 285 (1990).
[22] N. Matsunage and Y. Ootuka, J. Phys. Soc. Jpn. 62, 1745 (1993).
[23] Y. Ootuka and N. Matsunage, J. Phys. Soc. Jpn. 59, 1801 (1990).
[24] M. Lakner and H. von Löhneysen, Phys. Rev. Lett. 70, 3475 (1993).
[25] G. A. Thomas, Y. Ootuka, S. Kobayashi, and W. Sasaki, Phys. Rev. B 24, 4886 (1981).

Chapter 5

Conclusion

5.1 The Spin-Pair Model Revisited

As we mentioned in chapter 2, we first revisit the spin-pair model developed in that chapter, in view of the more recent data and results of chapter 4.

In figures 5.1a and 5.1b we have reproduced the $n = 0.79$ and $1.6 \times 10^{18} cm^{-3}$ data in the magnetic field $B = 1.5T$ (figs. 4.15 and 4.17) , together with the predictions of the spin-pair model for various concentrations.

The upper curve in each figure was generated using a concentration n equal to the actual donor concentration corresponding to the data. For both figures we used the $B = 1.5T$ data, which is the most pronounced data. As can be observed, the spin-pair model clearly is inadequate in describing even the magnitude of the data. This just confirms the results of chapter 2 that the model does break down for the concentrations $n/n_c \gtrsim 0.1$ (§2.5.1). Although the form of the prediction for $n/n_c \simeq 0.2$ is similar to that of the data[1], we can clearly see that this is not the case for the larger concentration $n/n_c \simeq 0.45$, where the curve has very little resemblance to the data.

In view of the scaling ideas of Bhatt-Lee, we also generated predictions for lower, scaled down concentrations. The results for these scaled down concentrations are included in figs. 5.1a and 5.1b, and we can see a good fit to the data. These curves are almost identical to the curves produced by the extended two-fluid model shown in figs. 4.15 and

[1]Note that the corresponding data used in fig. 2.13b of chapter 2 were obtained by using the "standard" method described in §4.2.1. There an itinerant contribution was subtracted from the data shown in fig. 5.1a, so as to match the resulting data to a Schottky specific heat. This is the reason why the curves in figs. 2.13 do not give a good account of the shape of the data.

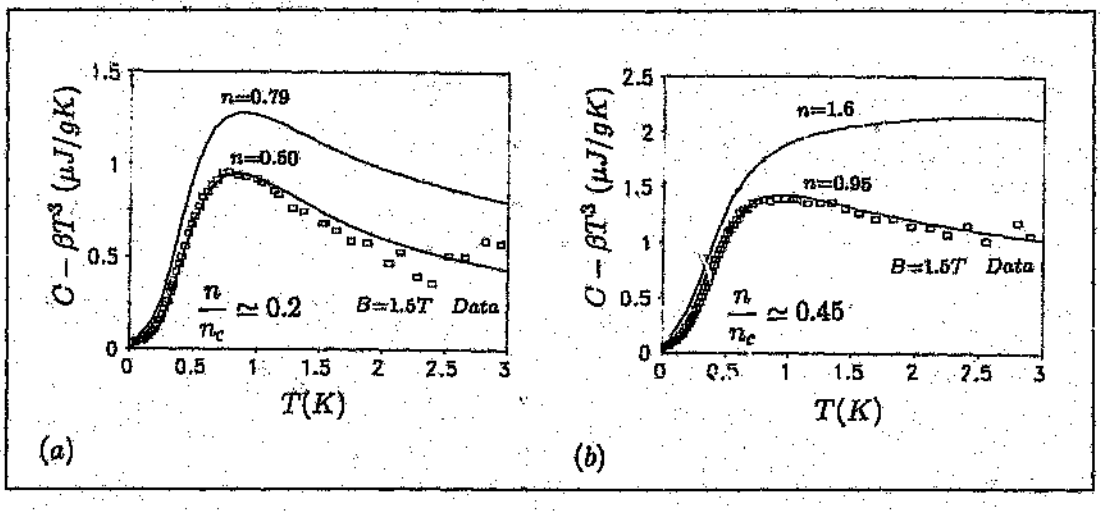


Figure 5.1: The $B = 1.5T$ specific heat data for the concentrations (a) $n = 0.79 \times 10^{18} cm^{-3}$ and (b) $n = 1.6 \times 10^{18} cm^{-3}$. The upper curves are the predictions of the spin-pair model, while the lower curves show these results when the concentrations are scaled down .

4.17. For $n/n_c \simeq 0.2$, we scaled the concentration by 63%, while for $n/n_c \simeq 0.45$ the scaling was 59%. The percentages are close, considering an almost doubling of the concentration.

So, by introducing a single parameter, the scaling factor for the concentration, we can use the spin-pair model to explain the specific heat data at even larger concentrations. This required scaling of the concentration could be interpreted in terms of larger cluster formation, or the freezing out of stronger coupled spin-pairs appearing at larger donor concentrations.

5.2 Conclusion

In conclusion, we have developed and tested two related models to describe the thermodynamic properties of metal-insulator (MI) systems in the presence of finite magnetic fields. Although we focussed on phosphorous doped silicon (Si:P), the models are general and should apply to similar system. Testing the predictions on other MI systems, such as GeSb, is a possible study for the future.

The spin-pair model of chapter 2 is based on the ideas put forward by Andres *et al.*[14] to explain their susceptibility data in very low magnetic fields. We have generalized

the zero-field spin-pair model to include the effects of finite magnetic fields, and to predict the behaviour of the specific heat and susceptibility. This model does not contain any free parameters, but our results support the results of Andres *et al.* that the spin-pair model becomes insufficient for donor concentrations $n/n_c \gtrsim 0.1$. However, as shown in the previous section, by scaling the actual concentrations, we can give a good description of the properties closer to the MI transition.

The extended two-fluid model is an extension of the zero-field two-fluid model introduced by Paalanen *et al.*[7]. Although this model does have several unknown parameters, the predictions of the specific heat and susceptibility are obtained in a form that allows for a more flexible analysis of the behaviour of the model and the experimental results. The analysis shows that the extended two-fluid model can successfully describe the properties of Si:P in zero and non-zero magnetic fields, for both the insulating phase and the metallic phase.

Overall, the results we have obtained are gratifying, and show that the two models should be useful in better understanding the properties of MI systems. Further experimental measurements, however, are required to test the predictions to the fullest. Measurements of the Wilson ratio would be very useful, and the thermodynamic properties at much lower temperatures will be required to better understand the properties of these systems.

Appendix A

Some Basic Theoretical and Experimental Results

A.1 The Partition Function Z and Thermodynamic Quantities

The partition function is the link between statistical mechanics and thermodynamics. With knowledge of the system's partition function all relevant thermodynamic properties of the system can be determined.

To determine the partition function we require the energy spectrum of the system. The partition function Z is then defined as

$$Z = \sum_i e^{-\beta E_i} \quad , \tag{A.1}$$

where the sum is over all possible states i, with E_i the energy of the state i, and $\beta = 1/k_B T$. If we do not have information on the allowed states, we must have at least the degeneracy of each level to evaluate Z.

From statistical mechanics we have that the probability $p(E_i)$ of the state i, with energy E_i, being occupied is proportional to the Boltzmann factor $e^{-\beta E_i}$. The partition function is obtained from the normalization condition $\sum p(E_i) = 1$ on this probability distribution, and we hence have

$$p(E_i) = \frac{1}{Z} e^{-\beta E_i} \quad . \tag{A.2}$$

From this the thermodynamic quantities can readily be obtained in terms of the partition function Z:

$$\begin{aligned}
\overline{E} &= \sum_i p(E_i) E_i = -\frac{\partial \ln Z}{\partial \beta} && (Energy) \\
C &= \frac{\partial \overline{E}}{\partial T} = k_B \beta^2 \frac{\partial^2 \ln Z}{\partial \beta^2} && (Specific\ Heat) \\
F &= E - TS = -kT \ln Z && (Helmholtz\ Free\ Energy) \\
S &= -\frac{1}{T}\frac{\partial \ln Z}{\partial \beta} + k_B \ln Z && (Entropy)\ . \qquad (A.3)
\end{aligned}$$

So the problem of determining the thermodynamic properties of the system depends on the knowledge of the partition function. For a large system of interacting particles (such as the impurity electrons in Si:P), the theoretical determination of the energy spectrum, and hence the partition function, can become impossible. Due to this difficulty, the modelling of the impurity electrons in disordered systems such as Si:P is done through the use of clusters of particles.

The system is divided into clusters of interacting particles, with the inter-cluster interactions considered as negligible. The partition function for a system of non-interacting subsystems is then simplified, and is just the product of the partition functions of the constituent subsystems:

$$Z = \prod_{clusters} Z_{cluster} \implies \ln Z = \sum_{clusters} \ln Z_{cluster}\ . \qquad (A.4)$$

So the problem reduces to studying the properties of finite clusters of spins. The isolated spin model, which leads to the Schottky specific heat and Curie susceptibility (next section), is just a special case where each cluster consists of a single spin. At low doping concentrations in Si:P, where the electronic interactions start to play an important role, the next step is to consider pairs of interacting particles, and is the basis of the models we have developed here. However, evidence[1] shows that the pair approximation can explain properties even at higher concentrations, and has use even at the MI transition.

A.2 The Isolated Spin System and Free Electron Model

In this section we review the thermodynamic properties of an isolated spin-1/2 system and a Fermi liquid (modelled by the free electron model). We specifically focus on

[1] Such as the analysis we have done.

the application to the donor electrons in Si:P.

The Isolated Spin-1/2 System

For sufficiently low concentrations, deep into the insulating phase of Si:P, the electron-electron interactions and the wave function overlap between donor electrons becomes negligible, and these electrons are then in isolated hydrogen-like donor states around the P^+ ions. At the temperatures of interest, $T \lesssim 1K$ ($k_B T \lesssim 0.08meV$, with k_B the Boltzman constant), the orbital excitations of these isolated donor electrons from the ground state (excitation energies $\gtrsim 1meV$) are suppressed. The only relevant excitations are the spin excitations. Therefore, at these low temperatures, we can regard these localized electrons as an isolated spin-1/2 system, or equivalently, each donor electron can be regarded as a two-level system, with a splitting $g\mu_B B$ in a magnetic field B. ($g \simeq 2$ is the electron g-factor, while μ_B is the Bohr magneton.)

The thermodynamic properties can then be easily determined, as described in §A.1, using the partition function of a two-level system: $Z = 2\cosh(\frac{1}{2}g\mu_B B/k_B T)$. The specific heat C_{Sch} and susceptibility χ of the system is then

$$C_{Sch} = nk_B \frac{y^2}{\cosh^2(y)} \tag{A.5}$$

$$\chi = \frac{1}{4}(g\mu_B)^2 \mu_0 \frac{\tanh(y)}{y} \frac{1}{k_B T} \quad , \tag{A.6}$$

where $y = \frac{1}{2}\frac{g\mu_B B}{k_B T}$ and n is the concentration of spins (μ_0 is the permeability of free space). Letting $B/T \to 0$ (or $B/T \ll 1$) and noting that $\tanh(y) \sim y$ for $y \ll 1$, we obtain the $B \to 0$ limit of the susceptibility χ_{Curie}, given by

$$\chi_{Curie} = \frac{c}{T} \quad , \tag{A.7}$$

where $c = (\mu_0 \mu_B^2/k_B)n$ is called the Curie constant. Eqn. (A.5) is just the well known Schottky specific heat for a two-level system, while eqn. (A.7) gives us the well known Curie susceptibility expected for a non-interacting spin-1/2 system.

The simple T^{-1} Curie law form is readily seen in experimental data by using a log-log plot of χ versus T, where the data lie on a straight line with slope -1.

The Schottky specific heat C_{Sch} has several properties worth noting:

1. Since C_{Sch} depends on T and B only through the variable $y = \frac{1}{2}g\mu_B B/k_B T$, changing the B-field just scales the temperature dependence of C_{Sch}.

2. The position of the peak T_m occurs at $y_{\max} = \frac{1}{2}g\mu_B B/k_B T_m \simeq 1.2$ (or $B[T]/T_m[K] \simeq 1.79$), and we therefore see a shift of the peak to higher temperatures as the magnetic field is increased.

3. The magnitude of the peak $C_{\max} = (k_B y_{\max}^2/\cosh^2(y_{\max}))n$ depends only on n, and for a fixed concentration, the peak height is independent of the magnetic field.

4. For large temperatures $k_B T \gg g\mu_B B$ ($y \ll 1$), the Schottky specific heat can be sufficiently approximated by its asymptotic form $C_{Sch} \sim 1/T^2$.

5. For systems where the spins are interacting, but a Schottky-type specific heat is still obtained, it has been useful to still use C_{Sch} to describe the data. Instead of using the applied field B and the actual concentration n of spins in eqn. (A.5), we use effective values B_{eff} and n_{eff}, which are obtained from fitting the data. For example, if $B_{eff} < B$ ($B_{eff} > B$) then it indicates predominantly antiferromagnetic (ferromagnetic) interactions present in the system. References [19], [20], or [5] do indicate the use of this procedure.

6. In the absence of a magnetic field, when $B = 0$, we see from (A.5) that the specific heat will vanish, since $y = 0$. So for this system we only expect a specific heat contribution in finite magnetic fields.

Since both the ^{31}P and ^{29}Si nuclei have spin 1/2, eqns. (A.5) and (A.6) are also used to describe the nuclear specific heat and susceptibility. Since the nuclear magnetic moment is about 3 orders of magnitude smaller than that of the electron, we do not need to consider the nuclear susceptibility here. We do, however, need to consider the nuclear specific heat, which can have a magnitude comparable to the electronic Schottky specific heat, but occurring at much lower temperatures ($T \sim 1mK$ for $B \sim 1T$). This is evident from points 2 and 3 above. We can use (A.5) to describe the nuclear specific heat, but for our purpose, since we are dealing with temperatures $T \gg 1mK$, we need only make use of point 4, and use the asymptotic form of C_{Sch}.

The Free Electron Model

Deep into the metallic phase of Si:P ($n \gtrsim 2n_c$), the donor electrons indicate a Fermi liquid behaviour, and their properties are then well described by the results of the free electron model (with modifications such as the effective mass).

The free-electron model predicts that the specific heat C_0 and susceptibility χ_0 are given by

$$C_0 = \gamma_0 T = \left(\frac{\pi^2}{2}\frac{k_B}{T_f}n\right)T \qquad \text{(A.8)}$$

$$\chi_0 = \frac{3}{2}\frac{\mu_0\mu_B^2}{k_B T_f}n \quad , \qquad \text{(A.9)}$$

where n is the number of electrons, k_B the Boltzman constant, μ_0 the permeability of free space, μ_B the Bohr magneton, and T_f the Fermi temperature. We have introduced the specific heat coefficient γ_0, since the two-fluid equations are written in terms of this.

With the introduction of an effective mass[2] for the electrons, the free-electron results can also describe the properties of electrons (or holes) in crystals, and in particular can be used to describe electrons in the conduction band of Si, and also the itinerant electrons in the impurity band.

So the expressions (A.8) and (A.9) can describe the Si conduction band electrons and the impurity itinerant electrons, with T_f determined by the particular system described. T_f depends on the structure of the silicon conduction band and therefore on factors such as the number of valleys in the conduction band and also the effective mass describing the low-lying states of the conduction band. The effective mass in Si is anisotropic (the longitudinal and transverse effective mass given respectively by $m_l = 0.916$ and $m_t = 0.190$ [4]), but for simplicity can be taken as an averaged constant determined from experimental data. T_f can then also be expressed (in terms of the Fermi energy E_f) as

$$E_f = k_B T_f = \frac{\hbar^2}{2m^*}(3\pi^2)^{2/3}\frac{n^{2/3}}{\nu^{2/3}} \quad , \qquad \text{(A.10)}$$

where ν is the number of valleys in the conduction band ($\nu = 6$ for Si), and m^* the effective mass of the electrons. The effective mass for Si, m_0^*, can be taken as[7]

$$m_0^* = 0.34 m_0 \quad , \qquad \text{(A.11)}$$

where m_0 is the free electron mass.

The impurity itinerant electrons also have a free-electron nature and appear to be well described by the expressions above, except that m^* is different from the Si conduction band effective mass m_0^* given in (A.11). The analysis of Paalanen *et al.*[7] shows that

$$m^* \simeq 1.3 m_0^*$$

[2]Refer to the "effective mass approximation" for a more detailed definition and use of the effective mass.

$$= 0.44m_0 \quad , \tag{A.12}$$

showing a mass enhancement over the Si conduction band electrons.

A.3 The Silicon Lattice Specific Heat and Diamagnetic Susceptibility

One contribution to the total specific heat that has to be considered is the phonon specific heat of the host silicon lattice in the Si:P system. This contribution will be dominant at temperatures $T \gtrsim 1K$. The Debye expression for the phonon specific heat can be used to describe this contribution, and is given by

$$C = 9Nk_B \left(\frac{T}{\theta_D}\right)^3 \int_0^{\theta_D/T} \frac{x^4 e^x}{(e^x-1)^2}\, dx \quad , \tag{A.13}$$

where θ_D is the Debye temperature of the solid, and N the number of Si atoms. For silicon the Debye temperature can be quoted as $\theta_D = 660 \pm 20\ K$ [5].

Since the temperatures we are interested in for our analysis are around $1K$ and less, we can say that $T << \theta_D$. For this case the upper limit in the integral of the above expression can be replaced by $+\infty$, and the specific heat for temperatures well below θ_D can then be expressed as

$$C = \frac{12\pi^4}{5} Nk_B \left(\frac{T}{\theta_D}\right)^3 = \beta T^3 \quad , \tag{A.14}$$

and so we see that the specific heat behaves cubic in T. The constant coefficient β is given by

$$\beta = \frac{12\pi^4}{5} \frac{Nk_B}{\theta_D^3} \quad . \tag{A.15}$$

For Si with a Debye temperature of $\theta_D = 660 \pm 20K$ and a concentration of $N = 2.15 \times 10^{22}/g$ we conclude that

$$\beta = 0.241 \pm 0.022\ \mu J/gK^4 \quad . \tag{A.16}$$

The Si host lattice also introduces a negative, T-independent diamagnetic contribution to the susceptibility. This diamagnetic susceptibility χ_{dia} can be obtained by measuring the susceptibility of pure silicon. This has been done by several researchers, and the results are shown below:

Author	Reference	Value for Si Diamagnetic Susceptibility
Andres *et al.*	[14]	$\chi_{dia} \simeq -(2.98 \pm 0.02) \times 10^{-7} emu/cm^3$
Ikehata *et al.*	[10]	$\chi_{dia} \simeq -1.16 \times 10^{-7} cgs/g$
Ootuka and Matsunaga	[16]	$\chi_{dia} \simeq -(1.16 \pm 0.10) \times 10^{-7} cgs/g$
		$\chi_{dia} \simeq -(1.24 \pm 0.06) \times 10^{-7} cgs/g$

The diamagnetic contribution of the orbital motion of the localized donor states in Si:P also needs to be considered. Ikehata *et al.*, however, claim that from the analysis of their susceptibility data, this diamagnetic contribution is negligibly small.

Appendix B

Mathematical Details for the Poisson Distributed Spin-Pair System

B.1 The Poisson Distribution

Here we want to determine the form of the distribution of nearest neighbours in a system such as Si:P where the donors are randomly positioned. We require a function $P(R)$ such that $P(R)dR$ gives us the probability of a nearest neighbour being in the range $(R, R+dR)$. For this purpose we use the binomial distribution, and also consider a bulk sample. Considering a bulk sample allows us to let $N, V \to \infty$ while keeping the density $n = N/V$ constant (the thermodynamic limit, with N the total number of donors in a volume V). We proceed as follows, referring to the fig. B.1:

Given donor #1, we want to determine the probability of its nearest neighbour #2 being at a separation in the interval $(R, R+dR)$. So we want to find the probability of donor #2 being inside the shell, and the rest of the donors being outside the sphere.

Firstly, we note, because of the random distribution of donors, the probability of finding a donor in a small volume Ω (small compared to the total volume V) is $p = \Omega/V$. Hence the probability of finding a donor inside the shell is $(4\pi R^2 dR)/V$, while the probability of finding a donor outside the sphere is $1 - \left(\frac{4}{3}\pi R^3\right)/V$. Using the binomial distribution, the probability of finding a donor inside the shell and the rest of the donors

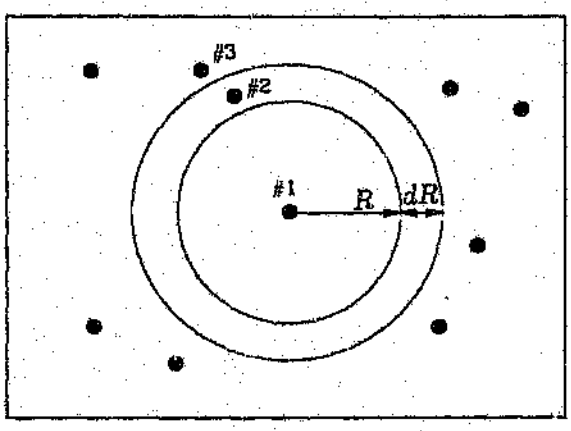


Figure B.1: A random spatial distribution of spins.

outside the sphere is

$$\begin{aligned} P(R)dR &= (N-1)\left(\frac{4\pi R^2 dR}{V}\right)\left(1-\frac{\frac{4}{3}\pi R^3}{V}\right)^{N-2} \\ &= \left(1-\frac{1}{N}\right)4\pi R^2 n\left(1-\frac{\frac{4}{3}\pi R^3 n}{N}\right)^{N-2} dR \quad . \end{aligned} \tag{B.1}$$

Considering now a bulk sample, we let $N \to \infty$ (but keep n fixed), and noting that $\lim_{N\to\infty}\left(1+\frac{x}{N}\right)^N = e^x$, we arrive at

$$P(R)dR = 4\pi R^2 n\, e^{-\frac{4}{3}\pi R^3 n} dR \quad , \tag{B.2}$$

which is the Poisson distribution we have used for the distribution of spin-pair separations.

Notice that in our models we consider *distinct* pairs of donor electrons. The Poisson distribution above does not strictly give us the distribution of distinct spin-pairs, but does give us a good approximation. In a random system such as this, there is difficulty and ambiguity in partitioning the donors into distinct nearest neighbour pairs, and to find a distribution in closed form. As an example, referring to fig. B.1, we see that donor #2 is a nearest neighbour to donor #1, but donors #1 and #2 do not form a pair because donor #3 is a nearest neighbour to donor #2. So the first problem is to find an algorithm to determine the distinct pairs, and the second problem is to find a distribution function in closed form.

B.2 The Distribution $P(J)dJ$ of Exchange Couplings J

We want to find the distribution function $P(J)$ such that $P(J)dJ$ gives us the probability of a spin-pair having a coupling J in the interval $(J, J+dJ)$. We obtain this distribution from the Poisson distribution (previous section) $P(R)$, using the Herring-Flicker [8] expression $J_{HF}(R)$ to relate the two variables J and R. The two functions are defined as follows:

$$\begin{aligned} P(R) &= 4\pi R^2 n e^{-\frac{4}{3}\pi R^3 n} \\ J_{HF}(R) &= 0.3\left(\frac{R}{a_B^*}\right)^{\frac{5}{2}} e^{-2\left(\frac{R}{a_B^*}\right)} \end{aligned} \quad , \tag{B.3}$$

where n is the concentration and a_B^* is the effective Bohr radius.

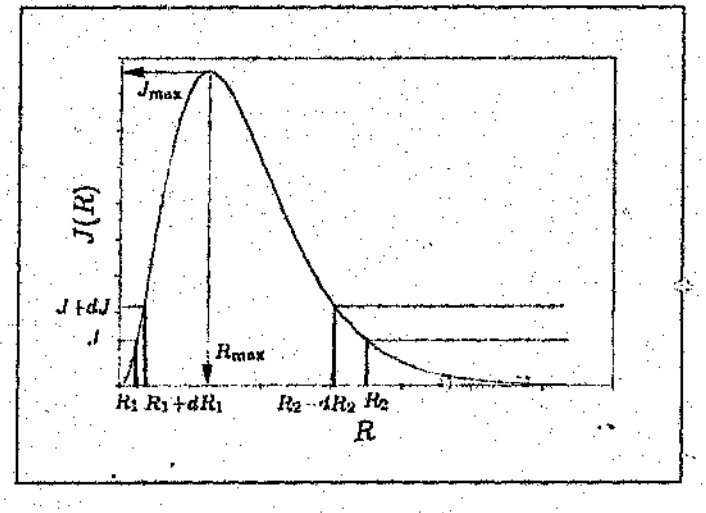


Figure B.2: Graphical aid to the determination of $P(J)$, showing a plot of the Herring-Flicker exchange coupling $J_{HF}(R)$.

Referring to fig. B.2, we proceed in the following way. Let J and dJ be fixed. We require the probability $P(J)dJ$ of a spin-pair having a coupling in the interval $(J, J+dJ)$. From fig. B.2 we can write

$$P(J)dJ = P_1 dR_1 + P_2 dR_2 \quad , \tag{B.4}$$

where $P_1 dR_1$ and $P_2 dR_2$ are the probabilities of finding a spin-pair with a separation in the interval (R_1, R_1+dR_1) and (R_2-dR_2, R_2) respectively. Note that we have two terms P_1

and P_2 corresponding to the regions below ($R_1 < R_{\max}$) and above ($R_{\max} < R_2$) the peak of $J_{HF}(R)$. For low concentrations, when the average spin-pair separation $\bar{R} \gg R_{\max}$, and the Herring-Flicker form J_{HF} becomes valid, the only region of significance will be to the right of the peak (the exponential tail), and we will then have $P(J)dJ \simeq P_2 dR_2$.

The probabilities $P_1 dR_1$ and $P_2 dR_2$ can be obtained from the Poisson distribution $P(R)$ in (B.3), and are given by

$$\begin{aligned} P_1 dR_1 &= P(R_1)dR_1 \\ P_2 dR_2 &\simeq P(R_2)dR_2 \quad . \end{aligned} \tag{B.5}$$

We can also write

$$\frac{dJ}{dR} = J'_{HF}(R) \tag{B.6}$$

and hence, noting the signs of the slopes in fig. B.2 on either sides of $R_{\max}$, we have $dJ \equiv J'_{HF}(R_1)dR_1 \equiv -J'_{HF}(R_2)dR_2$, which we can conveniently write as

$$dJ = \left|J'_{HF}(R_i)\right| dR_i \qquad for\ i = 1, 2 \quad . \tag{B.7}$$

Combining (B.4), (B.5), and (B.7) we obtain the distribution function $P(J)$:

$$P(J) = P_1(J) + P_2(J) = \frac{P(R_1)}{\left|J'_{HF}(R_1)\right|} + \frac{P(R_2)}{\left|J'_{HF}(R_2)\right|} \quad . \tag{B.8}$$

Note that R_1 and R_2 are the solutions of the equation $J = J_{HF}(R)$. However, $P(J)$ can be obtained without the need to solve this equation for each J. For this purpose we evaluate $P_1(J)$ and $P_2(J)$ separately, and parameterize each curve produced by these two functions with the parameters R_1 and R_2 :[1]

$$R_i \longmapsto \left(J_{HF}(R_i), \frac{P(R_i)}{\left|J'_{HF}(R_i)\right|}\right) = (J, P_i(J)) \qquad for\ i = 1, 2 \quad . \tag{B.9}$$

So by varying $R_1 \in [0, R_{\max}]$ and $R_2 \in [R_{\max}, \infty)$ and generating the above points $(J, P_i(J))$, we can easily obtain the functions $P_1(J)$ and $P_2(J)$, and hence the distribution function $P(J)$ from (B.8).

One point needs to be noted about eqn. (B.8) for the definition of $P(J)$. As $J \rightarrow J_{\max}$, where $J_{\max} = J_{HF}(R_{\max})$ is the maximum exchange coupling, we have $R_1, R_2 \rightarrow R_{\max}$

[1] The graph of a function $F(x)$ is the set of points $(x, F(x))$, and can be parameterized by using any map $x(t)$ onto the domain of the function F. The parameterization of the graph is the map $t \longmapsto (x(t), F(x(t)))$.

(fig. B.2). Since $J'_{HF}(R_{max}) = 0$, we see that the expression for $P(J)$ has a singularity as $J \to J_{max}$.

This singularity is integrable, and if we define the integral

$$p(J) = \int_0^J P(J)dJ \quad , \tag{B.10}$$

then we have that $p(J)$ is the probability of having $J \in [0, J]$. Hence

$$\begin{aligned} &(1) \quad p(0) = 0 \\ &(2) \quad p(J) = 1 \quad for \quad J \geq J_{max} \\ &(3) \quad p'(J) = P(J) \geq 0 \quad for \quad 0 \leq J \leq J_{max} \end{aligned} \tag{B.11}$$

and so $p(J)$ is a continuous function, increasing from $p(0) = 0$ to $p(J_{max}) = 1$, and then remaining constant for $J > J_{max}$. The form of $p(J)$ is determined in a similar fashion to determining $P(J)$. Referring to fig. B.2, the probability $p(J)$ can be written as

$$p(J) = P\left(R \in [0, R_1]\right) + P\left(R \in [R_2, \infty)\right) \quad , \tag{B.12}$$

where we use the notation $P\left(r \in [r_1, r_2]\right)$ to denote the probability of the separation $r \in [r_1, r_2]$. Using the Poisson distribution in (B.3), and noting that $P(R) = -\frac{d}{dR}e^{-\frac{4}{3}\pi R^3 n}$, we have

$$P\left(r \in [r_1, r_2]\right) = \int_{r_1}^{r_2} P(R)dR = e^{-\frac{4}{3}\pi r_1^3 n} - e^{-\frac{4}{3}\pi r_2^3 n} \quad . \tag{B.13}$$

Inserting this into (B.12), we finally arrive at

$$p(J) = 1 - e^{-\frac{4}{3}\pi R_1^3 n} + e^{-\frac{4}{3}\pi R_2^3 n} \quad , \tag{B.14}$$

where again we have $R_1 < R_{max} < R_2$ being the solutions of the equation $J_{HF}(R) = J$. The distribution function $P(J)$ is then obtained by differentiating $p(J)$, which can be evaluated numerically, or can be determined by parameterization using R_1 and R_2 as discussed for eqn. (B.8).

We can infer from the final form for $p(J)$ in (B.14), that as $J \to 0$ (referring to fig. B.2 and using $J_{HF}(R) \simeq 0.3(R/a_B^*)^{5/2}$ for $R/a_B^* \ll 1$), we have $p(J) \sim J^{6/5}$ and hence

$$P(J) \sim J^{1/5} \quad as \quad J \to 0 \quad . \tag{B.15}$$

We can also determine the average exchange coupling $\langle J \rangle = \int dJ P(J) J$, which can be written as

$$\langle J \rangle = \langle J_{HF}(R) \rangle = \int_0^\infty dR P(R) J_{HF}(R) \quad . \tag{B.16}$$

Defining $\tau = a_B^{*3} n_c$ we then have, in Rydberg units,

$$\langle J \rangle_{Ry} = 0.3 \cdot 4\pi\tau \left(\frac{n}{n_c}\right) \int_0^\infty dx\, x^{9/2}\, e^{-\frac{4}{3}\pi\tau\left(\frac{n}{n_c}\right)x^3 - 2x} \quad , \tag{B.17}$$

where $\langle J \rangle_{Ry}$ now depends only on n/n_c and τ. The quantity τ depends on the actual physical system in question[2], and for Si:P, with $a_B^* \simeq 15\mathring{A}$ and $n_c \simeq 3.5 \times 10^{18} cm^{-3}$, we have $\tau \simeq 0.0118$. Hence the average exchange coupling, in thermal (Kelvin) units, is then

$$\begin{aligned} \langle J \rangle_K &= 18.1 \left(\frac{n}{n_c}\right) \int_0^\infty dx\, x^{9/2}\, e^{-0.0494\left(\frac{n}{n_c}\right)x^3 - 2x} \\ &= I(n/n_c) \times \left(\frac{n}{n_c}\right) \quad , \end{aligned} \tag{B.18}$$

where the function $I(n/n_c)$ is plotted in fig. B.3, for $0 \leq n/n_c \leq 1$.

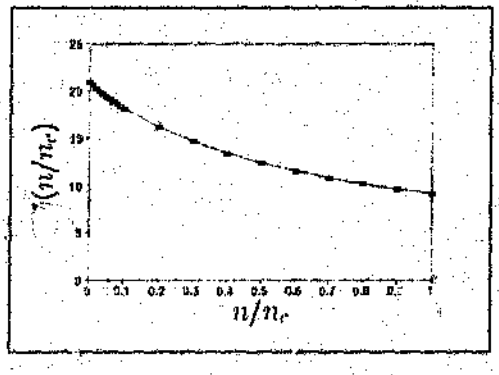


Figure B.3: A plot of the factor $I(n/n_c)$ appearing in expression (B.18), which was evaluated numerically.

So for $n/n_c \leq 1$, we have

$$\langle J \rangle_K \sim 10 \left(\frac{n}{n_c}\right) \quad . \tag{B.19}$$

[2]For an arbitrary physical system we could use the Mott criterion, which gives a good relationship between a_B^* and n_c for a large number of MI systems. The Mott criterion is $a_B^* \cdot n_c^{1/3} \simeq 0.25$. We then have a fixed value of $\tau \simeq 0.0156$.

B.3 Numerical Procedures

We use Simpson's rule for evaluating our integrals numerically, and the formula used for approximating definite integrals is given by

$$\int_a^b dx\ f(x) \simeq \frac{b-a}{6n}\left\{f(a)+f(b)+2\sum_{k=1}^{n-1} f(x_k)+4\sum_{k=0}^{n-1} f(\frac{x_k+x_{k+1}}{2})\right\} \quad , \qquad \text{(B.20)}$$

which is well suited for computer programming. Here n is the number of partitions of the interval $[a,b]$, while $x_k = a + k\cdot\Delta x$, with $\Delta x = (b-a)/n$ being the width of a partition.

We need to choose the parameters a, b, and n. For our purpose, referring to (2.18), (2.20), and (2.23), we have $a = 0$ and $b = \infty$, but since the integrands vanish exponentially for large arguments, we can choose b to be finite. Plots of the arguments in the various integrals indicate that we can choose $b \sim 25$ to obtain sufficient accuracy, while the number of partitions per unit interval was chosen to be $N_p = 5$ (with $n = N_p(b-a) \sim 125$).

Appendix C

Mathematical Details for the Extended Two-Fluid Model

C.1 Evaluation of the Integrals $I_\delta(y)$ and $I_\varepsilon(y)$

To use the extended two-fluid equations we need only evaluate the factors $\delta(y)$ and $\varepsilon(y)$. From the definitions of $\delta(y)$ and $\varepsilon(y)$, given in eqns. (3.22) and (3.25), we see that we have to evaluate the integrals $I_\delta(y)$ and $I_\varepsilon(y)$ which were defined in §3.1 of chapter 3 (eqns. (3.14) and (3.15)) and are given by

$$\begin{aligned} I_\delta(y) &= \int_0^{X_m} dx\, x^{-\alpha} F_C(x,y) \\ I_\varepsilon(y) &= \int_0^{X_m} dx\, x^{-\alpha} F_\chi(x,y) \quad . \end{aligned} \tag{C.1}$$

Both these integrals have to be evaluated numerically. This appendix looks at the techniques and assumptions used to determine the forms of the above two integrals. Note that we have defined $y = g\mu_B B/k_B T$ and $x = J/k_B T$. The functions $F_C(x,y)$ and $F_\chi(x,y)$ are defined in (3.6) and (3.8).

Our first concern is the upper limit X_m in the integral. It is defined as

$$X_m = \beta J_m = \frac{j_m}{T} \quad , \tag{C.2}$$

where $j_m = J_m/k_B$ is an upper cutoff for the exchange coupling. (We have used the lowercase j to convert the exchange coupling into thermal units.) j_m is unknown here but reference [7] gives us some indications as to its magnitude. A conservative lowerbound is

around 2 K and so we can safely expect that $j_m > 2K$. However, an upper cutoff of $j_m \simeq 150K$ is also found to produce results which are consistent with experimental res Sarachik *et al.*[15] also specify an upper cutoff of $j_m = 500\ K$, while Andres *et al.*[14] claim that a relevant fraction of donor pairs are coupled with exchange couplings larger than $4.2K$. So we can expect that at least $j_m \gg 1K$. Now, the temperature range that we a terested in is around 1K. The experimental data of Si:P showing the properties of interest near the M-I transition are in the temperature range $(10mK, 3K)$. For the specific heat, for example, the phonon contribution (which goes as T^3) completely overshadows the electronic contribution for $T \gtrsim 3K$. So, for our purposes, since $T \leq 3K$, we have

$$T \ll j_m \quad \Longrightarrow \quad X_m = \frac{j_m}{T} \gg 1 \quad . \tag{C.3}$$

As shown in the next section, both the functions $F_C(x,y)$ and $F_\chi(x,y)$ decay exponentially to zero as x tends to infinity i.e. $F(x,y) \sim e^{-x}$, $x \to \infty$. We can therefore extend the integrals to infinity and be assured of convergence, and hence we can take

$$\begin{aligned} I_\delta(y) &= \int_0^\infty dx\, x^{-\alpha} F_C(x,y) \\ I_\varepsilon(y) &= \int_0^\infty dx\, x^{-\alpha} F_\chi(x,y) \end{aligned} \tag{C.4}$$

and approximate the finite integrals in (C.1) by the infinite integrals in (C.4) above. The reason for doing this is that we eliminate one unknown parameter j_m, and the terms $I_\delta(y)$ and $I_\varepsilon(y)$ then depend on the temperature only through the term $y = g\mu_B B/k_B T \simeq 1.34\frac{B}{T}$. However, one more condition has to be considered when using (C.4) to approximate (C.1). The contribution of the integrands on the interval $[X_m, \infty)$ must obviously be negligible. As will be shown in §C.5, this will be true if we have $y \ll X_m$. So the condition

$$g\mu_B B \ll J_m \quad \Longrightarrow \quad B[T] \ll j_m[K] \tag{C.5}$$

will allow for the use of eqns. (C.4). The magnetic fields used in experiments is at most several Teslas, so, if we have that $j_m \gg 1K$, which we expect and as was assumed to get condition (C.3), then condition (C.5) will also be valid. So the use of conditions (C.3) and (C.5) both depend on the magnitude of the maximum exchange coupling j_m. We shall assume that both conditions hold, and that (C.4) correctly gives us the terms $I_\delta(y)$ and $I_\varepsilon(y)$. The case when these conditions do not hold, and we have to use (C.1), is considered in §C.6, where we introduce corrections to be made when the two conditions break down. In that section we also quantify the inequalities (C.3) and (C.5) to some extent.

For later reference, we consider the terms $I_1 = I_\delta(0)$ and $I_2 = I_\varepsilon(o)$ (defined in (3.22) and (3.25)). Using (C.4) above, we have that

$$\begin{aligned} I_1 &= I_\delta(0) = \int_0^\infty dx\, x^{-\alpha} \frac{3x^2 e^{-x}}{(1+3e^{-x})^2} \\ I_2 &= I_\varepsilon(0) = \int_0^\infty dx\, x^{-\alpha} \frac{e^{-x}}{(1+3e^{-x})} \end{aligned} \quad , \tag{C.6}$$

where we have used the fact that $\sinh(y)/y \to 1$ as $y \to 0$ for I_2. Both integrals depend only on the parameter α. Plots of both I_1 and I_2 for $\alpha \in [0,1]$ are shown in fig. C.1.

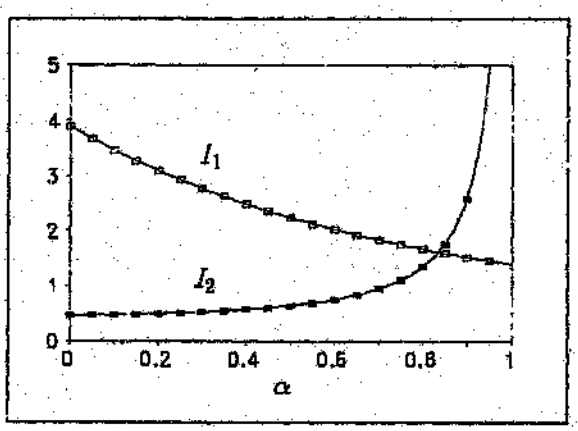


Figure C.1: A plot of the terms I_1 and I_2.

The curves drawn through the points are rational approximations, so as to eliminate the need to continually have to evaluate the above integrals numerically, and are given by

$$\begin{aligned} I_1 &\simeq 3.876 - 4.47\alpha + 2.74\alpha^2 - 0.77\alpha^3 \\ I_2 &\simeq \frac{0.462 - 0.391\alpha + 0.219\alpha^2 - 0.041\alpha^3}{1-\alpha} \end{aligned} \quad . \tag{C.7}$$

Both the integrals $I_\delta(y)$ and $I_\varepsilon(y)$ are evaluated numerically using Simpson's method for numerical integration (§C.3). However, two points have to be considered when evaluating these integrals numerically.

Firstly, the term $x^{-\alpha}$, which comes from the distribution of exchange couplings in (3.11), has a singularity at $x = 0$. Although this singularity is integrable, since $0 < \alpha < 1$

(§C.7), we have to consider the form of $F_C(x,y)$ and $F_\chi(x,y)$ for $x \to 0^+$ which is given by

$$\begin{aligned} \lim_{x\to 0} F_C(x,y) &= \frac{y^2}{(1+2\cosh y)} \\ \lim_{x\to 0} F_\chi(x,y) &= \frac{\sinh y}{y}\frac{1}{2(1+\cosh y)} \end{aligned} \quad . \tag{C.8}$$

So we can see, except for $F_C(x,y)$ at $y=0$, the integrands in both $I_\delta(y)$ and $I_\epsilon(y)$ have singularities at $x=0$. These singularities are integrable but precision problems arise with numerical integration, which does not enable us to evaluate these singularities. We use Simpson's rule for integration, which would require one to evaluate the integrand at $x=0$ (which is not possible). We can overcome this problem by not integrating from $x=0$, but from some arbitrary positive number, which must be chosen sufficiently small so as not to loose accuracy, and adds more complexity to the evaluation. Instead, we can convert the improper integral to a proper integral with no singularities present. This conversion is shown in more detail in §C.4.

Secondly, integration to infinity has to be considered when using numerical methods. Since the integrands decay exponentially to zero as x tends to infinity, it is possible to choose a finite upper limit for the integral so as to approximate the integration to infinity with negligible error. The derivation of a suitable upper limit U is shown in §C.5, and is found to be

$$U = M + y \;\; ; \;\; M \gtrsim 12 \quad . \tag{C.9}$$

In our analysis we choose $M=12$ to make the interval of integration as small as possible to increase the speed of calculations. It is of interest to look at the physical significance of this upper limit U. The contribution to the integrals for values of x larger than $M+y$ is negligible and this corresponds to the spin pairs that are frozen in the singlet state and do not contribute to the thermodynamic properties. This can easily be seen by substituting the definitions of x and y. The condition $x > U = M + y$ is then $\beta J > M + \beta g\mu_B B$. Multiplying through by $k_B T = 1/\beta$, we arrive at the inequality

$$J - g\mu_B B > M\,kT \tag{C.10}$$

and, by noting that the term on the left is just the first excitation energy of a spin pair with exchange coupling J (fig. 2.2), we see that the condition shows insufficient thermal energy for excitation and the spin remains in its ground state (frozen in the singlet state).

Therefore, for the evaluation of $\delta(y)$ and $\epsilon(y)$, we have the following expressions which are then evaluated numerically (§C.3):

$$\begin{aligned} I_\delta(y) &= \int_0^{M+y} dx\, x^{-\alpha} F_C(x,y) \\ I_\epsilon(y) &= \int_0^{M+y} dx\, x^{-\alpha} F_\chi(x,y) \quad . \end{aligned} \tag{C.11}$$

C.2 Extending Integrals to Infinity

The two integrals in (C.1) are both of the form

$$\int dx\, x^{-\alpha}\, f(x,y) \quad . \tag{C.12}$$

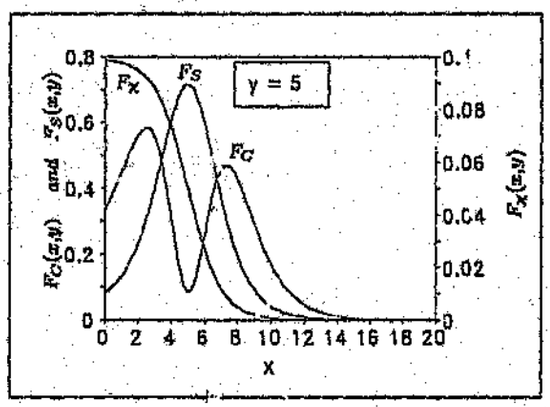


Figure C.2: Plots of the integrands $F_C(x,y)$, $F_\chi(x,y)$, and $F_S(x,y)$ to show the exponentially decaying tails.

Figure C.2 is a plot of $f(x,y)$ representing $F_C(x,y)$ and $F_\chi(x,y)$. (Note the scale change for $F_\chi(x,y)$.) We have also introduced the term $F_S(x,y)$ for completeness, which is the function used in the evaluation of the entropy. The functions $F_C(x,y)$ and $F_\chi(x,y)$, defined in (3.6) and (3.8), can be expressed as

$$\begin{aligned} F_C(x,y) &= \left(\frac{(x-y)^2 e^y + (x+y)^2 e^{-y} + x^2 + y^2(4+2\cosh(y))e^{-x}}{(1+(1+2\cosh(y))e^{-x})^2} \right) e^{-x} \\ F_\chi(x,y) &= \left(\frac{\sinh(y)}{y} \frac{1}{(1+(1+2\cosh(y))e^{-x})} \right) e^{-x} \end{aligned} \tag{C.13}$$

and so we can see that, for a fixed value of y, both functions decay exponentially with $x \to \infty$. This behaviour can also clearly be seen in fig. C.2. Hence we have that the integral to infinity does converge and, due to the exponential factor, we can also choose a finite upper limit, with a negligible error in the results. An analysis on a proper choice for a finite upper limit is done in §C.5.

C.3 Numerical Integration

We use Simpson's rule for approximating the integral. The reason for this is that the functions $F_C(x,y)$ and $F_\chi(x,y)$ are both smooth (continuously differentiable) and therefore ideally suited to the quadratic approximations used in Simpson's method. The formula used for approximating definite integrals

$$\int_a^b dx\, f(x) \simeq \frac{b-a}{6n}\left\{f(a)+f(b)+2\sum_{k=1}^{n-1} f(x_k)+4\sum_{k=0}^{n-1} f(\frac{x_k+x_{k+1}}{2})\right\} \quad , \qquad \text{(C.14)}$$

which is a formula well suited for computer programming. Here n is the number of partitions of the interval $[a,b]$, which obviously determines the accuracy of the formula, while $x_k = a + k\cdot\Delta x$, with $\Delta x = (b-a)/n$ being the width of a partition on which we use a quadratic approximation.

The only parameter we need to choose is the number of partitions n. It should be chosen as large as possible to improve accuracy, but also small enough to increase the speed of computations. Several calculations were made by varying n to find a sufficiently small value and still maintain the required accuracy. We found it sufficient to choose the number of partitions per unit interval as $N_p = 25$, where we then have $n = (b-a)\cdot N_p$, depending only on the limits of integration, which, as we shall see in §C.5, is not fixed, and was chosen to depend on the variable y.

C.4 Improper to Proper Integral Conversion

We are interested in converting an improper integral of the form

$$\int_0^{X_m} dx\, x^{-\alpha}\, f(x,y) \qquad \text{(C.15)}$$

to a proper integral which is easier to handle numerically. Since the function $f(x,y)$ is smooth ($f'(x,y) = \frac{\partial}{\partial x} f(x,y)$ is continuous), and since

$$g'(x) = \frac{d}{dx}\left(\frac{x^{1-\alpha}}{1-\alpha}\right) = x^{-\alpha} \quad , \tag{C.16}$$

we can use integration by parts: $\int g'(x) f(x) dx = g(x) f(x) - \int g(x) f'(x) dx$.

Hence, using (C.16), we have

$$\int dx\, x^{-\alpha}\, f(x,y) = \frac{x^{1-\alpha} f(x,y)}{1-\alpha} - \int dx\, \frac{x^{1-\alpha}}{1-\alpha}\, f'(x,y) \tag{C.17}$$

and, since the integrand in the integral on the right hand side has no singularities, we are left with the evaluation of a proper integral. Finally, inserting the limits of integration, we have

$$\int_0^{X_m} dx\, x^{-\alpha}\, f(x,y) = \frac{X_m^{1-\alpha} f(X_m,y)}{1-\alpha} - \int_0^{X_m} dx\, \frac{x^{1-\alpha}}{1-\alpha}\, f'(x,y) \quad . \tag{C.18}$$

Also, assuming that $f(x,y)$ decays exponentially with x for sufficiently large values (as does $F_C(x,y)$ and $F_\chi(x,y)$ shown in (C.13)), letting $X_m \to \infty$ we obtain

$$\int_0^{\infty} dx\, x^{-\alpha}\, f(x,y) = -\int_0^{\infty} dx\, \frac{x^{1-\alpha}}{1-\alpha}\, f'(x,y) \quad . \tag{C.19}$$

C.5 Upper Limit Analysis

Next we consider the choice for a proper finite upper limit to be able to evaluate numerically the integral (C.4). As mentioned earlier, we can do this since the integrand converges exponentially to zero and, by choosing this upper cutoff sufficiently large, we will have a negligible error in the numerical calculations. An alternative way would be to have a change of variable which will biject the interval $[0,\infty)$ onto a finite interval (e.g. $x = \tan(t)$). This procedure would however require one to be very careful in choosing the partition size used in the numerical integration. With a finite upper limit we can fix this partition size to simplify calculation procedures.

The purpose, therefore, is to find an upper limit U so that

$$\int_0^{U} dx\, x^{-\alpha}\, f(x,y) \simeq \int_0^{\infty} dx\, x^{-\alpha}\, f(x,y) \quad , \tag{C.20}$$

where $f(x,y)$ represents either $F_C(x,y)$, $F_\chi(x,y)$, or $F_S(x,y)$, corresponding respectively to the specific heat, susceptibility, and entropy.

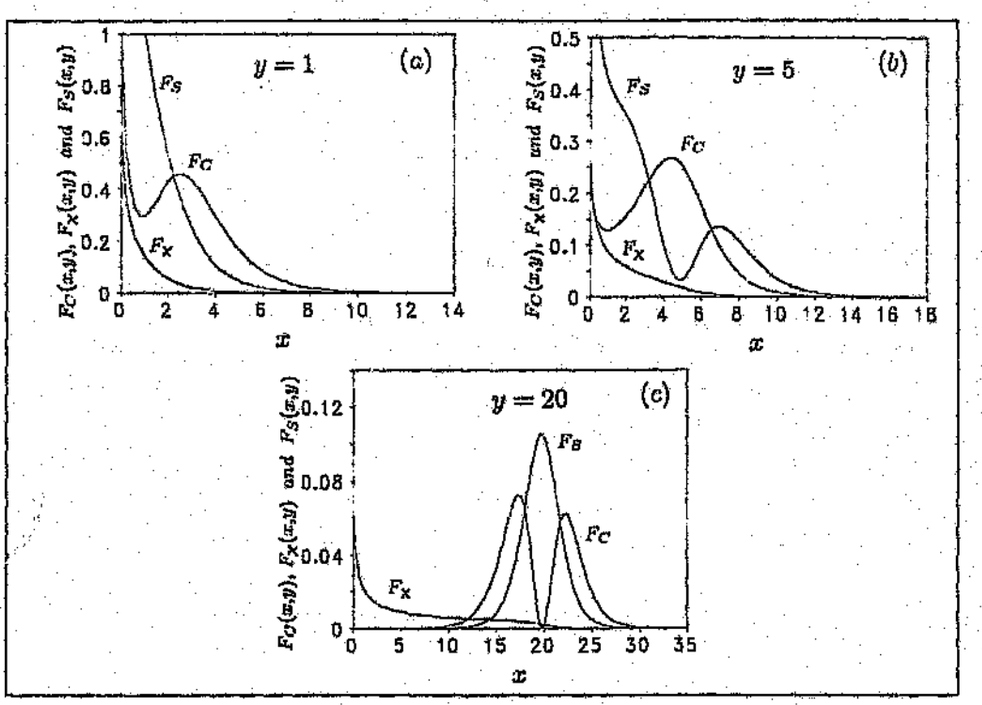


Figure C.3: Plots of the integrands $F_C(x,y)$, $F_\chi(x,y)$, and $F_S(x,y)$, for various values of y, to determine a suitable upper cutoff for the integration.

Figures C.3a, C.3b, and C.3c show plots of the integrand in the integral (C.20) for various values of the parameter y. The values $y = 1$, 5, and 20 were chosen arbitrarily to show the behaviour of the integrands with this parameter. We can clearly see a shift to the right in the features as y is increased. Observation of these three plots, and plots for several other values of y not shown, indicate that an upper cutoff for integration can be chosen as

$$U = M + y \quad , \tag{C.21}$$

where $M \gtrsim 12$. We choose $M = 12$ to minimize the interval and increase calculation speed.

From the above three plots, we can also see the need for condition (C.5) introduced in §C.1. The features of the integrands (where the integrands have non-negligible contributions) move to increasing x as y is increased. In particular, the dominant contributions for the specific heat and entropy are in a neighbourhood of $x = y$. So, for the integrands to have a negligible contribution in the interval $[X_{m_1}, \infty)$ so as to use expressions (C.4) to

approximate (C.1), we clearly need $X_m \gg y$.

Although this graphical analysis to find U appears to provide us with a useful upper limit, it would be more satisfying to be able to have some analytical way to quantify U. There is, and using some results from statistical mechanics, we can relate the forms of the functions shown in figs. C.3a to C.3c to physical principles. Since the integration is basically a sum of the contributions of all the spin-pairs for all possible exchange couplings, we can clearly note that the negligible parts of the integral correspond to those spin-pairs that do not contribute to the thermodynamic properties. These spin-pairs are essentially frozen in their ground state. To find the frozen pairs we can use the partition function of a spin-pair.

The energy levels of a spin-pair with exchange coupling J, in a magnetic field B, are shown in fig. C.4.

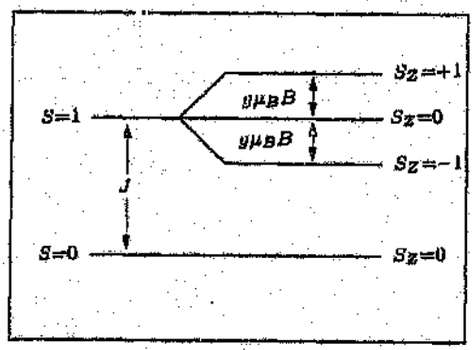


Figure C.4: Spin-pair energy levels.

The partition function (App. A.1) is given by

$$Z = 1 + e^{-x}\,(1 + 2\cosh(y)) \quad , \tag{C.22}$$

where $x = \beta J$ and $y = \beta g \mu_B B$. It is a standard result from statistical mechanics (eqn. (A.2)) that the probability of a given state being occupied is $e^{-\beta E}/Z$, with E being the energy of that state. So the probability of the ground state being occupied is

$$\frac{N_0}{N} = \frac{1}{Z} \quad , \tag{C.23}$$

where N_0/N is the fraction of spin-pairs in the singlet ground state. It should be noted that we are assuming $J > g\mu_B B$ (i.e. $x > y$) so that the singlet state is the ground state of

the pair. We focus on this case since we want to find an upper limit to the integration. In other words, we want to know how large x must be, and hence how large J should be, for the contributions to be negligible. So we want to find a condition for J which will enable us to regard the spin-pair as frozen in the ground state. The case when $J < g\mu_B B$ (i.e. $x < y$) will be mentioned at the end of this section. Fig. C.5 is a plot of $1/Z$ versus x, giving us an indication as to the probability of the singlet state being occupied for various exchange couplings. We can clearly see the freezing out into the singlet ground state for large couplings (large x-values, $x > y$) and also the vanishing probability at the low couplings (low x-values, $x < y$) where the triplet state crosses the singlet state to become the ground state.

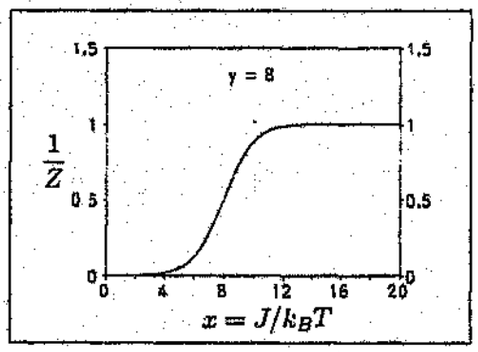


Figure C.5: A plot of $1/Z$ versus x, giving the probability of the singlet state of the spin-pair being occupied.

Using eqn. (C.23), we then have that the probability of the spin-pair being excited is $1 - \frac{1}{Z}$. Choosing an arbitrarily small number $\varepsilon > 0$, we can write the condition for a spin-pair to be frozen as

$$1 - \frac{1}{Z} < \varepsilon \quad . \tag{C.24}$$

This means that, if the probability of the pair being excited is less than ε, then we regard the spin-pair as being frozen in its ground state. The choice of ε will obviously depend on the required accuracy and also on the magnitude of the dominant contributions from unfrozen pairs to the thermodynamic quantities. We also need to consider the distribution function for the J-values. If the number of frozen pairs is much larger than the number of unfrozen pairs, then these frozen pairs could have a significant contribution to the proper-

ties. However, for any distribution function which decreases with J (such as the Bhatt-Lee distribution), this point need not be taken up for the large J coupled pairs.

Rewriting (C.24) as $Z < 1/(1-\varepsilon)$ and using the approximation $(1-\varepsilon)^{-1} \simeq 1+\varepsilon$ for $|\varepsilon| \ll 1$, we obtain the condition

$$Z < 1+\varepsilon \quad . \tag{C.25}$$

Inserting (C.22) for Z, we obtain the requirement that

$$e^x > \frac{1+2\cosh(y)}{\varepsilon} \quad . \tag{C.26}$$

So our condition is satisfied for $x > U$, where

$$U = \ln\left(\frac{1}{\varepsilon}\right) + \ln\left(1+2\cosh(y)\right) \quad . \tag{C.27}$$

Noting that $1+2\cosh(y) \leq 3e^y$ for each $y \geq 0$, we have that $\ln(1+2\cosh(y)) \leq \ln(3)+y$. We can clearly increase U for condition (C.26) to remain satisfied, and, by using this inequality, we can change the cutoff value (C.27) to the simpler expression

$$U = \ln\left(\frac{3}{\varepsilon}\right) + y \quad . \tag{C.28}$$

This expression is identical to (C.21) obtained from the graphical analysis. The term ΛI corresponds to the term $\ln(3/\varepsilon)$. For our choice of $M = 12$, we find that $\varepsilon = 1.8 \cdot 10^{-5}$ for the cutoff probability, i.e. a less than 0.0018 % chance of being excited defines our frozen pairs.

Equation (C.28) provides an upper cutoff to the summation over exchange couplings J. We could do a similar analysis for a lower cutoff corresponding to the case when $J < g\mu_B B$ (i.e. $x < y$) and finding the spin-pairs that are frozen in the ground state, which in this case is a triplet state. However, since the triplet state is a magnetic state, these frozen spin-pairs will have a significant contribution to the magnetization, and hence cannot be neglected in the summation. The contribution to the specific heat will vanish for these frozen spin-pairs. These points can be clearly seen by looking at fig. C.3c, which shows the integrand for a large y-value (large B-field). Notice the vanishing specific heat contribution and the major susceptibility contribution at the lower values of x (i.e. lower J-values). So, for the specific heat, we could choose a non-zero lower cutoff for the summation, which could be found in the same way as the upper cutoff, but for the susceptibility we

have to keep the lower cutoff at $x = 0$. However, it was chosen to keep the lower cutoff fixed at $x = 0$, so as to generalize the integration process for all the thermodynamic quantities. The main problem, handling the integration to infinity by finding an upper cutoff, is solved by the use of eqn. (C.28).

C.6 Details of the Corrections to the Extended Two-Fluid Equations

We now consider the required corrections that have to be made when the conditions

$$T \ll j_m \quad and \quad g\mu_B B \ll J_m = k_B j_m \tag{C.29}$$

given in (C.3) and (C.5) are not satisfied. These two conditions were used to extend our integrals to infinity and simplify the form of the equations. If the conditions do not hold, then we have to use the equations

$$\begin{aligned} I_\delta^*(y) &= \int_0^{X_m} dx\, x^{-\alpha}\, F_C(x,y) \\ I_\varepsilon^*(y) &= \int_0^{X_m} dx\, x^{-\alpha}\, F_\chi(x,y) \quad , \end{aligned} \tag{C.30}$$

where $X_m = \beta J_m = j_m/T$ is now considered as finite. We have used the "starred" variables $I_\delta^*(y)$ and $I_\varepsilon^*(y)$ to represent the original, correct functions in (C.1). The "unstarred" variables will represent the integrals to infinity, $I_\delta(y)$ and $I_\varepsilon(y)$, which we have already considered in the previous sections. Using the integral identity

$$\int_0^{X_m} f(x)dx = \int_0^{\infty} f(x)dx - \int_{X_m}^{\infty} f(x)dx \quad , \tag{C.31}$$

we can rewrite (C.30) in the form

$$\begin{aligned} I_\delta^*(y) &= \int_0^{\infty} dx\, x^{-\alpha}\, F_C(x,y) + \Delta_3 = I_\delta(y) + \Delta_3 \\ I_\varepsilon^*(y) &= \int_0^{\infty} dx\, x^{-\alpha}\, F_\chi(x,y) + \Delta_4 = I_\varepsilon(y) + \Delta_4 \quad , \end{aligned} \tag{C.32}$$

where

$$\Delta_3 = -\int_{X_m}^{\infty} dx\, x^{-\alpha}\, F_C(x,y) \tag{C.33}$$

$$\Delta_4 = -\int_{X_m}^{\infty} dx\, x^{-\alpha}\, F_\chi(x,y) \tag{C.34}$$

are respectively the corrections to the integrals $I_\delta(y)$ and $I_\varepsilon(y)$.

The extended two-fluid equations, given by (3.29) and (3.30), are

$$\begin{aligned} \frac{\gamma}{\gamma_0} &= \frac{m^*}{m_0^*} + \delta(y)\left(\frac{T}{T_0}\right)^{-\alpha} \\ \frac{\chi}{\chi_0} &= \frac{m^*}{m_0^*} + \varepsilon(y)\left(\frac{T}{T_0}\right)^{-\alpha} \end{aligned} \quad . \tag{C.35}$$

Using (3.22), (3.23), (3.25) and (3.26), we can write

$$\begin{aligned} \delta(y)\left(\frac{1}{T_0}\right)^{-\alpha} &= \left[\frac{\kappa k_B^{1-\alpha} T_f}{\pi^2}\frac{n_e}{n}\right] I_\delta(y) \\ \varepsilon(y)\left(\frac{1}{T_0}\right)^{-\alpha} &= \left[\frac{2}{3}\pi^2 g^2 \frac{\kappa k_B^{1-\alpha} T_f}{\pi^2}\frac{n_e}{n}\right] I_\varepsilon(y) \end{aligned} \quad . \tag{C.36}$$

The above equations, (C.35) and (C.36), are obtained when using the conditions (C.29). To take into account the correction, we need only replace the integrals $I_\delta(y)$ and $I_\varepsilon(y)$ by the integrals $I_\delta^*(y)$ and $I_\varepsilon^*(y)$. Using (C.32) and the definition for T_0 and β_0 in (3.23) and (3.26), we can obtain the correction by the following transformation:

$$\begin{aligned} \delta(y)\left(\frac{1}{T_0}\right)^{-\alpha} &\longrightarrow \delta(y)\left(\frac{1}{T_0}\right)^{-\alpha} + \frac{\Delta_3}{I_1}\left(\frac{1}{T_0}\right)^{-\alpha} \\ \varepsilon(y)\left(\frac{1}{T_0}\right)^{-\alpha} &\longrightarrow \varepsilon(y)\left(\frac{1}{T_0}\right)^{-\alpha} + \beta_0\frac{\Delta_4}{I_2}\left(\frac{1}{T_0}\right)^{-\alpha} \end{aligned} \quad . \tag{C.37}$$

Hence the corrected extended two-fluid model equations are then given by

$$\begin{aligned} \frac{\gamma}{\gamma_0} &= \frac{m^*}{m_0^*} + [\delta(y) + \Delta_\delta]\left(\frac{T}{T_0}\right)^{-\alpha} \\ \frac{\chi}{\chi_0} &= \frac{m^*}{m_0^*} + [\varepsilon(y) + \Delta_\varepsilon]\left(\frac{T}{T_0}\right)^{-\alpha} \end{aligned} \quad , \tag{C.38}$$

where

$$\begin{aligned} \Delta_\delta &= \frac{\Delta_3}{I_1} = -\frac{1}{I_1}\int_{x_m}^{\infty} dx\, x^{-\alpha} F_C(x,y) \\ \Delta_\varepsilon &= \beta_0\frac{\Delta_4}{I_2} = -\frac{\beta_0}{I_2}\int_{x_m}^{\infty} dx\, x^{-\alpha} F_\chi(x,y) \end{aligned} \tag{C.39}$$

are respectively the corrections to the factors $\delta(y)$ and $\varepsilon(y)$. As will be shown, these corrections Δ_δ and Δ_ε vanish when the conditions in (C.29) are satisfied, reducing the corrected equations (C.38) to their original form (C.35). We will also quantify the conditions in (C.29) to some extent.

Next, we look at the forms of Δ_δ and Δ_ε in more detail, and we can find some interesting general features of these functions. Since $\beta_0 = \left(\frac{2}{3}\pi^2 g^2\right)(I_2/I_1)$, $X_m = J_m/k_B T$ and $y = g\mu_B B/k_B T \simeq 1.34B/T$, we can write the full expressions for Δ_δ and Δ_ε:

$$\begin{aligned} \Delta_\delta &= \Delta_\delta(T,B,j_m) = -\frac{1}{I_1}\int_{j_m/T}^{\infty} dx\, x^{-\alpha}\, F_C(x, 1.34B/T) \\ \Delta_\varepsilon &= \Delta_\varepsilon(T,B,j_m) = -\frac{2}{3}\pi^2 g^2 \frac{1}{I_1}\int_{j_m/T}^{\infty} dx\, x^{-\alpha}\, F_\chi(x, 1.34B/T) \quad . \end{aligned} \tag{C.40}$$

The approximation in (C.7) can be used for I_1, while F_C and F_χ are shown in (C.13).

First, we shall look at the correction Δ_δ to $\delta(y)$. Figs. C.6a to C.6c show plots of Δ_δ versus the temperature T for various magnetic fields. Each plot corresponds to a different value of j_m, shown in the corner of each plot.

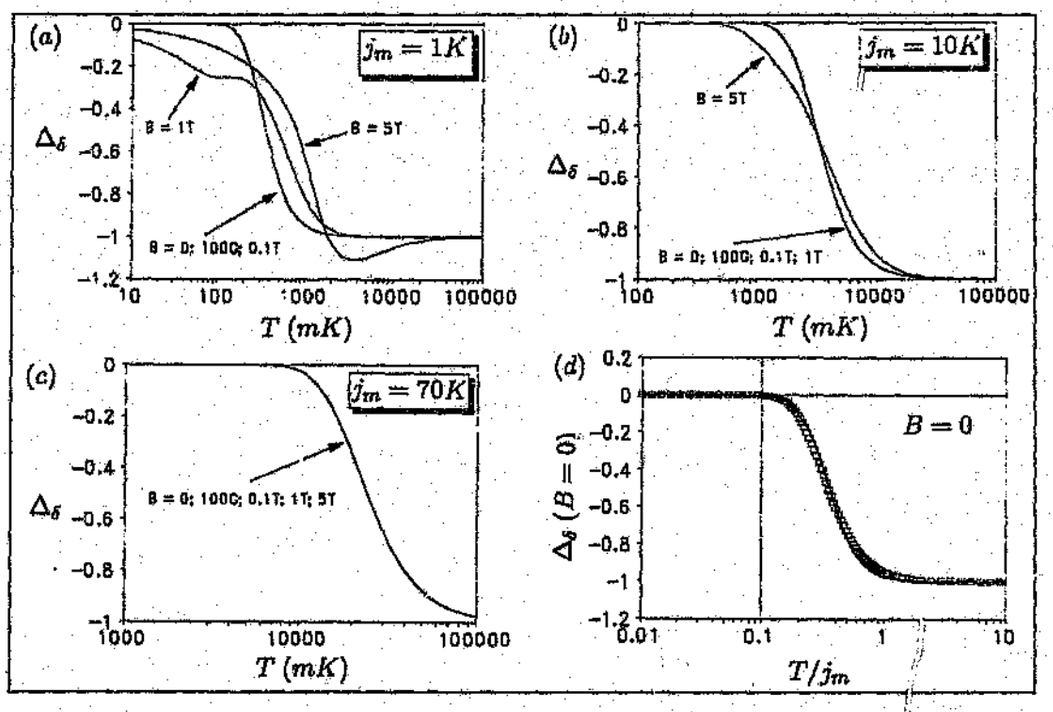


Figure C.6: Plots of the correction function Δ_δ.

Several properties of the correction Δ_δ can be obtained from these graphs:

1. The temperatures at which the correction vanishes ($\Delta_\delta \equiv 0$) are the temperatures for which we can use the uncorrected equations given in (C.35). Notice that this

temperature is B-field dependent. The origin of the conditions in (C.29) can also be inferred from these plots.

2. For increasing magnetic fields, the temperature at which the correction has to be taken into account ($\Delta_\delta \neq 0$) decreases (depending, of course, also on the parameter j_m). This leads to the restriction of the magnitude of the magnetic field B when using the uncorrected equations, as indicated in (C.29).

3. For the low magnetic fields, it can be clearly seen that the curves are indistinguishable from the zero-field curve. So, for low magnetic fields we can use the zero-field correction, which has a simpler expression and easier to work with. Looking at the three plots, we can use this zero-field correction when

$$B < \frac{1}{10} j_m \quad . \tag{C.41}$$

4. The zero-field correction is obtained from (C.40),

$$\Delta_\delta (T, B = 0, j_m) = \Delta_\delta \left(\frac{T}{j_m} \right) = -\frac{1}{I_1} \int_{j_m/T}^{\infty} dx \, x^{-\alpha} \, F_C(x, 0) \quad , \tag{C.42}$$

and is a function of only T/j_m. Fig. C.6d shows a plot of this zero-field correction versus T/j_m. The curve in the plot is a simple analytical approximation given by

$$\Delta_\delta \simeq \frac{-1}{1 + 0.0245 \, (T/j_m)^{-3.62}} \quad , \tag{C.43}$$

which can be used to find the effects of taking the correction into account. From fig. C.6d we can see that the correction becomes negligible for

$$\frac{T}{j_m} < 0.1 \quad . \tag{C.44}$$

Combining the conditions given in (C.41) and (C.44), it can be seen that we can ignore corrections due to the finite size of j_m when we have

$$B < \frac{1}{10} j_m \quad \textit{and} \quad T < \frac{1}{10} j_m \quad . \tag{C.45}$$

This gives us a quantitative form for the conditions in (C

Next, we look at the correction Δ_ε to the term $\varepsilon(y)$. Figs. C.7a to C.7c show plots of Δ_ε versus the temperature T for various values of B and j_m. Fig. C.7d shows the

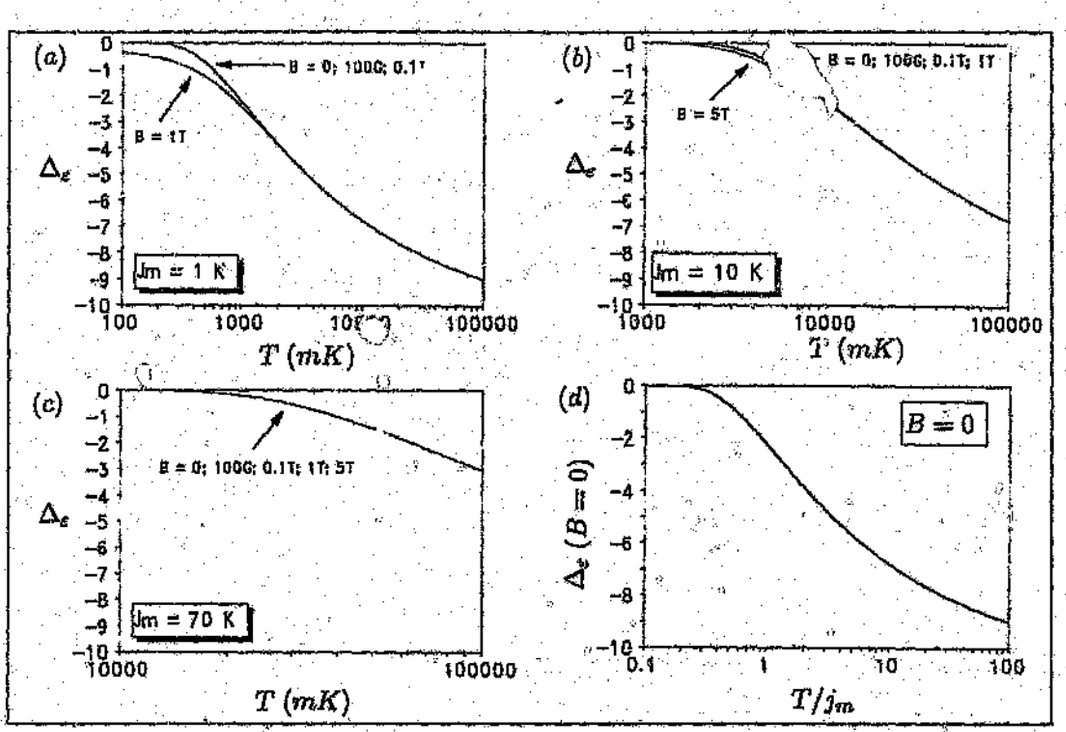


Figure C.7: Plots of the correction function Δ_e.

zero-field correction, plotted as a function of T/j_m. From the graphs it can be seen that the conclusions regarding Δ_j also hold for Δ_e. (See points 1 to 4.)

It should be noted that we have fixed $\alpha = 0.63$ in this section, which is the expected value close to the metal-insulator transition. Fig. C.8 shows the zero-field correction for various values of α. As can be seen, there is not much variation in changing the value of α, and the use of $\alpha = 0.63$ should be sufficient to give us a first order indication as to the effect of using the correction.

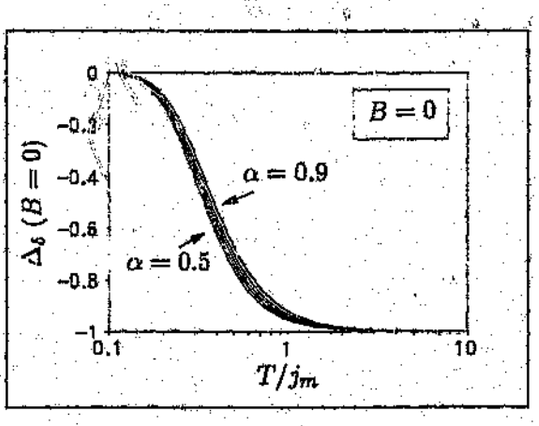


Figure C.8: The dependence of the zero-field correction Δ_δ on the parameter α.

C.7 Limits on α in the Extended Two-Fluid Model Formalism

The foundation of the extended two-fluid model is the distribution of exchange couplings

$$P(J)dJ = \kappa J^{-\alpha} \quad , \tag{C.46}$$

where κ is a normalization constant and α a parameter describing the distribution. The normalization constant κ cannot just be considered as an arbitrary fixed constant, since it will explicitly depend on the range of exchange couplings chosen in the formalism. This choice will also determine the allowed values α can assume.

We can write the normalization condition as

$$\int_{J_{\min}}^{J_{\max}} P(J)dJ = \kappa \int_{J_{\min}}^{J_{\max}} J^{-\alpha}dJ = 1 \quad , \tag{C.47}$$

where $J_{\min}$ and $J_{\max}$ are respectively lower and upper bounds for the range of exchange couplings considered. Hence

$$\kappa^{-1} = \int_{J_{\min}}^{J_{\max}} J^{-\alpha}dJ = \left\{ \begin{array}{ll} \dfrac{1}{1-\alpha}\left(J_{\max}^{1-\alpha} - J_{\min}^{1-\alpha}\right) & \alpha \neq 1 \\ \ln\left(\dfrac{J_{\max}}{J_{\min}}\right) & \alpha = 1 \end{array} \right\} \tag{C.48}$$

and κ therefore clearly depends on the choice of $J_{\min}$ and $J_{\max}$, including the term α. Let us consider some cases for $J_{\min}$ and $J_{\max}$:

1. $0 < J_{\min} < J_{\max} < \infty$: For this case the integral in (C.48) is a proper integral for each value of α. In this case the normalization condition, and hence κ, is well defined for each α.

2. $0 < J_{\min}$ & $J_{\max} \to \infty$: For this case the integral in (C.48) is an improper integral (of the second kind) of the form

$$\int_{a>0}^{\infty} dx\, x^{-\alpha}$$

and the normalization condition is well defined, with κ finite and non-zero, only for the values

$$\alpha > 1 \quad .$$

3. $J_{\min} = 0$ & $J_{\max} < \infty$: For this case the integral in (C.48) is again an improper one (of the first kind) of the form

$$\int_{0}^{b<\infty} dx\, x^{-\alpha}$$

and, for the normalization constant κ to be finite and non-zero, we require that

$$0 < \alpha < 1 \quad .$$

We include the condition $0 < \alpha$ to maintain the form of the distribution, since for $\alpha < 0$ we do not have a decreasing function of J in eqn. (C.46).

4. $J_{\min} = 0$ & $J_{\max} \to \infty$: For this case the integral in (C.48) is an improper integral (of both kinds) and does not converge for any value of α. For this case $\kappa \to 0$.

These four cases show the limits imposed on α depending on the choice of $J_{\min}$ and $J_{\max}$. We can ignore cases (2) and (4) where $J_{\max} \to \infty$. From a physical point of view there must be an upper bound to the exchange coupling, with $J_{\max}$ being finite. Case (1) is the most general and most physical of the four cases. This case imposes no restrictions on the value of α, but it does introduce two unknown parameters, $J_{\min}$ and $J_{\max}$, into the formalism.

For the extended Luttinger-liquid model we used case (3) in our formalism by letting $J_{\min} = 0$. By using this lowerbound, we include the possibility of having isolated spins in the system. It also eliminates the need for an extra unknown parameter. Choosing $J_{\max}$ as being finite does introduce an extra parameter, but, as the analysis in App. C.1

indicates, if $J_{\max}$ is sufficiently large, then it essentially does not appear in the formalism of the model as a variable. If $J_{\max}$ is not large enough, then it will appear explicitly in the model equations[1]. However, the use of case $J_{\min} = 0$ and $J_{\max} < \infty$ does introduce a limit on the values that α can take (case 3), and we require in the extended two-fluid model that

$$0 < \alpha < 1 \quad . \tag{C.49}$$

C.8 The Extended Two-Fluid Model in the Limit $\alpha \to 1_-$

In the previous section we established that, in our formalism of the extended two-fluid model, we require that $\alpha < 1$. Here we consider the effect of letting $\alpha \to 1_-$ ($\alpha \to 1$ and $\alpha < 1$) in the model, and show that the isolated spin-1/2 model (App. A.2) appears as a limiting case.

We do expect that, as the impurity concentration is decreased to well below the MI transition. the wave function overlap will become negligible, and an isolated spin-1/2 model should describe the system well.

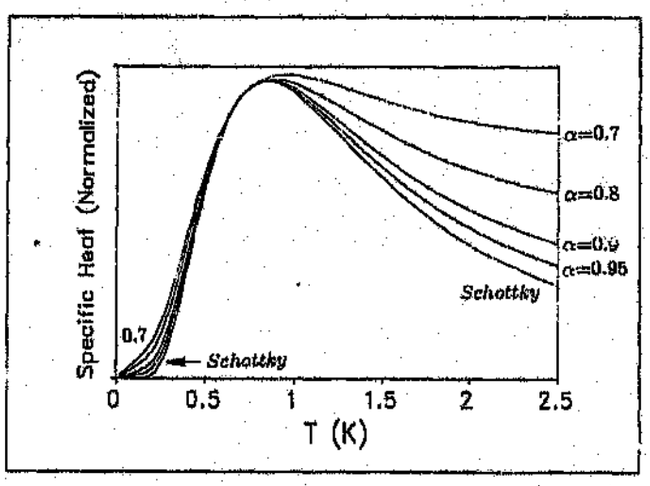


Figure C.9: The normalized specific heat for various α values, together with the Scottky specific heat, for comparison.

Figure C.9 shows the predicted specific heat in the extended two-fluid model for

[1]Refer to App. C.6, or refer to §3.8 of ch. 3 for a summary.

various values of the parameter α. The curves are arbitrarily normalized to show the evolution of the shape with increasing α. Also included in this figure is the Schottky specific heat describing an isolated spin-1/2 system, and we can see that the curves tend to this Schottky form as α is increased towards 1. So for the specific heat, in the limit $\alpha \to 1_-$, the extended two-fluid model reduces to an isolated spin model.

This is also the case for the susceptibility. For larger temperatures the susceptibility (eqn. (3.47)) goes as $T^{-\alpha}$, so, letting $\alpha \to 1$, we get the limiting behavior T^{-1}, which is the Curie form for isolated spins (eqn. (A.7)).

The limiting form of this model is a consequence of the exchange coupling distribution in (C.46) and the normalization condition in (C.47), using $J_{\min} = 0$ and $J_{\max} < \infty$. In the interval of interest, $[J_{\min}, J_{\max}] = [0, J_{\max}]$, $P(J) = \kappa J^{-\alpha} = (1-\alpha)J^{-\alpha}/J_{\max}^{1-\alpha}$, and, outside of this interval, we can take $P(J) = 0$. Then we can write

$$\int_{-\infty}^{+\infty} P(J)dJ = 1 \tag{C.50}$$

for the normalization condition in (C.47) which holds for each $\alpha < 1$. Also, the function $P(J)$ converges pointwise on $(-\infty, +\infty)$ as $\alpha \to 1$, with

$$\lim_{\alpha \to 1_-} P(J) = \begin{cases} 0 & J \neq 0 \\ \infty & J = 0 \end{cases} \quad . \tag{C.51}$$

From (C.50) and (C.51) we can infer that

$$\lim_{\alpha \to 1_-} P(J) = \delta(J) \quad , \tag{C.52}$$

indicating a Dirac-delta distribution in exchange couplings. The Dirac-delta distribution describes a system with no exchange couplings J, indicating that all the spins are isolated and not interacting with neighbours. So, in the limit $\alpha \to 1_-$, the distribution function $P(J)$ tends towards an isolated spin system, and is the reason why the non-interacting spin-1/2 model appears as a limiting case of the extended two-fluid model.

C.9 The Specific Heat Peak: Some Details

In this section we look at the Schottky-type specific heat peak, and consider some of the predictions made by the extended two-fluid model with regards to this peak. We obtain an expression which will be very useful in testing the model, and also in experimental data analysis.

The specific heat C of the localized contribution in the extended two-fluid model is given by eqn. (3.34):

$$C = \sigma\, \delta(y)\, T^{1-\alpha} \quad , \tag{C.53}$$

where the factor $\delta(y)$, with $y = g\mu_B B/k_B T$, is shown in fig. C.10.

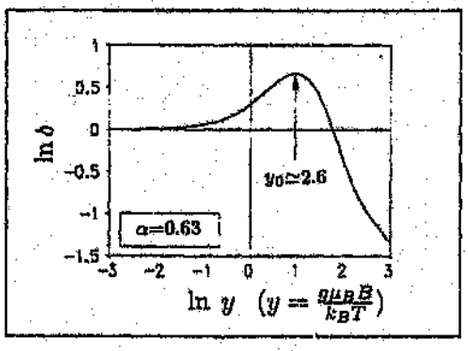


Figure C.10: A plot of $\ln(\delta)$ versus $\ln(y)$, for $\alpha = 0.63$. Indicated is the position y_0 of the maximum.

To find the details of the specific heat peak, we need to maximize C in eqn. (C.53), w.r.t. the temperature T. This condition for maximization can be expressed as $\frac{d\ln C}{d\ln T} = 0$ and, using eqn. (C.53), we obtain

$$\left.\frac{d\ln\delta}{d\ln y}\right|_{y\,=\,y_{\max}} = (1-\alpha) \quad . \tag{C.54}$$

$y_{\max} = (g\mu_B/k_B)\; B/T_{\max}$ is the solution of (C.54), where $T_{\max}$ is the temperature at which the specific heat peak occurs[2]. Noting that $\frac{d\ln\delta}{d\ln y}$ is the slope of the curve in fig. C.10, and that $(1-\alpha) > 0$ (§C.7), we can conclude that $y_{\max} < y_0$, where $y_0 \simeq 2.6$ is the position of the maximum in fig. C.10. Hence

$$T_{\max} = \left(\frac{g\mu_B}{k_B y_{\max}}\right) B \quad > \quad \left(\frac{g\mu_B}{k_B y_0}\right) B \simeq \frac{1}{2} B \quad , \tag{C.55}$$

with the peak position $T_{\max}$ increasing in proportion to the magnetic field B. This behaviour of $T_{\max} \propto B$ is similar to the Schottky specific heat peak (point 2 in §A.2), but differs from the behaviour of the peak position in the spin-pair model of chapter 2 (point 1 of §2.3.3).

[2] In addition, a second solution of (C.54) gives the position of the minimum in C. For example, refer to the $B = 0.7T$ curves in fig. 4.12 or 4.13.

Note that the slope $\frac{d\ln\delta}{d\ln y}$ obtains a maximum on $[0, y_0]$, and, referring to fig. 3.1b in chapter 3, we notice that this maximum slope decreases as α decreases. Since $(1-\alpha)$ increases with decreasing α, we will reach a critical value α_0 for which eqn. (C.54) will not have a solution i.e. the specific heat will not have a peak structure. Our numerical analysis of (C.54) shows that $0.55 < \alpha_0 < 0.60$. As an example, refer to fig. 4.14 of chapter 4. which shows plots of eqn. (C.53) for $\alpha = 0.4$, and indicates this absence of the Schottky-type peaks. This absence of a peak structure for sufficiently small α is due to the factor $T^{1-\alpha}$ in eqn. (C.53).

Inserting the solution of eqn. (C.54), $y_{\max} = (g\mu_B/k_B)\ B/T_{\max}$, into eqn. (C.53), we obtain the peak height $C_{\max}$:

$$C_{\max} = \sigma\ \delta(y_{\max})\ \left(\frac{g\mu_B}{k_B y_{\max}}\right)^{1-\alpha}\ B^{1-\alpha} \quad , \tag{C.56}$$

and from this expression we obtain a very useful equation relating the specific heat peak heights $C_{\max}(B_1)$ and $C_{\max}(B_2)$ in two magnetic fields B_1 and B_2:

$$\frac{C_{\max}(B_1)}{C_{\max}(B_2)} = \left(\frac{B_1}{B_2}\right)^{1-\alpha} \quad . \tag{C.57}$$

Both eqns.(C.56) and (C.57) indicate that the peak height increases as the magnetic field is increased. This is also observed in the spin-pair model of chapter 2 (point 2 of §2.3.3). This behaviour is in contract with the Schottky specific heat, which has a field-independent peak height (point 3 of §A.2), which occurs here when $\alpha \to 1$ (§C.8).

As a final note, we have assumed here that the parameter α does not depend on the field B. Our own analysis (point 1 of §4.6) indicates that α could possibly be affected by large fields ($\gg 1T$), but for small fields ($\lesssim 1T$) appears unaffected. Matsunaga and Ootuka [17] also claim that the effect on α is minute in their studies of the magnetization ($B \leq 0.3T$).

Appendix D

Evaluation of the Asymptotic Forms of $\delta(y)$ and $\varepsilon(y)$

D.1 Introduction

In this appendix we look at the asymptotic behavior of $\delta(y)$ and $\varepsilon(y)$ as $y \to \infty$. (Refer to §3.2 for the definitions of $\delta(y)$ and $\varepsilon(y)$) Since $y = g\mu_B B/k_B T$, we see that this asymptotic behavior gives us the low temperature form of the specific heat and susceptibility in a magnetic field ($B \neq 0$).

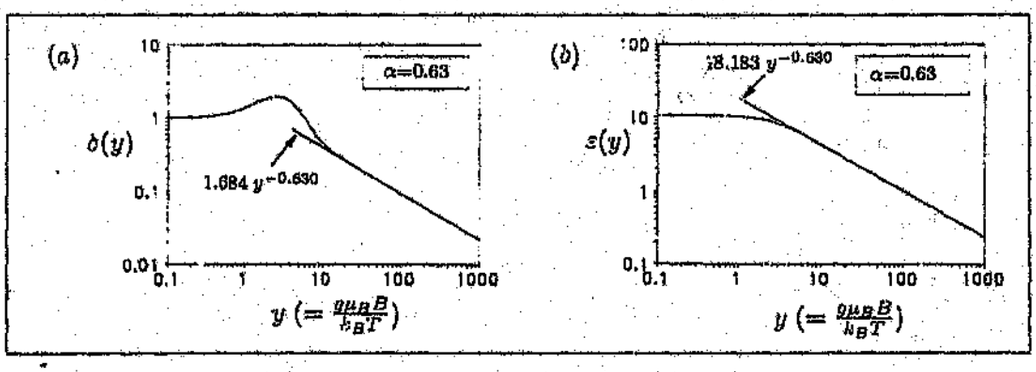


Figure D.1: Plots of the functions (a) $\delta(y)$, and (b) $\varepsilon(y)$, versus y. Also shown are the determined asymptotic forms.

Figures D.1a and D.1b show plots of the functions $\delta(y)$ and $\varepsilon(y)$ in log-log plots,

for $\alpha = 0.63$. For the large y-values, it can be seen that the graphs of both $\delta(y)$ and $\epsilon(y)$ have a linear form, and the straight lines included in both plots are best fits to the graphs for the large y-values. (The fitting was done for $y > 100$.) We can see that convergence between these fits and the graphs occurs at $y \sim 10$, and we have for the asymptotic form

$$\delta(y) \equiv^{y\gg 1} 1.684\, y^{-0.630} = 1.684\, y^{-\alpha} \tag{D.1}$$

$$\epsilon(y) \equiv^{y\gg 1} 18.183\, y^{-0.630} = 18.183\, y^{-\alpha} \ , \tag{D.2}$$

where it should be noted that the power of y is equal to the value $\alpha = 0.63$. In this appendix we use the symbol "$\equiv^{y\gg 1}$" to mean "for sufficiently large y behaves as".

The asymptotic forms given above appear to hold for other values of α as well. We will generalize and analytically show that this asymptotic form is valid, and derive expressions to the coefficients in the above equations. From eqns. (3.22) and (3.25) we have

$$\begin{aligned} \delta(y) &= \frac{I_\delta(y)}{I_\delta(0)} \\ \epsilon(y) &= \frac{I_\epsilon(y)}{I_\epsilon(0)} \end{aligned} \tag{D.3}$$

and so we need to evaluate the asymptotic forms of the integrals $I_\delta(y)$ and $I_\epsilon(y)$.

D.2 The Asymptotic Form of $I_\delta(y)$

We want to evaluate the asymptotic form of the integral $I_\delta(y)$ for large y-values (small temperatures T). From eqn. (3.14), we have

$$I_\delta(y) = \int_0^\infty dx\, x^{-\alpha} F_C(x,y) \ , \tag{D.4}$$

where

$$F_C(x,y) = \frac{(x-y)^2 e^{y-x} + (x+y)^2 e^{-y-x} + x^2 e^{-x} + y^2(4+2\cosh(y))e^{-2x}}{(1+(1+2\cosh(y))e^{-x})^2} \ . \tag{D.5}$$

Letting $x = yt$ in the integral, we then have

$$\begin{aligned} I_\delta(y) &= y^{-\alpha} \int_0^\infty dt\, t^{-\alpha}\, y F_C(yt,y) \\ &= y^{-\alpha} I(y) \end{aligned} \tag{D.6}$$

and we will show that $I(y)$ converges to a constant as y tends to infinity.

Now

$$yF_C(yt,y) = y^3\left(\frac{(1-t)^2e^{y(1-t)} + (1+t)^2e^{-y(1+t)} + t^2e^{-yt} + (4+2\cosh(y))e^{-2yt}}{(1+(1+2\cosh(y))e^{-yt})^2}\right) \tag{D.7}$$

and, using the fact that $2\cosh(y) \simeq e^y$ for $y \gg 1$, we have that

$$yF_C(yt,y) \equiv^{y\gg 1} y^3\left(\frac{(1-t)^2e^{y(1-t)} + (1+t)^2e^{-y(1+t)} + t^2e^{-yt} + 4e^{-2yt} + e^{y(1-2t)}}{\left(1+e^{-yt}+e^{y(1-t)}\right)^2}\right). \tag{D.8}$$

We have to consider three cases when evaluating the limiting form of the above expression. Since both the numerator and denominator contain the factor $e^{y(1-t)}$, the limiting form will depend on the integrating variable t (since the factor $1-t$ can be positive, negative and zero). We therefore have to partition the interval of integration into three regions: an interval where $1-t$ is positive, negative, and close to zero. For this purpose we choose $0 < \varepsilon < 1$ as an arbitrary constant and define our intervals to be $[0, 1-\varepsilon]$, $[1-\varepsilon, 1+\varepsilon]$, and $[1+\varepsilon, \infty)$. The integral $I(y)$ is then the sum of the three integrals

$$\Gamma_1 = \int_0^{1-\varepsilon} dt\, t^{-\alpha}\, yF_C(x,y) \quad , \tag{D.9}$$

$$\Gamma_2 = \int_{1-\varepsilon}^{1+\varepsilon} dt\, t^{-\alpha}\, yF_C(x,y) \quad , \text{ and} \tag{D.10}$$

$$\Gamma_3 = \int_{1+\varepsilon}^{\infty} dt\, t^{-\alpha}\, yF_C(x,y) \quad . \tag{D.11}$$

We shall now consider each case separately by looking at the asymptotic form of the term $yF_C(x,y)$ in the integrand.

Case 1: Integral Γ_1

Here we have $0 \le t \le 1-\varepsilon$ and hence $0 < \varepsilon \le 1-t \le 1$. Multiplying both the numerator and denominator in (D.8) by $e^{-y(1-t)}$ and then by $e^{-2y(1-t)}$, we obtain

$$yF_C(yt,y) \equiv^{y\gg 1} \frac{y^3}{e^{y(1-t)}}\left(\frac{(1-t)^2 + (1+t)^3e^{-2y} + t^2e^{-y} + 4e^{-y(1+t)} + e^{-yt}}{\left(1+e^{-y}+e^{-y(1-t)}\right)^2}\right) \tag{D.12}$$

and, by eliminating the terms that vanish in the limit as $y \to \infty$, we are left with

$$yF_C(yt,y) \equiv^{y\gg 1} \frac{y^3}{e^{y(1-t)}}\left(\frac{(1-t)^2 + e^{-yt}}{1}\right) \quad . \tag{D.13}$$

We have left the term e^{-yt} in the expression to make sure no problems arise for $t \to 0$. Hence we have

$$0 \le t \le 1-\varepsilon \implies yF_C(yt,y) \equiv^{y\gg 1} y^3\left((1-t)^2e^{-y(1-t)}+e^{-y}\right) \quad . \tag{D.14}$$

Therefore, for $y \gg 1$, we have

$$\begin{aligned}\Gamma_1 &\equiv \int_0^{1-\varepsilon} dt\, t^{-\alpha}\, y^3\left((1-t)^2e^{-y(1-t)}+e^{-y}\right) \\ &= y^3e^{-y}\int_0^{1-\varepsilon} dt\, t^{-\alpha}(1-t)^2e^{yt}+y^3e^{-y}\int_0^{1-\varepsilon} dt\, t^{-\alpha}\end{aligned} \tag{D.15}$$

and, since $0 \le t \le 1-\varepsilon$, we can see that $e^{yt} \le e^{y(1-\varepsilon)}$ and $(1-t)^2 \le 1$. So, for the right hand side (RHS) of the above expression, using the fact that

$$\xi = \int_0^{1-\varepsilon} dt\, t^{-\alpha} = \frac{(1-\varepsilon)^{1-\alpha}}{1-\alpha}, \tag{D.16}$$

we obtain the following inequality:

$$0 \le RHS \le \xi y^3\left(e^{-y\varepsilon}+e^{-y}\right). \tag{D.17}$$

Since $0 < \varepsilon < 1$ is an arbitrary fixed number, we come to the conclusion that the integral Γ_1 vanishes exponentially as $y \to \infty$. Hence

$$\Gamma_1 \equiv^{y\gg 1} 0 \quad . \tag{D.18}$$

Case 2: Integral Γ_2

Here we have $1-\varepsilon \le t \le 1+\varepsilon$ and hence $|1-t| < \varepsilon$. Again multiplying both the numerator and denominator by $e^{-y(1-t)}$, we obtain

$$yF_C(yt,y) \equiv^{y\gg 1} y^3\left(\frac{(1-t)^2+(1+t)^2e^{-2y}+t^2e^{-y}+4e^{-y(1+t)}+e^{-yt}}{\left(2\cosh\left(\frac{1}{2}y(1-t)\right)+e^{-\frac{1}{2}y(1+t)}\right)^2}\right) \tag{D.19}$$

and after eliminating the terms which exponentially decay to zero more rapidly, we are left with

$$yF_C(yt,y) \equiv^{y\gg 1} y^3\left(\frac{(1-t)^2+t^2e^{-y}+e^{-yt}}{4\cosh^2\left(\frac{1}{2}y(1-t)\right)}\right) \quad . \tag{D.20}$$

where the last two terms in the numerator, t^2e^{-y} and e^{-yt}, are maintained for the case $t=1$.

Next, we consider the form of the integral Γ_2. We will show that the last two terms in the numerator of (D.20) can be neglected in the evaluation of Γ_2. For this purpose, note that $\cosh x \geq 1$ for any x. Also, since $1-\varepsilon \leq t \leq 1+\varepsilon$, we have $t^2 \leq (1+\varepsilon)^2$ and $e^{-yt} \leq e^{-y(1-\varepsilon)}$. Therefore, from (D.10) and (D.20), we have

$$\begin{aligned} 0 \;\leq\; & \Gamma_2 - \int_{1-\varepsilon}^{1+\varepsilon} dt\, t^{-\alpha}\, y^3 \left(\frac{(1-t)^2}{4\cosh^2\left(\frac{1}{2}y(1-t)\right)} \right) \\ \equiv\; & {}^{y\gg 1} \int_{1-\varepsilon}^{1+\varepsilon} dt\, t^{-\alpha}\, y^3 \left(\frac{t^2 e^{-y} + e^{-yt}}{4\cosh^2\left(\frac{1}{2}y(1-t)\right)} \right) \\ \leq\; & y^3 (1+\varepsilon)^2 K e^{-y} + y^3 K e^{-y(1-\varepsilon)} \quad . \end{aligned} \tag{D.21}$$

Since $0 < \varepsilon < 1$ is an arbitrary constant, and $K = \int_{1-\varepsilon}^{1+\varepsilon} dt\, t^{-\alpha}$ is also fixed, we see that the above expression vanishes exponentially as $y \to \infty$. Hence, we conclude that

$$\Gamma_2 \equiv^{y\gg 1} \frac{y^3}{4} \int_{1-\varepsilon}^{1+\varepsilon} dt\, t^{-\alpha} \frac{(1-t)^2}{\cosh^2\left(\frac{1}{2}y(1-t)\right)} \quad . \tag{D.22}$$

Case 3: Integral Γ_3

Here we have $t \geq 1+\varepsilon$. From (D.8) it can be seen that the expression vanishes as $y \to \infty$ for all values of t. This leads us to conclude that the integral Γ_3 vanishes for $y \to \infty$. However, to be more correct, this is only the case when the interval of integration is finite. When the upper limit in the integration is taken as infinity, we have to be concerned about how the expression converges to zero.

Pulling out the slowest exponentially decaying factor, $e^{y(1-t)}$, from the numerator of (D.8), we have

$$yF_C(yt,y) \equiv^{y\gg 1} y^3 e^{-y(t-1)} \frac{(1-t)^2 + (1+t)^2 e^{-2y} + t^2 e^{-y} + 4e^{-y(1+t)} + e^{-yt}}{\left(1 + e^{-yt} + e^{-y(t-1)}\right)^2} \tag{D.23}$$

and hence, after eliminating all the vanishing terms from the numerator and denominator, we conclude that

$$yF_C(yt,y) \equiv^{y\gg 1} y^3 e^{-y(t-1)} (1-t)^2 \quad . \tag{D.24}$$

Since $t \geq 1+\varepsilon$ and $y > 1$, we can write $e^{-y(t-1)} = e^{-\frac{1}{2}y(t-1)} \cdot e^{-\frac{1}{2}y(t-1)} \leq e^{-\frac{1}{2}y\varepsilon} \cdot e^{-\frac{1}{2}(t-1)}$, and so the integral Γ_3 is given by

$$\Gamma_3 \;=\; y^3 \int_{1+\varepsilon}^{\infty} dt\, t^{-\alpha} (1-t)^2 e^{-y(t-1)}$$

$$\leq y^3 e^{-\frac{1}{2}y\varepsilon} \int_{1+\varepsilon}^{\infty} dt\, t^{-\alpha}(1-t)^2 e^{-\frac{1}{2}(t-1)}$$
$$= y^3 e^{-\frac{1}{2}y\varepsilon} K' \quad . \tag{D.25}$$

The integral K' above is finite, due to the exponential factor $e^{-\frac{1}{2}(t-1)}$, and so we see that the integral Γ_3 does indeed vanish exponentially as $y \to \infty$. Hence we conclude that

$$\Gamma_3 \stackrel{y\gg 1}{=} 0 \quad . \tag{D.26}$$

Conclusion

Combining the three case (D.18), (D.22), and (D.26), we conclude that

$$\begin{aligned} I(y) &\stackrel{y\gg 1}{=} \frac{1}{4}y^3 \int_{1-\varepsilon}^{1+\varepsilon} dt\, t^{-\alpha} \frac{(1-t)^2}{\cosh^2\left(\frac{1}{2}y(1-t)\right)} \\ &= \frac{1}{4}y^3 \int_{-\varepsilon}^{+\varepsilon} ds\, (1-s)^{-\alpha} \frac{s^2}{\cosh^2\left(\frac{1}{2}ys\right)} \\ &= \frac{1}{4}y^3 \int_0^{\varepsilon} ds\, \frac{s^2}{\cosh^2\left(\frac{1}{2}ys\right)} \left((1-s)^{-\alpha} + (1+s)^{-\alpha}\right) \quad . \end{aligned} \tag{D.27}$$

For sufficiently small ε, we can use the approximation $(1 \pm \varepsilon)^{-\alpha} \simeq 1 \mp \varepsilon\alpha$ to obtain

$$I(y) \stackrel{y\gg 1}{=} \frac{1}{2}y^3 \int_0^{\varepsilon} ds\, \frac{s^2}{\cosh^2\left(\frac{1}{2}ys\right)} \quad , \tag{D.28}$$

which is independent of α. Letting $\nu = \frac{1}{2}ys$, we get

$$\begin{aligned} \int_0^{\varepsilon} ds\, \frac{s^2}{\cosh^2\left(\frac{1}{2}ys\right)} &= \left(\frac{2}{y}\right)^3 \int_0^{\frac{1}{2}y\varepsilon} d\nu\, \nu^2\, Sech^2(\nu) \\ &\simeq \left(\frac{2}{y}\right)^3 \frac{\pi^2}{12} \end{aligned} \tag{D.29}$$

for sufficiently large y, where we have used the identity

$$\int_0^{\infty} d\nu\, \nu^2\, \mathrm{sec}\, h^2(\nu) = \frac{\pi^2}{12} \quad . \tag{D.30}$$

Finally, combining (D.3), (D.6), (D.28), and (D.29), we conclude that

$$\delta(y) \stackrel{y\gg 1}{=} \left(\frac{\pi^2}{3I_1}\right) y^{-\alpha} \quad . \tag{D.31}$$

D.3 The Asymptotic Form of $I_\varepsilon(y)$

Next, we want to evaluate the asymptotic form for the integral $I_\varepsilon(y)$ which is given by eqn. (3.15):

$$I_\varepsilon(y) = \int_0^\infty dx\, x^{-\alpha}\, F_\chi(x,y) \quad , \tag{D.32}$$

where

$$F_\chi(x,y) = \frac{\sinh(y)}{y} \frac{e^{-x}}{1+(1+2\cosh(y))\,e^{-x}} \quad . \tag{D.33}$$

Again, letting $x = yt$ in the above integral, we have

$$\begin{aligned} I_\varepsilon(y) &= y^{-\alpha} \int_0^\infty dt\, t^{-\alpha}\, y F_\chi(yt,y) \\ &= y^{-\alpha}\, I(y) \end{aligned} \tag{D.34}$$

and we will show that $I(y)$ converges to a constant value as $y \to \infty$. Using the fact that $\cosh(y) \simeq \sinh(y) \simeq \frac{1}{2}e^y$ for $y \gg 1$, we can write

$$\begin{aligned} yF_\chi(yt,y) &\underset{y\gg 1}{\equiv} \frac{1}{2}\frac{1}{1+e^{-y}+e^{-y(1-t)}} \\ &\simeq \frac{1}{2}\frac{1}{1+e^{-y(1-t)}} \quad , \end{aligned} \tag{D.35}$$

where we have used $1+e^{-y} \simeq 1$, and have kept the last term in the denominator since $(1-t)$ can be both positive and negative on the interval of integration. As in the previous section, to avoid possible problems at $t=1$, we partition the interval of integration into three regions: $[0, 1-\varepsilon]$, $[1-\varepsilon, 1+\varepsilon]$, and $[1+\varepsilon, \infty)$, where $0 < \varepsilon < 1$ is an arbitrary constant. Then $I(y)$ is the sum of three contributions:

$$\begin{aligned} \Gamma_1 &= \int_0^{1-\varepsilon} dt\, t^{-\alpha}\, yF_\chi(yt,y) \\ \Gamma_2 &= \int_{1-\varepsilon}^{1+\varepsilon} dt\, t^{-\alpha}\, yF_\chi(yt,y) \\ \Gamma_3 &= \int_{1+\varepsilon}^{\infty} dt\, t^{-\alpha}\, yF_\chi(yt,y) \end{aligned} \tag{D.36}$$

and we consider the asymptotic form of each of the terms in (D.36).

For the first case, we have $0 \le t \le 1-\varepsilon$ and so $0 < \varepsilon \le 1-t \le 1$. This gives us

$$yF_\chi(yt,y) \underset{y\gg 1}{\equiv} \frac{1}{2} \tag{D.37}$$

and, substituting into (D.36), we conclude that

$$\Gamma_1 \underset{y\gg 1}{\equiv} \frac{1}{2}\int_0^{1-\varepsilon} dt\, t^{-\alpha} = \frac{(1-\varepsilon)^{-\alpha}}{2(1-\alpha)} \quad . \tag{D.38}$$

For the second case, $1-\varepsilon \le t \le 1+\varepsilon$, the integral Γ_2 is given by

$$\begin{aligned}\int_{1-\varepsilon}^{1+\varepsilon} dt\, t^{-\alpha}\, yF_\chi(yt,y) &\equiv^{y\gg 1} \frac{1}{2}\int_{1-\varepsilon}^{1+\varepsilon} dt\, t^{-\alpha}\, \frac{1}{1+e^{-y(1-t)}} \\ &= \frac{1}{2}\int_{-\varepsilon}^{+\varepsilon} ds\, \frac{(1+s)^{-\alpha}}{1+e^{ys}} \quad . \end{aligned} \tag{D.39}$$

Since the integrand is bounded, by $(1-\varepsilon)^{-\alpha}$ say, on the interval $(-\varepsilon,\varepsilon)$, we have

$$0 \le \frac{1}{2}\int_{-\varepsilon}^{+\varepsilon} ds\, \frac{(1+s)^{-\alpha}}{1+e^{ys}} \le \varepsilon(1-\varepsilon)^{-\alpha} \quad . \tag{D.40}$$

For the third case, we have $t \ge 1-\varepsilon$ and so from (D.35) we have the asymptotic behaviour

$$yF_\chi(yt,y) \equiv^{y\gg 1} \frac{1}{2}e^{-y(t-1)} \quad . \tag{D.41}$$

Since $t-1 \ge \varepsilon$ and $y > 1$, we can use the inequality $e^{-y(t-1)} = e^{-\frac{1}{2}y(t-1)} \cdot e^{-\frac{1}{2}y(t-1)} \le e^{-\frac{1}{2}y\varepsilon} \cdot e^{-\frac{1}{2}(t-1)}$ and then conclude that

$$\begin{aligned}\Gamma_3 &\equiv^{y\gg 1} \int_{1+\varepsilon}^{\infty} dt\, t^{-\alpha}\, \frac{1}{2}e^{-y(t-1)} \\ &\le \frac{1}{2}e^{-\frac{1}{2}y\varepsilon}\int_{1+\varepsilon}^{\infty} dt\, t^{-\alpha}e^{-\frac{1}{2}(t-1)} \\ &= \frac{1}{2}K\, e^{-\frac{1}{2}y\varepsilon} \quad . \end{aligned} \tag{D.42}$$

Due to the exponential factor $e^{-\frac{1}{2}(t-1)}$, the integral K converges to a constant value. Since $\varepsilon > 0$ is an arbitrary constant, we see that the integral Γ_3 vanishes exponentially as $y \to \infty$. So

$$\Gamma_3 \equiv^{y\gg 1} 0 \quad . \tag{D.43}$$

Combining the results of the three cases, using (D.38), (D.39), and (D.43), we obtain

$$\begin{aligned} I(y) &= \Gamma_1 + \Gamma_2 + \Gamma_3 \\ &\equiv^{y\gg 1} \frac{(1-\varepsilon)^{-\alpha}}{2(1-\alpha)} + \frac{1}{2}\int_{-\varepsilon}^{+\varepsilon} ds\, \frac{(1+s)^{-\alpha}}{1+e^{ys}} + 0 \quad . \end{aligned} \tag{D.44}$$

Since $\varepsilon > 0$ can be chosen arbitrarily small, the inequality (D.40) shows that the second term in (D.44) becomes negligible, and hence

$$I(y) \equiv^{y\gg 1} \frac{1}{2(1-\alpha)} \quad . \tag{D.45}$$

Combining this result with (D.3) and (D.34), we conclude that

$$\varepsilon(y) \equiv^{y\gg 1} \left(\frac{2}{3}\pi^2 g^2\right)\frac{1}{2(1-\alpha)I_1}\, y^{-\alpha} \quad . \tag{D.46}$$

D.4 Conclusion

We can see that the graphical and mathematical analysis give us the same asymptotic behaviours for $\delta(y)$ and $\varepsilon(y)$. We can therefore be confident that the asymptotic forms are given by

$$\delta(y) \equiv \left(\frac{\pi^2}{3I_1}\right) y^{-\alpha} \quad for \quad y \gtrsim 15 \tag{D.47}$$

and

$$\varepsilon(y) \equiv \left(\frac{2}{3}\pi^2 g^2 \frac{1}{2(1-\alpha)I_1}\right) y^{-\alpha} \quad for \quad y \gtrsim 5 \ , \tag{D.48}$$

where the values of 15 and 5 are rough estimates from figs. D.1, giving us an indication of where the convergence between the graphs and their asymptotic forms occur. For $\alpha = 0.63$, we have the factors $(\pi^2/3I_1) \simeq 1.683$ and $\left(\frac{2}{3}\pi^2 g^2\right)/(2(1-\alpha)I_1) \simeq 18.193$, in close agreement with the values obtained from the graphical analysis (eqns. (D.1) and (D.2)).

Appendix E

Digitising Data

Before the arrival of the original specific heat data, towards the end of our studies, we had to digitize the specific heat and susceptibility data from published papers.

The data used for the analysis in chapter 2 were all digitized using a Hewlett-Packard (HP) digitizer. The references from which these data were obtained are given in the figure captions of the publication in §2.7. However, at the start of the analysis of the extended two-fluid model (chapters 3 and 4), the HP digitizer was out of order, and we required an alternative way to obtain the data.

For this purpose a computer was used. With the use of a computer mouse a digitizing program was written to extract the data from published figures. These figures were transferred into bitmap files with the use of a scanner, and these bitmaps were then displayed onto the computer screen, to be digitized with the use of the mouse.

After we obtained the original specific heat data, the corresponding digitized data were replaced with these original data. However, not all the data used in chapters 3 and 4 were obtained in original form, and the figure captions to these data indicate from which references the data were digitized.

There was one main problem that we encountered with digitizing the published figures, particularly when digitizing logarithmic plots, and then using these data with linear scales. Many of the published figures showed the data with logarithmic plots, and we now give a quick review of the problem encountered.

As an example, refer to fig. 1.2a of chapter 1, which represents a typical figure we needed to digitize. This figure is reproduced on the computer screen, and the mouse is used to determine the data points. The mouse would determine the screen coordinate, say u, of

a datum, which is then converted into the required physical quantity, say the temperature T. Since the screen coordinates are linear, and the figure scale logarithmic, the general transformation between u and T is of the form

$$T = a \exp(b \cdot u) \quad , \tag{E.1}$$

where a and b are constants depending on the actual figure used. An error analysis, using (E.1), then shows that the uncertainty (arising from the digitization process) in the quantity T can be approximated by

$$\Delta T \sim b\, T\, \Delta u \quad , \tag{E.2}$$

where Δu is the uncertainty in the screen coordinate u, which remains roughly constant. We therefore find that $\Delta T \propto T$. Using these digitized data in linear plots can therefore introduce large errors, particularly when T (and hence ΔT) is increased by an order of magnitude, as is the case in fig. 1.2a. (The same holds true for the errors generated in the specific heat C.)

Bibliography

[1] M.A. Paalanen and R.N. Bhatt, Physica B169, 223 (1991).

[2] M. Lakner and H. v. Löhneysen, Phys. Rev. Lett. 70, 3475 (1993).

[3] A.L. Efros and M. Pollack, Electron-Electron Interactions in Disordered Systems, Elsevier Science Publishers B.V, 1985, Chapter 3, p. 231-286.

[4] B.I. Shklovskii and A.L. Effros, Electronic Properties of Doped Semiconductors, Springer-Verlag (1984).

[5] M. Lakner, H. von Löhneysen, A. Langenfeld, and P. Wölfle, Phys. Rev. B50, 17064 (1994).

[6] M.A. Paalanen and R.N. Bhatt, Inst. Phys. Conf. Ser. No 95: Chapter 2, 69 (1989). (Paper presented at Int. Conf. Shallow Impurities in Semiconductors, Sweden 1988.)

[7] M.A. Paalanen, J.E. Graebner, R.N. Bhatt, and S. Sachdev, Phys. Rev. Lett. 61, 597 (1988).

[8] C. Herring and M. Flicker, Physical Review 134, A362 (1964).

[9] C. Paschke, H. v. Löhneysen, and Y. Ootuka, Phys. Rev. B49, 2170 (1994).

[10] S. Ikehata, T. Ema, S. Kobayashi, and W. Sasaki, J. Phys. Soc. Jpn. 50, 3655 (1981).

[11] R.N. Bhatt, M.A. Paalanen, and S. Sachdev, Journal De Physique 49, C8-1179 (1988).

[12] R.N. Bhatt and P.A. Lee, Phys. Rev. Lett. 48, 344 (1982).

[13] D. New and T.G. Castner, American Physical Society 29, 2077 (1984) .

[14] K. Andres, R.N. Bhatt, P. Goalwin, T.M. Rice, and R.E. Walstedt, Phys. Rev. B24, 244 (1981).

[15] M.P. Sarachik, A. Roy, M. Turner, M. Levy, D. He, L.L. Isaacs, and R.N. Bhatt, Phys. Rev B34, 387 (1986).

[16] Y. Ootuka and N. Matsunaga, J. Phys. Soc. Jpn. 59, 1801 (1990).

[17] N. Matsunaga and Y. Ootuka, J. Phys. Soc. Jpn. 62, 1745 (1993).

[18] M. Lakner and H. v. Löhneysen, Phys. Rev. Lett. 63, 648 (1989).

[19] N. Kobayashi, S. Ikehata, S. Kobayashi and W. Sasaki, Solid State Communications 32, 1147 (1979).

[20] H. v. Löhneysen and M. Lakner, Physica B165&166, 285 (1990).

[21] G.A. Thomas, Y. Ootuka, S. Kobayashi, and W. Sasaki, Phys. Rev. B24, 4886 (1981).

[22] H. Alloul and P. Dellouve, Phys. Rev. Lett. 59, 578 (1987).

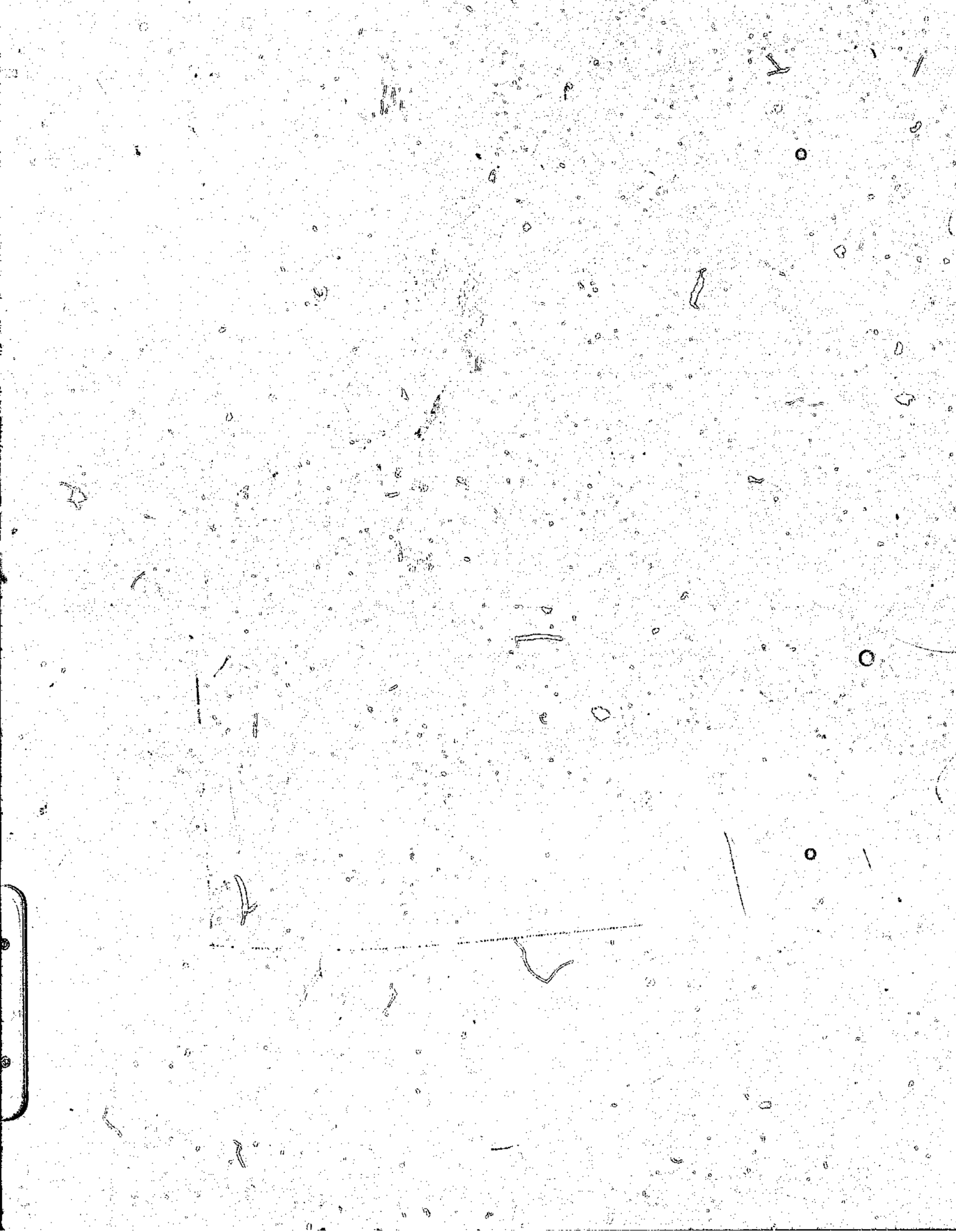
[23] M.A. Paalanen, A.E. Ruckenstein, and G.A. Thomas, Phys. Rev. Lett. 54, 1295 (1985).

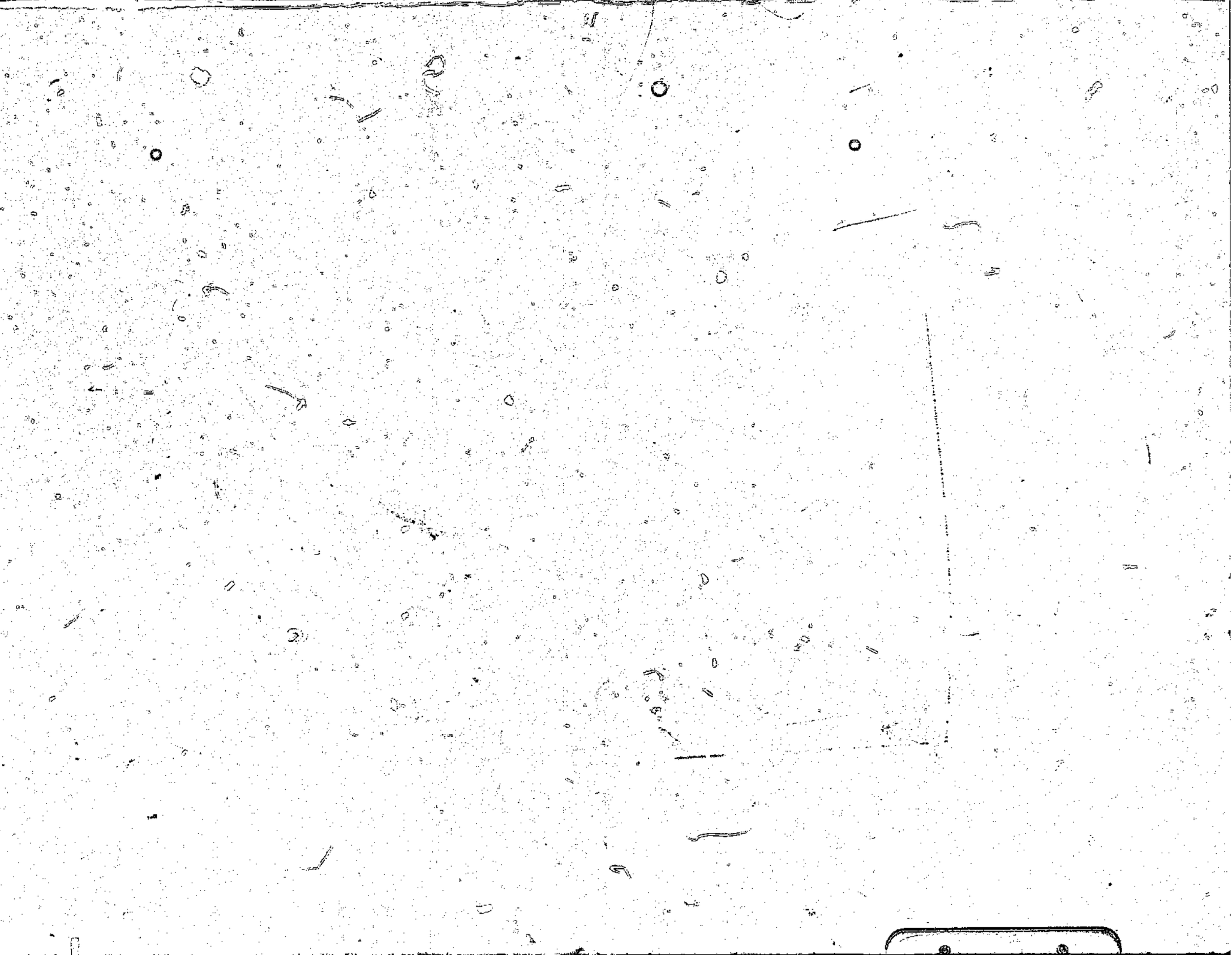
[24] M.J.R. Hoch and D.F. Holcomb, Phys. Rev. B38, 10550 (1988).

[25] S.T. Stoddart, M.J.R. Hoch, and U. Thomanschefsky, Phys. Rev. B46, 10007 (1992).

[26] M. Milovanivić, S. Sachdev, and R. N. Bhatt, Phys. Rev. Lett. 63, 82 (1989).

[27] R.N. Bhatt and D.S. Fisher, Phys. Rev. Lett. 68, 3072 (1992).





Author: Kasl Charles.
Name of thesis: Thermodynamics of metal-insulator systems.

PUBLISHER:
University of the Witwatersrand, Johannesburg
©2015

LEGALNOTICES:

Copyright Notice: All materials on the University of the Witwatersrand, Johannesburg Library website are protected by South African copyright law and may not be distributed, transmitted, displayed or otherwise published in any format, without the prior written permission of the copyright owner.

Disclaimer and Terms of Use: Provided that you maintain all copyright and other notices contained therein, you may download material (one machine readable copy and one print copy per page)for your personal and/or educational non-commercial use only.

The University of the Witwatersrand, Johannesburg, is not responsible for any errors or omissions and excludes any and all liability for any errors in or omissions from the information on the Library website.